

**The Investigation of Ultrafast Charge Dynamics within Conjugated Organic Ladder  
Semiconducting Materials for Optoelectronic Applications**

by

Meghan E. Orr

A dissertation submitted in partial fulfillment  
of the requirements for the degree of  
Doctor of Philosophy  
(Chemistry)  
in the University of Michigan  
2024

Doctoral Committee:

Professor Theodore G. Goodson III, Chair  
Professor Kevin Kubarych  
Professor Peter Ma  
Professor Paul Zimmerman

Meghan E. Orr

meorr@umich.edu

ORCID iD: 0009-0006-7095-3087

© Meghan E. Orr 2024

## **Dedication**

I would like to dedicate my PhD dissertation to my family. Their love and support have carried me throughout my entire life up to this very moment. I am truly grateful and blessed to have my family.

Thank you for your constant love and support, I love you all.

## **Acknowledgments**

I would like to thank my PhD advisor, Professor Theodore G. Goodson III for his support and guidance throughout the years. My interest in academic research began when I was an undergraduate researcher in Professor Goodson's lab in 2010. I am grateful that he gave me the opportunity to join his lab and have an undergraduate research experience, and it is because of that opportunity that I am on the career path that I am now.

Not only did this experience expand my academic universe, it also showed me the value of mentoring. During this experience, I had two great mentors who took the time to teach me research skills and leadership skills. I will forever be grateful to them for the advice and counsel they provided to me as an undergraduate researcher. Their mentorship has helped me be successful in my endeavors and gave me skills that I can use in any professional environment. Thank you, Professor Goodson and my mentors for giving me a strong foundation.

I would also like to thank my committee members: Professor Paul Zimmerman; Professor Kevin Kubarych; and Professor Peter Ma for their guidance and support during my PhD degree. I truly appreciate the time and attention you have accorded me during this time. Your support and dedication have molded me into the researcher I am today. In addition, I would like to thank my collaborators from University of Washington and University of Texas A&M for their scientific advice and guidance on research investigations. Also, I would be remiss if I didn't thank research funding agencies who have provided me financial support during my PhD.

I would like to thank all the Goodson group members that I have met during my PhD degree. These relationships began when I started as a rotator during my first year of graduate school and lasted to this very day to my PhD degree. None of this would be possible without them.

Finally, and most importantly, I would like to thank my entire family: my parents; my brother and his family; my grandparents; my uncles; my aunts; and my cousins. Thank you for everything that you have done for me over the years, I truly appreciate it.

## Table of Contents

<b>Dedication</b> .....	ii
<b>Acknowledgments</b> .....	iii
<b>List of Figures</b> .....	ix
<b>List of Tables</b> .....	xvii
<b>List of Equations</b> .....	xx
<b>List of Appendices</b> .....	xxi
<b>List of Abbreviations</b> .....	xxii
<b>Abstract</b> .....	xxiv
<b>Chapter I Introduction</b> .....	1
<b>I.1 Overview of Scientific Background</b> .....	1
<b>I.2 Motivation of Solar Energy</b> .....	2
<b>I.3 History of Solar Energy and Photovoltaic (PV) Devices</b> .....	4
<b>I.4 How Optoelectronic Application of Solar Energy Works</b> .....	6
<b>I.5 Generating Electrical Charges in a PV Device</b> .....	8
<b>I.6 Power Conversion Efficiency – Numerical Quantitation of Charge Generation</b> .....	10
<b>I.7 Overview of Materials Used in Optoelectronic Application of Solar Energy</b> .....	14
<b>I.8 Introducing the Optoelectronic Application of Organic Photovoltaic (OPV) Devices</b> <b>18</b>	
I.8.a Progression of Donor Material Structural Design in OPVs.....	20
I.8.b Progression of Acceptor Material Structural Design in OPVs – Nonfullerene Acceptor (NFA) .....	22
I.8.c Organic Ladder Materials Use in Optoelectronic Applications .....	24
<b>I.9 Ultrafast Spectroscopy and Investigating Charge Generation of Materials Used in     OPVs</b> 24	
<b>I.10 Synopsis of Dissertation Chapters</b> .....	29
<b>I.11 References</b> .....	33
<b>Chapter II Experimental Section</b> .....	37
<b>II.1 Overview</b> .....	37

<b>II.2 Steady-State Absorption</b> .....	37
II.2.a Introduction and Description of Steady-State Absorption.....	37
II.2.b General Description of Steady-State Absorption Experimental Setup.....	38
<b>II.3 Steady-State Emission Measurement</b> .....	40
II.3.a Introduction and Description of Steady-State Emission .....	40
II.3.b General Description of Steady-State Emission Experimental Setup .....	41
<b>II.4 Femtosecond Transient Absorption</b> .....	42
II.4.a Introduction to femtosecond transient absorption (fs-TA) and transient absorption (TA).....	42
II.4.b Description and Theory of TA and fs-TA.....	43
II.4.b.i Description of Three Main Signals Observed in TA Spectrum.....	46
II.4.c Laser Experimental Setup of fs-TA .....	50
II.4.d Transient Box Experimental Setup of fs-TA .....	51
II.4.e Data Analysis of fs-TA .....	52
<b>II.5 Time-resolved femtosecond Fluorescence Upconversion</b> .....	52
<b>II.6 References</b> .....	54
<b>Chapter III The Investigation of Ultrafast Dynamics for Organic Conjugated Ladder Oligomers Used in Optoelectronics Applications</b> .....	56
<b>III.1 Collaboration Statement</b> .....	56
<b>III.2 Abstract</b> .....	56
<b>III.3 Introduction</b> .....	57
<b>III.4 Experimental Section</b> .....	61
III.4.a Sample Preparation Information .....	61
III.4.b Steady-State Absorption and Emission.....	61
III.4.c femtosecond Transient Absorption.....	62
<b>III.5 Results Section</b> .....	64
III.5.a Steady-state Absorption and Emission Results .....	64
III.5.b femtosecond Transient Absorption Results.....	66
III.5.b.i High Energy Excitation Wavelength fs-TA Results.....	66
III.5.b.ii Middle Energy Excitation Wavelength fs-TA Results .....	70
III.5.b.iii Low Energy Excitation Wavelength fs-TA Results .....	73
<b>III.6 Discussion</b> .....	75
<b>III.7 Conclusion</b> .....	82
<b>III.8 References</b> .....	84

<b>Chapter IV Probing the Exciton Dynamics of Naphthalene-imide Based Nonfullerene Acceptors for Organic Photovoltaics</b> .....	90
<b>IV.1 Collaboration Statement</b> .....	90
<b>IV.2 Abstract</b> .....	91
<b>IV. 3 Introduction</b> .....	92
<b>IV.4 Experimental Section</b> .....	95
IV.4.a Steady-State Absorption and Emission Measurements .....	95
IV.4.b Fluorescence Quantum Yield Measurements .....	95
IV.4.c Two-photon Absorption Experiments.....	96
IV.4.d Time-resolved Fluorescence Upconversion .....	97
IV.4.e. femtosecond Transient Absorption.....	98
IV.4.f. Theoretical Calculations .....	100
<b>IV.5 Results</b> .....	100
IV.5.a. Steady-State Results of BNIAs .....	100
IV.5.b Two-photon absorption (TPA) Results of BNIAs .....	103
IV.5.c Time resolved Fluorescence Upconversion (UpC) Results of BNIAs .....	104
IV.5.d Femtosecond Transient Absorption (fs-TA) Results of BNIAs .....	105
IV.5.e Theoretical Calculations of BNIAs .....	111
<b>IV.6 Discussion</b> .....	114
<b>IV.7 Conclusion</b> .....	118
<b>IV.8 References</b> .....	119
<b>Chapter V Linear and Nonlinear Optical Properties of All-<i>cis</i> and All-<i>trans</i> Poly(<i>p</i>-phenylene vinylene)</b> .....	122
<b>V.1 Collaboration Statement</b> .....	122
<b>V.2 Abstract</b> .....	123
<b>V.3 Introduction</b> .....	124
<b>V.4 Experimental Section</b> .....	128
V.4.a Synthesis of Monomers and Polymers .....	128
V.4.b Entangled Two-Photon Absorption.....	128
<b>V.5 Result and Discussion</b> .....	129
V.5.a Design and synthesis of PPVs for this study .....	129
V.5.b Steady-state absorption and emission:.....	131
V.5.c Classical Two-Photon Absorption .....	132
V.5.d Time-resolved Fluorescence Upconversion .....	135



V.5.e Femtosecond Transient Absorption .....	136
V.5.f Entangled Two-photon Absorption .....	139
<b>V.6 Conclusion</b> .....	144
<b>V.7 References</b> .....	145
<b>Chapter VI Effect of Long-Lived Ground State Diradicaloids on the Photophysics of Semi-Ladder Thiophene-Based Polymer Aggregates for Organic Light Emitting Transistor (OLET) Applications</b> .....	150
<b>VI.1 Collaboration Statement</b> .....	150
<b>VI.2 Abstract</b> .....	151
<b>VI.3 Introduction</b> .....	152
<b>VI.4 Results</b> .....	158
VI.4.a Steady State Measurements .....	158
VI.4.b Two-photon Absorption or Two-photon Excited Fluorescence .....	162
VI.4.c Time-resolved Measurements .....	163
VI.4.d Transient Absorption Spectroscopy .....	166
VI.4.e Electron Paramagnetic Resonance (EPR) Spectroscopy .....	171
VI.4.f Quantum Chemical Calculations.....	172
<b>VI.5 Discussion</b> .....	175
<b>VI.6 Conclusion</b> .....	181
<b>VI.7 References</b> .....	183
<b>Chapter VII Summary of Dissertation and Future Outlook</b> .....	188
<b>VII.1 Summary of dissertation</b> .....	188
VII.1.a Summary of main results and conclusions of Chapters III – VI .....	189
<b>VII.2 Future Outlook of Research Investigating Organic Semiconducting Materials for Optoelectronic Applications</b> .....	192
<b>VII.3 Future Outlook of Ultrafast Laser Spectroscopy Research</b> .....	193
<b>VII.4 References</b> .....	196
<b>Appendices</b> .....	198

## List of Figures

- Figure I.1:** General picture of devices that are powered by solar energy. Example of solar powered devices demonstrated in this Figure are solar panels. Solar panels consist of individual nonmechanical devices called photovoltaics (PVs). Solar panels and PVs in these panels are mainly consist of silicon. Solar panels are one example of an optoelectronic application that utilizes solar energy. Citation: this Figure consists of online images from Microsoft PowerPoint – specifically, the grass and sky. .... 3
- Figure I.2:** General schematic of how the optoelectronic application of solar energy works: **Step 1)** Absorption of electromagnetic radiation of Sun (Sunlight); **Step 2)** Generating electrical charges; and **Step 3)** Creating electricity ..... 7
- Figure I.3:** General schematic showing the steps on charge generation that occurs between the two materials in a PV device. .... 9
- Figure I.4:** General schematic of a current-voltage (JV) curve. .... 10
- Figure I.5:** General visualization of charge generation occurring in a photovoltaic (PV) device between the two materials in a PV. The PV device is an example of organic photovoltaic (OPV) device. .... 17
- Figure I.6:** General schematic of an organic photovoltaic (OPV) device. The two materials in the active layer of the OPV device is Donor material: poly(3-hexylthiophene (P3HT) and Acceptor material: phenyl-C-butyric acid methyl ester derivative (PCBM) (which is also known as fullerene). An OPV device consists of many layers and materials that will generate charges or assist with separating and collecting charges that will be used to create electricity. .... 18
- Figure I.7:** General visualization of charge generation occurring with a Donor material that has a donor-acceptor structural framework. In this **Figure**, the example of Donor material with a donor-acceptor structural frame is poly[[4,8-bis[(2-ethylhexyl)oxy]benzo[1,2-b:4,5-b']dithiophene-2,6-diyl][3-fluoro-2 [(2ethylhexyl)carbonyl]thieno[3,4-b]-thiophenediyl]], (PTB7) polymer. The charge generation that is occurring within PTB7 can be considered as intramolecular charge generation..... 20
- Figure I.8:** Showing the historical progression in structural design of Donor and Acceptor materials used in organic photovoltaic (OPV) devices. **a)** in 2004, Donor and Acceptor materials: poly(3-hexylthiophene (P3HT) and Acceptor material: phenyl-C-butyric acid methyl ester derivative (PCBM); **b)** in 2010, Donor and Acceptor materials, poly[[4,8-bis[(2-ethylhexyl)oxy]benzo[1,2-b:4,5-b']dithiophene-2,6-diyl][3-fluoro-2 [(2ethylhexyl)carbonyl]thieno[3,4-b]-thiophenediyl]], (PTB7) polymer and PCBM; **c)** in 2011, Donor and Acceptor materials, P3HT and 4,7-bis(4-(N-hexyl-phthalimide)vinyl)benzo- [c]1,2,5-thiadiazole: (PI-BT). .... 22
- Figure II.1:** General schematic of steady-state absorption measurement. This figure is showing the main pieces of equipment required to conduct this measurement. Please note this schematic is not draw to scale or show accurate depiction of the steady-state absorption measurement. .... 38

<b>Figure II.2:</b> Steady-state absorption spectrum of a Coumarin 30, a reference laser dye, in methanol .....	39
<b>Figure II.3:</b> General schematic of steady-state emission spectrum .....	40
<b>Figure II.4:</b> General schematic of steady-state emission measurement. This figure is showing the main pieces of equipment required to conduct this measurement. Please note this schematic is not draw to scale or show accurate depiction of the steady-state absorption measurement .....	41
<b>Figure II.5:</b> General schematic of TA .....	42
<b>Figure II.6:</b> General schematic of three main signals in a transient absorption (TA) experiment	46
<b>Figure II.7:</b> General schematic of the fs-TA experimental setup in Goodson lab at the University of Michigan.....	50
<b>Figure II.8:</b> General schematic of time-resolved fluorescence upconversion experimental setup in the Goodson lab .....	53
<b>Figure III.1:</b> Structures of the BTps: BTP-5 on Top and has a <b>black</b> label; BTP-7 on the Bottom and has a <b>blue</b> label.....	60
<b>Figure III.2:</b> Steady-state absorption and emission spectra of BTP-5 and BTP-7 solutions in chloroform.....	64
<b>Figure III.3:</b> femtosecond transient absorption (fs-TA) spectra, from 0ps – ~1.0ps, of BTps obtained from high energy excitation wavelength: <b>a)</b> BTP-5 and <b>b)</b> BTP-7 .....	67
<b>Figure III.4:</b> femtosecond transient absorption (fs-TA) kinetic traces of BTps obtained from high energy excitation wavelength .....	69
<b>Figure III.5:</b> femtosecond transient absorption (fs-TA) spectra, from 0ps – 2ps, of BTps obtained from middle energy excitation wavelength: <b>a)</b> BTP-5 and <b>b)</b> BTP-7 .....	70
<b>Figure III.6:</b> femtosecond transient absorption (fs-TA) kinetic traces of BTps obtained from middle energy excitation wavelength .....	72
<b>Figure III.7:</b> femtosecond transient absorption (fs-TA) spectra, from 0ps – 2ps, of BTps obtained from middle energy excitation wavelength: <b>a)</b> BTP-5 and <b>b)</b> BTP-7 .....	73
<b>Figure III.8:</b> femtosecond transient absorption (fs-TA) kinetic traces of BTps obtained from low energy excitation wavelength .....	74
<b>Figure IV.1:</b> Molecular structures of BNIAAs: NITV (non-FREA) colored <b>green</b> , NIDT (FREA) highlighted <b>red</b> , and NIBT (FREA) highlighted <b>blue</b> . The terminal acceptor moiety, naphthalene imide, is colored <b>black</b> in all the BNIAAs, which have an acceptor – donor– acceptor architecture. ....	93
<b>Figure IV.2:</b> Normalized absorption and emission spectra of BNIAAs in chloroform – <b>a)</b> absorption spectra and <b>b)</b> emission spectra. The excitation wavelengths used to measure emission spectra are 560nm for NITV and NIDT and 600nm for NIBT. ....	100
<b>Figure IV.3:</b> Log-log plot of NITV in chloroform obtained from two-photon absorption (TPA) experiments using 650nm emission.....	104
<b>Figure IV.4:</b> Kinetic traces of the BNIAAs in chloroform obtained from time-resolved fluorescence upconversion (UpC) experiments .....	105

<b>Figure IV.5:</b> Time-resolved femtosecond transient absorption (fs-TA) spectra of NIBT in chloroform using 600nm pump. The recovery or decay of ground state bleach (GSB) signal is shown using golden/yellow arrow. The decay of excited state absorption (ESA) signal is shown using red arrows.....	106
<b>Figure IV.6:</b> Comparison of steady-state absorption spectrum to the early time of ground state bleach (GSB) spectrum from femtosecond transient absorption (fs-TA) results of NITV in chloroform using 600nm excitation.....	108
<b>Figure IV.7:</b> Comparison of excited state absorption (ESA) signals of BNIAs at a specific time. The time-resolved femtosecond transient absorption (fs-TA) spectra is normalized to the highest value in ground state bleach (GSB) at a specific time. <b>Figure D.10</b> in Appendix D shows the unnormalized spectra.....	109
<b>Figure IV.8:</b> Kinetics of ground state bleach (GSB) signals and reported decays ( $\tau_3$ ) from femtosecond transient absorption (fs-TA) of BNIAs in chloroform using 600nm excitation. <b>Inserted Graph:</b> shows full scale of kinetics of GSB signals and GSB decay ( $\tau_3$ ) of NIBT....	110
<b>Figure IV.9:</b> Kinetics of excited state absorption (ESA) signals from femtosecond transient absorption (fs-TA) of BNIAs in chloroform using 600nm – <b>a)</b> NITV; <b>b)</b> NIDT and <b>c)</b> NIBT. <b>Inserted Graph:</b> zoomed in scale of kinetics of ESA signals, showing the rise time, $\tau_{\text{rise}}$ , of ESA signals.....	110
<b>Figure IV.10:</b> Calculated excited state and HOMO/LUMO of BNIAs from time-dependent density functional theory (TD-DFT) using B3LYP/6-31G(d,p): <b>a)</b> NITV; <b>b)</b> NIDT ;and <b>c)</b> NIBT.....	111
<b>Figure IV.11:</b> Proposed mechanism of the intramolecular charge generation mechanism of the BNIAs.....	115
<b>Figure V.1:</b> Schematic energy diagram of a two-photon absorption process happens from ground state (GS) through virtual state (VS) to two-photon excited state (ES). The olefin geometry of all-trans PPV and all-cis PPV investigated here is also shown.....	126
<b>Figure V.2:</b> Synthesis of diblock copolymers containing either an all-cis or an all-trans PPV segment: Sequential stereoretentive ROMP of monomers <b>1</b> and <b>2</b> using catalyst <b>Ru-St</b> delivered poly-cis- <b>1-b-cis-2</b> . Subsequent PPV-selective photoisomerization afforded poly-cis- <b>1-b-trans-2</b> . .....	130
<b>Figure V.3:</b> Normalized steady state absorption ( $C = 25.0$ and $12.5 \mu\text{g/mL}$ , respectively) and emission ( $C = 4.2$ and $1.6 \text{ ng/mL}$ , respectively) spectra of poly-cis- <b>1-b-cis-2</b> and poly-cis- <b>1-b-trans-2</b> in chloroform. Excitations for poly-cis- <b>1-b-cis-2</b> and poly-cis- <b>1-b-trans-2</b> were 389 and 442 nm, respectively.....	131
<b>Figure V.4:</b> <b>(a)</b> Excitation power dependent classical TPA fluorescence (at 520 nm) and <b>(b)</b> two-photon excited fluorescence spectra of the investigated compounds. The excitation wavelength was 800 nm.....	134
<b>Figure V.5:</b> Fluorescence decay traces of poly-cis- <b>1-b-cis-2</b> and poly-cis- <b>1-b-trans-2</b> at the emissive wavelength of 517 nm after excitation at 400 nm. Inset are the emissive decay traces in 10 ps time window.....	135
<b>Figure V.6:</b> Femtosecond transient absorption spectra (fsTAS) for poly-cis- <b>1-b-cis-2</b> <b>(a)</b> and poly-cis- <b>1-b-trans-2</b> <b>(b)</b> corroborated with steady state absorption and emission spectra. Lower panel	

shows time traces of poly-cis-1-b-cis-2 and poly-cis-1-b-trans-2 in 1.6 ns and 20 ps (inset) time windows. The excitation wavelength for both compounds was 400 nm. .... 137

**Figure V.7:** Entangled two-photon absorption as a function of input photon flux (i.e., excitation power) for poly-cis-1-b-cis-2 and poly-cis-1-b-trans-2 in chloroform solution. ETPA scales linearly with the input photon flux, rather than quadratically for classical TPA. The linear trend yields an enhancement in the absorption rate at low input intensities compared to classical TPA. The ETPA rate is determined to be the difference between the photon counts per second transmitted through the solvent (chloroform) and the sample (PPVs) solution for a given input photon flux. .... 140

**Figure V.8:** Frontier molecular HOMO-1 through LUMO+1 orbitals of trans- (left panel) and cis-PPV (right panel) calculated at the CAM-B3LYP-D3/6-311+G(d,p)-SMD(CHCl<sub>3</sub>) level of theory. .... 143

**Figure VI.1:** Structures of the investigated polymers (TPTQ\_C and TPTQF\_C and their respective resonant forms) as well as the TPTQ Acceptor. .... 157

**Figure VI.2:** Absorption (a.) and emission (b) spectra of the two investigated polymers as well as the parent thiophene-based acceptor. .... 158

**Figure VI.3:** Two photon emission spectra (a.) and power dependence of the two photon excited emission (b.) of the investigated polymers in chloroform upon 800 nm excitation. .... 162

**Figure VI.4:** Fluorescence decay lifetimes of the investigated polymers obtained using time correlated single photon counting experiments. The inset shows the decay dynamics at earlier times. .... 163

**Figure VI.5:** Ultrafast fluorescence kinetics of the investigated polymers and TPTQ Acceptor using fluorescence upconversions. .... 165

**Figure VI.6:** Time resolved nanosecond transient absorption (nsTA) spectra of the investigated polymers with UV excitation of ~2.3 mJ. .... 167

**Figure VI.7:** Nanosecond transient absorption ESA kinetics of the investigated polymers with UV excitation of ~2.3 mJ. .... 168

**Figure VI.8:** Time resolved femtosecond transient absorption (fsTA) spectra of both the TPTQ\_C and TPTQF\_C polymers, as well as the TPTQ Acceptor at 348 nm excitation. .... 170

**Figure VI.9:** Electron paramagnetic resonance (EPR) measurements of the investigated molecules. On the right, the TPTQ\_C measurements were repeated at a lower concentration. .... 171

**Figure VI.10:** NTOs for TPTQ\_C, TPTQF\_C, and TPTQ acceptors.  $\lambda$  indicates the eigenvalue of the transition. .... 173

**Figure VI.11:** Structure for TPTQ\_C (X=S) and TPTQF\_C (X=O). .... 174

**Figure VI.12:** Mulliken spin densities for TPTQ\_C, TPTQF\_C, and TPTQ acceptor. Absolute values greater than 0.3 are labelled near the associated atoms. .... 174

**Figure VI.13:** EPR data of the TPTQ\_C compound analyzed. .... 179

**Figure VI.14:** Proposed energy level diagram for the diradicaloids observed for the TPTQ\_C and the zwitterions formed in the case of the TPTQF\_C. .... 180

<b>Figure C.1:</b> Normalized steady-state absorption spectra of the BTp solutions in chloroform from 200nm – 700nm. The purpose of this Figure is to show the capabilities of new UV-Vis spectrophotometer, Agilent Cary 60 UV-Vis Spectrophotometer. The new UV-Vis spectrophotometer has the capability of measuring a steady-state absorption spectrum from 190nm – 1100nm. For the steady-state absorption measurements of the BTp solutions, the range of 200nm – 700nm was used. ....	210
<b>Figure C.2:</b> Showing the location of the $\beta$ -, p- and $\alpha$ - bands on the normlized steady-state absorption spectra of BTp solutions in chloroform .....	211
<b>Figure C.3:</b> Normalized steady-state absorption and emission spectra of the <b>BTp</b> solutions in chloroform on one graph: <b>(a)</b> BTp-5, for emission spectrum, 310nm excitation is utilized and <b>(b)</b> BTp-7, for emission spectrum, 332nm excitation is utilized .....	211
<b>Figure C.3 (continued):</b> Normalized steady-state absorption and emission spectra of the BTp solutions in chlorofomr on one graph: <b>(a)</b> BTp-5, for emission spectrum, 310nm excitation is utilized and <b>(b)</b> BTp-7, for emission spectrum, 332nm excitation is utilized.....	212
<b>Figure C.4:</b> Normalized steady-state emission spectra of BTp solutions in chloroform obtained from different excitation wavelengths: <b>(a)</b> BTp-5 and <b>(b)</b> BTp-7. The emisson spectra is not dependent on excitation wavelength for both BTps. ....	212
<b>Figure C.4 (continued):</b> Normalized steady-state emission spectra of BTp solutions in chloroform obtained from different excitation wavelengths: <b>(a)</b> BTp-5 and <b>(b)</b> BTp-7. The emisson spectra is not dependent on excitation wavelength for both BTps solutions.....	213
<b>Figure C.5:</b> General schematic of ultraviolet (UV) and visible (Vis) femtosecond transient absorption (fs-TA) utilized to conducted experiments on BTp solutions. The UV probe is an extension to Vis probe fs-TA experiment used in previous studies. The UV probe is generated from a calcium fluoride (CaF <sub>2</sub> ) crystal. The range of the UV probe is 350nm – 750nm. ....	214
<b>Figure C.6:</b> Time-resolved femtosecond transient absorption (fs-TA) spectra, from 0ps (pre-pump baseline) – 1.3ns, of BTp solutions obtained from $\beta$ -band pump excitation wavelength: <b>(a)</b> BTp-5 and <b>(b)</b> BTp-7.....	214
<b>Figure C.6 (continued):</b> Time-resolved femtosecond transient absorption (fs-TA) spectra, from 0ps (pre-pump baseline) – 1.4ns of <b>BTp</b> solutions obtained from $\beta$ -band pump excitation wavelength: <b>(a)</b> <b>BTp-5</b> and <b>(b)</b> <b>BTp-7</b> .....	215
<b>Figure C.7:</b> Comparing differences in ESA signals from roughly 1.2ps to 1.4ns obtained from $\beta$ -band pump excitation wavelength of BTp solutions: <b>(a)</b> BTp-5 and <b>(b)</b> BTp-7 .....	215
<b>Figure C.7 (continued):</b> Comparing differences in ESA signals from roughly 1.2ps to 1.4ns obtained from $\beta$ -band pump excitation wavelength of BTp solutions: <b>(a)</b> BTp-5 and <b>(b)</b> BTp-7 .....	216
<b>Figure C.8:</b> Time-resolved femtosecond transient absorption (fs-TA) spectra, from 0ps (pre-pump baseline) – 1.4ns, of BTp solutions obtained from p-band pump excitation wavelength: <b>(a)</b> BTp-5 and <b>(b)</b> BTp-7 .....	217
<b>Figure C.9:</b> Time-resolved femtosecond transient absorption (fs-TA) spectra, from 0ps (pre-pump baseline) – 1.4ns of BTp solutions obtained from $\alpha$ -band pump excitation wavelength: <b>(a)</b> BTp-5 and <b>(b)</b> BTp-7 .....	218

<b>Figure C.9 (continued):</b> Time-resolved femtosecond transient absorption (fs-TA) spectra, from 0ps (pre-pump baseline) – 1.4ns of BTp solutions obtained from $\alpha$ -band pump excitation wavelength: <b>(a)</b> BTp-5 and <b>(b)</b> BTp-7.....	219
<b>Figure D.1:</b> Normalized emission spectra of BNIA in chloroform due to different excitation wavelengths – a) NITV; b) NIDT; and c) NIBT. For all BNIA, the emission maximum peak is not dependent on excitation wavelength.....	221
For all BNIA, the emission spectra measured by 600nm excitation is reported in the paper. ..	221
<b>Figure D.1 (continued):</b> Normalized emission spectra of BNIA in chloroform due to different excitation wavelengths – a) NITV; b) NIDT; and c) NIBT. For all BNIA, the emission maximum peak is not dependent on excitation wavelength.....	222
For all BNIA, the emission spectra measured by 600nm excitation is reported in the paper. ..	222
<b>Figure D.2:</b> Corrected emission spectra of BNIA in chloroform due to 400nm excitation. ....	222
<b>Insert graph:</b> Shows uncorrected emission spectra of BNIA. The additional peak at 800nm is a result of second harmonic generation due to 400nm excitation. ....	222
<b>Figure D.3:</b> Normalized absorbance and emission spectra of BNIA in chloroform. The emission spectra is corrected emission spectra due to 400nm excitation. ....	223
<b>Figure D.4:</b> Two-absorption emission spectra of BNIA using 800nm excitation from two-photon absorption (TPA) experiment.....	224
<b>Figure D.5:</b> Log-log plot of NIDT in chloroform obtained from two-photon absorption (TPA) experiments using 650nm emission.....	224
<b>Figure D.6:</b> Normalized time-resolved fluorescence upconversion (UpC) kinetics of BNIA in chloroform using 400nm excitation. For all BNIA, 650nm emission is used to measure fluorescence kinetics.....	226
<b>Insert Graph:</b> Shows rise time of fluorescence decay for all BNIA. ....	226
**The long <i>trise</i> is due to the samples being run to reflective mode of UpC.....	226
<b>Figure D.7:</b> Time-resolved femtosecond transient absorption (fs-TA) spectra of BNIA in chloroform using 600nm pump – <b>a)</b> NITV and <b>b)</b> NIDT. The recovery of ground state bleach (GSB) signal is shown using golden/yellow arrows in all three BNIA. The decay of excited state absorption (ESA) signal(s) is shown using red arrows.....	227
The time-resolved fs-TA of NIBT is reported in the paper (see <b>Figure 5</b> ).....	227
<b>Figure D.8:</b> Comparison of steady-state absorption spectrum to the early time of ground state bleach (GSB) signal from femtosecond transient absorption (fs-TA) results of BNIA in chloroform using 600nm excitation – <b>a)</b> NIDT and <b>b)</b> NIBT.....	228
The comparison of steady-state absorption spectrum to early time of GSB signal of NITV is reported in the paper.....	228
<b>Figure D.9:</b> Comparison of femtosecond transient absorption (fs-TA) excited state absorption (ESA) signals of BNIA in chloroform at a specific time using 600nm pump. This figure shows the un-normalized femtosecond transient absorption (fs-TA) spectra.....	229
**Rate: shows that rate of $\tau_3$ time component.....	229

*time component cannot be resolved since the components are within IRF (160fs) .....	230
**time component cannot be resolved due to the large standard deviation.....	230
<b>Figure D.10:</b> Kinetics of excited state absorption (ESA) signals from femtosecond transient absorption (fs-TA) of BNIA in chloroform using 600nm – <b>a)</b> NITV; <b>b)</b> NIDT and <b>c)</b> NIBT ..	230
<b>Insert Graph:</b> zoomed in scale of kinetics of ESA signals, showing the rise time, $\tau_{rise}$ , of ESA signals .....	230
<b>Figure D.10 (continued):</b> Kinetics of excited state absorption (ESA) signals from femtosecond transient absorption (fs-TA) of BNIA in chloroform using 600nm – <b>a)</b> NITV; <b>b)</b> NIDT and <b>c)</b> NIBT .....	231
<b>Insert Graph:</b> zoomed in scale of kinetics of ESA signals, showing the rise time, $\tau_{rise}$ , of ESA signals .....	231
* $\tau_{rise}$ *: this time component cannot be resolved, since it is within the IRF (160fs). Since this time component cannot be resolved, it is not the main rise time of the ESA. This time component helped fit the data.....	232
**Rate: shows that rate of $\tau_1$ time component .....	232
* $\tau_{rise}$ *: this time component cannot be resolved, since it is within the IRF (160fs). Since this time component cannot be resolved, it is not the main rise time of the ESA. This time component is helpful to fit the data. ....	232
<b>Figure D.11:</b> Comparison of steady-state emission spectra to femtosecond transient absorption (fs-TA) excited state absorption (ESA) spectra of BNIA in chloroform using 600nm pump – <b>a)</b> NITV; <b>b)</b> NIDT and <b>c)</b> NIBT.....	233
<b>Figure D.11 (continued):</b> Comparison of steady-state emission spectra to femtosecond transient absorption (fs-TA) excited state absorption (ESA) spectra of BNIA in chloroform using 600nm pump – <b>a)</b> NITV; <b>b)</b> NIDT and <b>c)</b> NIBT.....	234
<b>Figure D.12:</b> Comparing early time femtosecond transient absorption (fs-TA) spectra to a later time fs-TA– <b>a)</b> NITV; <b>b)</b> NIDT and <b>c)</b> NIBT. By comparing two times, this shows approximation of percentage of exciton generated to transfer to charge transfer (CT) state (ESA signal) and have the potential to become free charges.....	234
<b>a)</b> NITV: approximately 10%; <b>b)</b> NIDT: approximately 15%; and <b>c)</b> NIBT: approximately 40% .....	234
The approximation is determined by normalizing the early time of fs-TA spectra to the highest value. Then, dividing later time fs-TA spectrum by the highest value for the early time fs-TA spectrum.....	235
<b>Figure D.12 (continued):</b> Comparing early time femtosecond transient absorption (fs-TA) spectra to a later time fs-TA– <b>a)</b> NITV; <b>b)</b> NIDT and <b>c)</b> NIBT. By comparing two times, this shows approximation of percentage of exciton generated to transfer to charge transfer (CT) state (ESA signal) and have the potential to become free charges.....	235
<b>a)</b> NITV: approximately 10%; <b>b)</b> NIDT: approximately 15%; and <b>c)</b> NIBT: approximately 40% .....	235



The approximation is determined by normalizing the early time of fs-TA spectra to the highest value. Then, dividing later time fs-TA spectrum by the highest value for the early time fs-TA spectrum..... 236

The normalized spectra is reported in paper. For all BNIA, the fs-TA spectra are normalized to the highest value of ground state bleach (GSB) signal in the spectra..... 236

**Figure D.13:** Calculated higher excited states of lowest occupied molecular orbitals – LUMO+1, LUMO+2 and LUMO+3 – of BNIA from time-dependent density functional theory (TD-DFT) using B3LYP/6-31G(d,p) – **a)** NITV; **b)** NIDT; and **c)** NIBT ..... 239

## List of Tables

<b>Table I.1:</b> Summary of power conversion efficiency over the years, showing the impact of donor-acceptor structural framework design on Donor and Acceptor materials used in organic photovoltaic (OPV) devices. Figure I.11 shows structures for some of materials listed in this Table. ....	23
<b>Table III.1:</b> Shows the steady-state peaks and energy excitation wavelengths utilized in femtosecond transient absorption (fs-TA) experiments of BTps solutions .....	65
a) steady-state absorption and emission peaks of BTps in chloroform solution.....	65
b) energy excitation wavelengths utilized in the fs-TA experiments of BTps .....	65
<b>Table III.2:</b> Time components obtained from femtosecond transient absorption (fs-TA) of BTps due to high energy excitation wavelength .....	70
<b>Table III.3:</b> Time components obtained from femtosecond transient absorption (fs-TA) of BTps due to middle energy excitation wavelength .....	72
<b>Table III.4:</b> Time components obtained from femtosecond transient absorption (fs-TA) of BTps due to low energy excitation wavelength.....	75
<b>Table IV.1:</b> Summary of steady-state absorption and emission maximum peaks and fluorescence lifetimes ( $\tau_{\text{fluor}}$ ) of BNIAAs .....	103
<b>Table IV.2:</b> Summary of time components in picosecond (ps) of ground state bleach (GSB) and excited state absorption (ESA) signals from femtosecond transient absorption (fs-TA) results of BNIAAs in chloroform. See <b>Tables D.5 – D.8</b> in Appendix D for complete summary of time components (rise and decay times), amplitudes, and rates .....	111
<b>Table IV.3:</b> Summary of the Stokes Shift, and reorganization energy of $\lambda_{\text{EXC-CT}}$ , $\lambda_{\text{EMS-CT}}$ and calculated ( $\lambda$ ) of BNIAAs .....	117
$\lambda_{\text{EXC-CT}}$ : energy difference between exciton ( $S_{\text{EXC}}$ ) and charge transfer states $S_{\text{CT}}$ .....	117
$\lambda_{\text{EMS-CT}}$ : energy difference between steady-state emission maximum ( $\lambda_{\text{max}}^{\text{ems}}$ ) and $S_{\text{CT}}$ .....	117
<b>Table V.1:</b> Steady-state Absorption and Emission Properties of poly-cis-1-b-cis-2 and poly-cis-1-b-trans-2 in chloroform. ....	132
<b>Table V.2:</b> Summary of Classical TPA Cross-sections of the Copolymers in Chloroform .....	134
<b>Table V.3:</b> Summary of the Fluorescence Up-conversion with both Copolymers <sup>a</sup> .....	136
<b>Table V.4:</b> Transient Absorption Data for poly-cis-1-b-cis-2 and poly-cis-1-b-trans-2. <sup>a</sup> .....	139
<b>Table V.5:</b> ETPA Cross-sections for poly-cis-1-b-cis-2 and poly-cis-1-b-trans-2 in chloroform. ....	143

<b>Table VI.1:</b> Linear optical properties for the investigated polymers, TPTQ_C and TPTQF_C, and the TPTQ Acceptor in chloroform. ....	160
<b>Table VI.2:</b> Time resolved excited state lifetime dynamics of the investigated foldable polymers as well as the TPTQ acceptor in chloroform at the underlined wavelengths.....	164
<b>Table VI.3:</b> Ultrafast time resolved excited state lifetime dynamics of the investigated foldable polymers as well as the TPTQ acceptor in chloroform at the underlined wavelengths.....	166
<b>Table VI.4:</b> Purged (p) and unpurged (up) nsTAS ESA and GSB lifetime dynamics of the investigated molecules as well as the TPTQ acceptor in chloroform at their indicated wavelengths. ....	169
<b>Table VI.5:</b> Absorption spectra (nm) for TPTQ_C, TPTQF_C, and TPTQ acceptors from experiment and computational approaches. $S_0$ , $S_1$ , and $T_1$ stand for the singlet ground, first singlet excited, and first triplet excited states, respectively. Values in parentheses indicate oscillator strengths. ....	172
<b>Table VI.6:</b> Partial NPA charges (atomic unit) and bond distances (Å) in the ground and excited states of TPTQ_C and TPTQF_C. ....	174
<b>Table VI.7:</b> Diradical characters of TPTQ_C, TPTQF_C, and TPTQ acceptor, characterized by the unrestricted Hartree Fock (UHF) spin value $\langle S^2 \rangle$ and NOON. ....	175
<b>Table VI.8:</b> Calculated diradical character, $y$ , $\Delta EST$ and $J$ from the steady state measurements and two-photon absorption or two-photon excited fluorescence.....	177
<b>Table C.1:</b> Summary of emission peaks observed in the steady-state emission spectra of the BTP solutions in chloroform.....	210
<b>Table C.2:</b> Summary of time components and rates obtained from kinetic traces due to $\beta$ -band pump excitation wavelength: <b>(a)</b> BTP-5 and <b>(b)</b> BTP-7.....	216
<b>Table C.3:</b> Summary of time components and rates obtained from kinetic traces due to p-band pump excitation wavelength: <b>(a)</b> BTP-5 and <b>(b)</b> BTP-7.....	218
<b>Table D.1:</b> Summary two-photon absorption (TPA) cross sections ( $\delta_{TPA}$ ) and fluorescence quantum yield ( $\Phi_{Fl}$ ) of BNIA in chloroform using 800nm excitation for 640nm and 650nm emission	225
<b>Table D.2:</b> Time-resolved fluorescence upconversion (UpC) time components in picosecond (ps) of BNIA in chloroform.....	226
<b>Table D.3:</b> Time components, in picosecond (ps), of ground state bleach (GSB) signals at 600nm from femtosecond transient absorption (fs-TA) results of BNIA in chloroform using 600nm pump .....	229
*time component cannot be resolved since the component is within IRF (160fs) .....	229
<b>Table D.4:</b> Time components in picosecond (ps) of ground state bleach (GSB) signals at various wavelengths from femtosecond transient absorption (fs-TA) results of BNIA in chloroform using 600nm pump .....	230
<b>Table D.5:</b> Time components in picosecond (ps) of ground state bleach (GSB) and excited state absorption (ESA) signals from femtosecond transient absorption (fs-TA) results of BNIA in chloroform.....	232

**Table D.6:** Time components in picosecond (ps) of ground state bleach (GSB) and excited state absorption (ESA) signals from femtosecond transient absorption (fs-TA) results of BNIA in chloroform..... 232

**Table D.7:** Stokes Shift (difference in nm) and difference between steady-state absorption, emission and ESA peaks ..... 236

The information provides information for the proposed mechanism diagram of the BNIA, **Figure IV.11** in paper..... 236

**Table D.8:** Summary of calculated oscillator strength values from time-dependent density functional theory (TD-DFT) using B3LYP/6-31G(d,p)..... 240

\*\*Vertical transition: positive direction of movement from the ground state to an excited state:  $S_0 \rightarrow S_n$  ..... 240

## List of Equations

<b>Equation I.1</b>	$J_{sc} \times VOC \times FFP_{in} = PCE$ .....	12
<b>Equation II.1</b>	$\log oI  = \log1T = A$ .....	38
<b>Equation II.2</b>	$cl\varepsilon = A$ .....	39
<b>Equation II.3</b>	$\lambda_{ems\ max} - \lambda_{abs\ max} = \Delta\lambda$ .....	41
<b>Equation II.4</b>	$-\logIntensity_{pump} - OnIntensity_{pump} - Off = \Delta A$ .....	45
<b>Equation III.1</b>	$1\tau_1 + 1\tau_2 = k_1 + k_2 = k_{comb}$ .....	78
<b>Equation III.2</b>	$2v_2Kn_1 + \cos 22\pi rna = V$ .....	79
<b>Equation IV.1</b>	$EEXC - ECT = \lambda EXC - CT$ .....	116
<b>Equation V.1</b>	$\sigma_{sample} = 10b_{sample} - b_{std}\phi_{std}\sigma_{std}c_{std}n_{std}\phi_{sample}c_{sample}n_{sample}$ 133	
<b>Equation V.2</b>	$\delta R = B\hbar 2\varepsilon_0 2\omega_1 0\omega_2 0\delta \varepsilon_f - \varepsilon_g - 2\omega_0 \times 1(\omega_0 + \varepsilon_g - \varepsilon_e) -$ $ike/2\mu f e. e\mu g. e + 1\omega_0 - ikg2\mu f g. e\mu g g. e + 1\omega_0 - ikf2\mu f f. e\mu f g. e^2$ .....	133
<b>Equation V.3</b>	$\sigma_e = 2\pi\hbar\varepsilon_0 c 2AeTe\omega_i\omega_s\delta \varepsilon_f - \varepsilon_i - \omega_i - \omega_s \times j\{Disj_1 - \exp[-iT_e\Delta j_i]\Delta j_i +$ $Dsi(j)1 - \exp[-iT_e\Delta j_s]\Delta j_s\}^2$ .....	141
<b>Equation VI.1</b>	$A + D \leftrightarrow A \cdot - + D \cdot + \leftrightarrow A \cdot + D \cdot$ .....	177
<b>Equation VI.2</b>	$y = 1 - 1 - ES1uS1g - ET1uS1gES2g, S1g2$ .....	177
<b>Equation VI.3</b>	$\Delta EST = ES - ET = 2J$ .....	178
<b>Equation VI.4</b>	$D = 1.39 X 104(gr^2)$ .....	178
<b>Equation B.1</b>	$\Phi F = \Phi STD Grad x \eta x 2 Grad STD \eta STD 2$ .....	205
<b>Equation B.2</b>	$10_{sample} - std -$ $y_{intx}\phi_{fluox}\delta_{std}x[ ]_{std}x_{nstd}\phi_{fluosample}x_{sample}x_{n_{sample}} = \delta TPA$ .....	206

## List of Appendices

<b>Appendix A: Supporting Information for Chapter I</b> .....	199
<b>Appendix B: Collaborator Experimental Information</b> .....	204
<b>Appendix C: Supporting Information for Chapter III</b> .....	209
<b>Appendix D: Supporting Information for Chapter IV</b> .....	220

## List of Abbreviations

Here is a list of the abbreviations that are used in this thesis.

Organic semiconductor: OSC	Lowest occupied molecular orbital: LUMO
Energy gap: $E_{\text{gap}}$	kilo: 1,000
Field effect transistor: FET	Electronvolts: eV
Carrier mobility: $\text{V}^2\text{cm}^{-1}\text{s}^{-1}$	Wavenumber: $\text{cm}^{-1}$
United States: U.S.	Nanometer: nm
Department of Energy: DOE	Second: sec
Solar Energy Technologies Office: SETO	Femtosecond: fs ( $10^{-15}\text{sec}$ )
Energy Efficiency and Renewable Energy: EERE	Picosecond: ps ( $10^{-12}\text{sec}$ )
kilowatt-hour: kWh	Rate: $\text{s}^{-1}$
Cent: ¢	Hertz (Hz): $\text{s}^{-1}$
Watt (W): J/s	Frequency (Hz): $\text{s}^{-1}$
Photovoltaic: PV	Speed: m/s
Power conversion efficiency: PCE	Speed of light (c): $3.0 \times 10^8 \text{m/s}$
Unit of PCE: Percentage, %	Wavelength nm
Organic photovoltaic: OPV	Meter m
Bulk-heterojunction: BHJ	h (Planck's constant) $6.6260 \times 10^{-34} \text{J} \cdot \text{s}$
Nonfullerene acceptor: NFA	Joule (J) $\text{kg} \cdot \text{m}^2 \cdot \text{s}^{-2}$
Highest occupied molecular orbital: HOMO	kilogram kg

Organic light emitting diode: OLED

Fluorescence Quantum yield:  $\Phi_F$

Unit of  $\Phi_F$ : Percentage, %

Two-photon absorption: TPA

Two-photon absorption cross section:  $\delta_{\text{TPA}}$

Unit of  $\delta_{\text{TPA}}$ : Goeppert Mayer, GM

Entangled two-photon absorption: ETPA

Time-resolved fluorescence upconversion:  
UpC

Transient absorption: TA

femtosecond transient absorption: fs-TA

Ground state bleach: GSB

Stimulated emission: SE

Excited state absorption: ESA

Density functional theory: DFT

Time-dependent density functional theory:

TD-DFT



## **Abstract**

This dissertation is a collection of research investigations that focus on understanding the ultrafast charge dynamics of organic semiconducting materials designed for optoelectronic applications. Optoelectronic applications are devices that utilize energy or light to generate charges that will create electricity, transport charges, or emit light. Examples of optoelectronic applications are photovoltaics for solar energy, transistors, or light emitting diodes. The main objective of optoelectronic applications is developing devices that are highly efficient, effective and low-cost to manufacture. One approach to developing low-cost devices is to use materials that are relatively cost efficient and have the ability of utilizing energy, such as organic semiconducting materials. In order for devices of optoelectronic application to work, the organic semiconducting materials used to create these devices must have the ability to generate or transport charges throughout the devices. Ultrafast charge dynamics are the motion or driving force behind the ability of materials to generate and transport charges. Depending on the structure of the material used in these devices, the ultrafast dynamics will be different and affected by the structure of the organic semiconducting materials used in these devices.

My PhD work focused on investigating ultrafast charge dynamics of organic conjugated ladder semiconducting materials for optoelectronic applications. Based on the organic semiconducting materials studied, the types of ultrafast charge dynamics that I investigated concerning these organic semiconducting materials were: electron-phonon interaction; reorganization relaxation; exciton; intramolecular charge transfer; fluorescence; and radical formation. In doing so, I utilized femtosecond transient absorption (fs-TA) technology, a pump-probe laser experiment that provides information on excited state dynamics on the molecules.

Chapter III address the one of my PhD research investigation that focuses on investigating the ultrafast dynamics of organic ladder oligomers used in transistor applications. The results indicated that the longer conjugated length oligomer (seven fused rings) had slower decay times of the ultrafast dynamics due to the decrease in electron-phonon (electron-vibrational) interaction. As a result, the charge transport mechanism of the longer oligomer was therefore more efficient than the shorter oligomer, a key discovery.

Chapter IV address another one of my PhD research investigation that focuses the exciton dynamics and the intramolecular charge generation mechanism of acceptor-donor-acceptor small molecules that are designed for solar cell applications. These molecules varied in the type of donor unit (fused-ring or non-fused ring) used within the molecular structure design. In addition, these molecules varied in having a  $\pi$  bridge to connect the donor and acceptor units within the structure of these molecules. The results from this investigation provide insight into which molecular structure of an acceptor-donor-acceptor small molecule will best lead to the discovery of an efficient solar cell device. Chapters V and VI of this dissertation discusses the research investigations where I collaborated with my colleagues on other research investigations concerning the ultrafast charge dynamics of other organic polymeric semiconducting materials designed for optoelectronic applications.

The main objective of all the research investigations discussed in this dissertation is to increase the knowledge of ultrafast charge dynamics of organic semiconducting materials and to understand the structure-functional relationship between charge dynamics and these materials. Ideally, the information in this dissertation will lead to finding the optimal structural design of organic semiconducting materials that will lead to highly efficient and effective devices for optoelectronic applications.

## Chapter I

### Introduction

#### I.1 Overview of Scientific Background

Optoelectronic devices are defined as an equipment that contain components which can transport or generate charges or emit light. Examples of optoelectronic devices are solar cells, transistor, light emitting diodes. Organic materials that have the ability of moving charges are called organic semiconductors (OSCs). A material is defined as a semiconductor when the energy gap ( $E_{\text{gap}}$ ) between the conduction and valence bands of the material is within the range of 0.1eV – 3.0eV. Conduction band is a high energy level block that is unoccupied and can accept negative ionic charges (electrons) that have been given energy to move out of the conduction band.  $E_{\text{gap}}$  within the range of 0.0eV – 0.1eV, the material is defined as a conductor. An example of conductor material is metal. Then, for materials that have a  $\Delta E_{\text{gap}}$  that is greater than 3.0eV are known as insulators. Research has shown the benefit of using organic materials for optoelectronic devices is these materials have the potential to be low cost to developed, which will lower the cost of optoelectronic devices.

Devices of optoelectronic applications utilizes charge to create electricity, emit light or transport charge depending on the application. Charge is a property of matter that occurs when a particle generate and has its own force-field as a result of an outside force (energy, magnetic, or electric potential) being applied to the matter. Charge can have a negative or positive ionic character. Electron is the negative ionic form of charge. Hole is the positive ionic form of charge. Depending on the molecular structure of an OSC, the electron or hole or both will move effectively

within an OSC. One approach for investigating the ability of an OSC to move a charge is utilizing ultrafast laser spectroscopy.

Ultrafast laser spectroscopy uses coherent light radiation to excite an OSC and study what the material does once it is excited by light. Coherent light radiation can come in the form a frequencies or wavelength of electromagnetic radiation. Electromagnetic radiation is a type of energy that electrons can absorb and is an electric field and magnetic field that are perpendicular to each other and can flow through a vacuum or material at a set speed. Once an organic semiconducting material is excited, the material can experience a various emissive processes that could occur in these materials: fluorescence and phosphorescence. Fluorescence occurs when an electron relaxes from the lowest vibrational state in the excited singlet state to the ground state ( $S_1 \rightarrow S_0$ ) and light is emitted. Phosphorescence occurs when an electron relaxes from the lowest vibrational state in excited triplet state to ground state ( $T_1 \rightarrow S_0$ ) and light is emitted. In order to investigate the charge dynamics of organic materials, the excited state dynamics and emissive processes of these materials will need to be identified and studied.

## **I.2 Motivation of Solar Energy**

Solar energy is exciting because it has the potential to make a positive impact in society, and The United States' (U.S.) Department of Energy (DOE) and U.S. Congress are investing in research that focuses on this type of energy source.<sup>1-5</sup> Solar energy is a type of optoelectronic application that is a renewable source with the potential to lower costs of electricity used in residential, commercial and industrial sectors of society.<sup>1,2,6-8</sup> **Figure I.1** shows an example of devices that are powered by solar energy. The solar powered devices shown in **Figure I.1** are called solar panels. Solar panels consist of smaller individual nonmechanical devices called photovoltaics (PVs). PVs utilizes solar energy to create electricity that can used to power homes,

buildings or other devices. PVs can be created from many materials which will be discussed later in this Chapter. For solar panels, the common material used in PV devices of panels is silicon. Solar panels and PVs in these panels are one example of optoelectronic application of solar energy

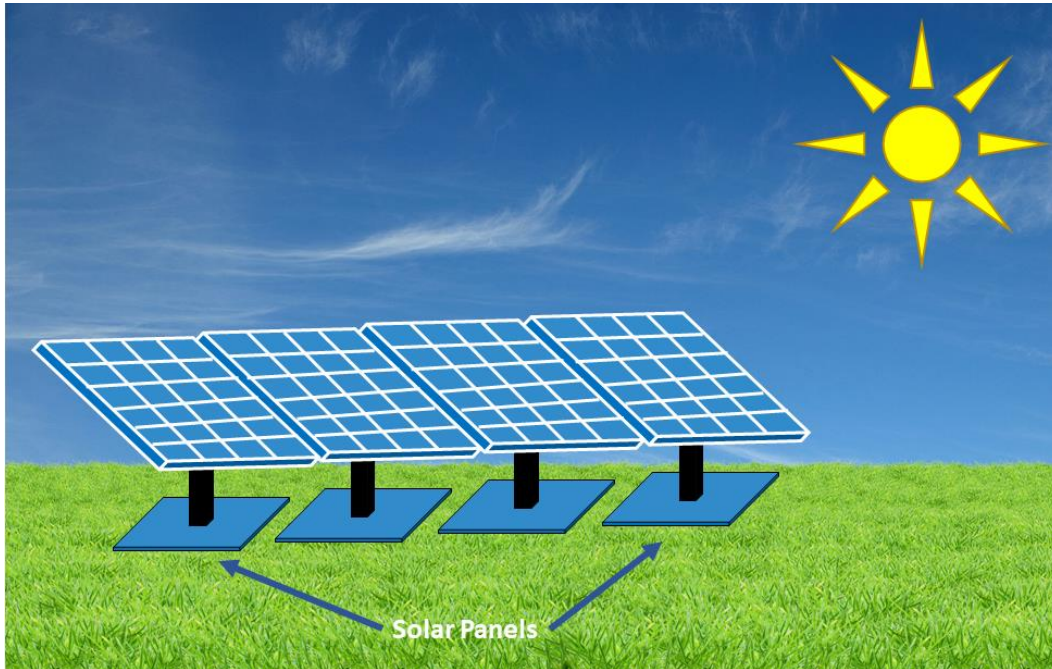


**Figure I.1:** General picture of devices that are powered by solar energy. Example of solar powered devices demonstrated in this Figure are solar panels. Solar panels consist of individual nonmechanical devices called photovoltaics (PVs). Solar panels and PVs in these panels are mainly consist of silicon. Solar panels are one example of an optoelectronic application that utilizes solar energy. Citation: this Figure consists of online images from Microsoft PowerPoint – specifically, the grass and sky.

that is used in society. Solar panels can be used on a rooftops of homes or at an electrical grid. For example, solar panels can be used to provide electricity to a community. This community can become part of a Community Solar. According to U.S. DOE, Community Solar is a solar project program that provides electricity that is generated from solar energy to a group of individuals or businesses. According to U.S. DOE, the advantages of Community Solar are it creates the opportunity for individuals to have access to solar energy and will lower energy costs. To recap, the advantages of optoelectronic application of solar energy are: 1) it is a renewable source of

energy; 2) it has the potential to lower energy costs; 3) it has the potential of creating a cleaner environment and 4) it has the potential to make a positive impact in society. As a result of these advantages, the U.S. DOE and U.S. Congress have invested funding and resources into research that focuses on solar energy with the goal of expanding the usage of this renewable energy source in society.

The *Solar Futures Study* focuses on transitioning and developing solar energy to a carbon-free electric grid by 2050. This series was released in 2021 and is a partnership between SETO and National Renewable Energy Laboratory (NREL). In September 2021, the SETO released a report that lists the new goals and targets to accomplish by 2035 and 2050. According to the SETO, solar energy could account for roughly 40% of the U.S.' electricity supply by 2035. Then, by 2050 the U.S' electricity supply could be supported by roughly 45% solar energy. In order to achieve those goals, the *Solar Futures Study* report shows there is a need for intense in cost reduction, supportive policies and large-scale electrification. Thus, the U.S. DOE, SETO, U.S. Congress are increasing the investment and providing funding to research that focuses on solar energy and its optoelectronic application. To recap, even though solar energy has been studied and investigated for many years, there is still a need to provide financial support and conduct research on this energy. Solar energy has many benefits that will help lower the cost of energy and make energy more accessible for everyone in society. Due to these benefits and positive potential, it is important to continue conducting research on solar energy in order to develop a more accessible energy source at lower costs.

### **I.3 History of Solar Energy and Photovoltaic (PV) Devices**

Solar energy and its optoelectronic applications, such as PV devices, have been studied and investigated for many years.<sup>17</sup> Recall, PV is a nonmechanical device that have the ability of

converting solar energy into electricity. The concept of PV was discovered by Charles E. Fritts in the 1883.<sup>16</sup> Fritts published a paper in *American Journal of Science* in 1883 that described his observations of a PV device created from selenium.<sup>16</sup> The cost of a selenium PV, at that time, was \$100. Fritts measured the resistance of the selenium PV device under many conditions including dark to light exposure. Fritts worked on the experiments with the assistance of Dr. Werner Siemens.<sup>16</sup> This was the beginning of solar powered applications.

During the early half of the 19<sup>th</sup> century, research was conducted and proved that sunlight could be utilized to generate charges in the many materials.<sup>17</sup> In 1904, Wilhelm Hallwachs showed that combining copper and cuprous oxide showed photosensitive could be enhanced.<sup>17</sup> In 1905, the first photoelectric effect was published by Albert Einstein. Then, William J. Bailey from the Carnegie Steel Company invented a solar collector that consisted of copper coils in an insulated box.<sup>17</sup> It wasn't until 1918, Robert Millikan developed the first experiment that proved the photoelectric effect that Albert Einstein proposed in 1905.<sup>17</sup> In 1921, Albert Einstein was awarded a Nobel Prize on his theories on the photoelectric effect. Then in 1932, Audobert and Stora showed that the photoelectric effect can occur in cadmium sulfide (CdS) inorganic semiconductors.<sup>17</sup>

The next major development in PV history occurred when Daryl Chapin, Calvin Fuller and Gerald Pearson developed the first silicon PV at Bell Labs.<sup>17</sup> This was the first PV that was able to convert enough of the sun's energy to power everyday appliances. In 1977, the U.S. DOE started the NREL and the objective of this laboratory is to have a facility dedicated to conducting research on solar energy. In 1982, the U.S. DOE and industry collaborated to develop the demonstration project called Solar One. The Solar One was a 10-megawatt central-receiver which showed the capability of power-tower systems and solar-thermal electric or concentrating solar power technology. By 1988, the final year of operation, Solar One was dispatched 96% of time.<sup>17</sup>

Then in 1985, University of South Wales developed a silicon PV that generated 20% efficiency, which broke the efficiency barrier at the time for under 1-sun conditions.<sup>17,18</sup> In 1991, President George Bush reestablished the U.S. DOE's Solar Energy Research Institute as NREL. In 1994, the construction of NREL was completed. Replacing the Solar Energy Research Institute, NREL became known as the most energy-efficient building compared to the other U.S. government buildings. During the same year, the NREL developed the first inorganic PV that had an efficiency of 30%.<sup>17</sup> The PV device consisted of gallium indium phosphide and gallium arsenide. Then in 1996, the U.S. DOE collaborated with industry again to develop Solar Two. Solar Two was upgraded to the Solar One project developed in the 1980s. The Solar Two was in operation until 1999. Then in 1999, Spectrolab, Inc. and NREL developed a PV cell that can convert 32.3% of the sunlight into electricity. This highly efficient PV consisted of three layers into one device. The design of PV received 50x more sunlight compared to other devices at that time.<sup>17</sup> In the same year, NREL developed a thin-film PV that had an efficiency of 18.8%. Presently, the highest world record of efficiency in PV 47.6% according to NREL.<sup>19-21</sup> This world-record PV device is a III-V concentrating PV cell with a four-junction architecture.<sup>19-21</sup>

#### **I.4 How Optoelectronic Application of Solar Energy Works**

The optoelectronic application of solar energy utilizing a device that has the capability of absorbing the energy of the Sun and converting that energy into electricity. The process of converting the energy of the Sun into electricity takes three steps 1) Absorption; 2) Generating electrical charges and 3) Creating electricity. **Figure I.2** shows the process utilized in the optoelectronic application of solar energy; converting the energy of the Sun into electricity. Starting with the first step, Absorption, there needs to be a device, such as a PV, that has the



capability of absorbing the energy of the Sun. The energy of the Sun that is being utilized in this application is the ultraviolet (UV), visible (Vis), and infrared (IR) regions of the electromagnetic

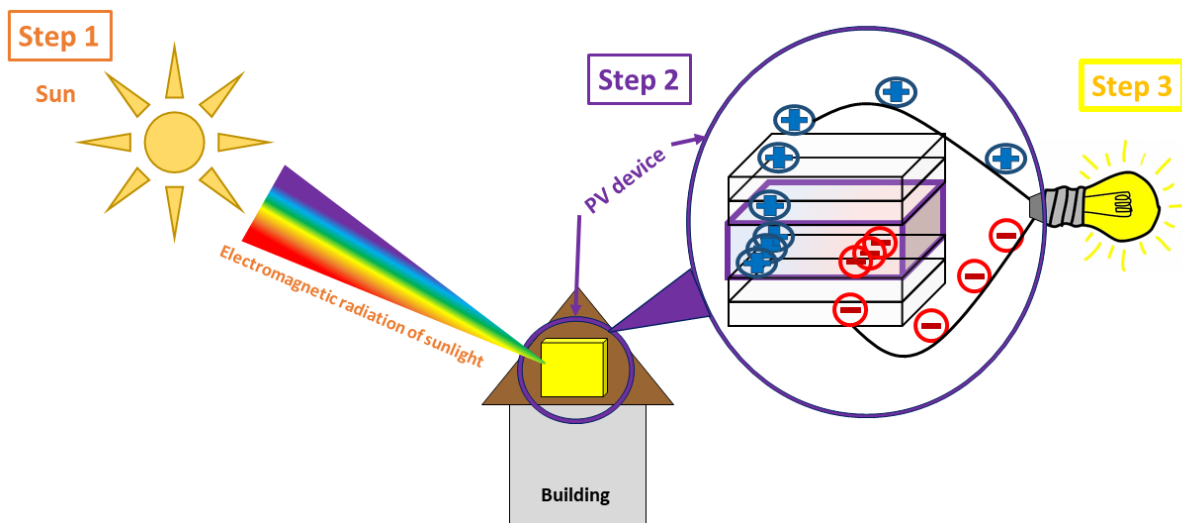


**Figure I.2:** General schematic of how the optoelectronic application of solar energy works: **Step 1**) Absorption of electromagnetic radiation of Sun (Sunlight); **Step 2**) Generating electrical charges; and **Step 3**) Creating electricity

radiation spectrum. Specifically, sunlight consists of 49.4% of IR, 42.3% of Vis, and 8% of UV radiation. It has been shown that the intensity of the spectral regions of the energy of the Sun varies throughout the day. Specifically, at sunset, there is more IR electromagnetic radiation. Then, at noon daylight, there is more UV electromagnetic radiation. Thus, the PV device utilized in this optoelectronic application needs to have the ability of absorbing the sunlight. The next step (see Step 2 in **Figure I.2**) of the process of converting sunlight into electricity is Generating electrical charges. In this step, once PV device absorbs sunlight, it takes the energy of the sunlight (the UV, Vis, and IR electromagnetic radiation of the solar energy) and uses that energy to generate electrical charges. Then in the final step, (see Step 3 in **Figure I.2**) creating electricity, the generated electrical charges will move throughout the device due to an internal electrical field within the PV device. At this point, the PV device is connected to an external device by wires and electrodes. The wires and electrodes connecting the PV and external device will assist with

directing the generated electrical charges from PV device to the external device. So now, with the assistance of wires and electrodes, the movement of the electrical charges from the PV device to the external device will generate electricity that can be used to power the external device.

### **I.5 Generating Electrical Charges in a PV Device**

The electrical charges generated in a PV device occur between two materials called the p-type and n-type. P-type materials are a type of conducting materials (conductor or semiconductor) made from molecules that have a lower concentration of electrons compared to the concentration of positive charges, holes, in the structure of these materials. P-type materials have the capability of efficiently and effectively moving holes compared to electrons. Examples of p-type materials are boron and aluminum. N-type materials are a type of conducting materials (conductor or semiconductor) made from molecules that have more concentration of electrons compared to the concentration of holes in the structure of these materials. N-type materials have the capability of efficiently and effectively moving electrons compared to holes. Examples of n-type materials are phosphorus, arsenic and antimony.

When these two materials are adjacent together in a PV device, these materials get excited by the electromagnetic radiation of the energy of the Sun. Specifically, these materials have the capability of absorbing the energy of the Sun associated by the electromagnetic radiation. When these materials absorb the electromagnetic radiation of the energy of the Sun, an exciton is created. An exciton is a coulombically bound hole and an electron in a pair. After an exciton is formed, the exciton will separate between the materials. The exciton separates so that the hole will stay on the p-type material and the electron will stay on the n-type material. Then, with the assistance of the p-type material, the holes will move the electrode and wires designed to accept the holes of the PV device. Then, with the assistance of the n-type material, the electrons will move to the

electrodes and wires designed to accept the electrons of the PV device. The movement of charges – hole and electrons – through the two materials, electrodes, and wires will create electricity that will be utilized to power an external device. The process described above is called charge generation. The process of charge generation can be viewed from material or energy level of the material. In this paragraph, the charge generation described is based on materials.

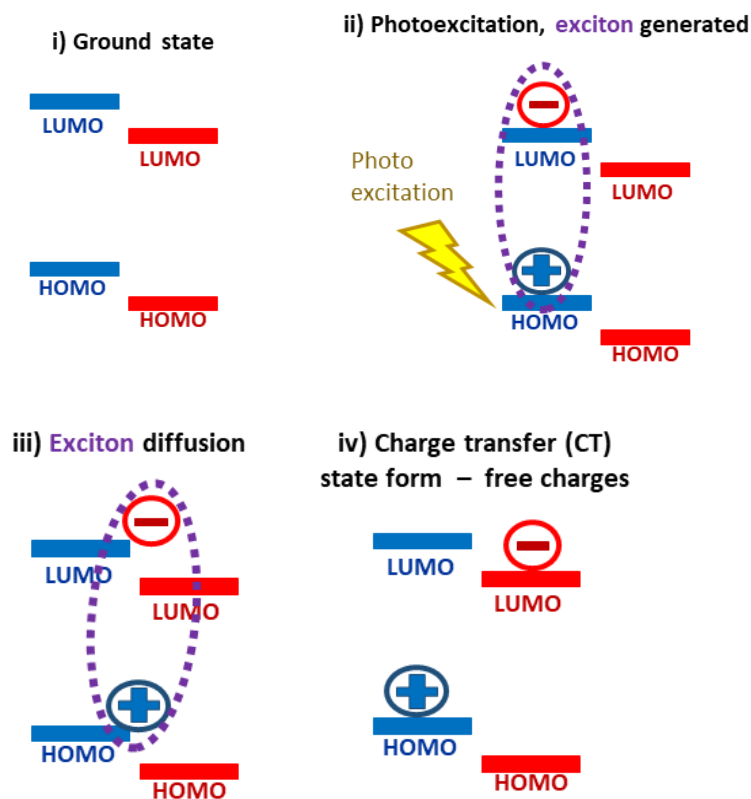


**Figure I.3:** General schematic showing the steps on charge generation that occurs between the two materials in a PV device.

Then, this next step in solar energy storage involves the charge generation materials. For both p-type and n-type materials, these materials will have their own valence and conduction energy bands. The valence and conduction energy bands of the p-type material will be at a higher energy compared to the valence and conduction energy bands of the n-type. There will be an offset between the valence and conduction energy bands of the p-type and n-type materials due to the

difference in absorption. The difference in energy gap is based on the LUMO of one material and the LUMO of the another material,  $E_{DA}$ . The mechanism that leads to creating electricity from the materials of PV is called charge generation. **Figure I.3** shows the steps of the charge generation mechanism within PV device. The charge generation mechanism starts with the two materials being in a neutral or ground state (Step 1 in **Figure I.3**). Then, photoexcitation occurs, the material gets excited by light, and an exciton is formed. Exciton is a coulombically bound hole and an electron in a pair (Step 2 in **Figure I.3**). The next step the solar energy storage process is the exciton will diffuse between the interface of the two materials (Step 3 **Figure I.3**). Step 4 is (see **Figure I.3**) a charge transfer state ( $S_{CT}$ ) which is formed due to the exciton splitting so that the electron is located on the LUMO of one material and the hole is located on the HOMO of the other material.

#### I.6 Power Conversion Efficiency – Numerical Quantitation of Charge Generation

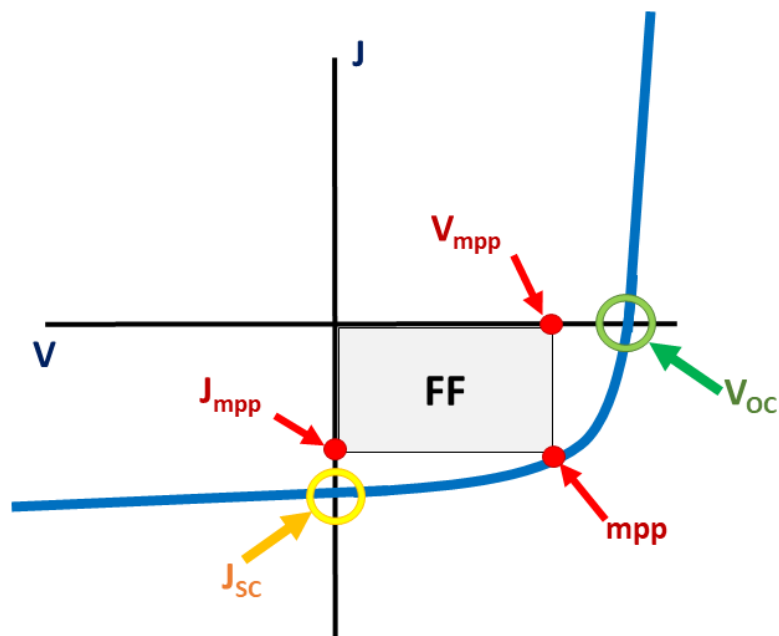


**Figure I.4:** General schematic of a current-voltage (JV) curve.

The numerical quantitative value used to measure the effectiveness of charge generation occurring in the PV is called power conversion efficiency (PCE). The units for PCE is percentage (%). Studies have shown there is a correlation between PCE and charge generation occurring within a PV. For example, when a PV has a high PCE, this suggests that there is an effective and efficient charge generation occurring between the two materials in the PV device. Then, when the PCE is relatively low, this suggest that the charge generation is not effective or efficient between the two materials in a PV device. The PCE of a PV is determined by the values obtained from results of a current-voltage (JV) curve measurements. A JV curve is a plot of current (J) is on the y-axis and voltage (V) is on the x-axis of the curve. The units for J are amperes (amps) and the units for V are voltage (V). **Figure I.4** shows a representative schematic of a JV curve. In order to conduct JV curve measurements, there needs to be a light source that corresponds to the sunlight or the UV, Vis, and IR region of electromagnetic radiation spectrum of the energy of the Sun. Typically, the light source used for these measurements is AM1.5G spectrum; this spectrum is known for stimulating the electromagnetic radiation spectrum of sunlight. In addition, in order to conduct these JV curve measurements, there needs to be a current or voltage that can be applied to the PV device. Typically, direct current (DC) is used for these measurements. DC defines the direction and flow of the current or voltage being used in these measurements. When DC is used, this ensures that the current or voltage will flow in the one uniformed direction; all the current or voltage will flow in the same direction. Then, the JV curve measurement is conducted under two conditions: when the light source is 'On' and when the light source is 'Off'. After running the JV curve under these two conditions, this will give the values needed to calculate the PCE.

From the JV curve measurements, the following values are determined: short-circuit current ( $J_{sc}$ ); open-circuit voltage ( $V_{oc}$ ) and fill factor (FF). The values obtained from a JV curve

are used to calculate the PCE. **Equation I.1** shows the mathematical expression used to calculate the PCE.

**Equation I.1**

$$\frac{J_{sc} \times V_{oc} \times FF}{P_{in}} = PCE$$

$V_{oc}$  is determined by the point on the JV curve when the current is ‘zero’. The  $V_{oc}$  is affected by the energy of the charge transfer state ( $E_{SCT}$ ) created during the charge generation process (Step 3 in **Figure I.3**). Recall, the  $S_{CT}$  is formed between the donor acceptor materials in the charge generation process when exciton dissociation or separate so that the hole stays on the HOMO of the donor material and electron stays on the LUMO of the acceptor. Thus, the  $E_{SCT}$  is determined at the interface between the donor and acceptor materials in the PV device when charge generation is occurring in between the two material.

The  $J_{sc}$  is determined when there is a ‘zero’ bias or no current or voltage is being applied to PV device during the JV curve measurement. On the JV curve,  $J_{sc}$  is determined at the point when y-axis equals ‘zero’.  $J_{sc}$  is affected by three factors: 1) the absorption rate of the donor and acceptor materials; 2) the effectiveness and efficiency of exciton dissociation; 3) the effectiveness and efficiency of charges being transported and collected at the electrodes of a PV device. The first factor that affects  $J_{sc}$ , absorption rate, is dependent on the ability of the donor and acceptor materials to absorb the sunlight or the AM1.5G spectrum light source utilized in the JV curve measurements. The second factor that affects the  $J_{sc}$  corresponds to the Step 3 of the charge generation process, exciton dissociation. The exciton ability to separate or split or dissociate into two charges, hole and electron. Then, the third factor corresponds to the last step of the charge generation process. Recall, the last step of the charge generation is after the  $S_{CT}$  is formed, the charges will continue to separate and increase the distance between them so there is little or no interaction between them; and as a result, the charges become free charges. At this point, the

charges are at a charge separated state,  $S_{CS}$ , and there is a sufficient distance between the holes and electrons to decrease probability of recombination occurring and an exciton is formed again. The free charges from the charge generation process will be collected by electrodes in the PV device. To summarize the  $J_{SC}$ , this value is very dependent on the charge generation between the two materials in PV device. This  $J_{SC}$  can provide insight into the efficiency of the charge generation occurring within a PV device; however, this value does not have a strong correlation to the efficiency of charge generation as PCE.

Then as for FF, this value is determined by creating a ‘square’ on the JV curve (see **Figure I.4**).  $J_{max}$  is determined by the highest current value obtained at the maximum power point.  $V_{max}$  is determined by the highest voltage value obtained at the maximum power point. The maximum power point is defined as curviest part or where the JV curve bends (see **Figure I.4**). The maximum power point can also be describe as the highest power output of the JV curve measurements. As shown in **Equation I.1**, the FF is the ratio of the maximum current and voltage obtained at the maximum power output of the experiment divided by  $J_{SC}$  and  $V_{OC}$ . In order to obtained the values required to calculate the FF, the JV curve measurements need to be conducted when the light source is turned on. Then final value needed to calculate the PCE is  $P_{in}$  (See **Equation I.1**)  $P_{in}$  is defined as the power density of the energy of the Sun. The units of  $P_{in}$  is  $kW/m^2$  or  $mW/cm^2$ . Typically, in a JV curve, the  $P_{in}$  is  $100\text{ mW/cm}^2$  or  $1\text{ kW/m}^2$ .

To summarize, the PCE is a numerical quantitative value used to measure the effectiveness of charge generation in a PV device. The values needed to calculate the PCE are obtained from the JV curve measurements. As **Figure I.4** show, the shape of the JV curve can varied and studies have shown there is not one curve shape that will lead to a high PCE and efficient charge generation for a PV device. Instead, research has focused on the values obtained for JV curve and investigate

the correlations between the values from a JV curve and PCE. By investigating and discovering correlations between values and PCE of PV devices, this will increase information and assist with finding materials that will have a high PCE and efficient charge generation occurring within the PV devices. As mentioned earlier, the two values obtained from a JV curve that have a correlation to the effectiveness and efficiency of charge generation process in PV device are  $J_{SC}$  and  $V_{OC}$ . These values are dependent on the energy or exciton or absorption of the charge generation process occurring between the two materials in a PV device. From studying and investigating the JV curves and PCEs of PV devices, this will lead to finding materials that will have an efficient charge generation and develop PV devices have the potential to be used in society. The NREL has recorded the PCE of various PV devices from 1970s to present day.<sup>20</sup> This NREL graph shows the historical perspective of PCE, materials and the types of PV devices investigated and studied for the optoelectronic application of solar energy.<sup>20</sup> As the NREL graph and research shows, the PCE of a PV is greatly affected by the materials use to create the device.<sup>20</sup> As a result, it is important to investigate and study the materials used to develop PV devices for solar energy.

### **I.7 Overview of Materials Used in Optoelectronic Application of Solar Energy**

As shown on the NREL graph, there are many types of devices and materials used in the optoelectronic application of solar energy.<sup>20</sup> According to the NREL graph, the common major categories of devices used in this application are: multijunction; thin-film technologies; single-junction gallium arsenide (GaAs); crystalline silicon (Si) cells; and PV. For each major category, the category is divided into smaller categories that describes the material details used in the device for that category. For example, in the PV device category, the smaller categories are: perovskite; organic; dye-sensitized; and inorganic; and quantum dots. Then, for each common major category, the category can be divided into the smaller categories and the labels of these categories describe



the materials used to create the device. For example, under the PV device category, the organic category can be divided into smaller groups based on the materials used in the PV, such as polymers or small molecules. Despite there being many common categories of devices used in the optoelectronic application of solar cell, there is not one category that is deemed that will be considered the best and optimal device for this optoelectronic application. Research has shown that major category has its advantages and disadvantages. For example, the advantage of dye-sensitized PV devices is these devices have promise to be used as artificial light sources for indoor conditions compared to other optoelectronic application of solar energy. Then, the advantage of Si PVs are these devices are known to have high efficiency for solar energy and are made out of one of the most abundant materials on Earth (silicon). Then, the advantage of quantum dot PV devices are these devices have low defect issues in their devices; thus, this leads to great device performance and photoluminescence yields. To summarize, there are many type of devices used in the optoelectronic application of solar energy and each devices have its own advantages and disadvantages. As stated previously, according to the SETO, the main overall objective of the optoelectronic application of solar cell is finding the best and optimal device that will lead to an efficient devices and lower the cost of solar energy; therefore, many approaches are being utilized to achieve this objective.

At this time, there is no major category that achieves the main objectives of the optoelectronic application of solar energy and SETO. As shown in the NREL graph all the common major categories show relatively high PCEs above 10%. As of 2022, the highest-record PCE for the optoelectronic application of solar energy is 46.7%. The highest record PCE is from an III-V concentrating PV cell under the multijunction cell category. However, having the highest record or high PCE does not correlate to low cost for the optoelectronic application of solar energy

because there is no guarantee that the materials, device making and manufacturing process will be low-cost as a result of a high PCE. Thus, another factor to consider for achieving the main objective of this optoelectronic application is having the ability to mass produced or upscale the device in a cost-effective manner. Recently, NREL conducted a cost analysis of the manufacturing process for PV devices and provided solutions to assist with costs and a sustainably approach for the manufacturing process. At this time, the only major common device category of solar energy that has the most benefits compared to other device category is Si PV. Currently, Si PV devices are the most common and practical device for the optoelectronic application of solar energy due to the relatively high PCEs and low cost of these devices. Si PV devices are roughly 85% of the world's market for PVs. The PCEs Si PV devices ranges from 18% – 22%. Studies have shown that the PCE of Si PV devices can reach up to 29%. Due to the decent and high PCEs of Si PVs, there devices are used as solar panels to power industry and residual aspects of society. According to a report by the NREL, the cost of a Si PV in 2018 was approximately on average 0.49¢/kWh. Recently, in an article reported in *pv magazine*, cost of a Si PV devices has dropped by 96% over the cross of two decades. Despite the great benefits of Si PV, these benefits do achieve the main objectives of the optoelectronic application for solar energy and SETO, which was discussed in Section I.3 on this chapter. In order to achieve those objectives, different approaches are being taken and investigated to determine which devices and materials will lead to high PCE and low cost for the optoelectronic application of solar energy.

The two main characteristics of materials used in the devices of the optoelectronic application for solar energy are semiconducting properties and the cost of the materials. In general, the materials used in these devices tend to be categorized as inorganic or organic materials that have a semiconducting characteristic. In other words, the materials used in the optoelectronic

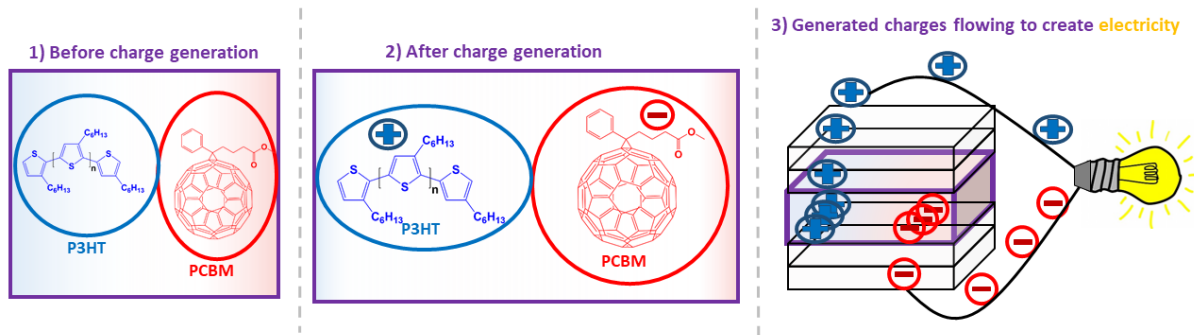


**Figure I.5:** General visualization of charge generation occurring in a photovoltaic (PV) device between the two materials in a PV. The PV device is an example of organic photovoltaic (OPV) device.

application of solar energy are semiconductors and these materials can be divided into two groups: inorganic or organic. See **Figure I.5** for general schematic of an organic solar cell (OPV) device generating electricity due to two organic materials within the device. Specifically, a semiconductor that is made out of an organic material is called an OSC, as discussed in Section I.1 of this chapter. Recall, a semiconductor material will have a  $E_{\text{gap}}$  between the conduction and valence bands or HOMO and LUMO of the material is within the range of approximately 0.1 eV – 3.0 eV (see Section I.1 of this chapter). When a material (inorganic or organic) has that range for  $E_{\text{gap}}$ , this allows the material to have the ability to move or transport charges and insulate charges, if needed. Having this duality property, makes semiconductors have an advantage compared to conductors or insulators for the optoelectronic application of solar energy. Another advantage of semiconductors is these materials tend to be cheaper or have a lower cost compared to conductors. Common inorganic materials used in devices are nanoparticles, perovskites, quantum dots, crystalline film that consists of silicon, gallium, titanium oxide, lead and other inorganic elements. Then, common OSC used in these devices are polymer, small molecules and fullerenes that consist of carbon, oxygen, fluorine, sulfur and other organic elements. Simply, the materials used in the devices for the optoelectronic application of solar energy are classified as

semiconductors and have a low cost. The sections discussed above provide an overview of I.3 – I.6, the optoelectronic application of solar energy has a vast history and many devices and materials are used in this application.

## I.8 Introducing the Optoelectronic Application of Organic Photovoltaic (OPV) Devices

In this dissertation, the optoelectronic application of solar energy that is the main focus of this dissertation is organic photovoltaic (OPV). OPVs is a type of solar energy optoelectronic application that uses OSCs to generate charges within the active layer of device in order to create electricity (see **Figure I.6**). OPVs is a subset of the major category of PV devices on the NREL graph and DOE website.<sup>1,20</sup> The early design of PV contained inorganic materials, such as selenium and silicon. In 1985, published in the journal of *Applied Physics*, Tang created the first successful OPV containing materials used in this device was copper phthalocyanine

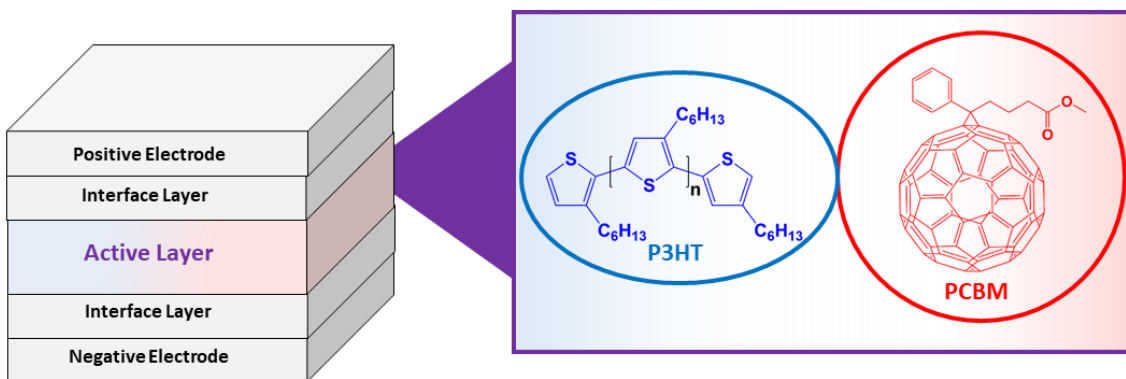


**Figure I.6:** General schematic of an organic photovoltaic (OPV) device. The two materials in the active layer of the OPV device is Donor material: poly(3-hexylthiophene (P3HT) and Acceptor material: phenyl-C-butylric acid methyl ester derivative (PCBM) (which is also known as fullerene). An OPV device consists of many layers and materials that will generate charges or assist with separating and collecting charges that will be used to create electricity.

(CuPc) and perylene tetracarboxylic derivative (PT). The PCE of this OPV was 1.0%. From this discovery, this led to research focusing organic materials to increase the PCEs in OPVs. Research has shown the advantages of OPV are the potential of creating low-cost devices, as with other PV

devices. Compared to other PV devices, the additional advantage of OPV is into flexible devices and mechanical function compared to other inorganic PV. Due to these unique characteristics, OPV devices can be used in various applications such as integrated solar power generation and self-powered electronics. As mentioned earlier in Section I.1, there is still a need to conduct research on PV and OPV for solar energy as an approach to lower energy costs and make energy more accessible in society. Despite PV research has been going on for several decades, there is still a need to develop OPVs with high PCEs that can be used in society. Recent and ongoing research in OPVs aims to develop solar cells with improved power conversion efficiencies and durability.

**Figure I.6** shows a schematic of an OPV device. In an OPV device there are multiple layers that have the function of generating or transporting charges. The donor and acceptor organic materials that generate charges for an OPV device are located in active layer of the device. Over the years, research has been conducted to determine the best combination of organic materials that will lead to high PCEs for OPVs. As mentioned in Section I.5, the types of materials used in OPV device are organic semiconductors, such as polymers and small molecules. In 1995, Heeger et al discovered the concept of bulk heterojunction (BHJ) OPV devices (Heeger Science 1995), where a blend of an electron-donating conjugated polymer and a fullerene derivative such as PC<sub>60</sub>BM (or PC<sub>70</sub>BM) acted as the electron acceptor material in the active layer, fullerenes dominated the field of OPVs due to their excellent electron-accepting and electron transport properties. With this the BHJ OPV device, Heeger et al developed a device that had roughly 5.5% PCE. This new design concept to the active layer of OPV device helped increase the promise that high PCE can be created for OPV devices. In early 2000s, reported power conversion efficiencies, PCEs, of P3HT:PCBM OPV was between 0.2- 5.5%. As more research was conducted on OPV and PCE,

there was still a need to find the optimal combination donor and acceptor materials that will increase the PCE for OPVs.

### *I.8.a Progression of Donor Material Structural Design in OPVs*

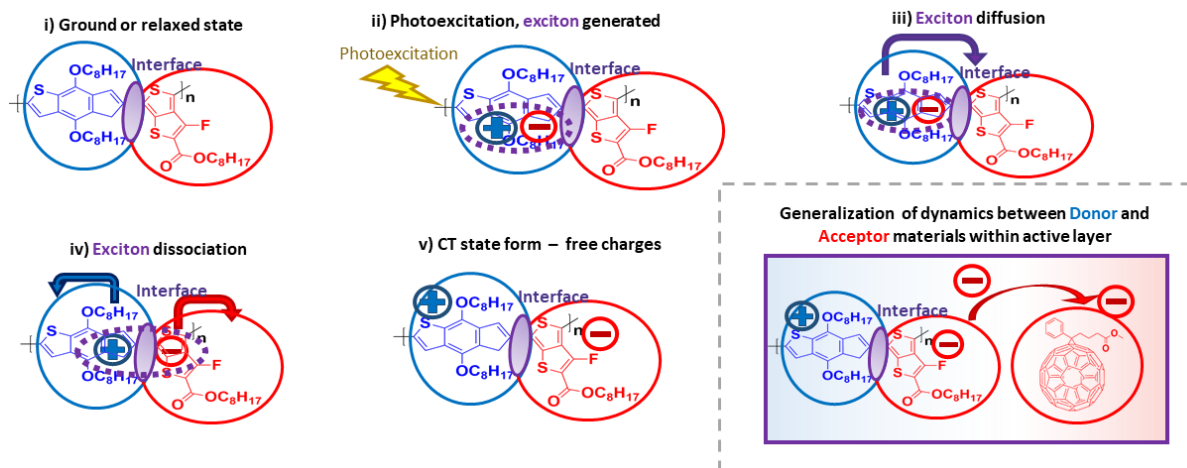


**Figure I.7:** General visualization of charge generation occurring with a Donor material that has a donor-acceptor structural framework. In this **Figure**, the example of Donor material with a donor-acceptor structural frame is poly[[4,8-bis[(2-ethylhexyl)oxy]benzo[1,2-b:4,5-b']dithiophene-2,6-diyl][3-fluoro-2 [(2ethylhexyl)carbonyl]thieno[3,4-b]-thiophenediyl]], (PTB7) polymer. The charge generation that is occurring within PTB7 can be considered as intramolecular charge generation.

As shown in the grey box, the Donor material with a donor-acceptor structural framework will most likely experience intramolecular charge generation before it undergoes charge generation with fullerene, the Acceptor material.

In 2010s, a new structural design was developed for the Donor material and the design is having a donor unit and an acceptor unit within the Donor material. One of the first and well known accounts of this structural design was the polymer PTB7. The polymer has a donor-acceptor structural framework. A reported PCE for PTB7:PCBM was 7.4% - an improvement from previous structural design. **Figure I.7** shows the donor-acceptor structural framework of PTB7 and the charge generation occurring between PTB7 and PCBM. With this new structural design, this donor-acceptor structural framework, charge generation can occur within Donor

material and improve PCE by increasing the efficiency of charge transporting and charge transfer occurring within an OPV device.

As shown in **Figure I.7**, when a Donor material has a donor-acceptor structural framework, charge generation can occur within that material before having charge generation with Acceptor material. As mentioned in Section I.4 and shown in **Figure I.3**, there are four steps in the charge generation mechanism: Initial step (Step 1) ground or relaxed state; Step 2 photoexcitation, generating an exciton; Step 3 exciton dissociation; and Step 4 charge transfer and charges become free charges. Since a Donor material has donor-acceptor units within its molecular structure, this will allow the opportunity for charge generation to occur within this material. The type of charge generation can be described as intramolecular charge generation. This intramolecular charge generation has an additional step that is not highlight in the intermolecular charge generation. The additional step, as shown in **Figure I.7**, is exciton diffusion, Step 3 in **Figure I.7**. Exciton diffusion is the when exciton diffuse or moves to the interface between the donor and acceptor unit within the Donor material. To clarify, intramolecular charge generation will have five steps and intermolecular charge generation will have four steps. When the Donor material has a donor-acceptor structural framework, it has its own CT dynamic and intramolecular charge generation to increase the probability of exciton become free charges before going through charge generation with Acceptor material. So now, it is important to investigate CT dynamics of Donor materials and find best combination of donor-acceptor for efficient charge generation to improve PCE of OPV The difference in energy gap is based on the LUMO of one material and the LUMO of the another material,  $E_{DA}$ .

*I.8.b Progression of Acceptor Material Structural Design in OPVs – Nonfullerene Acceptor (NFA)*

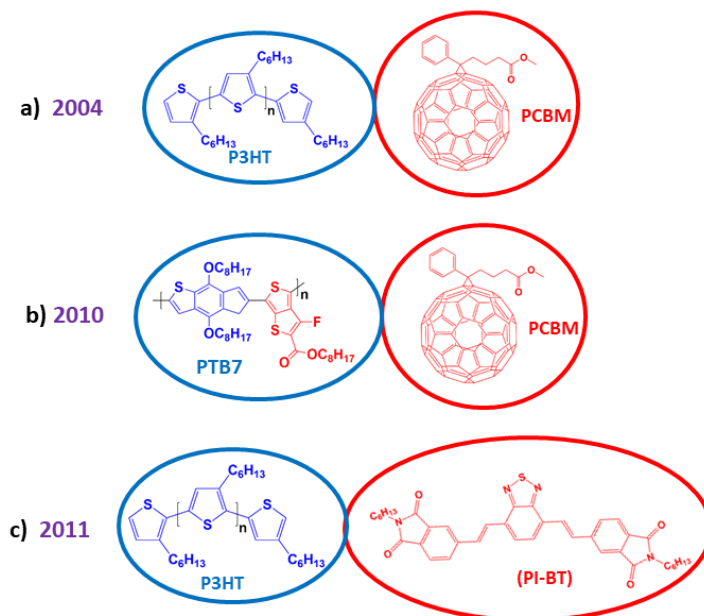


**Figure I.8:** Showing the historical progression in structural design of Donor and Acceptor materials used in organic photovoltaic (OPV) devices. **a)** in 2004, Donor and Acceptor materials: poly(3-hexylthiophene (P3HT) and Acceptor material: phenyl-C-butyric acid methyl ester derivative (PCBM); **b)** in 2010, Donor and Acceptor materials, poly[[4,8-bis[(2-ethylhexyl)oxy]benzo[1,2-b:4,5-b']dithiophene-2,6-diyl][3-fluoro-2-[(2ethylhexyl)carbonyl]thieno[3,4-b]-thiophenediyl]], (PTB7) polymer and PCBM; **c)** in 2011, Donor and Acceptor materials, P3HT and 4,7-bis(4-(N-hexyl-phthalimide)vinyl)benzo-[c]1,2,5-thiadiazole: (PI-BT).

With extensive research in OPVs, it was discovered that fullerene, PCBM, has disadvantages, such as: high synthetic costs; limited optical absorption; poor bandgap tunability; morphological instability. The motivation of this research is to find alternative acceptor materials. Efforts in the design and synthesis of nonfullerene acceptors (NFAs) produced major progress in 2014 with materials comparable to fullerene- and subsequently surpassing the state-of-the-art fullerene based OPV device in 2017. **Figure I.8** shows molecular structure of NFAs discovered over the years. The discovery of NFAs has led to another advantage of OPV which is having versatility in their active layer materials compared to other PV devices. Indeed, the PCE of OPVs have continued to



improve beyond 16% and are Over the years, the PCE of OPVs have achieved beyond 16% and are approaching to 19% – 20%. A main objective of this research is to find the correlation between organic material structural design and the PCE of solar cell devices.<sup>23-30</sup> One approach for increasing the PCE in OPVs is investigating the charge generation mechanism and finding the optimal structural design of organic materials used in a device.

Now, that Acceptor materials are NFAs this opens the design to for NFAs to have donor-acceptor structural framework as well. Presently, having both Donor and Acceptor materials with donor-acceptor structural framework, allows more possibilities to finding the best combination of donor-acceptor materials With energy diagrams, the advantage of NFAs with this new structural design is then energy gap between exciton/ excited singlet state can be adjusted for more effective charge generation. Also, decrease the possibility of losing exction in excited triplet state Now, need to investigate the CT dynamics of both D and A and find best combination of donor-acceptor units. Thus, nonfullerence acceptors (NFAs) are being develop to counter the disadvantages of fullerene As table shows, PCE of OPVs are improving to 18% due to this new structural design for Acceptor material. **Table I.1** shows a summary of the progression of power conversion efficiency due to the major structure framework design in Donor and Acceptor materials.<sup>23,31-34</sup>

**Table I.1:** Summary of power conversion efficiency over the years, showing the impact of donor-acceptor structural framework design on Donor and Acceptor materials used in organic photovoltaic (OPV) devices. Figure I.11 shows structures for some of materials listed in this **Table**.

OPVs	Year	Type	PCE (%)	Reference
P3HT:PCBM	2004	Fullerene	3.1%	31
PTB7:PBCM	2010	Fullerene	7.40	23
P3HT:PI-BT	2011	NFA	2.54	32
P3HT:O-IDTBR	2016	NFA	6.30	33
PM6:Y6:AQX-3	2021	NFA	18.01	34

### *1.8.c Organic Ladder Materials Use in Optoelectronic Applications*

When an organic oligomer can be systematically synthesized to create a series of the oligomer based on the conjugation length, the organic oligomer can be classified as fused organic ladder oligomer (OLO).<sup>35-38</sup> OLOs have a dominate planar conformation to minimize bond twisting within the molecular structure of these molecules. The advantage of having a planar confirmation that minimized bond twisting is to enhance conjugation and  $\pi$ - $\pi$  interaction within the molecular structure of these oligomers. Studies have shown the enhanced conjugation and  $\pi$ - $\pi$  interaction of an OLO increases the charge transport of the oligomer. By investigating OLOs, a correlation can be discovered between structure and the charge transport mechanism of these molecules. Then, the discovered correlation can provide a guideline to which oligomeric structure will lead to a high charge carrier mobility for organic oligomers used in transistor applications.

### **1.9 Ultrafast Spectroscopy and Investigating Charge Generation of Materials Used in OPVs**

One approach for investigating exciton dynamics and intramolecular charge generation of organic materials used in OPV is utilizing ultrafast laser spectroscopy. Studies have shown ultrafast laser spectroscopy can be utilized to investigate the optical and photophysical properties of organic semiconducting materials used in OPV devices.<sup>35-37,39-47</sup> The next paragraph describes studies that utilized ultrafast laser spectroscopy to investigate the exciton dynamics, intramolecular charge generation and other dynamics occurring in organic semiconducting materials used in OPV devices. In one study, the charge transfer dynamics of perylenediimide-thienoacene OLOs were investigated by utilizing photoluminescence (Streak camera) and transient absorption (femtosecond and nanosecond) spectroscopy.<sup>46</sup> It was found that the perylenediimide-thienoacene OLO with the five fused ring linker showed the optimal charge transfer dynamics due to the combination of efficient electron delocalization and slow charge transfer lifetime.<sup>46</sup> The results

discussed in this study provide an explanation to why the five fused ring linker perylene-diimide-thienoacene OLO demonstrated the best performance for an optoelectronic solar cell device.<sup>46</sup> This example study and other studies show ultrafast laser spectroscopy can be utilized as an approach for investigating a property of OLOs and provide an explanation for which molecular structure will have the best performance for an optoelectronic application.<sup>35–37,39–43,46</sup>

Ultrafast laser spectroscopy such as transient absorption, were utilized to investigate charge dynamics of molecules that have been functionalized by incorporating PDI monomer units to the molecular structure.<sup>43</sup> In Muthike et.al<sup>43</sup>, the charge dynamics of singlet fission were investigated for PDI-functionalized molecules that are categorized as PDI dendritic tetramers.<sup>43</sup> In this study, there are three PDI dendritic tetramers. Both PDI monomer unit and PDI dendritic tetramers show there is an excited triplet state in visible light region. Under nitrogen environment conditions, the PDI monomer unit has a longer decay of its excited triplet state compared to the PDI dendritic tetramers decays of their excited triplet state. According to the Muthike study, only the  $\alpha$  PDI dendritic tetramer showed that it could undergo iSEF. The other PDI dendritic tetramers,  $\beta$  and  $\beta$ C, can't undergo iSEF; despite the fact that these PDI dendritic tetramers contain excited triplet states. To summarize transient absorption can be used to investigate exciton dynamics of organic semiconducting materials used in OPV devices.

In a study conducted by Madu et al<sup>45</sup>, ultrafast laser spectroscopy was utilized to investigate the charge dynamics of PDI-functionalized molecules that are categorized as N-annulated PDI dimers. For a molecule to be described as N-annulated, a five-member ring with nitrogen has been added to the structure of the molecule. For the N-annulated PDI dimers, a five-member ring with nitrogen has been added to the middle portion of the PDI monomer unit. Each N-annulated PDI dimer was connected to a thiophene. The thiophene group was placed between the N-

annulated PDI monomer units. There were two N-annulated PDI dimers in this study. The two N-annulated PDI dimers were labelled as M1 and M1F. The difference between the two N-annulated PDI dimers was the connectivity between the thiophene and N-annulated PDI dimers. The reason for studying these N-annulated PDI dimer was to determine how the difference in connectivity, between unfused thiophene and fused thiophene, within the N-annulated PDI dimer affects the charge transfer and charge separation within the molecular structures. The ultrafast laser spectroscopy utilized in this study was transient absorption. The results obtained from transient absorption showed there was a difference in photoinduced intramolecular charge separation and excited triplet state formation between the two N-annulated PDI dimers. M1F had a faster charge separation lifetime compared to the M1 due to the increase in planarity of having a fused structure. The ultrafast transient absorption results of this study showed having a fused structure will lead to a more efficient charge separation for OPV devices.<sup>45</sup>

Previous studies has shown that ultrafast laser transient absorption spectroscopy has been utilized to investigate singlet fission in pentacene and other acene derivatives.<sup>39-41,47</sup> In a study conducted by Busby, they investigated singlet fission mechanism within tetracene, pentacene and hexacene crystals utilizing transient absorption spectroscopy. In that study, they concluded crystalline hexacene had a more efficient singlet fission compared to the other crystalline acenes due to hexacene having more favorably energetics that allowed an efficient mechanism.<sup>47</sup> Previous studies have utilized ultrafast photoconductivity measurements to investigate the charge transport mechanism and charge carrier mobilities of functionalized pentacene films.<sup>42,43</sup> In a study conducted by Day, they investigated the charge transport mechanism and charge carrier mobilities of functionalized pentacene and dicyanomethylenedihydrofuran (DCDHF) films by utilizing multiple ultrafast photoconductivity (transient, continuous wave, temperature and electric field

dependence) measurements.<sup>43</sup> In this study, they discovered that functionalized pentacene films show two decay time components within kinetic traces obtained from transient photoconductivity measurements. In this study, they determined functionalized pentacene films had longer charge carrier mobility and photogeneration efficiency compared to DCDHF film.<sup>43</sup> In this study, they concluded that the charge transport mechanism of pentacene films consistent of tunneling from small molecular polarons, trapping and bimolecular recombination. The tunneling from small molecular polarons occurred on tens to several hundred picosecond timescale. The trapping and bimolecular recombination occurred on hundreds of microsecond to seconds.<sup>43</sup> As for DCDHF film, the charge transport mechanism was due to charge carrier being trapped or recombination. The trapping and recombination of charge carrier occurred on hundreds picosecond (roughly 200ps) timescale.<sup>43</sup> In the Day study, they concluded the charge transport mechanism affects the charge carrier mobility of photogeneration efficiency of functionalized pentacene and DCDHF films. The longer charge mechanism of functionalized pentacene films created a higher charge carrier mobility and photogeneration efficiency compared to the DCDHF film.<sup>43</sup> In another study, they utilized Raman spectroscopy to investigate the effect of electron-phonon interaction on the charge transport of crystal OSC films.<sup>44</sup> In a study conducted by Sosorev, they determined the electron-phonon interaction of crystalline 2,5-difluoro-7,7,8,8-tetracyanoquinodimethane (F<sub>2</sub>-TCNQ) and 7,7,8,8-tetracyanoquinodim (TCNQ) films utilizing Raman spectroscopy and density functional theory calculations.<sup>44</sup> In this study, they concluded the combination of Raman spectroscopy and density functional theory calculations could provide insight the electron-phonon interactions of OSC crystals; thus, using this combination to provide guidelines for OSCs with low non-local electron-phonon interaction which would lead to high charge carrier mobilities.<sup>44</sup> As previous research has shown, ultrafast laser spectroscopy is a great tool for investigating the charge

transport mechanism of OSCs or photophysical properties of OLO.<sup>35–37,39–41,43,43–47</sup> In this paper, fs-TA will be utilized to investigate the charge transport mechanism of OLO for optoelectronic transistor application.

Previous studies have investigated the effect of conjugation length on the ultrafast dynamics of oligothiophenes.<sup>48,49</sup> In a study conducted by Gish et al, they investigated the ultrafast charge separation and recombination dynamics of naphthalene diimide end-capped thiophene oligomers. They also investigated the excited state dynamics of oligothiophenes without the naphthalene diimide to provide a control. By investigating both oligothiophenes with and without the naphthalene diimide end-caps, they were able to distinguish which ultrafast dynamics were due to the oligothiophenes compared to the naphthalene diimide. For both oligothiophenes with and without naphthalene diimide end-caps, Grish et al synthesized a series of between four to twelve thiophene rings. From their femtosecond transient absorption results, they showed there was a correlation between stimulated emission (SE) decay and the conjugation length of the oligothiophenes. The correlation was as the conjugation length increased, the SE decay increased. This correlation was also seen in another study conducted by Jones et al.<sup>49</sup> In the study conducted by Jones et al, they investigated the electron transfer of oligothiophenes with naphthalene diimide end caps. In this study, Jones et al also synthesized oligothiophenes without naphthalene diimide end caps to provide a control for their investigation. In both the Grish et al and Jones et al study, the explanation that they provided to explain the correlation between conjugation length and SE decay of oligothiophenes was the increased conjugation length created an increased structural disorder. The increased structural disorder indicated there was more energy available in the excited state could be used to emit radiative light, such as fluorescence. This explanation was further supported by the fluorescence quantum yields of these oligothiophenes.<sup>48,49</sup> The trend

between fluorescence quantum yield and conjugation length was not as obvious as the trend between SE decay and conjugation length of the oligothiophenes. The shortest oligothiophene (four thiophenes) had the lowest fluorescence quantum yield compared the longer oligothiophenes (six or more thiophenes). Regardless, of not having the obvious trend, the fluorescence quantum yield results supported that the longer oligothiophenes had more efficient (longer) fluorescence decay compared to the shorter oligothiophenes.

## **I.10 Synopsis of Dissertation Chapters**

In summary, this dissertation discusses research investigations that focus on the investigation of ultrafast charge dynamics within organic conjugated ladder semiconducting materials for optoelectronic applications. In order to investigate the ultrafast charge dynamics of these materials, I utilized ultrafast laser spectroscopy. My PhD work includes both research investigation that I led and collaborative works. The Table of Contents (see Page iv) shows the detailed information of Chapters in this dissertation. The next paragraphs below are synopses of each Chapters:

Chapter II is titled the *Experimental Section*. This Chapter contains information on the fundamentals, data analysis and setup of experiments utilized during my PhD. During my PhD, I had the opportunity to learn and gain skills in steady-state and ultrafast time-resolved and non-linear laser spectroscopy. The main conclusion of Chapter II is describing the experimental tools that I utilized to collect data and results of my PhD work and collaborative research investigations.

Chapter III is titled *The Investigation of the Ultrafast Dynamics within Organic Ladder Oligomers used in Optoelectronics Application*. Chapter III contains the results and conclusion of the research investigation regarding ultrafast charge dynamics of OLOs, called benzo[*k*]tetrathenes (BTps). Appendix C has the Supporting Information for this Chapter. From

the results obtained from fs-TA spectroscopy, the ultrafast charge dynamics and charge transport rates of BTps are investigated. The structural difference in the BTps is conjugation length. The results of this research investigation show there is a correlation between the conjugation length and charge transport rate of the BTps; as the conjugation length increases, the charge transport rate decreases. The main conclusions of this Chapter are 1) showing that fs-TA can be an alternative approach for predicting the charge carrier mobility and 2) providing a structural guideline from increasing the charge carrier mobility of OLOs.

Chapter IV is titled *Probing the Exciton Dynamics of Naphthalene-imide Based Nonfullerene Acceptors for Organic Photovoltaics*. Chapter IV contains results and conclusion of the research investigation regarding acceptor-donor-acceptor small molecule NFAs, called bis(naphthalene-imide)arylenelidenes (BNIAs). The Supporting Information for this Chapter is located in Appendix D. The structural differences between the BNIAs are donor units and  $\pi$ -conjugated lengths. From the results obtained from ultrafast time-resolved and non-linear laser spectroscopy and theoretical calculations, the exciton dynamics and the intramolecular charge generation mechanism of the BNIAs are investigated. The main conclusion of this research investigation is showing  $\pi$  bridges between the donor and acceptor of the BNIAs will lead to strong exciton dynamics and an efficient intramolecular charge generation for OPV device.

Chapter V is titled *Linear and Nonlinear Optical Properties of All-cis and All-trans Poly(p-phenylene vinylene)*. Chapter V contain results and conclusion of research investigation focuses on the excited state dynamics of all *trans* and all *cis* poly(p-phenylene vinylene) (PPV). From ultrafast time-resolved and non-linear laser spectroscopy and theoretical calculations, the photophysics of all *trans* and all *cis* PPV is investigated. Due to the faster excited state and fluorescence dynamics of is better for the optoelectronic application of organic light emitting



diodes OLEDs) since this isomer had faster excited state and fluorescence dynamics compared to all *cis* PPV. Then all *cis* PPV, it is better for quantum light application due to its relatively slow excited state and fluorescence dynamics. The main conclusion of this investigation is provide insight into which isomer of PPV will be better suited for optoelectronic application of organic light emitting diodes or quantum light; specifically, all *cis* PPV is better for OLEDs and all *trans* PPV is better suited for quantum light applications.

The title of Chapter VI is *Effect of Long-Lived Ground State Diradicaloids on the Photophysics of Semi-Ladder Thiophene-Based Polymer Aggregates for Organic Light Emitting Transistor (OLET) Applications*. Chapter VI contain results and conclusion of research investigation focuses on the excited state and radial character foldable donor-acceptor polymer for optoelectronic application of organic light emitting transistor (OLET). By utilizing fs-TA spectroscopy, the dynamics of excited singlet states and formation of excited triplet states within these polymers are investigated. In addition to fs-TA, results obtained other ultrafast laser spectroscopy, electron paramagnetic resonance experiments and theoretical calculations show the semi-ladder foldable donor-acceptor polymer that consisted of a furan within its acceptor unit had faster formation rate of excited triplet states compared to the semi-ladder polymer that consisted with a thiophene within its acceptor unit. The main conclusion of this Chapter is provide insight into the structural guideline of semi-ladder foldable donor-acceptor polymer for OLETs.

Chapter VII is titled *Summary of Dissertation and Future Outlook*. This Chapter will summarize the main conclusions of my PhD works and collaborative research investigations and contain on the future direction on ultrafast charge dynamics of OSCs, specifically, conjugated organic ladder semiconducting materials for optoelectronic applications.

In conclusion, the main objective of the research investigations that I work on during my PhD is understanding the structure-function relationship of OSCs for optoelectronic applications. Specifically, my PhD work focuses on understanding the structure-function relation of OSCs that had a conjugated or ladder structural design. The conjugation varied based on having completely fused ladder structure or having a co-oligomer with non-fused conjugation and different in electron affinity within the structure of the OSCs. The research investigation of this PhD work increased the knowledge of ultrafast charge dynamics these type OSCs and how the structural design of these OSCs can lead to more effective and efficient optoelectronic applications. Ideally, the information in this dissertation will lead to finding the optimal structural design of OSCs with a conjugated or ladder structural framework for optoelectronic applications, such as transistor and solar cell applications.

## I.11 References

- (1) U.S. Department of Energy. <https://www.energy.gov/solar> (accessed 2024-01-15).
- (2) U.S. Department of Energy Office Solar Energy Technologies Office. <https://www.energy.gov/eere/solar/photovoltaics> (accessed 2024-01-20).
- (3) Feblowitz, J. Renewable Energy World, 2021. <https://www.renewableenergyworld.com/solar/government-and-private-funding-we-need-both-for-the-energy-transition/#gref> (accessed 2024-02-02).
- (4) Committee on Science Space and Technology, 2020. <https://science.house.gov/2020/12/energy-act-of-2020> (accessed 2024-02-03).
- (5) U.S. Department of Energy Office Solar Energy Technologies Office. <https://www.energy.gov/eere/solar/organic-photovoltaics-research> (accessed 2024-01-19).
- (6) Inganäs, O. Organic Photovoltaics over Three Decades. *Adv. Mater.* **2018**, *30* (35), 1800388. <https://doi.org/10.1002/adma.201800388>.
- (7) Sharma, T.; Mahajan, P.; Adil Afroz, M.; Singh, A.; Yukta; Kumar Tailor, N.; Purohit, S.; Verma, S.; Padha, B.; Gupta, V.; Arya, S.; Satapathi, S. Recent Progress in Advanced Organic Photovoltaics: Emerging Techniques and Materials. *ChemSusChem* **2022**, *15* (5). <https://doi.org/10.1002/cssc.202101067>.
- (8) Tamai, Y. What's Next for Organic Solar Cells? The Frontiers and Challenges. *Adv. Energy Sustain. Res.* **2023**, *4* (1), 2200149. <https://doi.org/10.1002/aesr.202200149>.
- (9) Corbett, M. Federal Reserve History. <https://www.federalreservehistory.org/essays/oil-shock-of-1973-74> (accessed 2024-01-16).
- (10) Beasley, B. A. Energy History Online - Yale University, 2023. <https://energyhistory.yale.edu/the-oil-shocks-of-the-1970s/> (accessed 2024-01-16).
- (11) U.S. Energy Information. Annual Energy Review 2011. **2012**.
- (12) U.S. Energy Information Administration. <https://www.eia.gov/about/> (accessed 2024-01-14).
- (13) U.S. Energy Information Administration. [https://www.eia.gov/about/mission\\_overview.php](https://www.eia.gov/about/mission_overview.php) (accessed 2024-01-14).
- (14) OECD. *OECD Inventory of Support Measures for Fossil Fuels 2023*; 2023. <https://doi.org/10.1787/87dc4a55-en>.
- (15) Organisation for Economic Co-Operation and Development. <https://www.oecd.org/about/> (accessed 2024-01-12).
- (16) Fritts, C. E. On a New Form of Selenium Cell, and Some Electrical Discoveries Made by Its Use. *Am. J. Sci.* **1883**, *s3-26* (156), 465–472. <https://doi.org/10.2475/ajs.s3-26.156.465>.
- (17) U.S. Department of Energy Energy Efficiency and Renewable Energy. [chrome-extension://efaidnbmnnnibpcajpcglclefindmkaj/https://www1.eere.energy.gov/solar/pdfs/solar\\_timeline.pdf](chrome-extension://efaidnbmnnnibpcajpcglclefindmkaj/https://www1.eere.energy.gov/solar/pdfs/solar_timeline.pdf) (accessed 2024-02-06).
- (18) Green, M. A.; Blakers, A. W.; Narayanan, S.; Taouk, M. Improvements in Silicon Solar Cell Efficiency. *Sol. Cells* **1986**, *17* (1), 75–83. [https://doi.org/10.1016/0379-6787\(86\)90060-8](https://doi.org/10.1016/0379-6787(86)90060-8).
- (19) Bellini, E. Pv Magazine Group. <https://www.pv-magazine.com/2022/05/30/fraunhofer-ise-achieves-47-6-efficient-for-iii-v-four-junction-cpv-cell/> (accessed 2024-01-31).
- (20) National Renewable Energy Laboratory. <https://www.nrel.gov/pv/cell-efficiency.html> (accessed 2024-01-29).
- (21) Geisz, J. F.; France, R. M.; Schulte, K. L.; Steiner, M. A.; Norman, A. G.; Guthrey, H. L.; Young, M. R.; Song, T.; Moriarty, T. Six-Junction III–V Solar Cells with 47.1% Conversion

- Efficiency under 143 Suns Concentration. *Nat. Energy* **2020**, *5* (4), 326–335. <https://doi.org/10.1038/s41560-020-0598-5>.
- (22) Kolhe, N. B.; West, S. M.; Tran, D. K.; Ding, X.; Kuzuhara, D.; Yoshimoto, N.; Koganezawa, T.; Jenekhe, S. A. Designing High Performance Nonfullerene Electron Acceptors with Rylene Imides for Efficient Organic Photovoltaics. *Chem. Mater.* **2020**, *32* (1), 195–204. <https://doi.org/10.1021/acs.chemmater.9b03329>.
- (23) Liang, Y.; Xu, Z.; Xia, J.; Tsai, S.-T.; Wu, Y.; Li, G.; Ray, C.; Yu, L. For the Bright Future-Bulk Heterojunction Polymer Solar Cells with Power Conversion Efficiency of 7.4%. *Adv. Mater.* **2010**, *22* (20), E135–E138. <https://doi.org/10.1002/adma.200903528>.
- (24) Chong, K.; Xu, X.; Meng, H.; Xue, J.; Yu, L.; Ma, W.; Peng, Q. Realizing 19.05% Efficiency Polymer Solar Cells by Progressively Improving Charge Extraction and Suppressing Charge Recombination. *Adv. Mater.* **2022**, *34* (13), 2109516. <https://doi.org/10.1002/adma.202109516>.
- (25) Karki, A.; Gillett, A. J.; Friend, R. H.; Nguyen, T. The Path to 20% Power Conversion Efficiencies in Nonfullerene Acceptor Organic Solar Cells. *Adv. Energy Mater.* **2021**, *11* (15), 2003441. <https://doi.org/10.1002/aenm.202003441>.
- (26) Wadsworth, A.; Moser, M.; Marks, A.; Little, M. S.; Gasparini, N.; Brabec, C. J.; Baran, D.; McCulloch, I. Critical Review of the Molecular Design Progress in Non-Fullerene Electron Acceptors towards Commercially Viable Organic Solar Cells. *Chem. Soc. Rev.* **2019**, *48* (6), 1596–1625. <https://doi.org/10.1039/C7CS00892A>.
- (27) Wang, J.; Zhan, X. Fused-Ring Electron Acceptors for Photovoltaics and Beyond. *Acc. Chem. Res.* **2021**, *54* (1), 132–143. <https://doi.org/10.1021/acs.accounts.0c00575>.
- (28) Li, H.; Earmme, T.; Ren, G.; Saeki, A.; Yoshikawa, S.; Murari, N. M.; Subramaniyan, S.; Crane, M. J.; Seki, S.; Jenekhe, S. A. Beyond Fullerenes: Design of Nonfullerene Acceptors for Efficient Organic Photovoltaics. *J. Am. Chem. Soc.* **2014**, *136* (41), 14589–14597. <https://doi.org/10.1021/ja508472j>.
- (29) Hwang, Y.-J.; Li, H.; Courtright, B. A. E.; Subramaniyan, S.; Jenekhe, S. A. Nonfullerene Polymer Solar Cells with 8.5% Efficiency Enabled by a New Highly Twisted Electron Acceptor Dimer. *Adv. Mater.* **2016**, *28* (1), 124–131. <https://doi.org/10.1002/adma.201503801>.
- (30) Lin, Y.; Wang, J.; Zhang, Z.-G.; Bai, H.; Li, Y.; Zhu, D.; Zhan, X. An Electron Acceptor Challenging Fullerenes for Efficient Polymer Solar Cells. *Adv. Mater.* **2015**, *27* (7), 1170–1174. <https://doi.org/10.1002/adma.201404317>.
- (31) Riedel, I.; Parisi, J.; Dyakonov, V.; Schilinsky, P.; Waldauf, C.; Brabec, C. J. Toward Highly Efficient Photogeneration and Loss-Free Charge Transport in Polymer-Fullerene Bulk Heterojunction Solar Cells; Kafafi, Z. H., Lane, P. A., Eds.; Denver, CO, 2004; p 82. <https://doi.org/10.1117/12.557630>.
- (32) Bloking, J. T.; Han, X.; Higgs, A. T.; Kastrop, J. P.; Pandey, L.; Norton, J. E.; Risko, C.; Chen, C. E.; Brédas, J.-L.; McGehee, M. D.; Sellinger, A. Solution-Processed Organic Solar Cells with Power Conversion Efficiencies of 2.5% Using Benzothiadiazole/Imide-Based Acceptors. *Chem. Mater.* **2011**, *23* (24), 5484–5490. <https://doi.org/10.1021/cm203111k>.
- (33) Holliday, S.; Ashraf, R. S.; Wadsworth, A.; Baran, D.; Yousaf, S. A.; Nielsen, C. B.; Tan, C.-H.; Dimitrov, S. D.; Shang, Z.; Gasparini, N.; Alamoudi, M.; Laquai, F.; Brabec, C. J.; Salleo, A.; Durrant, J. R.; McCulloch, I. High-Efficiency and Air-Stable P3HT-Based Polymer Solar Cells with a New Non-Fullerene Acceptor. *Nat. Commun.* **2016**, *7* (1), 11585. <https://doi.org/10.1038/ncomms11585>.

- (34) Liu, F.; Zhou, L.; Liu, W.; Zhou, Z.; Yue, Q.; Zheng, W.; Sun, R.; Liu, W.; Xu, S.; Fan, H.; Feng, L.; Yi, Y.; Zhang, W.; Zhu, X. Organic Solar Cells with 18% Efficiency Enabled by an Alloy Acceptor: A Two-in-One Strategy. *Adv. Mater.* **2021**, *33* (27), 2100830. <https://doi.org/10.1002/adma.202100830>.
- (35) Cai, Z.; Vázquez, R. J.; Zhao, D.; Li, L.; Lo, W.; Zhang, N.; Wu, Q.; Keller, B.; Eshun, A.; Abeyasinghe, N.; Banaszak-Holl, H.; Goodson, T.; Yu, L. Two Photon Absorption Study of Low-Bandgap, Fully Conjugated Perylene Diimide-Thienoacene-Perylene Diimide Ladder-Type Molecules. *Chem. Mater.* **2017**, *29* (16), 6726–6732. <https://doi.org/10.1021/acs.chemmater.7b01512>.
- (36) Zheng, T.; Cai, Z.; Ho-Wu, R.; Yau, S. H.; Shaparov, V.; Goodson, T.; Yu, L. Synthesis of Ladder-Type Thienoacenes and Their Electronic and Optical Properties. *J. Am. Chem. Soc.* **2016**, *138* (3), 868–875. <https://doi.org/10.1021/jacs.5b10175>.
- (37) Eshun, A.; Cai, Z.; Awies, M.; Yu, L.; Goodson, T. Investigations of Thienoacene Molecules for Classical and Entangled Two-Photon Absorption. *J. Phys. Chem. A* **2018**, *122* (41), 8167–8182. <https://doi.org/10.1021/acs.jpca.8b06312>.
- (38) Chen, D.; Zhu, D.; Lin, G.; Du, M.; Shi, D.; Peng, Q.; Jiang, L.; Liu, Z.; Zhang, G.; Zhang, D. New Fused Conjugated Molecules with Fused Thiophene and Pyran Units for Organic Electronic Materials. *RSC Adv.* **2020**, *10* (21), 12378–12383. <https://doi.org/10.1039/D0RA01984D>.
- (39) Li, J.; Cao, H.; Zhang, Z.; Liu, S.; Xia, Y. Research Progress on Singlet Fission in Acenes and Their Derivatives. *Photonics* **2022**, *9* (10), 689. <https://doi.org/10.3390/photonics9100689>.
- (40) Basel, B. S.; Hetzer, C.; Zirzmeier, J.; Thiel, D.; Guldi, R.; Hampel, F.; Kahnt, A.; Clark, T.; Guldi, D. M.; Tykwinski, R. R. Davydov Splitting and Singlet Fission in Excitonically Coupled Pentacene Dimers. *Chem. Sci.* **2019**, *10* (13), 3854–3863. <https://doi.org/10.1039/C9SC00384C>.
- (41) Guo, D.; Ma, L.; Zhou, Z.; Lin, D.; Wang, C.; Zhao, X.; Zhang, F.; Zhang, J.; Nie, Z. Charge Transfer Dynamics in a Singlet Fission Organic Molecule and Organometal Perovskite Bilayer Structure. *J. Mater. Chem. A* **2020**, *8* (11), 5572–5579. <https://doi.org/10.1039/C9TA11022D>.
- (42) Ostroverkhova, O.; Cooke, D. G.; Shcherbina, S.; Egerton, R. F.; Hegmann, F. A.; Tykwinski, R. R.; Anthony, J. E. Bandlike Transport in Pentacene and Functionalized Pentacene Thin Films Revealed by Subpicosecond Transient Photoconductivity Measurements. *Phys. Rev. B* **2005**, *71* (3), 035204. <https://doi.org/10.1103/PhysRevB.71.035204>.
- (43) Day, J.; Subramanian, S.; Anthony, J. E.; Lu, Z.; Twieg, R. J.; Ostroverkhova, O. Photoconductivity in Organic Thin Films: From Picoseconds to Seconds after Excitation. *J. Appl. Phys.* **2008**, *103* (12), 123715. <https://doi.org/10.1063/1.2946453>.
- (44) Sosorev, A. Yu.; Maslennikov, D. R.; Chernyshov, I. Yu.; Dominskiy, D. I.; Bruevich, V. V.; Vener, M. V.; Paraschuk, D. Yu. Relationship between Electron–Phonon Interaction and Low-Frequency Raman Anisotropy in High-Mobility Organic Semiconductors. *Phys. Chem. Chem. Phys.* **2018**, *20* (28), 18912–18918. <https://doi.org/10.1039/C8CP03232G>.
- (45) Mics, Z.; Tielrooij, K.-J.; Parvez, K.; Jensen, S. A.; Ivanov, I.; Feng, X.; Müllen, K.; Bonn, M.; Turchinovich, D. Thermodynamic Picture of Ultrafast Charge Transport in Graphene. *Nat. Commun.* **2015**, *6* (1), 7655. <https://doi.org/10.1038/ncomms8655>.
- (46) Leonard, A. A.; Mosquera, M. A.; Jones, L. O.; Cai, Z.; Fauvell, T. J.; Kirschner, M. S.; Gosztola, D. J.; Schatz, G. C.; Schaller, R. D.; Yu, L.; Chen, L. X. Photophysical Implications of Ring Fusion, Linker Length, and Twisting Angle in a Series of Perylenediimide–Thienoacene Dimers. *Chem. Sci.* **2020**, *11* (27), 7133–7143. <https://doi.org/10.1039/D0SC02862B>.

- (47) Busby, E.; Berkelbach, T. C.; Kumar, B.; Chernikov, A.; Zhong, Y.; Hlaing, H.; Zhu, X.-Y.; Heinz, T. F.; Hybertsen, M. S.; Sfeir, M. Y.; Reichman, D. R.; Nuckolls, C.; Yaffe, O. Multiphonon Relaxation Slows Singlet Fission in Crystalline Hexacene. *J. Am. Chem. Soc.* **2014**, *136* (30), 10654–10660. <https://doi.org/10.1021/ja503980c>.
- (48) Gish, M. K.; Jones, A. L.; Papanikolas, J. M.; Schanze, K. S. Role of Structure in Ultrafast Charge Separation and Recombination in Naphthalene Diimide End-Capped Thiophene Oligomers. *J. Phys. Chem. C* **2018**, *122* (33), 18802–18808. <https://doi.org/10.1021/acs.jpcc.8b04074>.
- (49) Jones, A. L.; Gish, M. K.; Zeman, C. J.; Papanikolas, J. M.; Schanze, K. S. Photoinduced Electron Transfer in Naphthalene Diimide End-Capped Thiophene Oligomers. *J. Phys. Chem. A* **2017**, *121* (50), 9579–9588. <https://doi.org/10.1021/acs.jpca.7b09095>.

## Chapter II

### Experimental Section

#### II.1 Overview

The main objective of this Chapter is to describe the fundamentals, data analysis and setup of experiments that were utilized to collect data and results of research investigations that I led or collaborative in during my PhD degree. Appendix B is the Supporting Information for this Chapter and describes the fundamentals experiments and theoretical calculations conducted by collaborators to collect data and results of research investigations described in this dissertation. This Chapter does not contain specific experimental details of Chapter III and Chapter IV. Please refer to the following Chapters specific experimental details Chapter III for organic ladder oligomer samples, Chapter IV for NFA samples, and Chapters V and VI for collaborative works.

#### II.2 Steady-State Absorption

##### *II.2.a Introduction and Description of Steady-State Absorption*

Steady-state absorption is a measurement that collects data on the absorption properties of molecule.<sup>1</sup> For this measurement, the absorption properties that are being investigated is the amount and what range of light that a molecule can take in as a result of its molecular structure. The absorption properties of molecule provides insight into excited states of the molecules. The excited states of a molecule are defined as energy levels that are above the neutral or ground state,  $S_0$ . In order to sees these excited states, absorption is defined as the amount light that a molecule can take in. The equation for absorption is shown in **Equation II.1**.

**Equation II.1**

$$\log \frac{I_o}{I} = \log \frac{1}{T} = A$$

where,  $I_o$  is the intensity of input light;  $I$  is the intensity of the output light; other way to express the ratio of light intensities is transmission,  $T$ .  $T$  is defined as the ratio between the intensity of output light over the intensity of input light, -  $T = \frac{I}{I_o}$ . The steady-state portion of this measurement refers to the continuous intensity of the light source. The data collected from steady-state absorption measurements show the range of light that a molecule can take in based on the structure of the molecule

### II.2.b General Description of Steady-State Absorption Experimental Setup

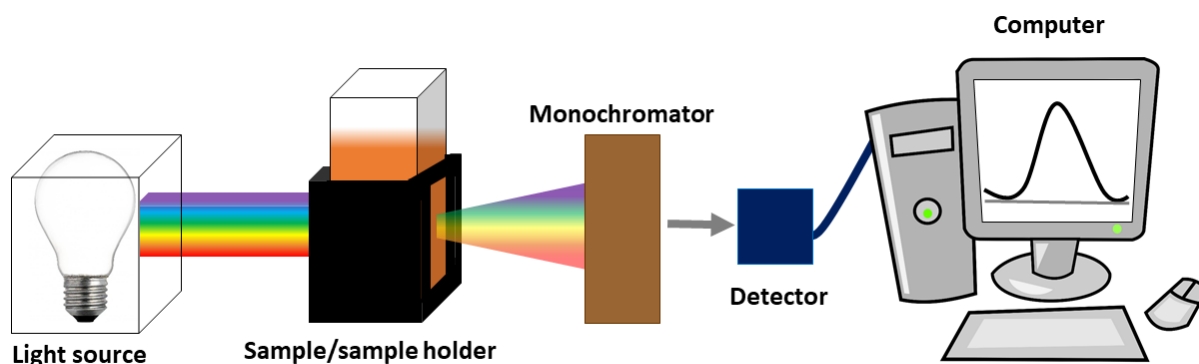


**Figure II.2:** General schematic of steady-state absorption measurement. This figure is showing the main pieces of equipment required to conduct this measurement. Please note this schematic is not draw to scale or show accurate depiction of the steady-state absorption measurement.

**Figure II.1** shows a general schematic of a steady-state absorption measurement. In order to conduct a steady-state absorption measurement, there needs to be a following pieces of equipment: light source, a sample holder, monochromator, detector and computer. The light source used in this measurement is a light that has the range within the ultraviolet – near infrared range of the electromagnetic radiation. The range of light utilized in steady-state absorption measurements is 190nm – 110nm. Beer-Lambert equation is a useful equation that used the



dependence of path length of a sample cuvette and molar extinction coefficient of molecule on its absorption properties. **Equation II.2** shows the Beer-Lambert:

**Equation II.III**

$$cl\varepsilon = A$$

where,  $A$  is the absorption of the molecule collected from the steady-state absorption measurement;  $c$  is the concentration of the molecule, units mol/L;  $l$  is the path length of the sample cuvette, units cm;  $\varepsilon$  is the molecular extinction coefficient, units L/ mol xcm. The steady-state absorption spectra of the collected using an Agilent 8453 spectrophotometer. Agilent Cary 60 UV-Vis Spectrophotometer. The Agilent Cary 60 UV-Vis Spectrophotometer contained a xenon lamp that could measure the steady-state absorption.

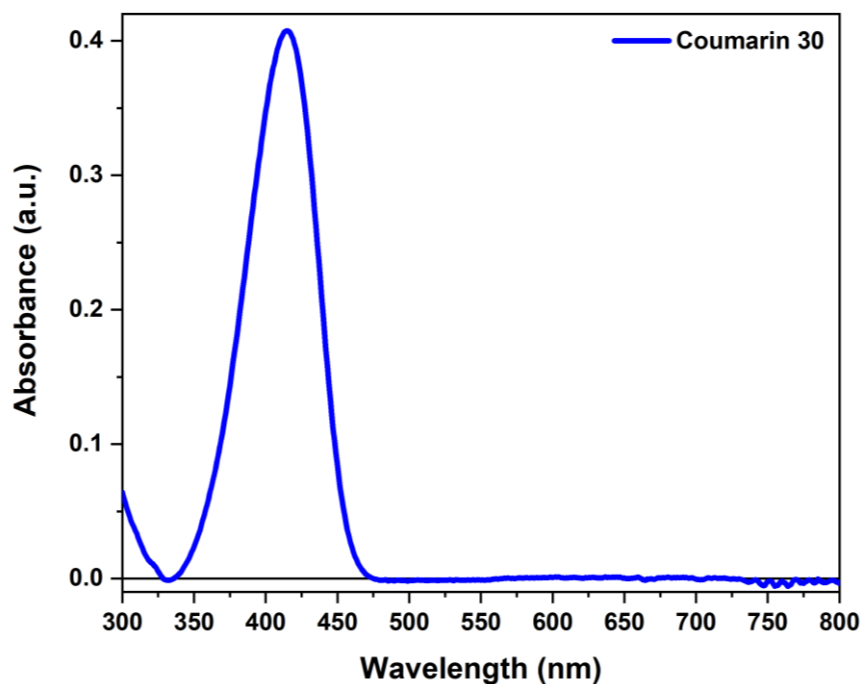


**Figure II.3:** Steady-state absorption spectrum of a Coumarin 30, a reference laser dye, in methanol

## II.3 Steady-State Emission Measurement

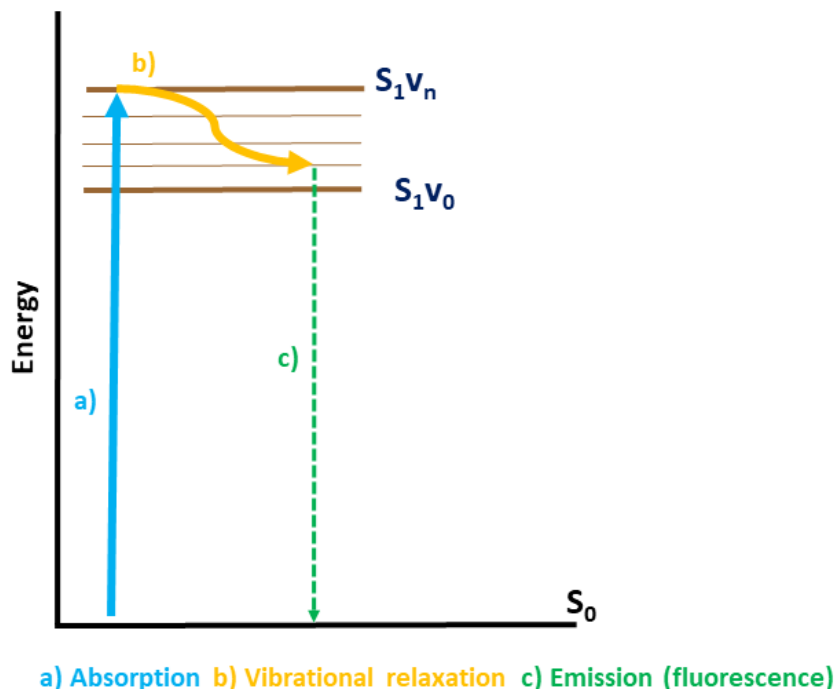


**Figure II.4:** General schematic of steady-state emission spectrum

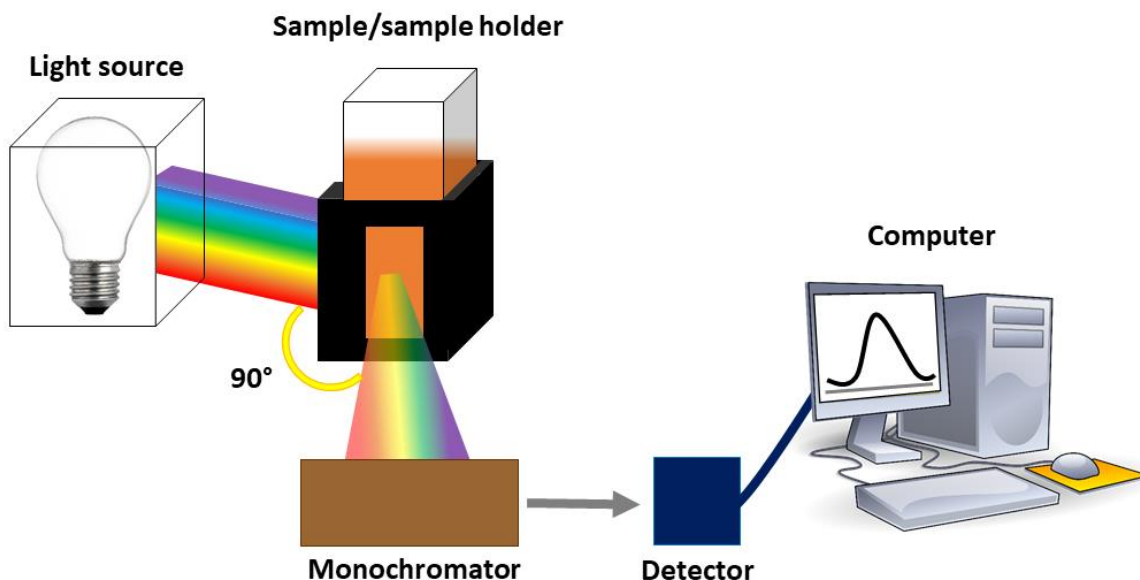
### II.3.a Introduction and Description of Steady-State Emission

Steady-state emission is a measurement that collects data on the absorption properties of molecule.<sup>2</sup> **Figure II.3** shows a general schematic of a steady-state emission occurring between the ground state,  $S_0$ , and an excited singlet state,  $S_1$ , within a molecule. For this measurement, the absorption properties that are being investigated is the amount and what range of light that a molecule can take in as a result of its molecular structure. The absorption properties of molecule provides insight into excited states of the molecules. The excited states of a molecule are defined as energy levels that are above the  $S_0$  (neutral or ground state). Stokes' shift shows the difference in wavelength of energy between absorption and emission. **Equation II.3** show a one form the of Stokes' shift:

**Equation IV**

$$\lambda_{ems\ max} - \lambda_{abs\ max} = \Delta\lambda$$

where,  $\Delta\lambda$  is the difference between the maximum peak of the steady-state emission and maximum peak of the steady-state absorption spectrum;  $\lambda_{ems\ max}$  is the maximum peak of the steady-state emission spectrum;  $\lambda_{abs\ max}$  is the maximum peak of the steady-state absorption spectrum. The steady-state portion of this measurement refers to the continuous intensity of the light source. The data collected from steady-state absorption measurements show the range of light that a molecule can take in based on the structure of the molecule

*II.3.b General Description of Steady-State Emission Experimental Setup*

**Figure II.5:** General schematic of steady-state emission measurement. This figure is showing the main pieces of equipment required to conduct this measurement. Please note this schematic is not drawn to scale or show accurate depiction of the steady-state absorption measurement

**Figure II.4** shows a general schematic of the state-steady emission measurement. Typically, the steady-state measurement is collected by a fluorimeter. The range of fluorescence measured in a fluorimeter varies based on the light source and the monochromator and detector.

Depending on these pieces of equipment, a steady-state emission can be measured from UV – NIR light. Typically, the sample holder used for these measurement has a 1.0cm path length and the sample holder is perpendicular to the light source as shown in **Figure II.4**. The reason for this orientation for the sample holder is to ensure that the fluorescence signal is being collected versus the absorption signal or signal from the light source. Ideally, the sample is prepared with a low concentration or optical density to prevent any artifacts during the measurements.<sup>3-6</sup>

## II.4 Femtosecond Transient Absorption

### II.4.a Introduction to femtosecond transient absorption (fs-TA) and transient absorption (TA)

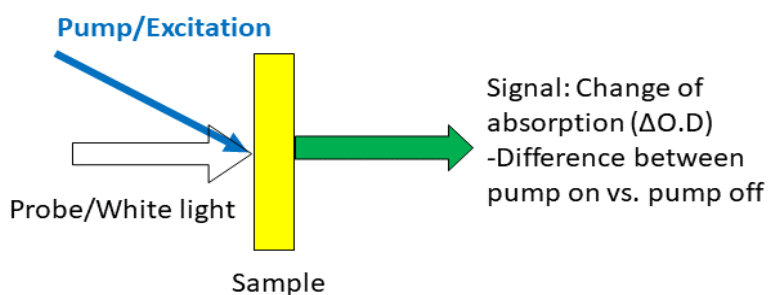


**Figure II.6:** General schematic of TA

femtosecond transient absorption (fs-TA) is the main ultrafast laser time-resolved experimental tool that I utilized to investigate the ultrafast charge dynamics within conjugated organic ladder semiconducting materials. fs-TA is a subset of an ultrafast laser time-resolved spectroscopy called transient absorption (TA).<sup>11</sup> TA is a pump-probe ultrafast time-resolved laser spectroscopy experiment that is utilized to determine the excited state dynamics of molecules. During a TA experiment, there are two sets of data collected and those data sets are spectra and kinetic traces. From the spectra and kinetic traces obtained from a TA experiment, these data sets are utilized to investigate the excited state dynamics of a molecule. Specifically, the excited state

dynamics measured in TA experiments are the energy and duration of excited states of a molecule. The spectrum obtained from a TA experiment shows the energy of the excited states of a molecule. Then, the kinetic traces obtained from a TA experiment shows how long or the duration of the excited state dynamics of a molecule. Recall, a Jablonski diagram provides insight into the radiative emissive mechanism of the excited state of a molecule. The advantage of TA experiment is both radiative and non-radiative emissive mechanism of the excited state of molecule is measured. Examples of the excited state mechanism of molecules that can be determined from TA results include, but not limited to the following, fluorescence, phosphorescence (radiative emissive mechanism), singlet fission, charge generation (non-radiative emissive mechanism) and other photophysical properties. TA experiments can measure these dynamics on the fs ( $10^{-15}$  sec) to microsecond ( $\mu\text{s}$ ,  $10^{-6}$  sec) timescale. The main objective of TA experiment is to create an energy diagram (similar to a Jablonski diagram) that shows the excited state dynamics (energy and duration of the excited state) of a molecule. In the sections below, I will describe the theory, experimental setup, data analysis and standards of fs-TA experiment I maintained and utilized during my PhD degree.

#### *II.4.b Description and Theory of TA and fs-TA*

As mentioned above, TA is a pump-probe ultrafast time-resolved laser spectroscopy experiments that provides insight into the excited state dynamics of molecules on the fs to  $\mu\text{s}$  timescale. During a TA experiment, a molecule is photo excited into excited states by a beam and then, other beam is used to detect which excited states of the molecules are populated. AddRefs By utilizing two beams during an experiment, TA is considered as pump-probe spectroscopy. The pump beam in a TA experiment gives the energy to a molecule so that the molecule gets excited into the excited state. The pump beam is also known as the excitation beam. Typically, the

excitation beam in a TA experiment is generated from a laser pulse that has enough energy to excite molecules from the ground state ( $S_0$ ) to an excited state. The energy of the excitation beam is determined by the steady-state absorption spectrum of a molecule. Recall, the steady-state absorption spectrum of a molecule provides insight into the energy of electronic states of a molecule. Specifically, the steady-state absorption spectrum of a molecule provides insight into the electronic transitions between the  $S_0$  and excited singlet states ( $S_n$ ). For example, the absorption maximum peak present in the steady-state absorption spectrum corresponds to the electronic transition between the  $S_0$  and the first excited singlet state,  $S_1$  (the electronic transition is  $S_0 \rightarrow S_1$ ). So, in order to ensure that a molecule can make the transition from ground state to a  $S_n$ , the molecule needs to absorb a discrete amount of energy and use that energy to move from the  $S_0$  to a  $S_n$ . For a TA experiment, the excitation beam is set at a specific energy that corresponds to an electronic transition in the steady-state absorption spectrum. Depending on what excited state dynamic is being investigated, the excitation beam is set at a specific energy in order to observe the study the excited state dynamic of a molecule.

The second beam utilized in a TA experiment is called the probe beam.<sup>11</sup> The probe beam of a TA experiment is a beam that has broad spectrum containing UV, Vis, or near-IR electromagnetic radiation.<sup>11</sup> In other words, the probe beam can have a range from 350nm – 2000nm, depending on which electromagnetic radiation is being generated. The probe beam is also known as a white light continuum. The white light continuum can be generated from a sapphire, calcium fluoride ( $\text{CaF}_2$ ) plate, or a xenon light source, depending on the timescale the TA experiment setup. For example, in an fs-TA experimental setup, a sapphire or  $\text{CaF}_2$  plate are used to generate Vis or UV white light continuum. Then, for a nanosecond-TA (ns-TA) experimental setup a xenon lamp is used to generate a UV to near-IR white light continuum. Add

Refs The objective of the white light continuum is to measure the excited state spectrum of a molecule during a TA experiment. The probe beam (white light continuum) shows which electronic states of a molecule are populated after a molecule has been excited by the pump beam.

During a TA experiment, the excitation beam will intermittently excited the molecule, while the white light continuum will be continuously hitting the molecule. The reason the excitation beam is intermittently exciting the molecule is the excitation beam is being discontinued by a chopper or shutter, creating an ‘On’ and ‘Off’ of the excitation beam. The ‘On’/’Off’ of the excitation beam allows the white light continuum to detect which electronic states of a molecule are populated after the molecule is excited by the excitation beam. The ‘On’/’Off’ of the excitation beam and the continuous white light continuum is the data measured and collected in a TA experiment. The data obtained from the TA experiment is called the change of absorption,  $\Delta A$ . **Equation II.4** shows the formula for the  $\Delta A$  in a TA experiment.

**Equation II.4** 
$$-\log \left( \frac{Intensity_{pump-On}}{Intensity_{pump-Off}} \right) = \Delta A$$

where  $Intensity_{pump-On}$  corresponds to the magnitude of the signal collected due to the excitation beam (pump beam) and the probe beam exciting and hitting the molecule at the same time; then  $Intensity_{pump-Off}$  corresponds to the magnitude of the signal collected due to only the probe beam hitting the molecule. For this condition, the excitation beam is ‘Off’ by being blocked by a chopper or shutter. Then, as with the Beer-Lambert’s law shown in Section II.1, the  $-\log$  of the difference in intensity between the excitation beam being ‘On’ then ‘Off’ to calculate the  $\Delta A$  obtained from the signals or data in a TA experiment. Depending on how the data is collected during a TA experiment, the  $\Delta A$  can be written at the change in transmission,  $\Delta T/T$  (see **Equation II.1**) Recall, from section II.1 Steady-state absorption, absorption and transmission are related to

each other as shown in the **Equation II.1**. For both  $\Delta A$  and  $\Delta T / T$ , these numerical values have no units. The data collected in a TA experiment is expressed as  $\Delta A$  or  $\Delta T / T$ . From the data of  $\Delta A$  or  $\Delta T / T$ , three main signals are observed in TA experiment. The three main signals are ground state bleach (GSB), stimulated emission (SE) or excited state absorption (ESA).

*II.4.b.i Description of Three Main Signals Observed in TA Spectrum*

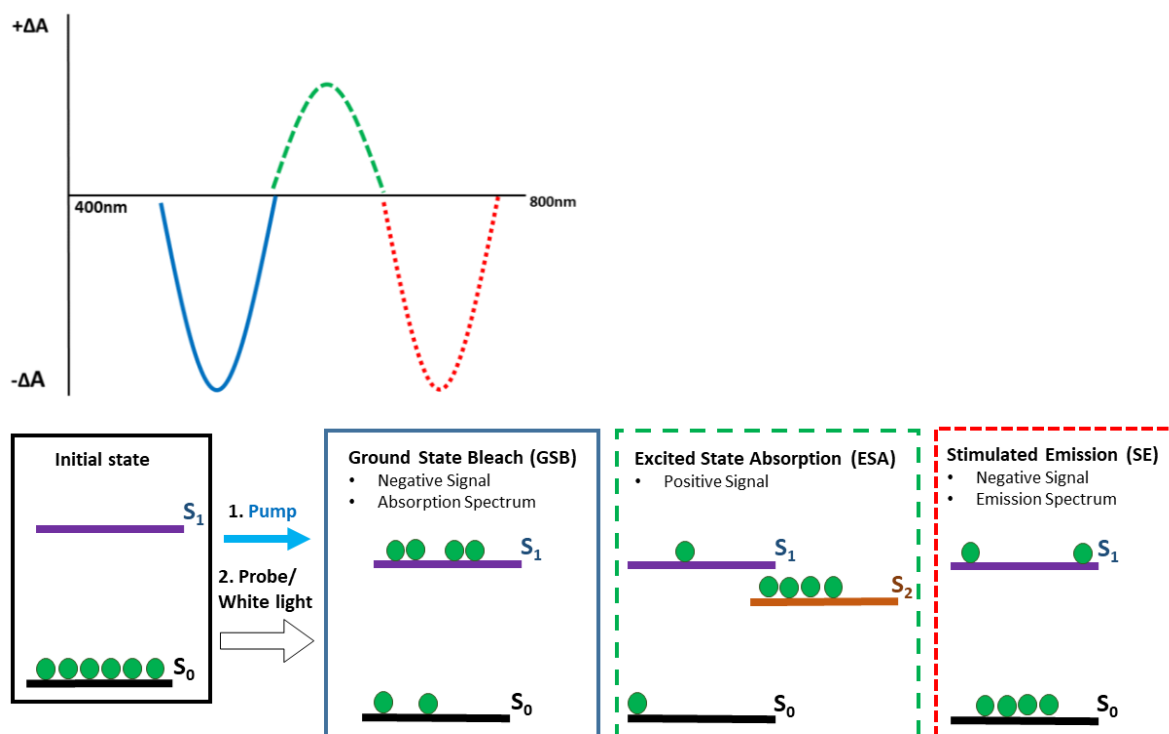


**Figure II.7:** General schematic of three main signals in a transient absorption (TA) experiment

**Figure II.6** shows a schematic a TA spectrum and energy diagram of electronic states representing the three main signals (GSB, SE, and ESA) of TA experiment where  $\Delta A$  is being measured. If  $\Delta T / T$  was being measured instead of  $\Delta A$ , the signs of the signals will be opposite (see Equation II.1 for explanation and relationship between absorbance and transmission). Typically, these three main signals are be visually observed in a spectrum data of a TA experiment. A TA spectrum is plotted as  $\Delta A$  versus wavelength in the units of nm (for  $\Delta T / T$ , the spectrum is



plotted as  $\Delta T / T$  versus wavelength in the units of nm). **Figure II.6** provides a visual schematic of signals and show the difference in population of molecules between the excited states which results in the three main signals observed in the spectrum obtained in a TA experiment. To clarify, the three main signals of TA are observed in both the spectrum and kinetic traces obtained from the data collected in an experiment. For now, the signals are being described and visually shown in a spectrum obtained in a TA experiment. Then, the kinetic traces of these signals will be described in another section of this Chapter, see Section II.

As shown in **Figure II.6**, the initial state of molecules in a TA experiment is these molecules are in  $S_0$ . Recall, the probe beam (white light continuum) is continuously hitting the molecules. Thus, at this initial state, molecules are being hit by the probe beam; however, the molecules are not being photo excited to an excited state due to the lower energy of the white light continuum. Typically, the excitation beam will have a higher energy compared to the probe beam; thus, the excitation beam will have enough energy to photo excite molecules from the  $S_0$  to another excited state. Also, recall, the excitation beam is being discontinued due to a chopper or shutter creating a ‘On’/‘Off’ condition. After the initial state, molecules will be photoexcited by the excitation beam and hit by the probe beam at the same time; the ‘On’ condition of the excitation beam. Then, the ‘Off’ condition of the excitation beam will occur, so the molecules are only being hit by the probe beam. The intensities or magnitudes of signals obtained from the ‘On’ and ‘Off’ conditions of the excitation beams are detected and collected. Based on the detected intensities, a GSB, ESA or SE signal will be observed in the spectrum of a TA experiment.

Starting with the GSB signal, this signal is due to the excited state having a higher population of molecules compared to the  $S_0$ . In other words, the GSB is due to a depletion of  $S_0$  as a result of molecules being photoexcited into to  $S_1$  or another excited state within the steady-

state absorption spectrum. The GSB is a negative signal that corresponds to the steady-state absorption spectrum of a molecule. In **Figure II.6**, the schematic is showing a GSB signal due to the  $S_1$  having a higher population of molecules compared to  $S_0$ . In general, GSB signal demonstrates that there are more molecules in the excited state compared to the  $S_0$  due to molecules being excited as a result of the excitation beam. The ESA signal is due to another excited state, other than the excited states associated with the steady-state absorption spectrum of molecule. As shown in **Figure II.6** the ESA signal corresponds to a  $S_n$ , another excited singlet state, having a higher population of molecules compared to the  $S_0$  and  $S_1$ . ESA signal is a positive signal on the TA spectrum of a molecule. Studies have shown that an ESA signal can correspond to both excited singlet states ( $S_n$ , another excited singlet state not associated with the GSB signal) and excited triplet states ( $T_n$ ). Then, the last signal is the SE. SE signal is due to the  $S_0$  having a higher population of molecules compared to the  $S_1$  or another excited state, such as  $S_n$  or  $T_n$ . As shown in **Figure II.6**, for the SE signal,  $S_0$  has a higher population of molecules in the  $S_0$  compared to the  $S_1$  and other excited states. The SE signal is a negative signal and it has the opposite population results compared to the GSB signal, which is opposite from the GSB signal. The GSB and SE signals can be expressed as Einstein coefficients.<sup>11</sup> Einstein coefficients describe the probability of spontaneous emission occurring compared to stimulated emission. Spontaneous emission is defined as the random relaxation of emitted light or energy being released from a higher excited state to a lower excited state. For example, spontaneous emission can occur from the  $S_1 \rightarrow S_0$ . SE is defined as light being emitted from molecules that absorbed energy while relaxing from a higher energy to lower energy states. Recall, in Section II of this chapter, SE is the explanation to how laser works. The Einstein coefficient of GSB is  $A_{12}$ . Then, SE the Einstein coefficient of SE is  $B_{21}$ . During a TA experiment, there is a possibility that from SE to occur due to excited molecules

absorbing energy from the probe beam (white light continuum) while relaxing from a higher energy to low energy states. Specifically, the probability of SE occurring is when molecules are undergoing the electronic transition of  $S_1 \rightarrow S_0$ . As molecules are relaxing from  $S_1$  to  $S_0$ , the molecules absorb energy from the probe beam as a result will emit light. Generally, SE signals corresponds to the steady-state emission spectrum of a molecule; since steady-state emission corresponds to the light being emitted from the  $S_1 \rightarrow S_0$ . From the three main signals measure in a TA experiment, the signals provide information on the energy of the excited states of molecules. In order to determine the duration of the of the excited states of molecules, a TA experiment needs to be able to measure and collected data corresponding to units of time.

The kinetic traces obtained from a TA experiment provides information on the duration of excited states on molecules. During a TA experiment,  $\Delta A$  (or  $\Delta T / T$ ) and time data are collected and both sets of data are used to create kinetic traces. The kinetic traces are plotted as  $\Delta A$  versus time. As mentioned above, the  $\Delta A$  are due to the data collected to represent the three main signals of a TA experiment – GSB, ESA and SE. Fig shows a schematic representation of kinetic traces of the three main signals. As shown in Fig, all kinetic traces show an exponential curve. As for the time data obtained in a TA experiment, the data is dependent on the pulse width of the excitation and probe beams and the length of a delay stage used in the experimental setup of the TA experiment. The delay stage is a piece of equipment that determine how length of kinetic trace. For example, a delay stage can have a length of 2ns or 8ns or longer depending on the delay stage. The instrument response function (IRF) of a TA experiment determines the resolution of the experiment. The IRF determines the lowest value of time that can be accurately resolved in a TA experiment. IRF provides supporting evidence of the timescale for a TA experiment. For example, a fs-TA experiment will have a IRF on the fs timescale; thus, proving that the fs-TA experiment

can accurately resolved The instrument response function of the experiment was approximately 160fs for Vis and 140fs for UV. To summarize, the next section will describe the fs-TA experimental setup that I maintained and utilized for the research investigations that I led or participated in during my PhD degree.

#### II.4.c Laser Experimental Setup of fs-TA

A Spectra-Physics ultrafast amplified laser system and Ultrafast System Helios, transient absorption spectrometer were used to create the fs-TA experimental setup. The fs-TA experimental set up started with a Millennia Pro continuous wave at 532nm laser (power of 4.3W) and a Tsunami Ti:Sapphire mode-locked laser to generate 790nm femtosecond (approximate pulse width: 80fs) pulse with output power of 250mW and repetition rate of 80MHz. The generated

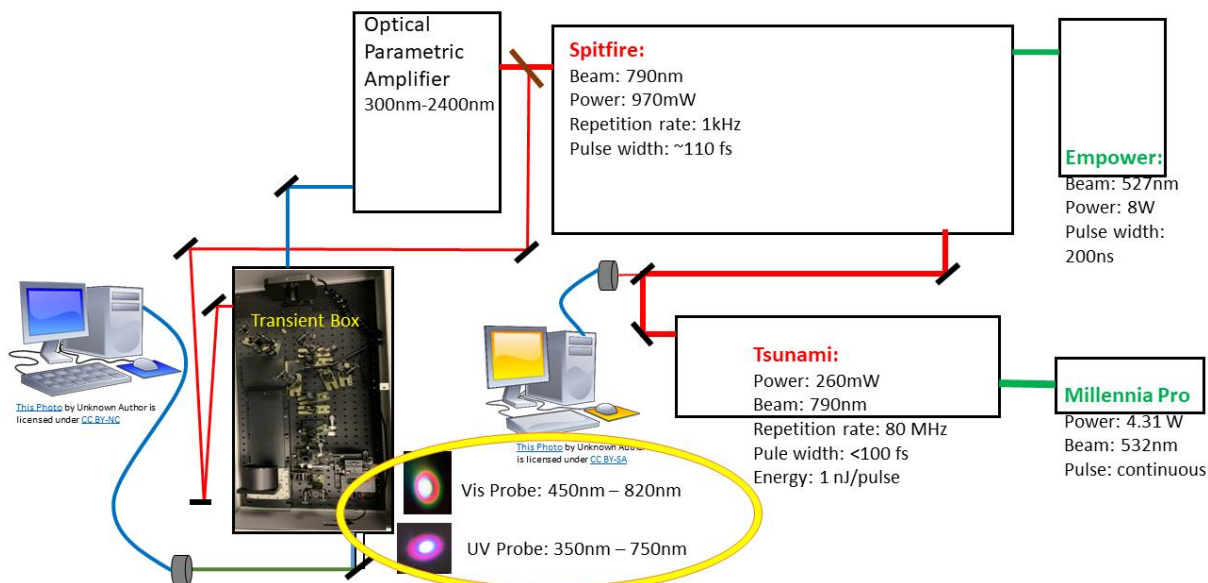


**Figure II.8:** General schematic of the fs-TA experimental setup in Goodson lab at the University of Michigan

790nm femtosecond pulse and 527nm pulse (approximate pulse width: 200ns) from an Empower Q-switched laser with an output power of 8W and repetition rate of 1kHz were directed into the cavity of a Spitfire Amplifier laser to generate an amplified 790nm output beam with:

approximate pulse width of 110 fs; repetition rate of 1kHz; and approximate output power of 1W. The 790nm amplified femtosecond pulse was directed into a beamsplitter that split the pulse into two portions that were used to generate the pump and probe beams for the fs-TA experiments. At the beamsplitter, approximately 15% of 790nm amplified femtosecond the pulse was used to generate the probe beam and other roughly 85% was directed into the Spectra-Physics Optical Parametric Amplifier (OPA-800C). Within the cavity of the OPA-800C, a 600nm pump was generated. A neutral density filter was used to attenuate the power of the 600nm pump to an average power of less than 1mW or approximate pump energy of 1.0 $\mu$ J/pulse. After the Spitfire amplifier, the amplified 790nm femtosecond pulse was directed into a beamsplitter, where approximately 5% of the amplified pulse was used to generate the probe beam for fs-TA experiment and other approximately 95% was used to pump the Ultrafast Optical Parametric Amplifier – 800C (OPA-800C). In order to generate the UV pumps, the signal beam, which was generated from optical parametric generation, went through two barium borate crystals to undergo fourth harmonic generation within the OPA-800C cavity.

#### *II.4.d Transient Box Experimental Setup of fs-TA*

The instrument response function of the experiment was approximately 160fs Vis. UV 140fs. TA experiments can be conducted on inorganic or organic molecules in the solution or film phase. Mentioned that only a small percentage is actually being excited during the TA experiment due to the beam diameter; however, the probe beam was directed through a computer-controlled delay line and focused onto a 3mm sapphire plate that generated a visible white light continuum. The visible white light continuum ranged from 450nm – 800nm. The probe beam/white light continuum and sample signal were directed and focused onto an Ocean Optics spectrometer and charge-coupled device (CCD), which collected the difference in absorbance signal ( $\Delta A$ ) as a result

of the pump being on versus off due to the optical chopper. The Helios software from Ultrafast System was used for data acquisition.

The probe beam was directed through a computer-controlled delay line and focused onto a rectangular calcium fluoride window with a 3mm thickness. The rectangular calcium fluoride window was placed on a rotating stage to prevent damage due high pulse energy probe consistently hitting the calcium fluoride window. The rectangular calcium fluoride window generated a UV white light continuum that ranged from 350nm – 750nm. The UV white light continuum/UV probe and sample signal were directed and focused onto an Ocean Optics spectrometer and charge-coupled device (CCD), which collected the difference in absorbance signal ( $\Delta A$ ) as a result of the UV pump being on versus off due to the optical chopper.

#### *II.4.e Data Analysis of fs-TA*

The data collected in a TA experiment if the spectrum and kinetics of the excited state for a molecule.<sup>12-14</sup> The Helios software, by Ultrafast Systems Inc., was used for data acquisition and the data analysis was done using Surface Xplorer and Origin Pro software. The fs-TA experimental set-up described in this paper was used in previous research.<sup>4,6</sup> The difference between described and previous fs-TA experimental set-up was a visible probe was used instead a UV probe.<sup>4,6</sup>

### **II.5 Time-resolved femtosecond Fluorescence Upconversion**

Time-resolved femtosecond fluorescence upconversion (UpC) experiment measure the fluorescene lifetime a molecule.<sup>15,16</sup> **Figure II.8** shows the experimental setup for a UpC experiment. As shown in **Figure II.8**, the experimental setup contained a Spectra-Physics Millennia Pro Laser to pump a Spectra-Physics Tsunami Ti:Sapphire mode-locked laser to generate an output beam of 800nm with a repetition rate of 80MHz, pulse width of approximately

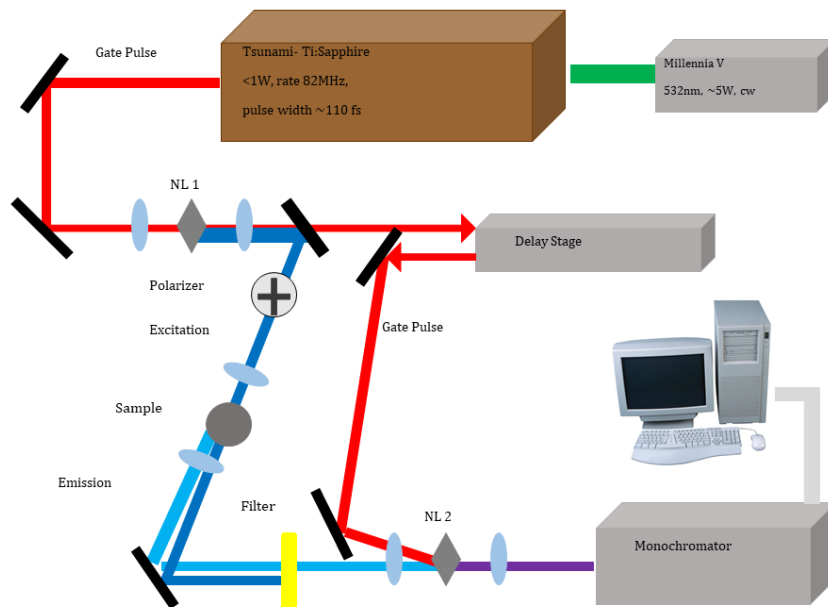


**Figure II.9:** General schematic of time-resolved fluorescence upconversion experimental setup in the Goodson lab

100fs, and output power of range from 400mW – 700mW. The pump excitation wavelength used in a experiment is generated by second harmonic generation. Typically, 400nm excitation wavelength is used since the Tsunami generates a 800nm output beam. A barium borate (BBO) nonlinear crystal is used to generate second harmonic generation. The efficiency of this process is approximately 10% is 400nm, while the 90% is 800nm. The 400nm excitation beam is used to excite a molecule, while the 800nm is used to detect the signal at another BBO crystal. At the second BBO nonlinear crystal, the fluorescence emission of a molecule and 800nm gate beam undergoes sum frequency mixing to generate an upconverted signal which was directed and focused into the monochromator and photomultiplier tube.<sup>17,18</sup> The UpC experiment can measure fluorescence from 110fs to roughly 2.0ns. The fluorescence lifetime collected in a UpC experiments provides information the duration a molecule will emit radiative fluorescence compared to other emissive processes.

## II.6 References

- (1) Eshun, A.; Cai, Z.; Awies, M.; Yu, L.; Goodson, T. Investigations of Thienoacene Molecules for Classical and Entangled Two-Photon Absorption. *J. Phys. Chem. A* **2018**, *122* (41), 8167–8182. <https://doi.org/10.1021/acs.jpca.8b06312>.
- (2) Clark, T. B.; Orr, M. E.; Flynn, D. C.; Goodson, T. Synthesis and Optical Properties of Two-Photon Absorbing GFP-Type Probes. *J. Phys. Chem. C* **2011**, *115* (15), 7331–7338. <https://doi.org/10.1021/jp2005925>.
- (3) Ricci, F.; Mandal, H.; Wajahath, M.; Burdick, R. K.; Villabona-Monsalve, J. P.; Hussain, S.; Goodson, T. Investigations of Coherence in Perovskite Quantum Dots with Classical and Quantum Light. *J. Phys. Chem. C* **2023**, *127* (7), 3579–3593. <https://doi.org/10.1021/acs.jpcc.2c08455>.
- (4) Madu, I. K.; Jiang, H.; Laventure, A.; Zimmerman, P. M.; Welch, G. C.; Goodson, T. Impact of Ring-Fusion on the Excited State Decay Pathways of N-Annulated Perylene Diimides. *J. Phys. Chem. C* **2021**, *125* (19), 10500–10515. <https://doi.org/10.1021/acs.jpcc.1c01964>.
- (5) Fisher, L.; Vázquez, R. J.; Howell, M.; Muthike, A. K.; Orr, M. E.; Jiang, H.; Dodgen, B.; Lee, D. R.; Lee, J. Y.; Zimmerman, P.; Goodson, T. Investigation of Thermally Activated Delayed Fluorescence in Donor–Acceptor Organic Emitters with Time-Resolved Absorption Spectroscopy. *Chem. Mater.* **2022**, *34* (5), 2161–2175. <https://doi.org/10.1021/acs.chemmater.1c03668>.
- (6) Muthike, A. K.; Carlotti, B.; Madu, I. K.; Jiang, H.; Kim, H.; Wu, Q.; Yu, L.; Zimmerman, P. M.; Goodson, T. The Role of the Core Attachment Positioning in Triggering Intramolecular Singlet Exciton Fission in Perylene Diimide Tetramers. *J. Phys. Chem. B* **2021**, *125* (19), 5114–5131. <https://doi.org/10.1021/acs.jpcc.1c02534>.
- (7) Williams, A. T. R.; Winfield, S. A.; Miller, J. N. Relative Fluorescence Quantum Yields Using a Computer-Controlled Luminescence Spectrometer. *The Analyst* **1983**, *108* (1290), 1067. <https://doi.org/10.1039/an9830801067>.
- (8) Makarov, N. S.; Drobizhev, M.; Rebane, A. Two-Photon Absorption Standards in the 550–1600 Nm Excitation Wavelength Range. *Opt. Express* **2008**, *16* (6), 4029. <https://doi.org/10.1364/OE.16.004029>.
- (9) Xu, C.; Webb, W. W. Measurement of Two-Photon Excitation Cross Sections of Molecular Fluorophores with Data from 690 to 1050 Nm. *J. Opt. Soc. Am. B* **1996**, *13* (3), 481. <https://doi.org/10.1364/JOSAB.13.000481>.
- (10) Vázquez, R. J.; Kim, H.; Kobilka, B. M.; Hale, B. J.; Jeffries-EL, M.; Zimmerman, P.; Goodson, T. Evaluating the Effect of Heteroatoms on the Photophysical Properties of Donor–Acceptor Conjugated Polymers Based on 2,6-Di(Thiophen-2-Yl)Benzo[1,2-b:4,5-B']Difuran: Two-Photon Cross-Section and Ultrafast Time-Resolved Spectroscopy. *J. Phys. Chem. C* **2017**, *121* (27), 14382–14392. <https://doi.org/10.1021/acs.jpcc.7b01767>.
- (11) Berera, R.; Van Grondelle, R.; Kennis, J. T. M. Ultrafast Transient Absorption Spectroscopy: Principles and Application to Photosynthetic Systems. *Photosynth. Res.* **2009**, *101* (2–3), 105–118. <https://doi.org/10.1007/s11120-009-9454-y>.
- (12) Bonneau, R.; Wirz, J.; Zuberbuhler, A. D. Methods for the Analysis of Transient Absorbance Data (Technical Report). *Pure Appl. Chem.* **1997**, *69* (5), 979–992. <https://doi.org/10.1351/pac199769050979>.
- (13) Lemmetyinen, H.; Tkachenko, N. V.; Valeur, B.; Hotta, J.; Ameloot, M.; Ernsting, N. P.; Gustavsson, T.; Boens, N. Time-Resolved Fluorescence Methods (IUPAC Technical Report). *Pure Appl. Chem.* **2014**, *86* (12), 1969–1998. <https://doi.org/10.1515/pac-2013-0912>.



- (14) Beckwith, J. S.; Rumble, C. A.; Vauthey, E. Data Analysis in Transient Electronic Spectroscopy – an Experimentalist’s View. *Int. Rev. Phys. Chem.* **2020**, *39* (2), 135–216. <https://doi.org/10.1080/0144235X.2020.1757942>.
- (15) Adegoke, O. O.; Jung, I. H.; Orr, M.; Yu, L.; Goodson, T. Effect of Acceptor Strength on Optical and Electronic Properties in Conjugated Polymers for Solar Applications. *J. Am. Chem. Soc.* **2015**, *137* (17), 5759–5769. <https://doi.org/10.1021/ja513002h>.
- (16) Franken, P. A.; Hill, A. E.; Peters, C. W.; Weinreich, G. Generation of Optical Harmonics. *Phys. Rev. Lett.* **1961**, *7* (4), 118–119. <https://doi.org/10.1103/PhysRevLett.7.118>.
- (17) Carlotti, B.; Cai, Z.; Kim, H.; Sharapov, V.; Madu, I. K.; Zhao, D.; Chen, W.; Zimmerman, P. M.; Yu, L.; Goodson, T. Charge Transfer and Aggregation Effects on the Performance of Planar vs Twisted Nonfullerene Acceptor Isomers for Organic Solar Cells. *Chem. Mater.* **2018**, *30* (13), 4263–4276. <https://doi.org/10.1021/acs.chemmater.8b01047>.
- (18) Carlotti, B.; Madu, I. K.; Kim, H.; Cai, Zhengxu.; Jiang, H.; Muthike, A. K.; Yu, L.; Zimmerman, P. M.; Goodson, T. Activating Intramolecular Singlet Exciton Fission by Altering  $\pi$ -Bridge Flexibility in Perylene Diimide Trimers for Organic Solar Cells. *Chem. Sci.* **2020**, *11* (33), 8757–8770. <https://doi.org/10.1039/D0SC03271A>.

## Chapter III

### The Investigation of Ultrafast Dynamics for Organic Conjugated Ladder Oligomers Used in Optoelectronics Applications

#### III.1 Collaboration Statement

This Chapter describes the results and conclusion of a collaborative research investigation between Professor Theodore G. Goodson III's group, Department of Chemistry, University of Michigan and Professor Lei Fang's group, Department of Chemistry, Texas A&M University (*Collaborator*). The authors of this research investigation are: **Meghan E. Orr**; Shao-Jiun Yang; Professor Lei Fang; and Professor Theodore G. Goodson III. **Meghan E. Orr's** (author of this dissertation) contribution to this work is: sample preparation for steady-state measurements and femtosecond transient absorption (fs-TA) experiments; conducting the mentioned measurements and experiments; performing data analysis for all mentioned measurements and experiments; and writing and editing the paper of this research investigation. The *Collaborator* contribution to this research investigation is provided samples and assisted with the editing the manuscript of this research investigation.

#### III.2 Abstract

Femtosecond transient absorption (fs-TA) spectroscopy is utilized to investigate the ultrafast dynamics in the charge transport of organic ladder oligomers (OLOs) The ultrafast

dynamics of the charge transport mechanism for benzo[*k*]tetraphenes (BTps) OLOs are investigated. The structural difference between the BTps is the conjugation length of these OLOs ranges from five to seven fused rings. For the fs-TA experiments conducted on the BTps, multiple energy excitation wavelengths are utilized to gain a full understanding of the charge transport mechanism. From the fs-TA results, the charge transport rates of BTps are determined. These results show a correlation between the conjugation length and charge transport rate of the BTps; as the conjugation length increases, the charge transport rate decreases. Based on these results, BTP5 has a faster charge transport rate compared to BTP7 due to the strong electron-phonon interaction within this OLO. The fs-TA results of the BTps predict that BTP7 will have a higher charge carrier mobility compared to BTP5 since this OLO has a weak electron-phonon interaction. The fs-TA results discussed in the paper will provide an approach for predicting the charge carrier mobility of OLOs for optoelectronic applications, such as transistor applications.

### III.3 Introduction

There is great excitement around the use of organic oligomers to transport charges in optoelectronic devices, such as transistor applications.<sup>1-5</sup> The advantages of using organic oligomers for transistor applications stem from their potential to create low-cost and flexible devices.<sup>1,5-7</sup> This has led to an intensified interest in the discovery of optimal oligomeric structures that can effectively transport charges for device applications.<sup>2,5,7</sup> Research has shown the measured numerical result of charge transport is charge carrier mobility.<sup>5,6,8</sup> Charge carrier mobility is defined as the speed of charges (negative or positive) flowing through a molecule due to an applied voltage and it has the units of  $\text{cm}^2\text{V}^{-1}\text{s}^{-1}$ .<sup>2,8,9</sup> It has been reported that the charge carrier mobility of an organic oligomer can reach up to  $50 \text{ cm}^2\text{V}^{-1}\text{s}^{-1}$ .<sup>5,10,11</sup> One approach for improving the charge carrier mobility of organic oligomers is investigating the correlation between

the charge transport mechanism and oligomeric structures.<sup>2,5,6,8</sup> Over the years, research has been conducted to investigate the charge transport mechanism of organic oligomers.<sup>5,6,8,12</sup> The two factors that affect the charge transport mechanism are the transfer integral (electronic coupling) and reorganization energy.<sup>1,6</sup> Electronic coupling is due to the overlap of  $\pi$  orbitals between molecules or the intermolecular interaction between molecules.<sup>1,3,6,12</sup> Studies have shown there are two parts for reorganization energy in the charge transport mechanism of organic molecules.<sup>1,6</sup> One part of reorganization energy refers to the external changes of energy in the system environment due to charge transport.<sup>6</sup> The other part of reorganization energy describes the internal changes or loss of energy as a result of charge transport occurring within a molecule.<sup>1,6,13</sup> A common approach for investigating the electronic coupling of the charge transport mechanism is studying the morphology, packing and intermolecular interaction of organic oligomer crystals in films.<sup>1,12,14</sup> Theoretical studies are another approach for investigating the electronic coupling and reorganization energy of the charge transport mechanism by determining which computational calculation will provide the best model for describing the rate of charge transport within organic oligomers.<sup>15-23</sup> In addition to electronic coupling and reorganization energy, a theoretical study found electron-phonon interactions can affect the charge transport mechanism of organic oligomers as well.<sup>16</sup> Since there are multiple factors that can affect the charge transport mechanism of organic oligomers, this suggests there are multiple factors that can impact the charge carrier mobility of organic oligomers as well.<sup>2,5,6,8</sup> When an organic oligomer can be systematically synthesized to create a series of the oligomer based on the conjugation length, the organic oligomer can be classified as an organic ladder oligomer (OLO).<sup>24-32</sup> OLOs have a dominate planar conformation to minimize bond twisting within the molecular structure of these molecules.<sup>24,32</sup> The advantage of having a planar confirmation that minimized bond twisting is to enhance

conjugation and  $\pi$ - $\pi$  interaction within the molecular structure of these oligomers.<sup>24,32</sup> Studies have shown the enhanced conjugation and  $\pi$ - $\pi$  interaction of an OLO increases the charge transport of the oligomer.<sup>24,32</sup> By investigating OLOs, a correlation can be discovered between structure and the charge transport mechanism of these molecules.<sup>24,26,32</sup> Then, the discovered correlation can provide a guideline to which oligomeric structure will lead to a high charge carrier mobility for organic oligomers used in transistor applications.<sup>6,11,26</sup> Studies have shown ultrafast laser spectroscopy can be utilized to investigate the optical and photophysical properties of OLOs.<sup>24,32-42</sup> For example, the charge transfer dynamics of perylenediimide-thienoacene OLOs were investigated by utilizing photoluminescence (Streak camera) and transient absorption (femtosecond and nanosecond) spectroscopy.<sup>40</sup> It was found the perylenediimide-thienoacene OLO with the five fused ring linker showed optimal charge transfer dynamics due to the combination of efficient electron delocalization and slow charge transfer lifetime.<sup>40</sup> The results discussed in this study provide an explanation to why the five fused ring linker perylenediimide-thienoacene OLO demonstrated the best performance for an optoelectronic solar cell device.<sup>40</sup> This example study and other studies show ultrafast laser spectroscopy can be utilized as an approach for investigating a property of OLOs and provide an explanation for which molecular structure will have the best performance for an optoelectronic application.<sup>24,32-37,40,42</sup>

Recently, a series of OLOs named benzo[*k*]tetraphenes, BTps, were synthesized to be materials used in optoelectronic applications, such as transistors.<sup>43</sup> The BTP series had a range of conjugation lengths; the conjugation lengths ranged from five to thirteen fused rings. The intermolecular interaction of BTP films were investigated by utilizing grazing incidence wide-angle x-ray scattering and density functional theory calculations. A trend between conjugation length and intermolecular interaction of the BTP films was observed; as the conjugation length

increased, the intermolecular interaction increased.<sup>43</sup> In addition, the effect of temperature on the crystalline of BTp films was observed as well. When room temperature was used to develop the film the film was developed at room temperature, the BTp with seven fused rings (BTp7) showed the best crystalline. When annealing temperature was used to develop the film, the BTp with eleven fused rings (BTp11) showed the best crystalline. It was found BTp7, for room temperature, and BTp11, for annealed, had the best crystalline best and packing within the films of these OLOs due to combination of intermolecular interaction and molecular mobility.<sup>43</sup> The study conducted on the BTps provided insight into the effect of conjugation length on the intermolecular interaction within films of these OLOs. The results from this study show the BTps have the potential to be good organic oligomer materials for optoelectronic application.<sup>43</sup>

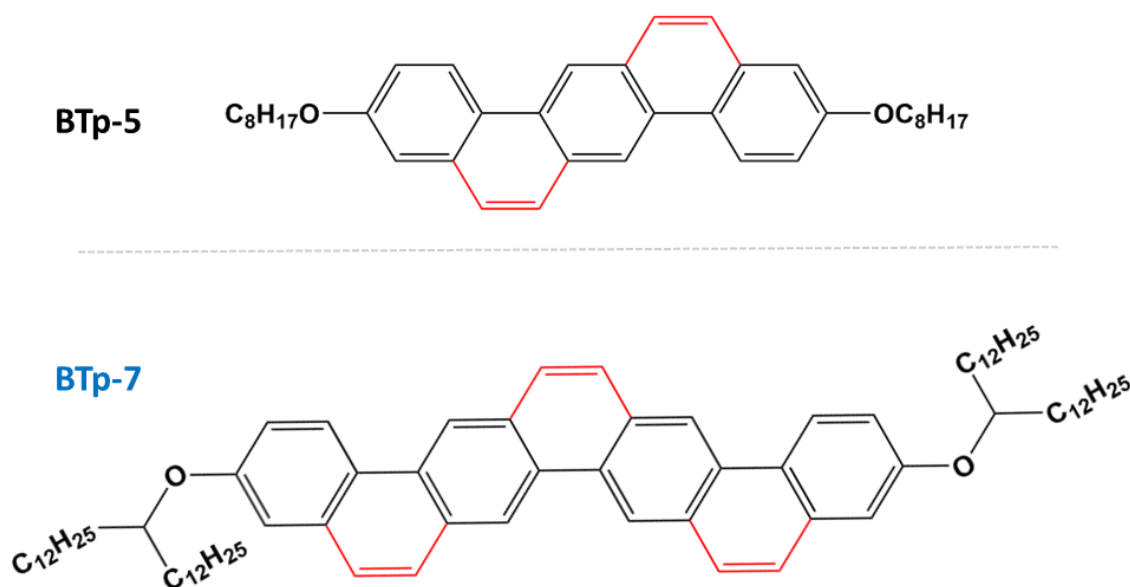


**Figure III.10:** Structures of the BTps: BTp-5 on Top and has a **black** label; BTp-7 on the Bottom and has a **blue** label.

In this paper, we are utilizing femtosecond transient absorption (fs-TA) spectroscopy to investigate if there is a correlation between ultrafast dynamics and charge carrier mobility of the BTps. fs-TA spectroscopy will determine if there are any ultrafast dynamics that affect the charge

transport mechanism of these OLOs. The structures of the investigated BTps are shown in **Figure III.1**. As mentioned earlier, there are multiple factors to consider when investigating the charge transport mechanism of organic oligomers and those factors are: 1) electronic coupling; 2) reorganization energy; and 3) electron-phonon interaction. From the previous study conducted on the BTps<sup>43</sup>, discussed above, the electronic coupling factor of the charge transport mechanism has been investigated by studying the intermolecular interaction of BTps films.<sup>43</sup> As a result, the other factors, electron-phonon interaction and reorganization energy, will be investigated in this paper to determine how these dynamics affect the charge transport mechanism and charge carrier mobility of the BTps. Once the ultrafast components of electron-phonon interaction and reorganization energy are determined from the fs-TA experiments, these ultrafast components will be used to determine the charge transport rate of the BTps. The charge transport rates of the BTps will provide insight to the charge carrier mobility of these OLOs. This work will provide an approach for predicting the charge carrier mobility of OLOs by discovering a correlation between conjugation length of oligomers and the ultrafast dynamics (electron-phonon interaction and reorganization energy) of charge transport mechanism obtained from fs-TA spectroscopy.

### **III.4 Experimental Section**

#### *III.4.a Sample Preparation Information*

BTp-5 and BTp-7 were synthesized according to the reported procedures and the characterizations were in agreement with the literature report.<sup>43</sup>

#### *III.4.b Steady-State Absorption and Emission*

The steady-state absorption spectra of the BTps were collected using an Agilent Cary 60 UV-Vis Spectrophotometer. The Agilent Cary 60 UV-Vis Spectrophotometer contained a xenon lamp that could measure the steady-state absorption spectrum from 190nm – 1100nm (see Figure

C.1 in Appendix C). Steady-state absorption measurements were conducted on liquid solutions of the BTps in chloroform. A quartz cuvette, with a 1.0cm path length, was used as the sample holder for these measurements. The steady-state absorption spectra of the BTp solution were measured from 200nm – 800nm. The BTp liquid solutions had an optical density of 1.0 for these measurements. The steady-state absorption measurements described in this paper has used in a previous report<sup>44</sup>; however, another Agilent UV-Vis Spectrophotometer was used.<sup>44</sup>

The steady-state emission spectra of the BTps were collected using a Horiba Scientific PTI QuantaMaster 3633 fluorimeter. The steady-state emission measurements were conducted on liquid solutions of BTps in chloroform. A quartz cuvette with a 1.0cm path length was used as a sample holder for the BTps solutions. The BTps solutions had an optical density of 0.2 for the steady-state emission measurements. The steady-state emission spectra of the BTp solution were measured from 320nm – 700nm. The steady-state emission measurements described in this paper have been used in previous reports.<sup>44,45</sup>

#### *III.4.c femtosecond Transient Absorption*

Femtosecond transient absorption (fs-TA) experiments were conducted on liquid solutions of the BTps. The BTps solutions were prepared in chloroform. The BTps solutions had an optical density ranging from 0.8 – 0.9 for these experiments. The fs-TA experimental setup contained a Spectra-Physics ultrafast amplified laser system and Ultrafast Systems Helios transient absorption spectrometer. The Spectra-Physics ultrafast amplified laser system contained a Millennia Pro laser (continuous wave at 532nm with a power of 4.3W) that was used to pump a Tsunami Ti:Sapphire oscillator mode-locked laser (pulsed at 790nm; output power: 260mW; repetition rate: 80MHz; approximate pulse width: 80fs) and Empower Q-switched laser (pulsed at 527nm; output power: 8W; repetition rate: 1kHz; approximate pulse width: 200ns) were used within the Spitfire amplifier



cavity to generate an amplified 790nm femtosecond pulse with: an approximate pulse width of 110 fs; repetition rate of 1kHz; and approximate output power of 1W. After the Spitfire amplifier, the amplified 790nm femtosecond pulse was directed into a beamsplitter, where approximately 5% of the amplified pulse was used to generate the probe beam for fs-TA experiment and other approximately 95% was used to pump the Ultrafast Optical Parametric Amplifier – 800C (OPA-800C). In order to generate the UV pumps, the signal beam, which was generated from optical parametric generation, went through two barium borate crystals to undergo fourth harmonic generation within the OPA-800C cavity. The UV pumps generated for these experiments ranged from 310nm – 397nm. The average power of UV pumps ranged from 0.5mW – 0.6mW. The approximate pump energy of UV pumps was 0.5 $\mu$ J/pulse – 0.6 $\mu$ J/pulse. After the beamsplitter and OPA-800C, both probe/ amplified 790nm femtosecond pulse and UV pump beams were directed into an Ultrafast System Inc. Helios fs-TA spectrometer. Specifically, the UV pump was directed into an optical chopper and focused onto the BTp solution that was placed in a quartz cuvette with a 2mm path length. The probe beam was directed through a computer-controlled delay line and focused onto a rectangular calcium fluoride window with a 3mm thickness. The rectangular calcium fluoride window was placed on a rotating stage to prevent damage due high pulse energy probe consistently hitting the calcium fluoride window. The rectangular calcium fluoride window generated a UV white light continuum that ranged from 350nm – 750nm. The UV white light continuum/UV probe and sample signal were directed and focused onto an Ocean Optics spectrometer and charge-coupled device (CCD), which collected the difference in absorbance signal ( $\Delta A$ ) as a result of the UV pump being on versus off due to the optical chopper. See Figure C.5 in Appendix C for schematic of the fs-TA experimental optical set up described in this paper. The instrument response function of these fs-TA experiment was approximately 140fs.

The Helios software, by Ultrafast Systems Inc., was used for data acquisition and the data analysis was done using Surface Explorer and Origin Pro software. The fs-TA experimental set-up described in this paper was used in previous research.<sup>45,46</sup> The difference between described and previous fs-TA experimental set-up was a visible probe was used instead a UV probe.<sup>45,46</sup>

### III.5 Results Section

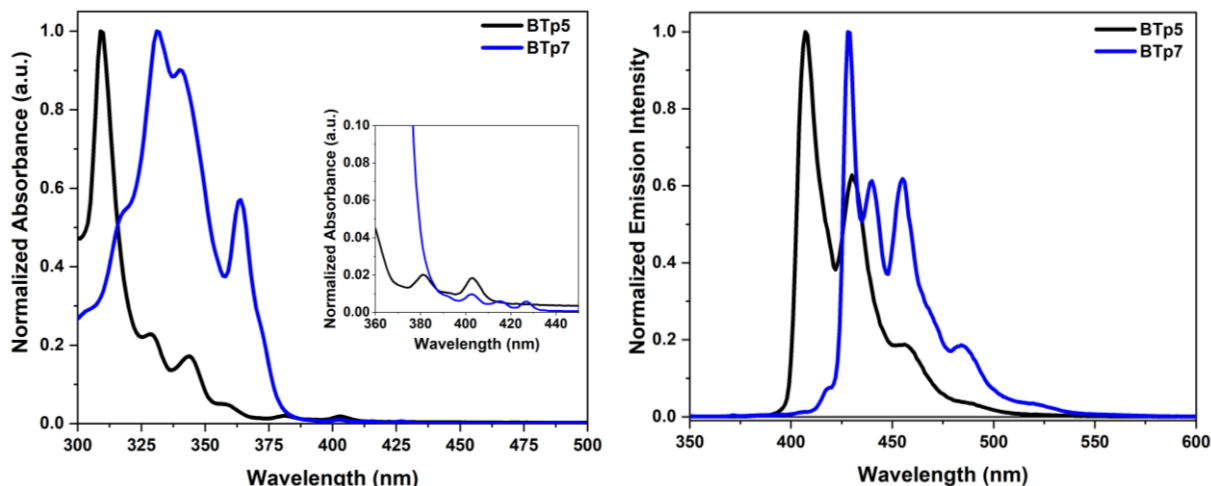


**Figure III.11:** Steady-state absorption and emission spectra of BTP-5 and BTP-7 solutions in chloroform

#### III.5.a Steady-state Absorption and Emission Results

The steady-state absorption and emission results of BTPs show these OLOs have strong vibronics due to the overlapping of vibrational and electronic states caused by  $\pi$ - $\pi^*$  transitions. **Figure III.2** shows the steady-state absorption and emission spectra of the BTP solutions in chloroform. Studies show that peaks present in the steady-state absorption spectra of organic oligomers are caused by  $\pi$ - $\pi^*$  transitions.<sup>47-49</sup> For both BTP-5 and BTP-7, the peaks present in the steady-state absorption spectra indicate there are overlapping vibrational and electronic states. This overlapping of vibrational and electronic states can be described as vibronic peaks or transitions.<sup>47</sup> Both BTP-5 and BTP-7 show there is a progression of vibronic peaks. Previous studies<sup>50,51</sup> have found a vibronic progression is an indication of electron or exciton delocalization

**Table III.1:** Shows the steady-state peaks and energy excitation wavelengths utilized in femtosecond transient absorption (fs-TA) experiments of BTp solutions

- a) steady-state absorption and emission peaks of BTps in chloroform solution  
b) energy excitation wavelengths utilized in the fs-TA experiments of BTps

Absorption peaks (nm <sup>a</sup> /eV <sup>b</sup> )				Emission peaks (nm <sup>a</sup> )	
Oligomer	Peak 1	Peak 2	Peak 3	Peak 1	Peak 2
<b>BTp-5</b>	310/4.0	344/3.6	380/3.2	407	430
<b>BTp-7</b>	332/3.7	362/3.4	400/3.1	429	440

occurring within the molecular structure of organic oligomers.<sup>50,51</sup> This vibronic progression observed in the steady-state absorption spectra of the BTps indicates the electron is delocalized along the structure of these OLOs. The trend observed in the steady-state absorption spectra of the BTps is as the conjugation length increases, the absorption peaks increased in wavelength. Another perspective of this trend is that, as the conjugation length of the BTps increases, the energy of the absorption peaks decreased. This trend has been observed in the steady-state absorption spectra of other OLOs.<sup>24,32,43,52</sup> The observed trend is attributed to the conjugation length of OLOs. As the conjugation length of OLOs increased, this increased the electron delocalization; thus, lowering the energy of absorption transition. The steady-state absorption results of the BTps are supported by the previous study conducted on the BTps.<sup>43</sup> The trend observed in steady-state absorption spectra of the BTps is also observed in the steady-state emission spectra (see **Figure III.2**). The observed trend present in both the steady-state absorption and emission spectra is as the conjugation length of the BTps increases, absorption or emission peaks increased in wavelength or decreased in energy. **Table III.1** shows the steady-state absorption and emission peaks of the BTps. This trend has also been observed in the steady-state absorption and emission spectra other OLOs that have fused rings within their oligomeric structure, such as acene

derivatives.<sup>51,53,54</sup> This observed trend suggests the BTPs have strong vibronic peaks due to fused ring conjugation and  $\pi$ - $\pi$  interaction of these OLOs.

### *III.5.b femtosecond Transient Absorption Results*

femtosecond transient absorption (fs-TA) experiments are conducted on the BTPs to investigate the time components of ultrafast dynamics occurring within these OLOs. The time components of ultrafast dynamics obtained from these experiments could provide insight into the charge transport mechanism of the BTPs. Specifically, the fs-TA experiments will determine if there are any ultrafast time components that correspond to the electron-phonon interaction and/or reorganization energy dynamics that could affect the charge transport mechanism of BTPs. To get obtain a full understanding the charge transport mechanism of BTPs, multiple energy excitation wavelengths are utilized for these experiments. In a study, dependenceDependance studies were conducted utilizing photoconductivity experiments as an approach to fully understanding the charge carrier dynamics of organic crystal films for optoelectronic applications.<sup>37</sup> **Table III.1** shows the energy excitation wavelengths utilized for the fs-TA experiments of the BTPs. The energy excitation wavelengths correspond to major vibronic peaks present in the steady-state absorption spectra of the BTPs. The main objective of this paper is to determine if there is a correlation between ultrafast dynamics obtained from fs-TA and charge carrier mobility of BTPs. Thus, it is key to collect as much information about the ultrafast dynamics of the BTPs in order to understand the charge transport mechanism and how ultrafast dynamics, such as electron-phonon interaction and reorganization energy, affect the charge carrier mobility of these OLOs.

#### *III.5.b.i High Energy Excitation Wavelength fs-TA Results*

The high energy excitation wavelength fs-TA results of the BTPs show there are different ultrafast dynamics occurring within these OLOs. **Figure III.3** shows the time resolved fs-TA

spectra of the BTPs obtained from the high energy excitation wavelength ranging from 0ps (pre-pump excitation) – roughly 2ps. The time resolved fs-TA spectra of the BTPs does not show any SE signals corresponding to the steady-state emission (see **Figure III.2** and **Table III.1** for steady-state emission). Since there are no SE signals present in the fs-TA spectra of the BTPs, this indicates the BTPs do not exhibit a significant amount of radiative decay such as fluorescence. The lack of

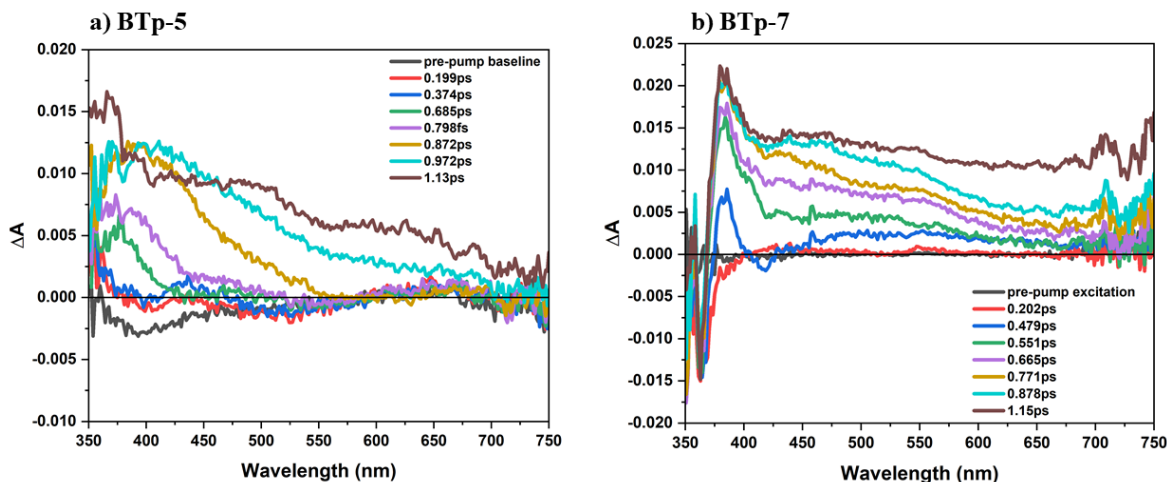


**Figure III.12:** femtosecond transient absorption (fs-TA) spectra, from 0ps – ~1.0ps, of BTPs obtained from high energy excitation wavelength: **a) BTP-5** and **b) BTP-7**

SE signal suggests the BTPs experience a non-radiative process, such as charge transport. When comparing the fs-TA spectra of the BTPs, the spectra show different signals between these OLOs. For BTP-5, the fs-TA spectra only show one main positive signal, while the fs-TA spectra of BTP-7 shows more than one signal. The time resolved fs-TA spectrum of BTP-5 shows one main positive signal that corresponds to an excited state absorption (ESA) signal. The observed ESA signal ranges from fs- from 350nm – 750nm. This broad ESA signal seems to be a characteristic of OLOs. In a study, where the charge transfer dynamics of perylenediimide-thienoacene OLOs were investigated utilizing transient absorption spectroscopy, the transient absorption spectra of these OLOs showed a broad ESA as well.<sup>40</sup> The broad ESA signal present in transient absorption spectra could provide insight to the electron delocalization occurring within the excited state of

the OLOs. There is no GSB signal that corresponds to the steady-state absorption of BTP-5 (see **Figure III.2** and **Table III.1** for steady-state absorption). The lack of GSB signal present does not indicate that BTP-5 only has an ESA signal because there is a chance that GSB signal could not be detected since the GSB range is beyond the UV probe (350nm – 750nm) range. As for the time resolved fs-TA spectrum of BTP-7, there are two signals present in the spectrum. One signal is described as an ESA signal since the signal is positive. Unlike BTP-5, the ESA signal of BTP-7 does not decrease in magnitude at longer probe wavelengths (beyond 650nm); the signal is positive during the entire range of the spectrum. Since the ESA signal of BTP-7 does not decrease in magnitude, it suggests the ESA signal of BTP-7 has wider range compared to the ESA signal of BTP-5. As mentioned above, this broad ESA signal could be a characteristic of OLOs since this broad ESA has been observed in other OLOs.<sup>40</sup> The broad ESA signal present in the fs-TA spectra could provide insight into the electron delocalization occurring within the BTPs. Since BTP-7 has the broader ESA signal, this suggest that BTP-7 has more electron delocalization compared to BTP-5. This observation supports the trend present in the steady-state results of these OLOs.

The second signal observed in the time resolved fs-TA spectrum of BTP-7 is negative and corresponds to a GSB signal. As shown in **Figure III.2** and **Table III.1**, the steady-state absorption of BTP7 ranges from 300nm – 450nm. The negative signal present in the fs-TA spectrum is within the steady-state absorption range of BTP7; thus, the present negative signal corresponds to a GSB signal. However, the GSB signal is not as dominant as the ESA signal which ranges from 370nm – beyond the UV probe range of 750nm (UV probe ranges 350nm – 700nm). At the high energy excitation wavelength, the fs-TA spectra of the BTPs shows there is a difference in the range of the ESA signal due to the structure of the BTPs. The trend observed is that as the conjugation length of the BTP increases, the range of the ESA signal increases. The

broadness of ESA signal observed in the fs-TA spectra of the BTps could suggest that BTP has more electron delocalization occurring in its excited compared to BTP-5 due to the increased conjugation of BTP-7.

**Figure III.4** shows the fs-TA kinetic traces of BTps and **Table III.2** shows the time components of the kinetic traces obtained from the high energy excitation wavelength. For both

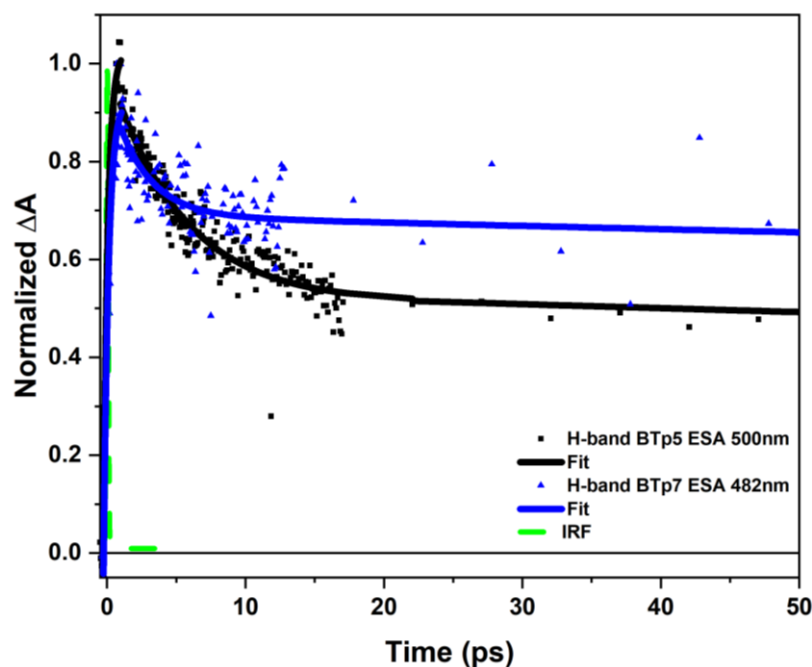


**Figure III.13:** femtosecond transient absorption (fs-TA) kinetic traces of BTps obtained from high energy excitation wavelength

BTps, kinetic traces are fitted a multi exponential decay. Both kinetic traces of BTps show an extremely long-lived component that can not be resolved within the time delayed of the fs-TA experiment. However, this extremely long-lived component is not the focus of these results; since it is clearly not an ultrafast component on the femtosecond timescale. Regardless, the kinetic traces of the BTps show there are two ultrafast time components,  $\tau_1$  and  $\tau_2$  (see **Figure III.4** and **Table III.2**). When comparing the  $\tau_1$  of BTP-5 to BTP-7, BTP-5 has a 2x slower time component compared to BTP-7. The trend observed is as the conjugation length increases, the  $\tau_1$  becomes

faster. As for the second time component,  $\tau_2$ , this component is similar between both BTps, especially when considering the error for the component. Unlike for  $\tau_1$ , there is no obvious trend between  $\tau_2$  and the conjugation length of BTps.

**Table III.2:** Time components obtained from femtosecond transient absorption (fs-TA) of BTps due to high energy excitation wavelength

Time components obtained from high energy excitation wavelength (ps)	
BTp-5	BTp-7
ESA 500nm	ESA 482nm
$\tau_1: 5.3 \pm 0.4$	$\tau_1: 2.4 \pm 0.8$
$\tau_2: 415 \pm 50$	$\tau_2: 459 \pm 100$

*III.5.b.ii Middle Energy Excitation Wavelength fs-TA Results*

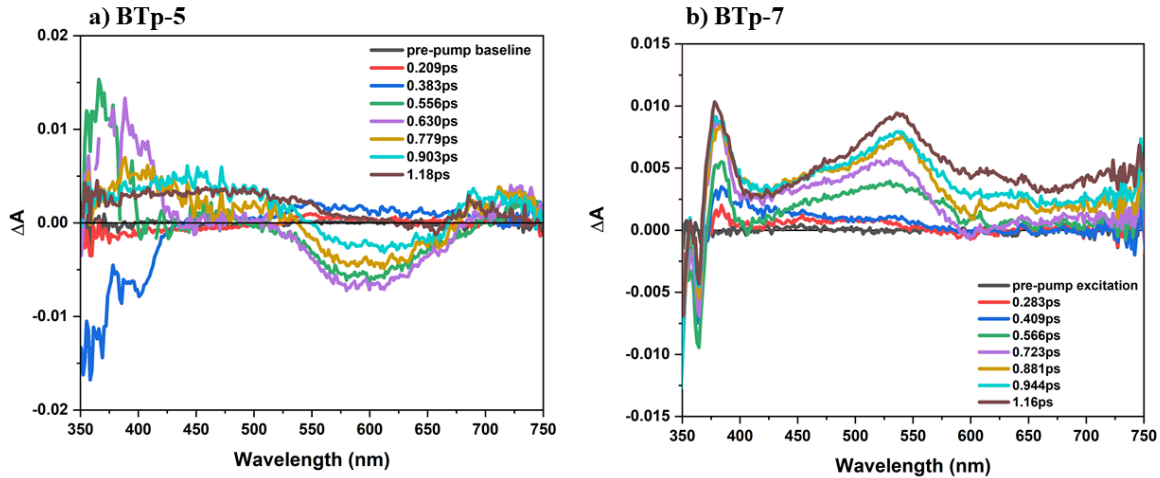


**Figure III.14:** femtosecond transient absorption (fs-TA) spectra, from 0ps – 2ps, of BTps obtained from middle energy excitation wavelength: **a)** BTp-5 and **b)** BTp-7

The time resolved fs-TA spectra obtained from middle energy excitation wavelength show different dynamics compared to the fs-TA spectra obtained from high energy excitation wavelength. **Figure III.5** shows the time resolved fs-TA spectra of the BTps obtained from the middle energy excitation wavelength ranging from 0ps (pre-pump excitation) – roughly 2ps. As with the high energy excitation wavelength, there are no SE signals corresponding to the steady-



state emission of the BTPs (see **Figure III.2** and **Table III.1** for steady-state emission). Unlike the high energy excitation wavelength, the time resolved fs-TA spectra of BTP5 obtained from the middle energy excitation wavelength show two signals present in the spectrum of these OLO. From 0ps (pre-pump excitation) to 2ps, there is one signal that shows a combination negative and positive signals within the steady-state absorption range of BTP-5 (see **Figure III.5.a**). After 2ps, there is second signal is observed and that signal an ESA signal. The ESA signal has a range from 350nm – 600nm. The range of ESA signal obtained from the middle energy excitation wavelength has a shorter range compared to the ESA signal obtained from the high energy excitation wavelength. For BTP-5, the different energy excitation wavelengths are showing different signals in the time resolved fs-TA spectra of this OLO. The observed differences could suggest the charge transport mechanism is different between the two energy excitation wavelengths for BTP-5. As for BTP7, there is no difference in signals between the middle and high energy excitation wavelengths. For both the middle and high energy excitation wavelengths, the time resolved fs-TA spectrum show GSB and ESA signals. Unlike BTP-5, from 0ps (pre-pump excitation) – 2ps, the observed signal does not have a mixture of negative and positive signals. For BTP-7, from 0ps – 2ps, the GSB signal shows the typical decrease in magnitude over time. When comparing the ESA signals of BTPs obtained from middle energy excitation wavelength, the trend observed in the high energy excitation wavelength is present in this energy excitation wavelength as well. The observed trend is as the conjugation length of the BTP increases, the range of the ESA signal increases as well.

**Figure III.6** shows the kinetic traces and **Table III.3** shows the time components of the kinetic traces obtained for middle energy excitation wavelength from the fs-TA experiments of the

BTps. As with the high energy excitation wavelength, the kinetic traces obtained from the middle energy excitation wavelength are fitted to a multi-exponential decay. As with the high energy

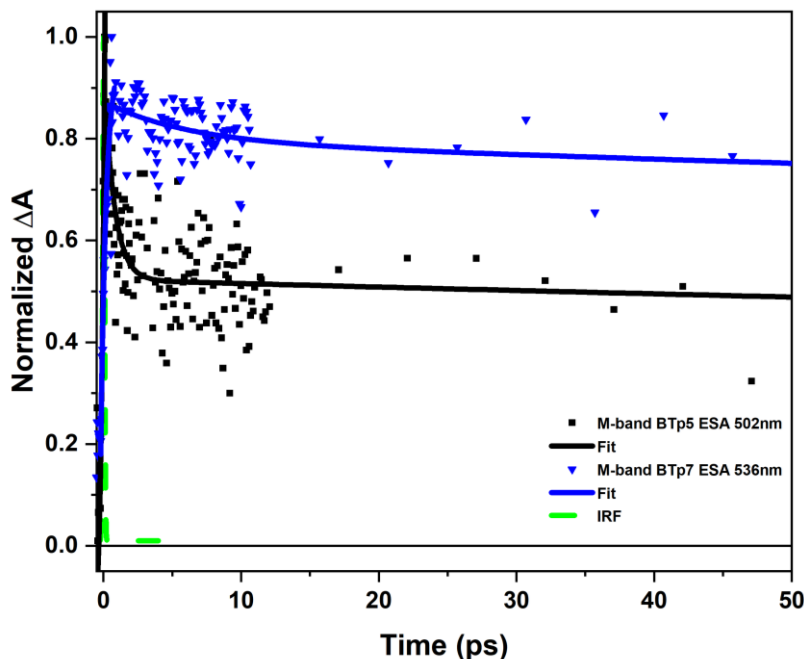


**Figure III.15:** femtosecond transient absorption (fs-TA) kinetic traces of BTps obtained from middle energy excitation wavelength

excitation wavelength, the middle energy excitation wavelength shows there is an extremely long-lived component that is not the focus of this paper; since it does not show an ultrafast femtosecond time component. As shown in **Figure III.6** and **Table III.3**, there are two ultrafast dynamics present in the kinetic traces obtained from the middle energy excitation. When comparing the first

**Table III.3:** Time components obtained from femtosecond transient absorption (fs-TA) of BTps due to middle energy excitation wavelength

Time components obtained from middle energy excitation wavelength (ps)	
BTp-5	BTp-7
ESA 502nm	ESA 536nm
$\tau_1: 0.761 \pm 0.1$	$\tau_1: 5.9 \pm 4.1$
$\tau_2: 318 \pm 81$	$\tau_2: 336 \pm 60$

time component,  $\tau_1$ , of the BTPs, the  $\tau_1$  of BTP5 is 9x faster compared to BTP7. As for the second time component,  $\tau_2$ , this component is similar between the BTPs especially when considering the error on this component. For the middle energy excitation wavelength, the observed trend between  $\tau_1$  and the BTPs is that as the conjugation length increases, the  $\tau_1$  becomes slower. As for  $\tau_2$ , there is no obvious trend between the conjugation length of the BTPs and this time component.

### III.5.b.iii Low Energy Excitation Wavelength fs-TA Results

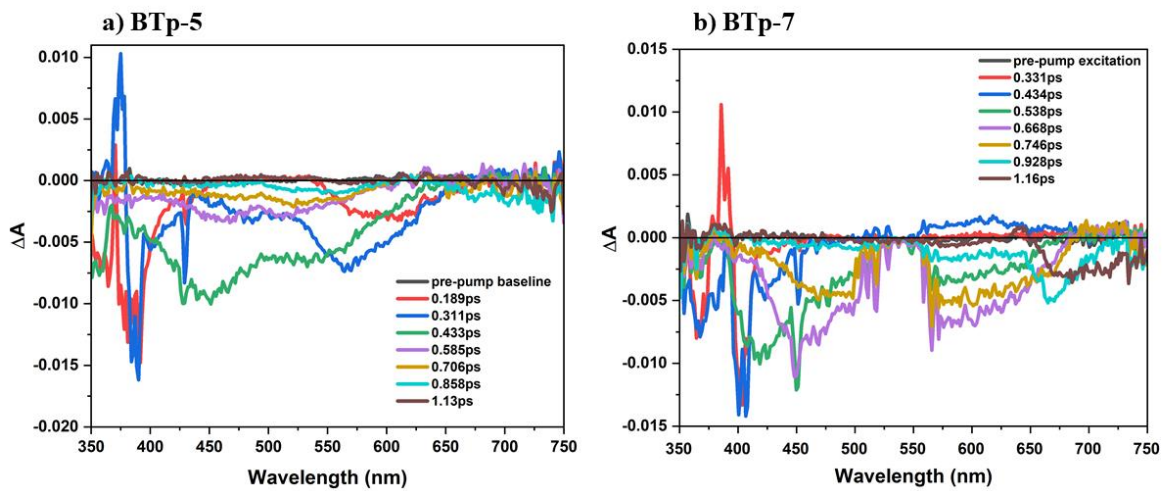


**Figure III.16:** femtosecond transient absorption (fs-TA) spectra, from 0ps – 2ps, of BTPs obtained from middle energy excitation wavelength: **a)** BTP-5 and **b)** BTP-7

The time resolved fs-TA spectra of the BTPs obtained from low energy excitation wavelength show different signals compared to the other two energy excitation wavelengths.

**Figure III.7** shows the time resolved fs-TA spectra of the BTPs obtained from the low energy excitation wavelength from 0ps (pre-pump excitation) – 2ps. Unlike the previous energy excitation wavelengths, there are no ESA signals that are dominant in spectra for both BTPs. For both BTPs, the main signals present are observed from 0ps (pre-pump excitation) – 2ps. The main signals show a combination of negative and positive signals. The main signals cannot be simply assigned to an only GSB or SE signals since there is a combination of negative and positive signals within the main signals. Based on the time resolved fs-TA spectra obtained from the low energy

excitation wavelength, it suggests that the charge transport mechanism is different at this energy excitation compared to the previous energy excitation wavelengths.

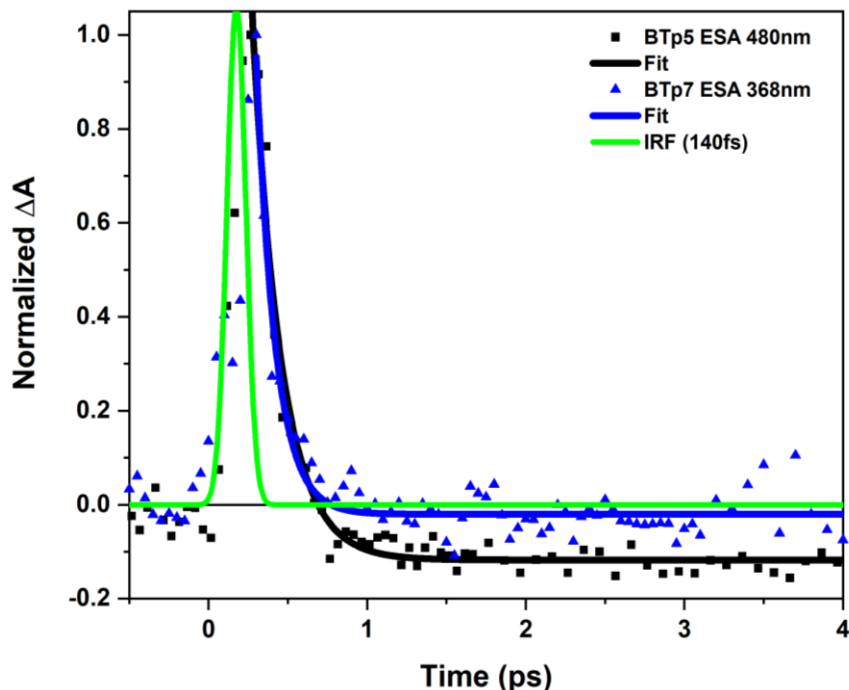


**Figure III.17:** femtosecond transient absorption (fs-TA) kinetic traces of BTPs obtained from low energy excitation wavelength

**Figure III.8** shows the kinetic traces of BTPs obtained from the low energy excitation wavelength fs-TA experiments. For the low energy excitation wavelength, the kinetic traces show one ultrafast time component. Unlike the previous energy excitation wavelengths, the kinetic traces are fitted to a one exponential decay and have only one time component,  $\tau_1$ . **Table III.4** shows the time components of  $\tau_1$  for this energy excitation wavelength. As **Figure III.8** shows, the  $\tau_1$  of BTP-7 cannot be fully resolved since it is within the error of the IRF of 140fs. As for BTP-5, the time component of  $\tau_1$  is 0.181ps (181 fs). Unlike the previous energy excitation wavelengths, there is no obvious trend between conjugation length of the BTPs and  $\tau_1$ . The fs-TA

results obtained from this low energy excitation wavelength show the charge transport mechanism is different at this wavelength compared to the previous energy excitation wavelengths for the BTps.

**Table III.4:** Time components obtained from femtosecond transient absorption (fs-TA) of BTps due to low energy excitation wavelength

Time components obtained from low energy excitation wavelength (ps)	
BTp-5	BTp-7
ESA 480nm	ESA 368nm
$\tau_1: 0.181 \pm 0.009$	$\tau_1: 0.122 \pm 0.01$

### III.6 Discussion

The results described above show there are ultrafast dynamics that affect the charge transport mechanism of the BTps. As mentioned earlier, the two dynamics of the charge transport mechanism that are investigated in this work are electron-phonon interaction and reorganization energy. Electron-phonon interaction (coupling) describes the interconnection between an electron and a quantized particle-like vibrational mode that is caused by oscillating atoms within the lattice of the organic semiconducting system.<sup>16,55,56</sup> As mentioned earlier, reorganization energy describes the energy lost in a system due to electron-phonon interaction and this energy has two parts: external and internal.<sup>1,6,13</sup> The fs-TA results of the BTps show the time components of ultrafast dynamics, electron-phonon interaction and reorganization energy, occurring on the femtosecond to hundreds of picosecond timescale within these oligomers. The charge transport rates of the BTps will determine which OLO will have the higher charge carrier mobility. From there, a correlation may be discovered between conjugation length and the charge carrier mobility of these OLOs. The objective of this work is to show that fs-TA spectroscopy can be used as an

approach for predicting the charge carrier mobility of OLOs. As discussed earlier, the structure of the BTps shows that these OLOs have the ability of transporting charges and this observation is supported by the steady-state absorption and emission results of the oligomers. The steady-state absorption and emission results of the BTps show these oligomers are capable of transporting charges due to strong vibronic coupling as a result of the conjugation and  $\pi$ - $\pi$  interaction in the structures of these molecules. Based on the structures, the BTps can be viewed as building blocks of graphene.<sup>43</sup> It is known that the structure of graphene consist of carbon rings fused together by double bonds creating a network of  $sp^2$  hybridization.<sup>43,57</sup> The structure of graphene can be viewed as consisting of building blocks of acenes and tetrphenes.<sup>43</sup> The BTps can also be classified as the building blocks of graphene since there are benzo and tetraphene portions within the structure of graphene.<sup>43</sup> Since the BTps consist of building blocks of graphene, this indicates the BTps could have similar photophysical or charge carrier dynamics of graphene. The fs-TA results of the BTps show two ultrafast time components that range from femtoseconds to hundreds of picoseconds, which could correspond to the electron-phonon interaction or reorganization energy dynamics of the charge transport mechanism for these OLOs. The timescale of the first time component,  $\tau_1$ , ranges from approximately 0.7ps – 6.0ps (see **Tables III.2 – III.3**). The timescale of the second time component,  $\tau_2$ , ranges from approximately 300ps – 500ps (see **Tables III.2 – III.3**). To clarify, only the high and middle energy excitation wavelengths show two ultrafast time components. The low energy excitation wavelength only shows one ultrafast time component, which will be discussed later. Studies have investigated the charge carrier dynamics of graphene and determined the timescale for electron-phonon interaction occurring within this material.<sup>58–62</sup> Based on these studies, when a time component has a timescale of less than tens of picoseconds, the time component corresponds to a vibrational relaxation or decay caused by electron-phonon

interaction.<sup>63,64</sup> For the BTPs, since the timescale of  $\tau_1$  ranges from less than tens of picoseconds, this first time component corresponds to the vibrational decay of electron-phonon interaction. Studies that investigated the charge carrier dynamics of graphene and other organic materials have shown that after the vibrational relaxation of electron-phonons, the excited state of the molecule will renormalize before the electron-phonon interaction changes to other interaction, such as electron-electron interaction.<sup>59,60,63–66</sup> This renormalization of the excited state occurs on the timescale of hundreds of picoseconds.<sup>59,60,63–66</sup> For the BTPs, based on the timescale of the  $\tau_2$ , this time component corresponds to the renormalization process of the excited state. Since  $\tau_2$  corresponds to the renormalization of the excited state, this definition relates to the internal part of reorganization energy that was described earlier.<sup>1,6,13</sup> The  $\tau_2$  time component is providing the amount of time it takes for energy to be lost due to electron-phonon interactions occurring within these OLOs. From the fs-TA experiments, the timescales of electron-phonon vibrational decay and reorganization relaxation dynamics are determined for the charge transport mechanism of these BTPs.

For both the high and middle energy excitation wavelengths, the rates of electron-phonon vibrational decay ( $\tau_1$ ) and reorganization relaxation ( $\tau_2$ ) are obtained from the fsTA data. Starting with the high energy excitation wavelength, the electron-phonon vibrational decay rate of BTP-5 is  $3.2 \times 10^{11} \text{s}^{-1}$  and of BTP-7 is  $5.1 \times 10^{11} \text{s}^{-1}$  (see **Tables III.2** and **III.3**). The electron-phonon vibrational decay rate of BTP-7 is 1.6x faster than that of BTP-5. The reorganization relaxation rate of BTP-5 is  $2.0 \times 10^9 \text{s}^{-1}$  and of BTP-7 is  $1.2 \times 10^9 \text{s}^{-1}$ . The reorganization relaxation rate of BTP-5 is also 1.6x faster compared to the rate of BTP-7. To provide a quantitative perspective of which BTP will have the faster rate or more efficient charge transport properties, the combined rate of

both electron-phonon vibrational decay and reorganization relaxation rates will be calculated. To calculate the combined rate, the following equation is used:

**Equation III.1** 
$$\frac{1}{\langle\tau_1\rangle} + \frac{1}{\langle\tau_2\rangle} = k_1 + k_2 = k_{comb}$$

where  $k_{comb}$  is the calculated rate obtained from combining both electron-phonon vibrational decay and reorganization relaxation rates, unit:  $s^{-1}$ ;  $\langle\tau_1\rangle$  is the average of the first time component that corresponds to the electron-phonon vibrational decay and  $k_1$  is the rate of electron-phonon vibrational decay;  $\langle\tau_2\rangle$  is the average of the second time component that corresponds to the reorganization relaxation and  $k_2$  is the rate of reorganization relaxation. The electron-phonon vibrational decay and reorganization relaxation rates of the BTPs are due to a non-radiative mechanism since these rates are obtained from the ESA results which are not near the SE or any other radiative excited state. A form of **Equation III.1** was used in a study to calculate the electron transfer rate between cadmium selenide quantum dots and titanium dioxide from transient absorption experiments.<sup>67</sup> In that study, the time components corresponded to the average lifetime of the radiative decay of the quantum dots. In this work, **Equation III.1** is used to calculate the non-radiative decay rate of the BTPs by combining rate of electron-phonon vibrational decay and reorganization relaxation rates obtained from fs-TA experiments conducted on these OLOs. The  $k_{comb}$  of BTP-5 is  $4.2 \times 10^{11} s^{-1}$  and of BTP-7 is  $2.6 \times 10^{11} s^{-1}$ . Based on the high energy excitation wavelength, the  $k_{comb}$  of BTP-5 is 1.6x faster than the  $k_{comb}$  of BTP-7. The faster rate of BTP-5 suggests that this OLO has a higher probability of electron-phonon interaction occurring within this OLO compared to BTP-7. Since BTP-5 has a higher probability of electron-phonon interaction, it is suggested that this OLO has the stronger electron-phonon interaction between these OLOs. The middle energy excitation wavelength fs-TA results show different rates of the ultrafast dynamics compared to the high energy excitation wavelength results for the BTPs. For



the middle energy excitation wavelength, the electron-phonon vibrational decay rate of BTP-5 is  $4.2 \times 10^{12} \text{s}^{-1}$  and of BTP-7 is  $5.0 \times 10^{11} \text{s}^{-1}$ . The electron-phonon vibrational decay rate of BTP-5 is **8.4x** faster compared to BTP-7. The reorganization relaxation rate of BTP-5 is  $1.3 \times 10^{11} \text{s}^{-1}$  and of BTP-7 is  $1.2 \times 10^{10} \text{s}^{-1}$ . The reorganization relaxation rate of BTP-5 is 1.1x faster compared to BTP-7. Using **Equation III.1**, the  $k_{comb}$  of the BTPs based on middle energy excitation wavelength are determined. The  $k_{comb}$  of BTP-5 is  $4.3 \times 10^{12} \text{s}^{-1}$  and rate of BTP-7 is  $5.1 \times 10^{11} \text{s}^{-1}$ . Based on the middle energy excitation wavelength, the  $k_{comb}$  of BTP5 is **8.5x** faster compared to BTP-7. As with the high energy excitation wavelength, the  $k_{comb}$  of BTP5 suggest that this OLO has a stronger electron-phonon interaction compared to BTP-7.

Studies have investigated the effect of electron-phonon interaction (coupling) of graphene and other organic semiconducting materials to investigate how this coupling affects the charge carrier dynamics of these organic materials.<sup>8,16,55,60,66,68-73</sup> Studies have also investigated the correlation between electron-phonon coupling and conjugation length of organic molecules.<sup>69,72,74</sup> From those studies, the correlation between electron-phonon coupling and conjugation length of organic molecules is that as the conjugation length increases, the electron-phonon interaction decreases.<sup>69,72,74</sup> In one study, an equation was derived to provide a mathematical model of the correlation between electron-phonon coupling,  $V$ , and the conjugation length (the number of  $\pi$  states) within an organic molecular structure.<sup>72</sup> The expression was given as,

**Equation III.2** 
$$\frac{2v^2}{Kn} \left( 1 + \cos^2 \frac{2\pi p}{na} \right) = V$$

where  $p$  was an integer indexing the electronic state;  $v$  was the derivative of distance to nearest-neighbor interaction;  $K$  was the strength of the radial force constant model; and  $n=N_\pi$ , the number of  $\pi$  states.  $\pi$  states refer to the overlap of electrons in  $p$ -orbitals that creates a double bond or conjugation. From this expression, it shows that the correlation between electron-phonon

coupling and conjugation length of an organic material is inversely proportional; as the conjugation length increases, the electron-phonon interaction decreases. In this study and other studies, the explanation for this correlation is as the number of  $\pi$  states (conjugation length) increases within the molecular structure of an organic material, the delocalization of electrons increased; as a result, this decreases the vibrational interaction between electrons within the lattice of a molecule thus, decrease the electron-phonon coupling.<sup>69,72,74</sup> From the fs-TA results of the BTps, the strength of electron-phonon interaction is determined by the  $k_{comb}$ . Since BTP-5 has the higher  $k_{comb}$  compared to BTP-7, this OLO has the stronger electron-phonon interaction.

There have been reports of probing other conjugated systems in terms of their electron-phonon interaction and charge carrier mobility in optoelectronic devices. Studies have used other measurements and experiments to investigate the conjugation length and charge carrier mobility of organic semiconducting materials.<sup>75-77</sup> In a previous study<sup>76</sup>, it was determined that for unsubstituted and alpha-thiophene oligomers, as the conjugation length of the oligomers increased, the charge carrier mobility increased.<sup>76</sup> The provided explanation for this trend was that this type of substituted thiophene oligomers created an efficient intermolecular charge transfer as a result of long-range structural ordering in the thin film. To determine the ordering of thiophene oligomers in thin films, Garnier et al used X-ray structural characterization. Similar X-ray analysis has been carried out on the BTps.<sup>43</sup> From the X-ray analysis of the BTps, it was found that BTP-7 had a higher intermolecular interaction compared to BTP-5.<sup>43</sup> Based on this interaction, it suggested that BTP-7 would have a higher charge mobility as well.<sup>43</sup> This correlation was also found in a series of symmetrical oligomers in a study by Murphy et. al.<sup>75</sup> It was found that increases in charge mobility correlated to increasing conjugation length with measured mobility ranging from  $0.02\text{cm}^2\text{V}^{-1}\text{s}^{-1}$  to  $0.06\text{cm}^2\text{V}^{-1}\text{s}^{-1}$ . In the case of the BTP-5 it was determined that

BTp-5 charge carrier mobility was  $2.5 \text{ cm}^2\text{V}^{-1}\text{s}^{-1}$ . This is approximately 100 times larger than in the case of the symmetrical oligomers in the Murphy study, and it is predicted that BTp-7 will have a larger carrier mobility based on the weaker electron-phonon interaction observed from fsTA results. Based on the fsTA results, BTp=7 has a slower  $k_{comb}$  in comparison to BTp-5 which indicates that this OLO will have a higher charge carrier mobility.

As for the low energy excitation wavelength, the fs-TA experiments of the BTps show there is an ultrafast dynamic with an extremely fast time component (see **Figure III.8** and **Table III.4**). For both BTp-5 and BTp-7, the timescale of this ultrafast dynamic is less than 2ps (see **Table III.4**). This extremely fast time component does not correlate to the timescales of electron-phonon vibrational decay or reorganization energy that were discussed earlier. Since this extremely fast time component does not correspond to the ultrafast dynamics of the charge transport mechanism, it suggests this ultrafast dynamic is different and is not associated with the charge transport mechanism of the BTps. This other ultrafast dynamic has been seen in previous investigations of graphene and its charge carrier dynamics.<sup>58,60,61,78</sup> This fs-TA result suggests that not all absorbed or transferred charges will be participate in the charge transport mechanism and be measure for charge carrier mobility of an OLO for transistor applications. Depending on which level within an excited state an electron or charge carrier get excited to, the electron will either experience the dynamics of the charge transport mechanism or experience another ultrafast dynamic that is not associated with the charge transport mechanism. The low energy excitation wavelength result provides a full understanding of ultrafast dynamics that can occur within the BTps and which dynamics will associate with the charge transport mechanism of these OLOs.

From the high and middle energy excitation wavelengths, the  $k_{comb}$ s of the BTps show there is a correlation between conjugation length and the charge transport mechanism. Recall, for the

high energy excitation wavelength, the  $k_{comb}$  of BTP-5 is  $1.6 \times 10^{11} \text{s}^{-1}$  and of BTP-7 is  $2.6 \times 10^9 \text{s}^{-1}$ . As for middle energy excitation wavelength, the  $k_{comb}$  of BTP-5 is  $2.2 \times 10^{12} \text{s}^{-1}$  and of BTP-7 is  $5.1 \times 10^{11} \text{s}^{-1}$ . From the  $k_{comb}$ s, the trend that is present is as the conjugation length increases, the  $k_{comb}$  decreases; this trend is present in both energy excitation wavelengths. As mentioned previously, the  $k_{comb}$  provides a quantitative value to the electron-phonon interaction and reorganization energy dynamics of the charge transport mechanism for the BTPs. When a BTP has a fast  $k_{comb}$ , this indicates the OLO will have a strong electron-phonon interaction and low charge carrier mobility. From the fs-TA results, BTP-7 will most likely have the higher charge carrier mobility compared to BTP-5 since it has the weaker electron-phonon interaction. The reported charge carrier mobility of BTP-5 is  $2.5 \text{cm}^2 \text{V}^{-1} \text{s}^{-1}$ .<sup>43,79</sup> Based on the fs-TA results, the charge carrier mobility of BTP-7 will be greater than  $2.5 \text{cm}^2 \text{V}^{-1} \text{s}^{-1}$  since it has the slower  $k_{comb}$  and weak electron-phonon interaction.

### III.7 Conclusion

In conclusion, the results discussed in this paper show ultrafast dynamics obtained from fs-TA spectroscopy can predict the charge carrier mobility of OLOs. From the fs-TA results, the charge transport rates,  $k_{comb}$ , of the BTPs are determined. For the high energy excitation wavelength, the  $k_{comb}$  of BTP-5 is 1.6x faster than the  $k_{comb}$  of BTP-7. For the middle energy excitation wavelength, the  $k_{comb}$  of BTP-5 is 8.5x faster compared to BTP-7. Since BTP-7 has a slower  $k_{comb}$ , this OLO has a weaker electron-phonon interaction compared to BTP-5 due to its extended conjugation length. Due to the weaker electron-phonon interaction, BTP-7 will have a higher charge carrier mobility compared to BTP-5. The results discussed in this work provide insight into which molecular structure of an OLO will lead to high charge carrier mobility for optoelectronic

applications. From this paper, fs-TA spectroscopy can be used as approach for predicted the charge carrier mobility of OLO for optoelectronic applications.

### III.8 References

- (1) Wang, C.; Dong, H.; Jiang, L.; Hu, W. Organic Semiconductor Crystals. *Chem. Soc. Rev.* **2018**, *47* (2), 422–500. <https://doi.org/10.1039/C7CS00490G>.
- (2) Paterson, A. F.; Singh, S.; Fallon, K. J.; Hodsdon, T.; Han, Y.; Schroeder, B. C.; Bronstein, H.; Heeney, M.; McCulloch, I.; Anthopoulos, T. D. Recent Progress in High-Mobility Organic Transistors: A Reality Check. *Adv. Mater.* **2018**, *30* (36), 1801079. <https://doi.org/10.1002/adma.201801079>.
- (3) Sirringhaus, H. 25th Anniversary Article: Organic Field-Effect Transistors: The Path Beyond Amorphous Silicon. *Adv. Mater.* **2014**, *26* (9), 1319–1335. <https://doi.org/10.1002/adma.201304346>.
- (4) Jiang, H.; Hu, W. The Emergence of Organic Single-Crystal Electronics. *Angew. Chem. Int. Ed.* **2020**, *59* (4), 1408–1428. <https://doi.org/10.1002/anie.201814439>.
- (5) Fratini, S.; Nikolka, M.; Salleo, A.; Schweicher, G.; Sirringhaus, H. Charge Transport in High-Mobility Conjugated Polymers and Molecular Semiconductors. *Nat. Mater.* **2020**, *19* (5), 491–502. <https://doi.org/10.1038/s41563-020-0647-2>.
- (6) Dong, H.; Fu, X.; Liu, J.; Wang, Z.; Hu, W. 25th Anniversary Article: Key Points for High-Mobility Organic Field-Effect Transistors. *Adv. Mater.* **2013**, *25* (43), 6158–6183. <https://doi.org/10.1002/adma.201302514>.
- (7) Liu, K.; Ouyang, B.; Guo, X.; Guo, Y.; Liu, Y. Advances in Flexible Organic Field-Effect Transistors and Their Applications for Flexible Electronics. *Npj Flex. Electron.* **2022**, *6* (1), 1. <https://doi.org/10.1038/s41528-022-00133-3>.
- (8) Coropceanu, V.; Cornil, J.; Da Silva Filho, D. A.; Olivier, Y.; Silbey, R.; Brédas, J.-L. Charge Transport in Organic Semiconductors. *Chem. Rev.* **2007**, *107* (4), 926–952. <https://doi.org/10.1021/cr050140x>.
- (9) Reese, C.; Bao, Z. Organic Single-Crystal Field-Effect Transistors. *Mater. Today* **2007**, *10* (3), 20–27. [https://doi.org/10.1016/S1369-7021\(07\)70016-0](https://doi.org/10.1016/S1369-7021(07)70016-0).
- (10) Mei, J.; Diao, Y.; Appleton, A. L.; Fang, L.; Bao, Z. Integrated Materials Design of Organic Semiconductors for Field-Effect Transistors. *J. Am. Chem. Soc.* **2013**, *135* (18), 6724–6746. <https://doi.org/10.1021/ja400881n>.
- (11) Jurchescu, O. D.; Popinciuc, M.; van Wees, B. J.; Palstra, T. T. M. Interface-Controlled, High-Mobility Organic Transistors. *Adv. Mater.* **2007**, *19* (5), 688–692. <https://doi.org/10.1002/adma.200600929>.
- (12) Zhang, X.; Dong, H.; Hu, W. Organic Semiconductor Single Crystals for Electronics and Photonics. *Adv. Mater.* **2018**, *30* (44), 1801048. <https://doi.org/10.1002/adma.201801048>.
- (13) Bromley, S. T.; Mas-Torrent, M.; Hadley, P.; Rovira, C. Importance of Intermolecular Interactions in Assessing Hopping Mobilities in Organic Field Effect Transistors: Pentacene versus Dithiophene-Tetrathiafulvalene. *J. Am. Chem. Soc.* **2004**, *126* (21), 6544–6545. <https://doi.org/10.1021/ja049762a>.
- (14) Huang, Y.; Wang, Z.; Chen, Z.; Zhang, Q. Organic Cocrystals: Beyond Electrical Conductivities and Field-Effect Transistors (FETs). *Angew. Chem. Int. Ed.* **2019**, *58* (29), 9696–9711. <https://doi.org/10.1002/anie.201900501>.
- (15) Wang, L.; Nan, G.; Yang, X.; Peng, Q.; Li, Q.; Shuai, Z. Computational Methods for Design of Organic Materials with High Charge Mobility. *Chem Soc Rev* **2010**, *39* (2), 423–434. <https://doi.org/10.1039/B816406C>.

- (16) Coropceanu, V.; Li, Y.; Yi, Y.; Zhu, L.; Brédas, J.-L. Intrinsic Charge Transport in Single Crystals of Organic Molecular Semiconductors: A Theoretical Perspective. *MRS Bull.* **2013**, *38* (1), 57–64. <https://doi.org/10.1557/mrs.2012.313>.
- (17) Shuai, Z.; Li, W.; Ren, J.; Jiang, Y.; Geng, H. Applying Marcus Theory to Describe the Carrier Transports in Organic Semiconductors: Limitations and Beyond. *J. Chem. Phys.* **2020**, *153* (8), 080902. <https://doi.org/10.1063/5.0018312>.
- (18) Zhu, G.; Zheng, S. Exploring the Hole Mobility of Oligothiophene Based Donors with Different Spatial Symmetry and Conjugation Length of Backbone: A Theoretical Insight. *Int. J. Quantum Chem.* **2022**, *122* (1), e26820. <https://doi.org/10.1002/qua.26820>.
- (19) Sahoo, S. R.; Sahu, S.; Sharma, S. Charge Transport, Optical and Nonlinear Optical Properties of  $\text{CF}_3$ -Substituted Acene Compounds: A DFT Study. *Theor. Chem. Acc.* **2017**, *136* (9), 99. <https://doi.org/10.1007/s00214-017-2131-x>.
- (20) Fan, J.; Lin, L.; Wang, C.-K. Molecular Stacking Effect on Photoluminescence Quantum Yield and Charge Mobility of Organic Semiconductors. *Phys. Chem. Chem. Phys.* **2017**, *19* (44), 30147–30156. <https://doi.org/10.1039/C7CP05451C>.
- (21) Nan, G.; Shi, Q.; Shuai, Z.; Li, Z. Influences of Molecular Packing on the Charge Mobility of Organic Semiconductors: From Quantum Charge Transfer Rate Theory beyond the First-Order Perturbation. *Phys. Chem. Chem. Phys.* **2011**, *13* (20), 9736. <https://doi.org/10.1039/c1cp00001b>.
- (22) Lederer, J.; Kaiser, W.; Mattoni, A.; Gagliardi, A. Machine Learning–Based Charge Transport Computation for Pentacene. *Adv. Theory Simul.* **2019**, *2* (2), 1800136. <https://doi.org/10.1002/adts.201800136>.
- (23) Nan, G.; Wang, L.; Yang, X.; Shuai, Z.; Zhao, Y. Charge Transfer Rates in Organic Semiconductors beyond First-Order Perturbation: From Weak to Strong Coupling Regimes. *J. Chem. Phys.* **2009**, *130* (2), 024704. <https://doi.org/10.1063/1.3055519>.
- (24) Cai, Z.; Vázquez, R. J.; Zhao, D.; Li, L.; Lo, W.; Zhang, N.; Wu, Q.; Keller, B.; Eshun, A.; Abeyasinghe, N.; Banaszak-Holl, H.; Goodson, T.; Yu, L. Two Photon Absorption Study of Low-Bandgap, Fully Conjugated Perylene Diimide-Thienoacene-Perylene Diimide Ladder-Type Molecules. *Chem. Mater.* **2017**, *29* (16), 6726–6732. <https://doi.org/10.1021/acs.chemmater.7b01512>.
- (25) Cai, Z.; Awais, M. A.; Zhang, N.; Yu, L. Exploration of Syntheses and Functions of Higher Ladder-Type  $\pi$ -Conjugated Heteroacenes. *Chem* **2018**, *4* (11), 2538–2570. <https://doi.org/10.1016/j.chempr.2018.08.017>.
- (26) Chen, D.; Zhu, D.; Lin, G.; Du, M.; Shi, D.; Peng, Q.; Jiang, L.; Liu, Z.; Zhang, G.; Zhang, D. New Fused Conjugated Molecules with Fused Thiophene and Pyran Units for Organic Electronic Materials. *RSC Adv.* **2020**, *10* (21), 12378–12383. <https://doi.org/10.1039/D0RA01984D>.
- (27) Durban, M. M.; Kazarinoff, P. D.; Segawa, Y.; Luscombe, C. K. Synthesis and Characterization of Solution-Processable Ladderized n-Type Naphthalene Bisimide Copolymers for OFET Applications. *Macromolecules* **2011**, *44* (12), 4721–4728. <https://doi.org/10.1021/ma2004822>.
- (28) Chen, J.; Yang, K.; Zhou, X.; Guo, X. Ladder-Type Heteroarene-Based Organic Semiconductors. *Chem. – Asian J.* **2018**, *13* (18), 2587–2600. <https://doi.org/10.1002/asia.201800860>.
- (29) Moscatelli, A.; Livingston, K.; So, W. Y.; Lee, S. J.; Scherf, U.; Wildeman, J.; Peteanu, L. A. Electric-Field-Induced Fluorescence Quenching in Polyfluorene, Ladder-Type Polymers, and

- MEH-PPV: Evidence for Field Effects on Internal Conversion Rates in the Low Concentration Limit. *J. Phys. Chem. B* **2010**, *114* (45), 14430–14439. <https://doi.org/10.1021/jp101307p>.
- (30) Wu, J.-S.; Cheng, S.-W.; Cheng, Y.-J.; Hsu, C.-S. Donor–Acceptor Conjugated Polymers Based on Multifused Ladder-Type Arenes for Organic Solar Cells. *Chem. Soc. Rev.* **2015**, *44* (5), 1113–1154. <https://doi.org/10.1039/C4CS00250D>.
- (31) Yuan, Z.; Xiao, Y.; Yang, Y.; Xiong, T. Soluble Ladder Conjugated Polymer Composed of Perylenediimides and Thieno[3,2- *b*]Thiophene (LCPT): A Highly Efficient Synthesis via Photocyclization with the Sunlight. *Macromolecules* **2011**, *44* (7), 1788–1791. <https://doi.org/10.1021/ma1026252>.
- (32) Zheng, T.; Cai, Z.; Ho-Wu, R.; Yau, S. H.; Shaparov, V.; Goodson, T.; Yu, L. Synthesis of Ladder-Type Thienoacenes and Their Electronic and Optical Properties. *J. Am. Chem. Soc.* **2016**, *138* (3), 868–875. <https://doi.org/10.1021/jacs.5b10175>.
- (33) Li, J.; Cao, H.; Zhang, Z.; Liu, S.; Xia, Y. Research Progress on Singlet Fission in Acenes and Their Derivatives. *Photonics* **2022**, *9* (10), 689. <https://doi.org/10.3390/photonics9100689>.
- (34) Basel, B. S.; Hetzer, C.; Zirzmeier, J.; Thiel, D.; Guldi, R.; Hampel, F.; Kahnt, A.; Clark, T.; Guldi, D. M.; Tykwinski, R. R. Davydov Splitting and Singlet Fission in Excitonically Coupled Pentacene Dimers. *Chem. Sci.* **2019**, *10* (13), 3854–3863. <https://doi.org/10.1039/C9SC00384C>.
- (35) Guo, D.; Ma, L.; Zhou, Z.; Lin, D.; Wang, C.; Zhao, X.; Zhang, F.; Zhang, J.; Nie, Z. Charge Transfer Dynamics in a Singlet Fission Organic Molecule and Organometal Perovskite Bilayer Structure. *J. Mater. Chem. A* **2020**, *8* (11), 5572–5579. <https://doi.org/10.1039/C9TA11022D>.
- (36) Ostroverkhova, O.; Cooke, D. G.; Shcherbyna, S.; Egerton, R. F.; Hegmann, F. A.; Tykwinski, R. R.; Anthony, J. E. Bandlike Transport in Pentacene and Functionalized Pentacene Thin Films Revealed by Subpicosecond Transient Photoconductivity Measurements. *Phys. Rev. B* **2005**, *71* (3), 035204. <https://doi.org/10.1103/PhysRevB.71.035204>.
- (37) Day, J.; Subramanian, S.; Anthony, J. E.; Lu, Z.; Twieg, R. J.; Ostroverkhova, O. Photoconductivity in Organic Thin Films: From Picoseconds to Seconds after Excitation. *J. Appl. Phys.* **2008**, *103* (12), 123715. <https://doi.org/10.1063/1.2946453>.
- (38) Sosorev, A. Yu.; Maslennikov, D. R.; Chernyshov, I. Yu.; Dominskiy, D. I.; Bruevich, V. V.; Vener, M. V.; Paraschuk, D. Yu. Relationship between Electron–Phonon Interaction and Low-Frequency Raman Anisotropy in High-Mobility Organic Semiconductors. *Phys. Chem. Chem. Phys.* **2018**, *20* (28), 18912–18918. <https://doi.org/10.1039/C8CP03232G>.
- (39) Mics, Z.; Tielrooij, K.-J.; Parvez, K.; Jensen, S. A.; Ivanov, I.; Feng, X.; Müllen, K.; Bonn, M.; Turchinovich, D. Thermodynamic Picture of Ultrafast Charge Transport in Graphene. *Nat. Commun.* **2015**, *6* (1), 7655. <https://doi.org/10.1038/ncomms8655>.
- (40) Leonard, A. A.; Mosquera, M. A.; Jones, L. O.; Cai, Z.; Fauvell, T. J.; Kirschner, M. S.; Gosztola, D. J.; Schatz, G. C.; Schaller, R. D.; Yu, L.; Chen, L. X. Photophysical Implications of Ring Fusion, Linker Length, and Twisting Angle in a Series of Perylenediimide–Thienoacene Dimers. *Chem. Sci.* **2020**, *11* (27), 7133–7143. <https://doi.org/10.1039/D0SC02862B>.
- (41) Busby, E.; Berkelbach, T. C.; Kumar, B.; Chernikov, A.; Zhong, Y.; Hlaing, H.; Zhu, X.-Y.; Heinz, T. F.; Hybertsen, M. S.; Sfeir, M. Y.; Reichman, D. R.; Nuckolls, C.; Yaffe, O. Multiphonon Relaxation Slows Singlet Fission in Crystalline Hexacene. *J. Am. Chem. Soc.* **2014**, *136* (30), 10654–10660. <https://doi.org/10.1021/ja503980c>.
- (42) Eshun, A.; Cai, Z.; Awies, M.; Yu, L.; Goodson, T. Investigations of Thienoacene Molecules for Classical and Entangled Two-Photon Absorption. *J. Phys. Chem. A* **2018**, *122* (41), 8167–8182. <https://doi.org/10.1021/acs.jpca.8b06312>.



- (43) Lee, J.; Li, H.; Kalin, A. J.; Yuan, T.; Wang, C.; Olson, T.; Li, H.; Fang, L. Extended Ladder-Type Benzo[ *k* ]tetraphene-Derived Oligomers. *Angew. Chem. Int. Ed.* **2017**, *56* (44), 13727–13731. <https://doi.org/10.1002/anie.201707595>.
- (44) Ricci, F.; Mandal, H.; Wajahath, M.; Burdick, R. K.; Villabona-Monsalve, J. P.; Hussain, S.; Goodson, T. Investigations of Coherence in Perovskite Quantum Dots with Classical and Quantum Light. *J. Phys. Chem. C* **2023**, *127* (7), 3579–3593. <https://doi.org/10.1021/acs.jpcc.2c08455>.
- (45) Madu, I. K.; Jiang, H.; Laventure, A.; Zimmerman, P. M.; Welch, G. C.; Goodson, T. Impact of Ring-Fusion on the Excited State Decay Pathways of N-Annulated Perylene Diimides. *J. Phys. Chem. C* **2021**, *125* (19), 10500–10515. <https://doi.org/10.1021/acs.jpcc.1c01964>.
- (46) Muthike, A. K.; Carlotti, B.; Madu, I. K.; Jiang, H.; Kim, H.; Wu, Q.; Yu, L.; Zimmerman, P. M.; Goodson, T. The Role of the Core Attachment Positioning in Triggering Intramolecular Singlet Exciton Fission in Perylene Diimide Tetramers. *J. Phys. Chem. B* **2021**, *125* (19), 5114–5131. <https://doi.org/10.1021/acs.jpcc.1c02534>.
- (47) Spano, F. C. The Spectral Signatures of Frenkel Polarons in H- and J-Aggregates. *Acc. Chem. Res.* **2010**, *43* (3), 429–439. <https://doi.org/10.1021/ar900233v>.
- (48) Mondal, R.; Tönshoff, C.; Khon, D.; Neckers, D. C.; Bettinger, H. F. Synthesis, Stability, and Photochemistry of Pentacene, Hexacene, and Heptacene: A Matrix Isolation Study. *J. Am. Chem. Soc.* **2009**, *131* (40), 14281–14289. <https://doi.org/10.1021/ja901841c>.
- (49) Rieger, R.; Müllen, K. Forever Young: Polycyclic Aromatic Hydrocarbons as Model Cases for Structural and Optical Studies. *J. Phys. Org. Chem.* **2010**, *23* (4), 315–325. <https://doi.org/10.1002/poc.1644>.
- (50) Lim, J. A.; Lee, H. S.; Lee, W. H.; Cho, K. Control of the Morphology and Structural Development of Solution-Processed Functionalized Acenes for High-Performance Organic Transistors. *Adv. Funct. Mater.* **2009**, *19* (10), 1515–1525. <https://doi.org/10.1002/adfm.200801135>.
- (51) Ahn, T.-S.; Müller, A. M.; Al-Kaysi, R. O.; Spano, F. C.; Norton, J. E.; Beljonne, D.; Brédas, J.-L.; Bardeen, C. J. Experimental and Theoretical Study of Temperature Dependent Exciton Delocalization and Relaxation in Anthracene Thin Films. *J. Chem. Phys.* **2008**, *128* (5), 054505. <https://doi.org/10.1063/1.2822310>.
- (52) Zhang, X.; Matzger, A. J. Effect of Ring Fusion on the Electronic Absorption and Emission Properties of Oligothiophenes. *J. Org. Chem.* **2003**, *68* (25), 9813–9815. <https://doi.org/10.1021/jo035241e>.
- (53) Burdett, J. J.; Müller, A. M.; Gosztola, D.; Bardeen, C. J. Excited State Dynamics in Solid and Monomeric Tetracene: The Roles of Superradiance and Exciton Fission. *J. Chem. Phys.* **2010**, *133* (14), 144506. <https://doi.org/10.1063/1.3495764>.
- (54) Okamoto, H.; Yamaji, M.; Gohda, S.; Sato, K.; Sugino, H.; Satake, K. Photochemical Synthesis and Electronic Spectra of Fulminene ([6]Phenacene). *Res. Chem. Intermed.* **2013**, *39* (1), 147–159. <https://doi.org/10.1007/s11164-012-0639-1>.
- (55) Perroni, C.; Gargiulo, F.; Nocera, A.; Ramaglia, V.; Cataudella, V. The Effects of Different Electron-Phonon Couplings on the Spectral and Transport Properties of Small Molecule Single-Crystal Organic Semiconductors. *Electronics* **2014**, *3* (1), 165–189. <https://doi.org/10.3390/electronics3010165>.
- (56) Cheng, Y.-C.; Silbey, R. J. A Unified Theory for Charge-Carrier Transport in Organic Crystals. *J. Chem. Phys.* **2008**, *128* (11), 114713. <https://doi.org/10.1063/1.2894840>.

- (57) Li, X.; Tao, L.; Chen, Z.; Fang, H.; Li, X.; Wang, X.; Xu, J.-B.; Zhu, H. Graphene and Related Two-Dimensional Materials: Structure-Property Relationships for Electronics and Optoelectronics. *Appl. Phys. Rev.* **2017**, *4* (2), 021306. <https://doi.org/10.1063/1.4983646>.
- (58) Sun, D.; Divin, C.; Berger, C.; De Heer, W. A.; First, P. N.; Norris, T. B. Hot Carrier Cooling by Acoustic Phonons in Epitaxial Graphene by Ultrafast Pump-probe Spectroscopy. *Phys. Status Solidi C* **2011**, *8* (4), 1194–1197. <https://doi.org/10.1002/pssc.201001134>.
- (59) Strait, J. H.; Wang, H.; Shivaraman, S.; Shields, V.; Spencer, M.; Rana, F. Very Slow Cooling Dynamics of Photoexcited Carriers in Graphene Observed by Optical-Pump Terahertz-Probe Spectroscopy. *Nano Lett.* **2011**, *11* (11), 4902–4906. <https://doi.org/10.1021/nl202800h>.
- (60) Roberts, A. T.; Binder, R.; Kwong, N. H.; Golla, D.; Cormode, D.; LeRoy, B. J.; Everitt, H. O.; Sandhu, A. Optical Characterization of Electron-Phonon Interactions at the Saddle Point in Graphene. *Phys. Rev. Lett.* **2014**, *112* (18), 187401. <https://doi.org/10.1103/PhysRevLett.112.187401>.
- (61) Breusing, M.; Kuehn, S.; Winzer, T.; Malić, E.; Milde, F.; Severin, N.; Rabe, J. P.; Ropers, C.; Knorr, A.; Elsaesser, T. Ultrafast Nonequilibrium Carrier Dynamics in a Single Graphene Layer. *Phys. Rev. B* **2011**, *83* (15), 153410. <https://doi.org/10.1103/PhysRevB.83.153410>.
- (62) Malic, E.; Winzer, T.; Bobkin, E.; Knorr, A. Microscopic Theory of Absorption and Ultrafast Many-Particle Kinetics in Graphene. *Phys. Rev. B* **2011**, *84* (20), 205406. <https://doi.org/10.1103/PhysRevB.84.205406>.
- (63) Sharma, T.; Tailor, N. K.; Choudhury, N.; Kumar, D.; Saini, S. K.; Mitra, A.; Kumar, M.; De, P.; Satapathi, S. Observation of Strong Electron-Phonon Interaction in Polymeric Diluted Organic Semiconductor. *Chem. Phys.* **2023**, *564*, 111706. <https://doi.org/10.1016/j.chemphys.2022.111706>.
- (64) Malard, L. M.; Fai Mak, K.; Castro Neto, A. H.; Peres, N. M. R.; Heinz, T. F. Observation of Intra- and Inter-Band Transitions in the Transient Optical Response of Graphene. *New J. Phys.* **2013**, *15* (1), 015009. <https://doi.org/10.1088/1367-2630/15/1/015009>.
- (65) Winnerl, S.; Orlita, M.; Plochocka, P.; Kossacki, P.; Potemski, M.; Winzer, T.; Malic, E.; Knorr, A.; Sprinkle, M.; Berger, C.; De Heer, W. A.; Schneider, H.; Helm, M. Carrier Relaxation in Epitaxial Graphene Photoexcited Near the Dirac Point. *Phys. Rev. Lett.* **2011**, *107* (23), 237401. <https://doi.org/10.1103/PhysRevLett.107.237401>.
- (66) Borysenko, K. M.; Mullen, J. T.; Barry, E. A.; Paul, S.; Semenov, Y. G.; Zavada, J. M.; Nardelli, M. B.; Kim, K. W. First-Principles Analysis of Electron-Phonon Interactions in Graphene. *Phys. Rev. B* **2010**, *81* (12), 121412. <https://doi.org/10.1103/PhysRevB.81.121412>.
- (67) Hines, D. A.; Forrest, R. P.; Corcelli, S. A.; Kamat, P. V. Predicting the Rate Constant of Electron Tunneling Reactions at the CdSe–TiO<sub>2</sub> Interface. *J. Phys. Chem. B* **2015**, *119* (24), 7439–7446. <https://doi.org/10.1021/jp5111295>.
- (68) Masino, M.; Salzillo, T.; Brillante, A.; Della Valle, R. G.; Venuti, E.; Girlando, A. Experimental Estimate of the Holstein Electron–Phonon Coupling Constants in Perylene. *Adv. Electron. Mater.* **2020**, *6* (8), 2000208. <https://doi.org/10.1002/aelm.202000208>.
- (69) Banks, P. A.; D’Avino, G.; Schweicher, G.; Armstrong, J.; Ruzié, C.; Chung, J. W.; Park, J.; Sawabe, C.; Okamoto, T.; Takeya, J.; Sirringhaus, H.; Ruggiero, M. T. Untangling the Fundamental Electronic Origins of Non-Local Electron–Phonon Coupling in Organic Semiconductors. *Adv. Funct. Mater.* **2023**, *33* (38), 2303701. <https://doi.org/10.1002/adfm.202303701>.

- (70) Li, W.; Ren, J.; Shuai, Z. A General Charge Transport Picture for Organic Semiconductors with Nonlocal Electron-Phonon Couplings. *Nat. Commun.* **2021**, *12* (1), 4260. <https://doi.org/10.1038/s41467-021-24520-y>.
- (71) Novko, D.; Kralj, M. Phonon-Assisted Processes in the Ultraviolet-Transient Optical Response of Graphene. *Npj 2D Mater. Appl.* **2019**, *3* (1), 48. <https://doi.org/10.1038/s41699-019-0131-5>.
- (72) Devos, A.; Lannoo, M. Electron-Phonon Coupling for Aromatic Molecular Crystals: Possible Consequences for Their Superconductivity. *Phys. Rev. B* **1998**, *58* (13), 8236–8239. <https://doi.org/10.1103/PhysRevB.58.8236>.
- (73) Yi, Y.; Coropceanu, V.; Brédas, J.-L. Nonlocal Electron-Phonon Coupling in the Pentacene Crystal: Beyond the  $\Gamma$ -Point Approximation. *J. Chem. Phys.* **2012**, *137* (16), 164303. <https://doi.org/10.1063/1.4759040>.
- (74) Kato, T.; Yamabe, T. Electron-Phonon Interactions in Photoinduced Excited Electronic States in Fluoroacenes. *J. Chem. Phys.* **2005**, *123* (2), 024301. <https://doi.org/10.1063/1.1950670>.
- (75) Murphy, A. R.; Chang, P. C.; VanDyke, P.; Liu, J.; Fréchet, J. M. J.; Subramanian, V.; DeLongchamp, D. M.; Sambasivan, S.; Fischer, D. A.; Lin, E. K. Self-Assembly, Molecular Ordering, and Charge Mobility in Solution-Processed Ultrathin Oligothiophene Films. *Chem. Mater.* **2005**, *17* (24), 6033–6041. <https://doi.org/10.1021/cm0515350>.
- (76) Garnier, F.; Deloffre, F.; Horowitz, G.; Hajlaoui, R. Structure Effect on Transport of Charge Carriers in Conjugated Oligomers. *Synth. Met.* **1993**, *57* (2–3), 4747–4754. [https://doi.org/10.1016/0379-6779\(93\)90812-B](https://doi.org/10.1016/0379-6779(93)90812-B).
- (77) Kazantsev, M. S.; Beloborodova, A. A.; Kuimov, A. D.; Koskin, I. P.; Frantseva, E. S.; Rybalova, T. V.; Shundrina, I. K.; Becker, C. S.; Mostovich, E. A. Synthesis, Luminescence and Charge Transport Properties of Furan/Phenylene Co-Oligomers: The Study of Conjugation Length Effect. *Org. Electron.* **2018**, *56*, 208–215. <https://doi.org/10.1016/j.orgel.2018.01.010>.
- (78) Sun, D.; Wu, Z.-K.; Divin, C.; Li, X.; Berger, C.; De Heer, W. A.; First, P. N.; Norris, T. B. Ultrafast Relaxation of Excited Dirac Fermions in Epitaxial Graphene Using Optical Differential Transmission Spectroscopy. *Phys. Rev. Lett.* **2008**, *101* (15), 157402. <https://doi.org/10.1103/PhysRevLett.101.157402>.
- (79) Saito, Masatoshi; Nakano, Yuki; Nakamura, Hiroaki; and Kondo, Hirofumi. Compound for Organic Thin Film Transistor and Organic Thin-Film Transistor Using Sample. US 2011/0220884 A1.

## Chapter IV

### Probing the Exciton Dynamics of Naphthalene-imide Based Nonfullerene Acceptors for Organic Photovoltaics

#### IV.1 Collaboration Statement

This Chapter describes the results and conclusion of a collaborative research investigation between Professor Theodore G. Goodson III's group (author of this dissertation and *Collaborator 1*), Department of Chemistry, University of Michigan and Professor Samson A. Jenekhe's group (*Collaborator 2*), Department of Chemical Engineering and Department of Chemistry, University of Washington. The authors of this research investigation are: **Meghan E. Orr**; Dr. Haraprasad Mandal; Sarah M. West; Professor Samson A. Jenekhe; and Professor Theodore G. Goodson III. **Meghan E. Orr's** (author of this dissertation) contribution to this research investigation is: sample preparation for steady-state measurements and femtosecond transient (fs-TA) experiments; conducting the previously listed measurements and experiments; performing data analysis of previously listed measurements and experiments; and writing and editing the paper of this research investigation. The contribution of *Collaborator 1* to this research investigation is: sample preparation for quantum yield measurement, two-photon absorption (TPA), time-resolved fluorescence upconversion (UpC); conducted the listed measurements and experiments; and conducting data analysis on listed measurement and experiments. The contribution of *Collaborator 2* to this research investigation is performing density functional theory (DFT) and

time-dependent DFT theoretical calculations; conducting data analysis on theoretical calculations; and writing and editing paper of this research investigation.

## IV.2 Abstract

Highly efficient organic photovoltaic devices were recently reported for bis(naphthalene-imide)arylenelidenes (BNiAs), a class of nonfullerene acceptors (NFAs). The BNiAs had fused-ring donor moieties (indacenodithienothiophene or indenodithiophene-benzothiadiazole) or a non-fused donor moiety (thienylene vinylene). The BNiA with a non-fused ring donor moiety (NITV) had a 2x less efficient solar cell device compared to the fused-ring BNiAs, NIDT and NIBT. Herein, we report the use of ultrafast time-resolved laser spectroscopy and theoretical calculations to investigate the exciton dynamics and the intramolecular charge generation mechanism of the BNiAs. Time-resolved fluorescence upconversion results show these small molecules have a fast fluorescence lifetime; therefore, these small molecules will most likely to undergo intramolecular charge generation. The femtosecond transient absorption results show geminate decay (charge recombination decay and exciton decay) of NIBT is roughly **5x – 6x** slower than the decay of NITV and NIDT. From the theoretical calculations and femtosecond transient absorption results an energy diagram of the intramolecular charge generation occurring in the BNiAs is created. The energy diagram shows the reorganization energy between exciton and charge transfer states of NIBT is **31%** smaller compared to the other BNiAs. Interestingly, despite the differences in donor moieties, NITV (non-FREA) and NIDT have similar reorganization energy, exciton dynamics and intramolecular charge generation. The results of the BNiAs shows the benzothiadiazole  $\pi$  bridges on the donor moiety of NIBT leads to strong exciton dynamics and an efficient intramolecular charge generation for NFA small molecules. Ultimately,

the results discussed in this paper provide insight to finding a correlation between structure of small molecule NFAs and efficiency of organic photovoltaics.

### IV. 3 Introduction

Organic photovoltaics (OPVs) are a promising source of renewable energy with the potential to be low-cost to manufacture on large scales, can be made into flexible devices that could be readily integrated with buildings, and have improved versatility in their active layer materials compared to their inorganic counterparts.<sup>1-10</sup> Due to these unique characteristics, OPV devices can be used in various applications such as integrated solar power generation and self-powered electronics.<sup>9</sup> Recent and ongoing research in OPVs aims to develop solar cells with improved power conversion efficiencies (PCEs) and durability.<sup>1-4</sup> Towards this end, understanding the charge generation mechanism and structure-function relationships of OPV materials are essential.<sup>5-7,11-15</sup>

Historically, since the discovery of bulk heterojunction OPV devices,<sup>16</sup> where a blend of an electron-donating conjugated polymer and a fullerene derivative such as PC<sub>60</sub>BM (or PC<sub>70</sub>BM) acted as the electron acceptor material in the active layer, fullerenes dominated the field of OPVs due to their excellent electron-accepting and electron transport properties.<sup>1,3</sup> However, there are many disadvantages of fullerene-based acceptors for OPVs including limited optical absorption in the visible and near infrared regions, high cost, poor tunability of molecular structure, and poor morphological stability of OPV devices.<sup>4,7</sup> The motivation of this research is to find alternative acceptor materials.<sup>1,9,13-15,17</sup> Efforts in the design and synthesis of nonfullerene acceptors (NFAs) produced major progress in 2014 with materials comparable to fullerene and subsequently surpassing the state-of-the-art fullerene based OPV device in 2017.<sup>13-15</sup> Over the years, the PCE of OPVs have achieved beyond 16% and are approaching to 19% – 20%.<sup>9,13,17-22</sup> A main objective

of this research is to find the correlation between organic material structural design and the PCE of solar cell devices.<sup>5-7,11-15</sup> One approach for increasing the PCE in OPVs is investigating the charge generation mechanism and finding the optimal structural design of organic materials used in a device.

Recently, the Jenekhe group designed and synthesized a class of small molecule NFAs

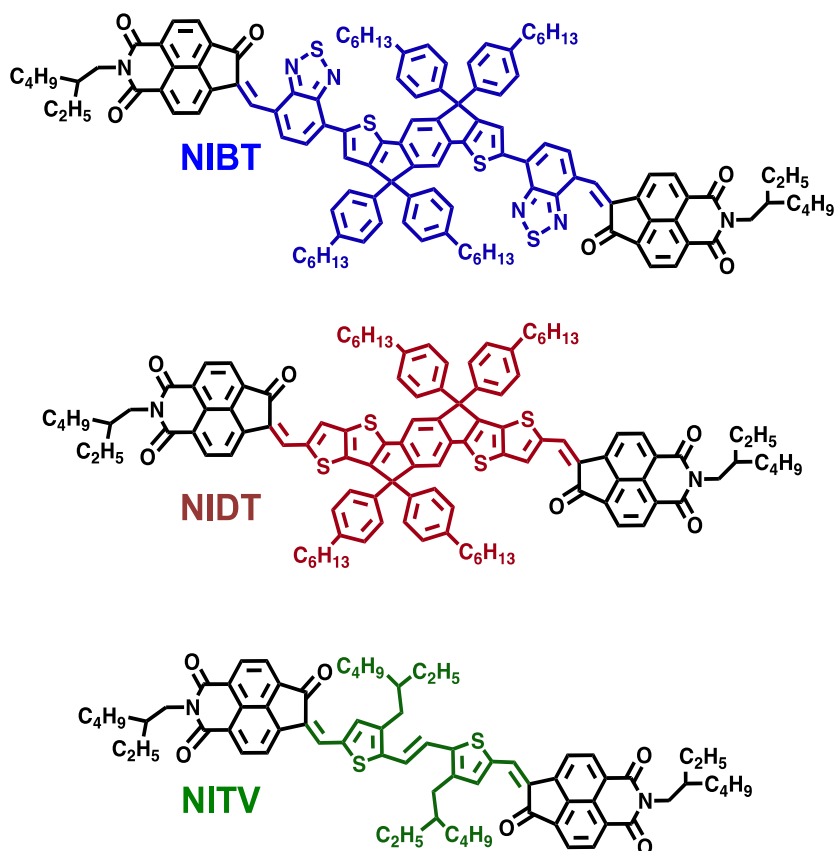


**Figure IV.18:** Molecular structures of BNIA: NITV (non-FREA) colored **green**, NIDT (FREA) highlighted **red**, and NIBT (FREA) highlighted **blue**. The terminal acceptor moiety, naphthalene imide, is colored **black** in all the BNIA, which have an acceptor – donor– acceptor architecture.

called bis(naphthalene-imide)arylenelidene

(BNIA) with acceptor-donor-acceptor

architecture<sup>23</sup>; whose

molecular structures are shown in **Figure IV.1**<sup>23</sup>

The three BNIA feature methane-bridges between

the end-capping naphthalene imide moiety, which is colored black in

**Figure IV.1** and a central donor moiety which is either a non fused-ring,

thienylene vinylene (TVT), or a fused-ring, indacenodithienothiophene (IDTT) or indenodithiophene-benzothiadiazole (IDTBT) (see **Figure IV.1**). The BNIA with a non-fused ring donor unit is called NITV. Since NITV has a non-fused ring donor unit, this BNIA is

classified as a non-fused ring electron acceptor (nonFREA).<sup>7</sup> The other two BNIAs with a fused-ring as the donor units are called NIDT and NIBT. Since both NIDT and NIBT have a fused ring donor unit, these BNIAs are classified as fused ring electron acceptors (FREAs).<sup>1</sup> Unlike conventional rylene-diimide based NFAs that are bridged through single bonds on the naphthalene backbone<sup>23</sup> in the novel BNIAs, the naphthalene-imide acceptor moieties are connected to the donor moiety structure via a methine group<sup>23</sup>. This endowed the BNIAs with enhanced planarity, excellent electrochemical redox stability, good electron mobilities and improved photovoltaic performance compared to traditional rylene-diimide based OPV devices. The donor polymer poly[[4,8-bis[5-(2-ethylhexyl)-2-thienyl]benzo[1,2-b:4,5-b']dithiophene-2,6-diyl]-2,5-thiophenediyl[5,7-bis(2-ethylhexyl)-4,8-dioxo-4H,8H-benzo[1,2-c:4,5-c']dithiophene-1,3-diyl]] (PBDB-T) was used to evaluate the photovoltaic properties of the BNIAs, giving the PCEs: NITV (4.8%); NIDT (10.0%); and NIBT (10.8%).<sup>23</sup> The reported PCEs show there is a large difference in photovoltaic efficiency between the non-FREA (NITV) and FREA (NIDT and NIBT) BNIAs. This difference suggests a critical need for investigating the exciton dynamics of the charge generation mechanism for this class of OPV materials.

In this paper, we will investigate the charge generation and CT dynamics of non-FREA and FREA BNIAs by using ultrafast time-resolved and nonlinear optical laser spectroscopy and theoretical calculations. The results discussed in this paper will provide insight to the differences in charge generation and CT dynamics between non-FREA and FREA small molecules NFAs with an acceptor-donor-acceptor structural design. By investigating differences in the structural design – a non-FREA or FREA small molecule NFA – this will provide guidance to which structural design will generate an efficient charge generation for OPVs. The results discussed in this paper



will increase the knowledge of organic material structural design and charge generation in order to find a correlation between organic material structural design and PCE.

## IV.4 Experimental Section

### *IV.4.a Steady-State Absorption and Emission Measurements*

The steady-state absorption and emission measurements were performed on liquid solutions of the BNIA in chloroform. The BNIA liquid solutions had an optical density of 0.3 or less for these steady-state measurements. The steady-state absorption spectra of the BNIA were collected using an Agilent 8453 spectrophotometer. The steady-state emission spectra of the BNIA were collected using a Horiba Scientific PTI QuantaMaster 3633 fluorimeter. For all steady-state measurements, the BNIA liquid solutions were placed in quartz cuvettes with a 1.0 cm path length. The spectrophotometer and fluorimeter used to collect the steady-state absorption and emission measurements have been used and described in previous reports.<sup>24,25-27</sup>

### *IV.4.b Fluorescence Quantum Yield Measurements*

The Williams comparative method was used to measure the fluorescence quantum yields ( $\Phi_F$ ) of the BNIA in liquid solutions at various wavelengths.<sup>28</sup> The same instruments used in the steady-state measurements described above were used for the quantum yield measurements of the BNIA. The solvent chloroform was used to make the liquid solutions of BNIA for the fluorescence quantum yield measurements. For these measurements, a series of dilutions were created for each BNIA system. The starting BNIA solutions had with an optical density of 0.1. For the reference standard solutions, the following reference standards and solvents were used Coumarin 307 in methanol; [2-[2-[4-(dimethylamino)phenyl]ethenyl]-6-methyl-4H-pyran-4-ylidene]-propanedinitrile (DCM) in methanol; and Styryl 9M in chloroform. The reported quantum yields of these reference standards were: Coumarin 307 in methanol,  $\Phi_F$ : 0.307; DCM in

methanol,  $\Phi_F$ : 0.35; and Styryl 9M in chloroform,  $\Phi_F$ : 0.54.<sup>29-31</sup> The reference standard solutions were prepared in a similar manner to the BNIA solutions. Coumarin 307 solutions were used to measure the quantum yields in the 450nm – 500nm range. DCM solutions were used to measure the quantum yields at 650nm. A quartz cuvette with a 1.0cm path length was used as the sample holder for the BNIA liquid solutions and the reference standard solutions. The Williams comparative method, that is described in this paper, has been used in previous research.<sup>24-26,32,33</sup>

#### *IV.4.c Two-photon Absorption Experiments*

Two-photon absorption (TPA) cross-sections of the NITV and NIDT were determined using the two-photon induced fluorescence technique.<sup>24-26,34</sup> The TPA experimental setup contained a Spectra-Physics Millennia Pro laser (continuous wave at 532nm with a power of 5W) which was used to pump a Spectra-Physics Tsunami Ti:Sapphire, mode-locked laser, to generate an output beam of 800nm with a repetition rate of 80MHz and pulse width of approximately 100fs. The Tsunami 800nm output beam was used as the excitation beam and the output power was set to 100mW for the experiment. For this experiment, the samples were liquid solutions of the NITV and NIDT in chloroform with an optical density of 0.3. During the experiments, the samples were placed in quartz cuvettes with a 1.0 cm path length. The 800nm excitation beam excited the BNIA samples and generated two-photon induced fluorescence signals, which were collected by a Hamamatsu photomultiplier tube and photocounting unit and a Newport Oriel Cornerstone monochromator. The photomultiplier tube and monochromator were placed perpendicular to the 800nm excitation beam to ensure that the two-photon induced fluorescence signals were collected. For NITV and NIDT, the two-photon induced fluorescence spectra were recorded from 400nm-800nm. To determine and verify that two-photon absorption occurred in the BNIA, power dependence measurements were conducted and the values of power versus count intensity were

recorded. For the power dependence measurements, a neutral density filter was placed before the NITV and NIDT samples and the two-photon induced fluorescence count intensities were recorded at a specific wavelength and various powers. Then, a log-log plot of the two-photon induced fluorescence count intensity versus power were created for the NIDT samples and the slope was determined. If the slope of log-log plot had a value  $\sim 2.0$ , then the occurrence of TPA in the sample was inferred. The TPA cross-sections of the NITV and NIDT were calculated using reference standards and [2-[2-[4-(dimethylamino)phenyl]ethenyl]-6-methyl-4H-pyran-4-ylidene]-propanedinitrile (DCM) in methanol (TPA cross-section:  $\delta=5.1$ )<sup>35</sup>. The TPA experiment and calculations, described in this paper, have been used and described in previous reports.<sup>24,36,37,32</sup>

#### *IV.4.d Time-resolved Fluorescence Upconversion*

Time-resolved femtosecond fluorescence upconversion (UpC) experiments were performed on liquid solutions of the BNIAs. The UpC experimental setup contained a Spectra-Physics Millennia Pro laser (continuous wave at 532nm with a power of 5W) that was used to pump a Spectra-Physics Tsunami Ti:Sapphire mode-locked laser to generate an output beam of 800nm with a repetition rate of 80MHz, pulse width of approximately 100fs, and output power of approximately 700mW. The 800nm beam of the Tsunami Ti:Sapphire laser generated the gate and excitation beams for the experiments. From the Tsunami Ti:Sapphire laser, the 800nm gate beam was directed into a CDP FOG 100 fluorescence upconversion optical setup. Specifically, from the Tsunami Ti:Sapphire laser, the 800nm gate beam was directed onto a  $\beta$ -barium borate (BBO) nonlinear crystal to undergo second harmonic generation. The BBO nonlinear crystal converted approximately 10% of the 800nm gate beam to 400nm and the generated 400nm beam was used to excite the BNIAs during the experiments. After the BBO nonlinear crystal, a dichroic mirror was used to separate the 400nm excitation and 800nm gate beams. The 400nm excitation

beam was directed through a set of filters, a Berek compensator and focused onto the samples. The samples were liquid solutions of BNIA's prepared in chloroform and had an optical density of 0.2. The samples were placed in rotating quartz sample cell with a 1mm path length. Due to the filters, the power of 400nm excitation beam was approximately 14mW or a pump energy of approximately 0.18nJ/pulse. After the 400nm excitation beam was focused on the samples and generated fluorescence signals, a filter was used to block the 400nm excitation and the fluorescence of the BNIA's were directed to a second BBO nonlinear crystal. During the excitation of the samples, after the dichroic mirror, the other 90% of 800nm gate beam was directed through a computer-controlled delay stage and onto the second BBO nonlinear crystal. At the second BBO nonlinear crystal, the emission of BNIA's and 800nm gate beam undergoes sum frequency mixing to generate an upconverted signal which was directed and focused into the monochromator and photomultiplier tube. The software Lumex and DM51292 were used for data acquisition and setting the monochromator wavelength. The Origin Pro software was used for data analysis. The time-resolved fluorescence upconversion experimental setup, described in this paper, have been used and described in previous reports.<sup>27,38-40,34</sup>

#### *IV.4.e. femtosecond Transient Absorption*

Femtosecond transient absorption (fs-TA) experiments were conducted on BNIA solutions. A Spectra-Physics ultrafast amplified laser system and Ultrafast System Helios, transient absorption spectrometer were used to create the fs-TA experimental setup. The fs-TA experimental set up started with a Millennia Pro continuous wave at 532nm laser (power of 4.3W) and a Tsunami Ti:Sapphire mode-locked laser to generate 790nm femtosecond (approximate pulse width: 80fs) pulse with output power of 250mW and repetition rate of 80MHz. The generated 790nm femtosecond pulse and 527nm pulse (approximate pulse width: 200ns) from an Empower

Q-switched laser with an output power of 8W and repetition rate of 1kHz were directed into the cavity of a Spitfire Amplifier laser to generate an amplified 790nm output beam with: an approximate pulse width of 110 fs; repetition rate of 1kHz; and approximate output power of 1W. The 790nm amplified femtosecond pulse was directed into a beamsplitter that split the pulse into two portions that were used to generate the pump and probe beams for the fs-TA experiments. At the beamsplitter, approximately 15% of 790nm amplified femtosecond the pulse was used to generate the probe beam and the other roughly 85% was directed into the Spectra-Physics Optical Parametric Amplifier (OPA-800C). Within the cavity of the OPA-800C, a 600nm pump was generated. A neutral density filter was used to attenuate the power of the 600nm pump to an average power of less than 1mW or approximate pump energy of 1.0 $\mu$ J/pulse. Both probe and pump beams were directed into the Helios transient absorption spectrometer. Specifically, the pump beam was directed into an optical chopper and focused onto BNIA solutions in a quartz cuvette with a 2mm path length. The BNIA solutions were prepared using chloroform and had an optical density ranging from 0.5 – 0.8 for experiments. The probe beam was directed through a computer-controlled delay line and focused onto a 3mm sapphire plate that generated a visible white light continuum. The visible white light continuum ranged from 450nm – 800nm. The probe beam/white light continuum and sample signal were directed and focused onto an Ocean Optics spectrometer and charge-coupled device (CCD), which collected the difference in absorbance signal ( $\Delta A$ ) as a result of the pump being on versus off due to the optical chopper. The instrument response function of the experiment was approximately 160fs. The Helios software from Ultrafast System was used for data acquisition. The Surface Xplorer and Origin Pro software were used for data analysis. The fs-TA experimental setup and data analysis, described in this paper, have been used in previous reports.<sup>27,26</sup>

#### IV.4.f. Theoretical Calculations

Gas-phase molecule density functional theory (DFT) and time-dependent density functional theory (TD-DFT) calculations were performed using the Gaussian 16 suite of programs at the B3LYP/631-G(d,p) level of theory.<sup>41</sup> The alkyl chains were replaced with methyl groups to reduce the computational time costs. Vertical electronic transitions were calculated using 12 excited states for each molecule.<sup>23</sup>

### IV.5 Results

#### IV.5.a. Steady-State Results of BNIA s

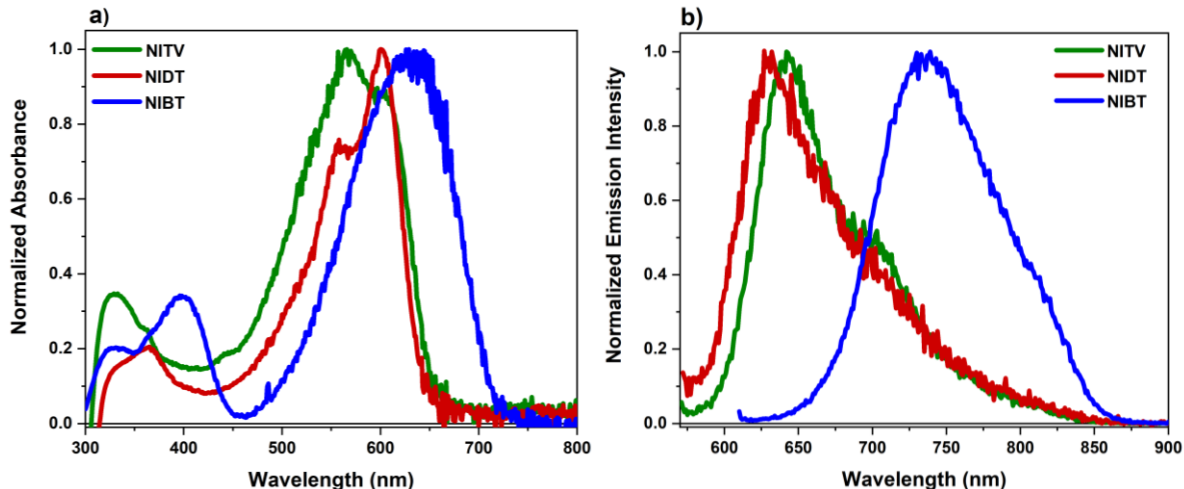


**Figure IV.19:** Normalized absorption and emission spectra of BNIA s in chloroform – **a)** absorption spectra and **b)** emission spectra. The excitation wavelengths used to measure emission spectra are 560nm for NITV and NIDT and 600nm for NIBT.

**Figure IV.2** shows the steady-state absorption (**Figure IV.2.a**) and emission (**Figure IV.2.b**) spectra of the BNIA s in chloroform. The steady-state absorption and emission peaks for the BNIA solutions are summarized in **Table IV.1**. All the BNIA s have a broad absorption with a strong intense peak in the visible region and a less intense peak in the UV region. The peaks in the UV range (from 320nm – 400nm) of the BNIA s are connected with a  $\pi\text{-}\pi^*$  transition. Previous studies on similar donor-acceptor systems have attributed the UV spectral region as due to a  $\pi\text{-}\pi^*$  transition. As for the visible region peaks (range from 560nm – 628 nm) in the absorption spectra

of the BNIAAs, these peaks could be due to a transition between the  $S_0$  and first excited singlet state,  $S_1$ . As shown in other studies, the visible peaks present in the absorption spectrum is another characteristic of molecules that have a structural framework consisting of donor and acceptor moieties. These studies have shown the visible peaks in the absorption spectra of donor acceptor systems corresponds to the  $S_0 \rightarrow S_1$  transition and provide insight to the intramolecular charge transfer (ICT) character of these molecules. This  $S_0 \rightarrow S_1$  of the BNIAAs could be between a locally excited (LE) state occurring on one portion of the small molecules or charge transfer between the donor and acceptor units creating a charge transfer (CT) state. It is significant to determine the type of state involved in the electronic transition of  $S_0 \rightarrow S_1$  because it can affect the ICT character of the molecules. Theoretical calculations performed on the BNIAAs will provide more insight to the type of state that affects the ICT character of the BNIAAs. The theoretical calculation results of the BNIAAs will be discussed later in this results section (see Results Section III.4).

As shown in **Figure IV.2.a**, the visible peaks in the steady-state absorption spectra show the absorption maxima ( $\lambda_{\max}^{\text{abs}}$ ) of the BNIAAs and show there is a difference in vibronic features between these molecules. Since the  $\lambda_{\max}^{\text{abs}}$  and vibronic features of the BNIAAs are in the visible peaks, the  $\lambda_{\max}^{\text{abs}}$  and vibronic features corresponds the electronic transition of  $S_0 \rightarrow S_1$  and will affect ICT character of these small molecules. For the vibronic features, only NITV (a non-FREA) and NIDT (a FREA) show vibronic peaks in the visible range of their absorption spectra (see **Table IV.1** for  $\lambda_{\max}^{\text{abs}}$ , which are underlined, and peaks corresponding to vibronic features). For NITV, the vibronic feature at 566nm is more intense compared to the feature at 600nm. As for NIDT, the vibronic feature at 600nm is more intense compared to the feature at 604nm. As for NIBT (FREA), there are no vibronic peaks present in its visible absorption; there is only one board peak at 628nm. Studies have observed the vibronic features in the visible peaks in the steady-state absorption

spectra of molecules that have a structural framework consisting of donor and acceptor moieties as well. The vibronic features of the BNIA s discussed in this paper will provide insight into the delocalization of electrons or excitons and how the delocalization is affected by the structure of these molecules. The vibronic features and exciton delocalization of the BNIA s will be discussed later in this section (see section III.3). The exciton delocalization of the BNIA s will show there is a difference in ICT character.

The  $\lambda_{\max}^{\text{abs}}$  (nm) of the BNIA s due to the conjugation length increases. The  $\lambda_{\max}^{\text{abs}}$  of the BNIA s are: 566nm for NITV; 604 nm for NIDT to 628 nm in NIBT (the  $\lambda_{\max}^{\text{abs}}$  in is underlined in **Table IV.1**). The difference in conjugation length between the BNIA s is due to the donor moieties of these small molecules. NIBT has the longest  $\pi$ -conjugated length of the BNIA s due to its donor moiety, IDTBT, containing the additional benzothiadiazole  $\pi$  bridges on its IDTT donor unit. Then, NIDT has the second longest  $\pi$ -conjugated length due to the IDTT core. Finally, NITV has the shortest  $\pi$ -conjugation length because of the comparatively small TVT donor moiety.

As with the  $\lambda_{\max}^{\text{abs}}$ , the emission maxima ( $\lambda_{\max}^{\text{ems}}$ ) of the BNIA show there is a difference in the maxima due to the  $\pi$ -conjugated length of these small molecules. **Figure IV.2.b** shows the steady-state emission spectra of the BNIA solutions in chloroform. **Table IV.1** shows the  $\lambda_{\max}^{\text{ems}}$  of the BNIA solutions (the  $\lambda_{\max}^{\text{ems}}$  is underlined in **Table IV.1**). The  $\lambda_{\max}^{\text{ems}}$  of the BNIA s is independent of the excitation wavelengths ( $\lambda_{\max}^{\text{abs}}$  and vibronic features) (see **Figures D.1** and **D.2** in Appendix D). The  $\lambda_{\max}^{\text{ems}}$  corresponds to the transition between the  $S_1 \rightarrow S_0$ . The correlation between the  $\pi$ -conjugated length and  $\lambda_{\max}^{\text{ems}}$  of the BNIA s is as the  $\pi$ -conjugated length increases, the  $\lambda_{\max}^{\text{ems}}$  shifts to the red. In other words, as the  $\pi$ -conjugated length of the BNIA s increases, the energy of the  $\lambda_{\max}^{\text{ems}}$  decreases. The Stokes Shift of the BNIA s is calculated and the values are shown in **Table IV.1**. NIDT has the smallest Stokes Shift compared to NITV and NIBT.



Studies have shown that when a molecule has a small Stokes Shift, this suggest that the molecule has a more ridge and planar structure.<sup>26,34</sup> Since NIDT has the smallest Stokes shift between the BNIA, this indicates the NIDT has the most ridge and planar structure between the BNIA. Then, NIBT has the least ridge and planar structure of the BNIA since it has the largest Stokes Shift. The more ridge and planar structure of NIDT could suggest this small molecule will have a more effective charge generation; however, additional results will need to be considered to support this observation (see below).

To summarize, the main observation of the steady-state results of the BNIA show there is a correlation between  $\pi$ -conjugated length and maxima peaks ( $\lambda_{\max}^{\text{abs}}$  and  $\lambda_{\max}^{\text{ems}}$ ); as the  $\pi$ -conjugated length increases, the maxima shifts to the red, and the energy gap decreases. NIBT has the smallest energy gap between the BNIA due to its longest  $\pi$ -conjugated length. In addition, the steady-state results show the BNIA have different vibronic features that will impact the charge and exciton dynamics of these systems. Based on the Stokes Shift, NIBT has the largest stokes and suggests has the largest ICT character.

**Table IV.1:** Summary of steady-state absorption and emission maximum peaks and fluorescence lifetimes ( $\tau_{\text{fluor}}$ ) of BNIA

BNIA	Absorption Peaks (nm)	Emission peaks (nm)	Stokes Shift (nm)	$\tau_{\text{fluor}}$ (ps)
<b>NITV</b>	<u>566</u> , 600	<u>643</u> , 700	77	$36 \pm 6.8$
<b>NIDT</b>	560, <u>604</u>	<u>630</u>	26	$50 \pm 9.9$
<b>NIBT</b>	<u>628</u>	<u>737</u> , 810	109	$41 \pm 2.8$

#### *IV.5.b Two-photon absorption (TPA) Results of BNIA*

The two-photon absorption (TPA) cross sections ( $\delta_{\text{TPA}}$ ) of BNIA provide insight in to the transition dipole moments of these small molecules. A log-log plot of power versus two-photon

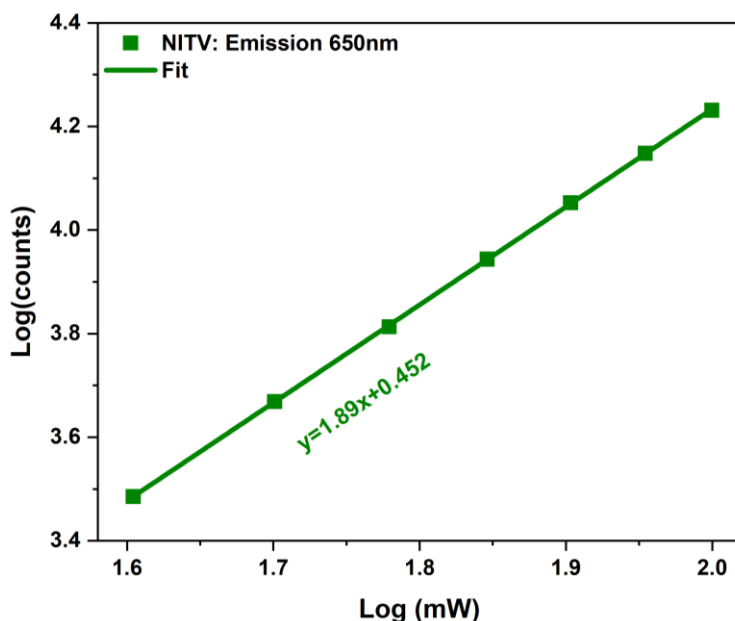


**Figure IV.20:** Log-log plot of NITV in chloroform obtained from two-photon absorption (TPA) experiments using 650nm

fluorescence intensity of NITV obtained from the TPA experiments are shown in **Figure IV.3**. When comparing NITV, the non-FREA, has the higher  $\delta_{\text{TPA}}$  compared to NIDT, the FREA. Since the NITV has the higher  $\delta_{\text{TPA}}$ , this suggests that NITV has a higher transition dipole compared to NIDT. The high transition dipole of NITV might suggest that a non-FREA will have stronger ICT character compared to a FREA, like NIDT. Even though NIBT and NIDT are both considered as FREA, one can assume that the transition dipole moments will be similar; however, there is not enough information to support that assumption. Especially, since NIDT and NIBT have different  $\pi$ -conjugated lengths due to the additional benzothiadiazole  $\pi$  bridges in NIBT; therefore, there is a chance that the transition dipole moment will be affected by the  $\pi$  bridges of NIBT (see below electronic structure calculations).

#### *IV.5.c Time resolved Fluorescence Upconversion (UpC) Results of BNIAs*

Time-resolved fluorescence upconversion (UpC) experiments are conducted on the BNIAs to determine the fluorescence lifetime ( $\tau_{\text{fluor}}$ ). **Figure IV.4** shows the kinetics traces of the BNIAs

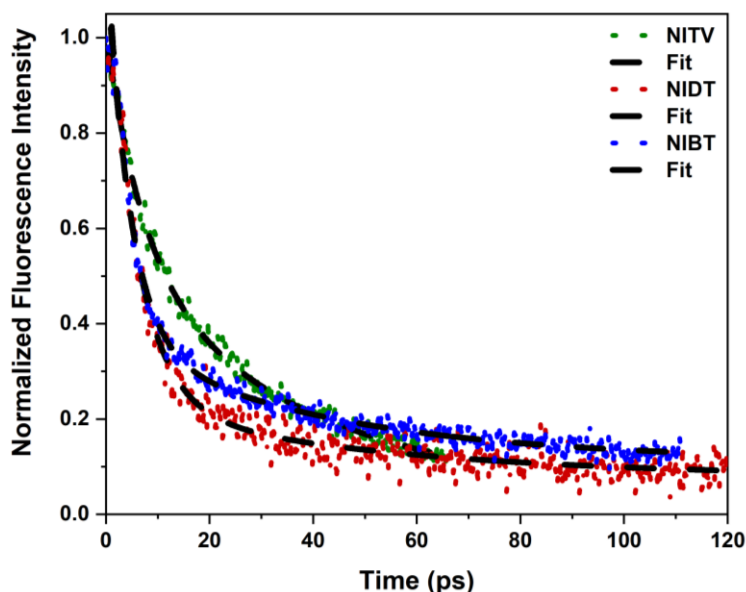


**Figure IV.21:** Kinetic traces of the BNIA in chloroform obtained from time-resolved fluorescence upconversion (UpC) experiments

obtained from UpC. **Figure D.4** in the Appendix D shows the full scale and zoomed-in scale of the kinetic traces. The kinetic traces of the BNIA are fitted to a multi-exponential function; an exponential growth is used to determine the rise time,  $\tau_{\text{rise}}$ , and then, a bi-exponential decay is used to determine the decay time components,  $\tau_1$  and  $\tau_2$  ( $\tau_{\text{fluor}}$ ). **Table IV.1** shows the  $\tau_{\text{fluor}}$  of the BNIA obtained from UpC. **Table D.2** in the Appendix D shows all the time components of the BNIA obtained by UpC. The  $\tau_{\text{fluor}}$  of the BNIA is based on the emission of 650nm; this emission is used for all the BNIA. The  $\tau_{\text{fluor}}$  of the BNIA are: 36ps for NITV; 50ps for NIDT; and; 41ps for NIBT. When considering the error of  $\tau_{\text{fluor}}$ , the  $\tau_{\text{fluor}}$  of the BNIA are comparable and there is not a huge significant difference in the  $\tau_{\text{fluor}}$  decay times.

#### *IV.5.d Femtosecond Transient Absorption (fs-TA) Results of BNIA*

**Figure IV.5** shows a representative time-resolved fs-TA spectrum of NIBT in chloroform using 600nm as the pump wavelength. The time-resolved fs-TA spectra of NITV and NIDT in chloroform using 600nm as the pump wavelength are shown in **Figure D.8** of the Appendix D.

There are four parameters to compare in these fs-TA results: 1) identification of negative (bleach) signals; 2) differences in vibronic progression present in fs-TA spectra; 3) identification and intensity of positive (ESA) signals present in spectra; and 4) kinetic traces, time components (decay and rise times), and rates. These observations will provide insight into how the  $\pi$ -conjugated length and fused or nonfused structures affect the exciton dynamics and intramolecular charge generation of the BNIAAs.

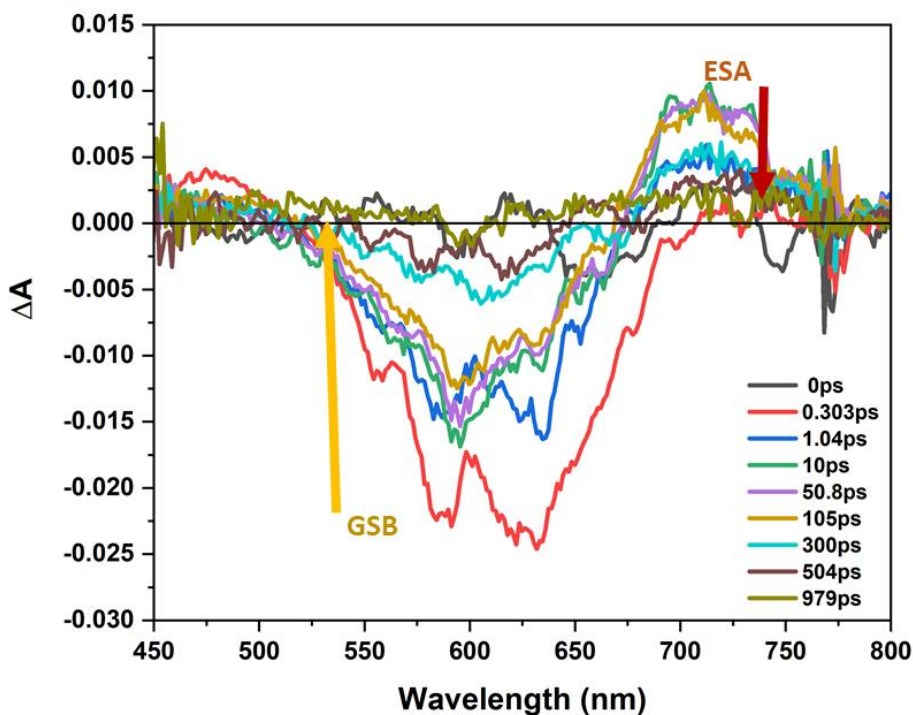


**Figure IV.22:** Time-resolved femtosecond transient absorption (fs-TA) spectra of NIBT in chloroform using 600nm pump. The recovery or decay of ground state bleach (GSB) signal is shown using golden/yellow arrow. The decay of excited state absorption (ESA) signal is shown using red arrows.

For all BNIAAs, the time resolved fs-TA spectra (**Figures IV.5** and **D.8** in Appendix D) have negative signals that are identified as ground state bleach (GSB) signals since these signals closely match the steady-state absorption spectra (see **Figure IV.2.a**). The GSB signal provides insight into the dynamics of the  $S_1$ . For all fs-TA spectra of BNIAAs, there are no negative signals that match the steady-state emission spectra (see **Figure IV.2.b**). Due to the lack of negative

signals that match the emission spectra of the BNIAAs, this observation indicates that there are no stimulated emission (SE) signals. There is a difference in vibronic progression among the BNIAAs as a result of the differences in the  $\pi$ -conjugated length and fused and unfused structures. **Figure IV.6** shows the comparison of steady-state absorption spectrum to fs-TA GSB spectrum at an early time of the NITV. The comparison of steady-state absorption spectra to fs-TA GSB spectra at an early time for the other BNIAAs (NIDT and NIBT) are shown in Appendix D in **Figure D.9**. The vibronic progression present in the GSB signals of NITV and NIBT are different from the vibronic features present in the steady-state absorption spectra (see **Figures IV.2.a, IV.6, and D.9.c** in Appendix D) For NITV, when comparing the GSB spectrum at an early time to steady-state absorption spectrum, the GSB spectrum shows a distinguished vibronic progression that is not present in the steady-state absorption spectrum. For NIBT, there is some vibronic progression present in the early time GSB spectrum compared to its steady-state absorption spectrum; however, it is not as intense as the case for NITV (See **Figure D.9.c** in Appendix D). For NIDT, the GSB spectrum at an early time and its steady-state absorption spectrum are very similar (See **Figure D.9.a** in Appendix D). For the case of the two fused BNIAAs the vibronic progression was observed and for the nonfused BNIA the vibronic progression was not observed.

For all BNIAAs, the time resolved fs-TA spectra (see **Figures IV.6 and D.8** in Appendix D) have ESA signals that are due to transiently excited states in the time-resolution of the TA experiment. The ESA for the case of NIBT (see **Figure IV.5**) the ESA is found at 710 nm. For the case of NITV the ESA is found at 630 nm. Finally, for the case of NIDT the ESA is found at 640 nm. The kinetic traces obtained from fs-TA experiments conducted on the BNIAAs show how the  $\pi$ -conjugated lengths affect the time components (decay and rise times) and rates. **Figure IV.7** shows the kinetic traces of the GSB signals at 600nm obtained from fs-TA results for the three

BNIAs. **Tables IV.2** shows the time components, rates and amplitudes of GSB signals at 600nm. **Tables D.5** and **D.6** in Appendix D shows the time components, rates and amplitudes of GSB signals at various wavelengths. The GSB signal kinetic traces of the BNIAs are fitted a bi- or tri-exponential decay. The longest decay time components of the GSB signals range from 43.5ps – 273ps. As shown in Table S.5 the  $\tau_1$  component is on the order of 100s of fs. For the case of  $\tau_2$  it was found to be on the order of a few ps. The kinetic traces of the ESA signals observed in the fs-

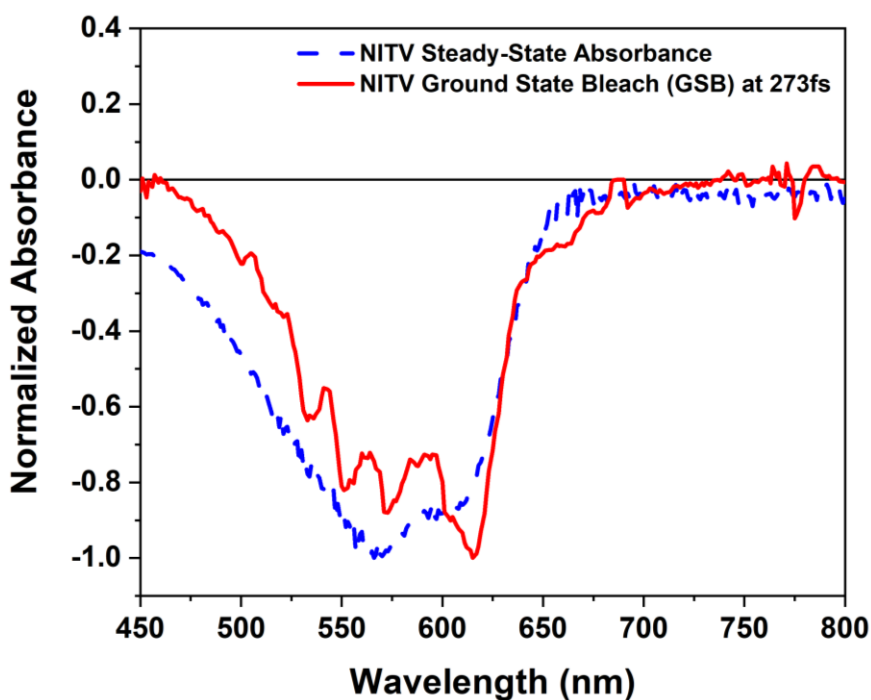


**Figure IV.23:** Comparison of steady-state absorption spectrum to the early time of ground state bleach (GSB) spectrum from femtosecond transient absorption (fs-TA) results of NITV in chloroform using 600nm excitation.

TA spectra of the BNIAs using 600nm as pump are illustrated in **Figure IV.9**. **Figure D.11** in the Appendix D shows kinetic traces at a second wavelength within the ESA signals of the BNIAs. **Table IV.2** shows the  $\tau_{\text{rise}}$  and decay time ( $\tau_2$ ) components of kinetic traces of the ESA signals present in **Figure IV.8** obtained from time-resolved fs-TA spectra of BNIAs. **Tables D.7** and **D.8** in Appendix D shows all time components, amplitudes of and rates of wavelengths present in **Figures D.9** and **D.11** of the ESA signals. In the case of the ESA traces there is a rise time in all

three BNIA on the order of a few ps. The decay component of the ESA traces was found to be on the order of 10s to 100s of ps.

**Table D.6** in Appendix D shows kinetic traces at an additional wavelength (560nm for NITV; 554nm for NIDT, and 629nm for NIBT) within the GSB signals of the BNIA. For these additional wavelengths, the kinetic traces show two decay time components. The  $\tau_1$  of these additional wavelengths is similar to  $\tau_1$  of 600nm. Then, the  $\tau_2$  of these additional wavelengths is

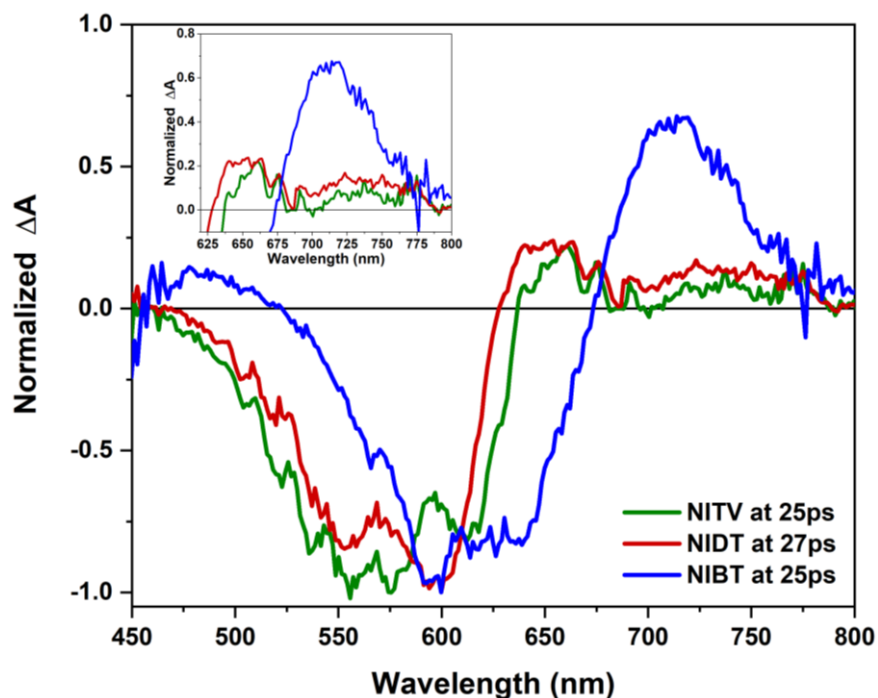


**Figure IV.24:** Comparison of excited state absorption (ESA) signals of BNIA at a specific time. The time-resolved femtosecond transient absorption (fs-TA) spectra is normalized to the highest value in ground state bleach (GSB) at a specific time. **Figure D.10** in Appendix D shows the un-normalized spectra.

similar to  $\tau_2$  of 600nm. The difference in the number of time components shown in the kinetic traces of the GSB signals indicates that certain energy or vibrational levels within the  $S_1$  will undergo different relaxation processes. Regardless, for all kinetic traces of the GSB signals, there is a direct correlation between  $\pi$ -conjugated lengths and the long decay component. As shown in **Figure IV.8** and **Table IV.2** (see **Table D.5** and **D.6** in Appendix d as well), NIBT, the longest  $\pi$ -

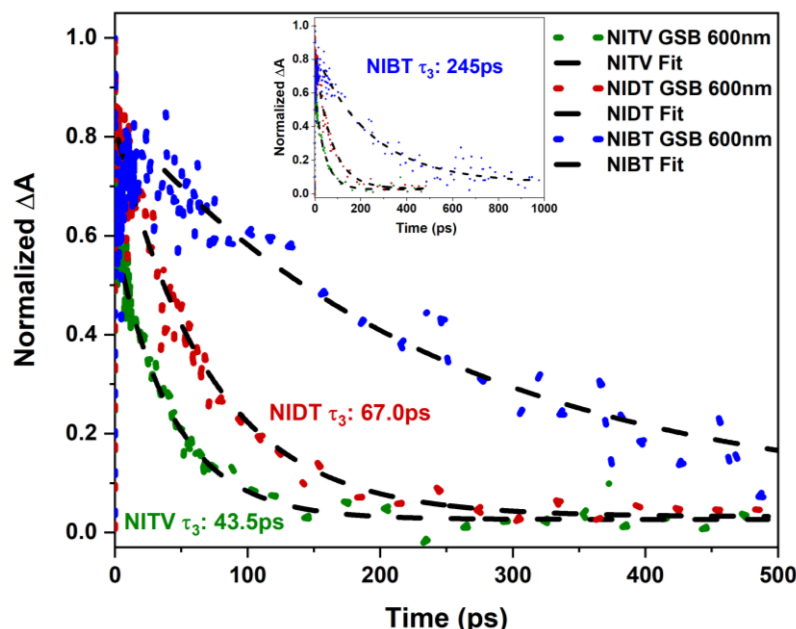


**Figure IV.25:** Kinetics of ground state bleach (GSB) signals and reported decays ( $\tau_3$ ) from femtosecond transient absorption (fs-TA) of BNIA in chloroform using 600nm excitation. **Inserted Graph:** shows full scale of kinetics of GSB signals and GSB decay ( $\tau_3$ ) of NIBT.

conjugated length BNIA, has the longest decay time compared to NITV and NIDT. Then, NITV, the shortest  $\pi$ -conjugated length BNIA, has the shortest longest  $\tau_{\text{exc}}$  compared to the other BNIA. Specifically, the longest decay of NIBT is approximately **4x** slower than NIDT and **6x** than NITV decay time component of NIDT.

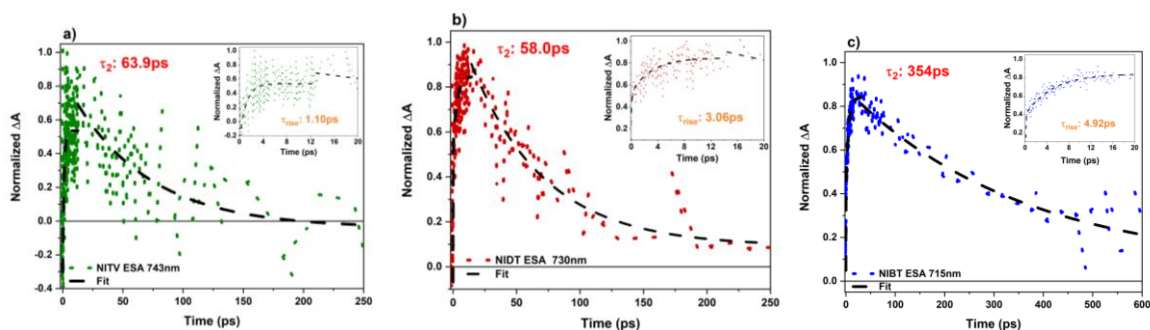


**Figure IV.26:** Kinetics of excited state absorption (ESA) signals from femtosecond transient absorption (fs-TA) of BNIA in chloroform using 600nm – **a)** NITV; **b)** NIDT and **c)** NIBT. **Inserted Graph:** zoomed in scale of kinetics of ESA signals, showing the rise time,  $\tau_{\text{rise}}$ , of ESA signals.



**Table IV.2:** Summary of time components in picosecond (ps) of ground state bleach (GSB) and excited state absorption (ESA) signals from femtosecond transient absorption (fs-TA) results of BNIA in chloroform. See **Tables D.5 – D.8** in Appendix D for complete summary of time components (rise and decay times), amplitudes, and rates

BNIA	fs-TA peak	Time Component 2 (ps)	Time Component 3 (ps)	Rates (s <sup>-1</sup> )
NITV	GSB 600nm	$\tau_2: 1.24 \pm 0.444$	$\tau_{EXC}: 43.5 \pm 1.48$	$k_{EXC}: 2.30E+10$
	ESA 743nm	$\tau_{rise}: 1.10 \pm 0.24$	$\tau_{CR}: 63.9 \pm 13.6$	$k_{CT}: 9.09E+11$
NIDT	GSB 600nm	$\tau_2: 6.36 \pm 4.88$	$\tau_{EXC}: 67.0 \pm 2.69$	$k_{EXC}: 1.49E+10$
	ESA 730nm	$\tau_{rise}: 3.06 \pm 0.86$	$\tau_{CR}: 58.0 \pm 5.09$	$k_{CT}: 3.27E+11$
NIBT	GSB 600nm	$\tau_2: 4.80 \pm 1.16$	$\tau_{EXC}: 245 \pm 19$	$k_{EXC}: 4.08E+09$
	ESA 715nm	$\tau_{rise}: 4.92 \pm 0.38$	$\tau_{CR}: 354 \pm 42$	$k_{CT}: 2.03E+11$

#### IV.5.e Theoretical Calculations of BNIA

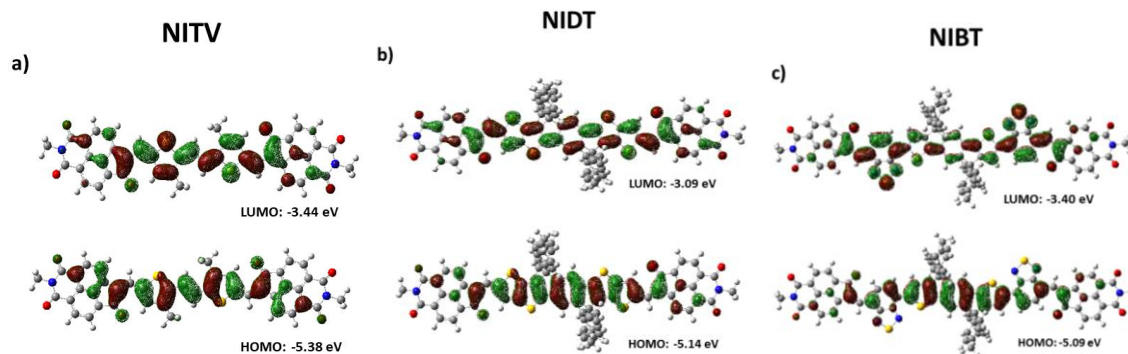


**Figure IV.10:** Calculated excited state and HOMO/LUMO of BNIA from time-dependent density functional theory (TD-DFT) using B3LYP/6-31G(d,p): a) NITV; b) NIDT ;and c) NIBT

Density functional theory (DFT) and time-dependent density functional theory (TD-DFT) calculations are performed on the BNIA to provide insight into the exciton delocalization, oscillator strengths and reorganization energies of these small molecules. **Figure IV.10** shows the

frontier molecular orbitals of the HOMO and LUMO of the BNIAAs. The frontier molecular orbitals of LUMO+1 – LUMO+3 of the BNIAAs are shown in **Figure D.14** of the Appendix D. The HOMO and LUMO (see **Figure IV.10**) shows the delocalization of the electron density on the structure of these small molecules. Studies have shown molecular orbitals obtained from DFT and TD-DFT calculations provide insight into exciton delocalization occurring in molecules by observing the electron density on molecular orbitals. The HOMOs and LUMOs of the BNIAAs corresponds to the  $S_0 \rightarrow S_1$  transition. The HOMOs and LUMOs of the BNIAAs show the exciton delocalization is affected by the  $\pi$ -conjugation lengths of these small molecules. For NITV, the electron density of the HOMO and LUMO is delocalized across the entire molecule – across the donor moiety, TVT, and acceptor moieties, naphthalene imides. As for NIDT, the electron density of the HOMO and LUMO is delocalized on the donor moiety, IDTT, and partially on the acceptor moieties, naphthalene imides. As for NIBT, the electron density of the HOMO is mainly localized on the main donor moiety, IDTT. As for the LUMO, the electron density is more delocalized on the benzothiadiazole  $\pi$ -bridges and IDTT versus the naphthalene imides. The electron density on the LUMO of NIBT shows the benzothiadiazole  $\pi$ -bridge is preventing the electron density to be delocalized on the naphthalene imides moieties within the structure of these small molecule. As a result, NIBT has different exciton delocalization compared to NITV and NIDT due to the benzothiadiazole  $\pi$ -bridge between the donor and acceptor moieties of this small molecule. For NITV and NIDT, the HOMOs and LUMOs of these small molecules shows the exciton delocalization occurring across both donor and acceptor moieties within their structure. As for NIBT, the HOMO and LUMO is showing the exciton delocalization occurs mainly on its donor moiety, IDTBT, which contains IDTT core with benzothiadiazole  $\pi$ -bridges. The HOMOs and LUMOs of the BNIAAs show the NITV and NIDT have more exciton delocalization compared to

NIBT since the electron density spreads over both the donor and acceptor moieties of these small molecules. The difference in exciton delocalization between the BNIAs is due to variation of  $\pi$ -conjugation lengths within these small molecules. The exciton delocalization of the BNIAs could affect the intramolecular charge generation occurring within these small molecules.

The calculated oscillator strengths of the BNIAs show the most probable electronic transition is  $S_0 \rightarrow S_1$ , which supports the steady-state absorption results. The calculated oscillator strengths of the BNIAs are shown in **Table D.10** in the Appendix D. Studies have shown the calculated oscillator strengths of molecules show which transition will most likely to occur. For the BNIAs, their calculated oscillator strengths show NITV and NIDT have similar strengths but are different from NIBT. The calculated oscillator strengths of NITV and NIDT are 3.17 and 3.36. The calculated oscillator strength of NIBT is 2.90. The calculated oscillator strengths correspond to the  $S_0 \rightarrow S_1$  observed in the steady-state absorption spectra of the BNIAs (see **Figure IV.2.a** and **Table IV.1**). As mentioned in the steady-state section (see Section III.1), the  $S_0 \rightarrow S_1$  corresponds to the ICT character of the BNIAs. The calculated oscillator strengths of the BNIAs supports the most probable electronic transition occurring is  $S_0 \rightarrow S_1$  that corresponds to the ICT character of the BNIAs. As seen in the  $\lambda_{\max}^{\text{abs}}$  of BNIAs, the difference in oscillator strength is due to the variation in  $\pi$ -conjugated lengths of the BNIAs. NIBT has a lower oscillator strength compared to NITV and NIDT due to its small energy gap as a result of the long  $\pi$ -conjugated length. The calculated oscillator strengths of the BNIAs supports the most probable electronic transition is  $S_0 \rightarrow S_1$ , which corresponds to the ICT character of these small molecules.

The calculated reorganizational energy ( $\lambda$ ) of BNIAs show the  $\lambda$  is different between the BNIAs due to the variation in the  $\pi$ -conjugated length of these small molecules. Studies have defined the calculated  $\lambda$  as the energy associated with geometry changes when going from a neutral

to a charged-state geometry. **Table IV.3** shows the calculated  $\lambda$  of the BNIA. The correlation between the  $\pi$ -conjugated lengths and calculated  $\lambda$  of the BNIA is as the  $\pi$ -conjugated lengths increases, the calculated  $\lambda$  decreases. NITV, the shortest  $\pi$ -conjugated length of the BNIA has a calculated  $\lambda$  of 360meV. The value of the NITD is 223 meV. Then, the calculated  $\lambda$  of NIBT, the longest  $\pi$ -conjugated length of the BNIA is 188meV. The calculated  $\lambda$  value of 360meV for NITV is 1.6x larger the value of NITD and 1.9x larger the value of NIBT.

## IV.6 Discussion

From the steady-state, time-resolved and electronic structure results described above there are interesting differences between the three BNIA systems. As mentioned previously, while the measurements with the solar devices indicated that the NIBT system had the largest PCE it important to understand the mechanism for this effect in comparison to the other BNIA systems studied. Differences in the absorption max, stokes shift, fluorescence lifetime, intensities of the vibronic progression observed, ground state bleach decay times, excited state absorption decay times, and energies of the excited state absorption peaks suggest that there are differences in the photophysical processes in the three systems. Many of these results point to the NIBT system having a substantially different charge transfer character and lifetime which may promote better charge separation for efficient solar to electron capture. A strong correlation between the  $\pi$ -conjugated length and absorption and emission maxima peaks. In this case, the NIBT system had the smallest energy gap. The vibronic character of the spectra suggested strong coupling in these systems with the NITD having the most intense vibronic progression and presents the most rigid and planar structure. However, the NIBT system had the largest stokes shift which may be a prelude to its very strong ICT character.

The major differences between the BNIAAs was observed from the fsTA measurements. Here it was found that for the ESA signals there was a correlation the charge transfer rate. NIBT, the longest  $\pi$ -conjugated length BNIA, had the lowest rate compared to NITV and NIDT. The  $k_{CT}$  of NIBT was almost half that obtained for NITV and NIDT. The differences in  $k_{CT}$  between the BNIAAs provides insights in to the effect of  $\pi$ -conjugated lengths and fused and non-fused structures on the intramolecular charge generation of these small molecules. The differences in the dynamics of these systems can be analyzed further by considering the connection of the reorganizational energy and the charge transfer kinetics and energetics. Despite NIDT and NIBT

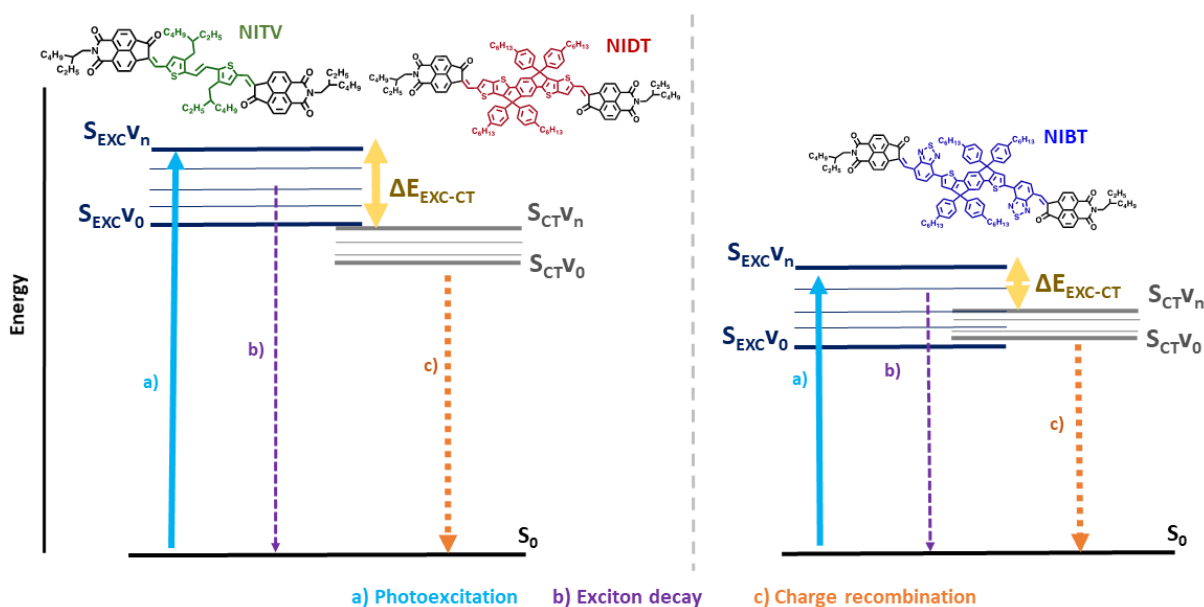


**Figure IV.27:** Proposed mechanism of the intramolecular charge generation mechanism of the BNIAAs.

both being FREAs, these molecules have different kinetics. Interestingly, NITV and NIDT – a non-FREA and FREA – have similar kinetics. The fs-TA results show that not only is there a difference in kinetics between non-FREA and FREA BNIAAs; there is a difference between FREA BNIAAs – NIDT and NIBT – as well. The un-normalized time-resolved fs-TA of BNIAAs are shown in Figure S.10 of the Supporting Information. A similar approach has been done in Liu to calculate

the populations of polaron between neat polymer and blend films using fs-TA.<sup>51</sup> Typically, lower  $\lambda$  values are desired for higher charge transport properties in  $\pi$ -conjugated molecules.<sup>48,49</sup> The improved molecular planarity and rigidity of the FREAs (NIBT and NIDT) likely contributes to the enhanced photoinduced charge carrier generation rate and reduced bimolecular recombination that were previously observed for NIDT and NIBT compared to NITV.<sup>31</sup> From the spectroscopic data obtained one can determine the reorganization energies for the BNIA. Shown in Table xxx are the energies of steady-state peaks, fs-TA signals, and the energy difference between peaks and signals. The steady-state absorption and GSB signals from fs-TA results provide the energy of the exciton state,  $S_{EXC}$ . Then, the ESA signal from the fs-TA provide the energy of the  $S_{CT}$ . In order to determine the proximity of these excited states to each other, the energy gap or the difference in energy between these states are calculated. Starting with the  $S_{EXC}$ , Stokes shift or the energy gap between the absorption and emission maximum peaks is calculated, see **Table IV.3**. This energy gap shows the energy range of the  $S_{EXC}$ . Then, to determine the energy gap between  $S_{EXC}$  and  $S_{CT}$ ,  $\lambda_{EXC-CT}$ , the following equation is used:

**Equation IV.1** 
$$E_{EXC} - E_{CT} = \lambda_{EXC-CT}$$

where,  $\lambda_{EXC-CT}$  is the difference in energy or the energy gap between the  $S_{EXC}$  and  $S_{CT}$ ;  $E_{EXC}$  is the energy of the  $S_{EXC}$  obtained from the state steady-state absorption and GSB signal from fs-TA results; and  $E_{CT}$  is the energy of the  $S_{CT}$  obtained from ESA signals from the fs-TA results. **Table IV.3** shows the determined  $\Delta E_{EXC-CT}$  and **Table D.7** in the Appendix D for the energy values used to calculate the  $\lambda_{EXC-CT}$  and other energy gaps. The trend observed in the  $\Delta E_{EXC-CT}$  is as the conjugation length increases, the  $\lambda_{EXC-CT}$  decreases. This trend is supported by the calculated

reorganization energies,  $\lambda$ , obtained from theoretical calculations as well. A similar trend is captured in the electronic structure calculations as in our time-resolved and steady state experiments. Typically, lower  $\lambda$  values are desired for higher charge transport properties in  $\pi$ -conjugated molecules.<sup>48,49</sup> The improved molecular planarity and rigidity of the FREAs (NIBT and NIDT) likely contributes to the enhanced photoinduced charge carrier generation rate and reduced bimolecular recombination that were previously observed for NIDT and NIBT compared to NITV.<sup>31</sup>

Interestingly, the  $\lambda_{\text{EXC-CT}}$  of NITV and NIDT are very similar. The  $\lambda_{\text{EXC-CT}}$  of NIDT is 3meV larger compare the NITV. Despite the difference in structure between NITV and NIDT (non-FREA versus FREA), these two small molecules have similar  $\lambda_{\text{EXC-CT}}$ . When comparing the  $\lambda_{\text{EXC-CT}}$  of NIBT to NITV and NIDT, there is roughly 100meV difference; thus the  $\lambda_{\text{EXC-CT}}$  of NIBT is **31% smaller** compared to the  $\lambda_{\text{EXC-CT}}$  of the other BNIA. The difference in  $\lambda_{\text{EXC-CT}}$  among the BNIA is not due to the donor unit being non fused-ring versus fused-ring; however, the fact that NIBT has benzothiadiazole  $\pi$ -bridges between its donor and acceptor units.

**Table IV.3:** Summary of the Stokes Shift, and reorganization energy of  $\lambda_{\text{EXC-CT}}$ ,  $\lambda_{\text{EMS-CT}}$  and calculated ( $\lambda$ ) of BNIA

$\lambda_{\text{EXC-CT}}$ : energy difference between exciton ( $S_{\text{EXC}}$ ) and charge transfer states  $S_{\text{CT}}$

$\lambda_{\text{EMS-CT}}$ : energy difference between steady-state emission maximum ( $\lambda_{\text{max}}^{\text{ems}}$ ) and  $S_{\text{CT}}$

BNIA	Stoke Shift (meV)	$\lambda_{\text{EMS-CT}}$ (meV)	$\lambda_{\text{EXC-CT}}$ (meV)	Theoretical $\lambda$ (meV)
NITV	262	55	318	360
NIDT	246	75	321	223
NIBT	292	-71	220	188

Studies have shown that the calculated  $\lambda$  provides insight into structural distortions that occurs during the charge transfer of a charge generation mechanism. When a molecule consisting of donor and acceptor moieties in their structure has a low calculated  $\lambda$ , this indicates the molecule will have reduced structural distortions and more effective charge transfer. Since NIBT has the lowest calculated  $\lambda$  between the BNIAAs, this suggests that this small molecule will have a more effective charge transfer compared to NITV and NIDT due to minimal structural distortion during the charge transfer.

#### **IV.7 Conclusion**

The results discussed in this paper provides insight to finding a correlation between the structure of small molecule NFAs and PCE of OPVs. NIBT is a FREA small molecule NFA that has benzothiadiazole  $\pi$ -bridges between its main donor unit, IDTT and acceptor units, naphthalene imides. As a result of the  $\pi$  bridges, NIBT has an efficient intramolecular charge generation and exciton dynamics compared to NITV and NIDT. NIBT has a small  $\lambda_{\text{EXC-CT}}$  which increases the probability of having efficient charge generation. Due to the benzothiadiazole  $\pi$ -bridges, NIBT has a strong CT; thus, slower charge recombination compared to NITV and NIDT. From the results discussed in this paper, the results show a FREA (NIDT and NIBT) small molecule can have strong charge transfer and more efficient charge generation compared to a non-FREA (NITV). However, it is not just simply a small molecule NFA being a FREA or non-FREA. The structure of a FREA small molecule needs to have an additional  $\pi$  bridge – such as benzothiadiazole  $\pi$ -bridge – between donor unit and acceptor unit in order to have efficient intramolecular charge generation and exciton dynamics within the small molecule NFA. More research needs to be conducted to support this correlation between small molecule FREA with an additional unit within its structure and PCE of OPV. This correlation could provide insight to understanding the structure-function relationship of small molecule NFAs and PCE of OPVs.



## IV.8 References

- (1) Armin, A.; Li, W.; Sandberg, O. J.; Xiao, Z.; Ding, L.; Nelson, J.; Neher, D.; Vandewal, K.; Shoaee, S.; Wang, T.; Ade, H.; Heumüller, T.; Brabec, C.; Meredith, P. A History and Perspective of Non-Fullerene Electron Acceptors for Organic Solar Cells. *Adv. Energy Mater.* **2021**, *11* (15), 2003570. <https://doi.org/10.1002/aenm.202003570>.
- (2) Hedley, G. J.; Ruseckas, A.; Samuel, I. D. W. Light Harvesting for Organic Photovoltaics. *Chem. Rev.* **2017**, *117* (2), 796–837. <https://doi.org/10.1021/acs.chemrev.6b00215>.
- (3) Sharma, T.; Mahajan, P.; Adil Afroz, M.; Singh, A.; Yukta; Kumar Tailor, N.; Purohit, S.; Verma, S.; Padha, B.; Gupta, V.; Arya, S.; Satapathi, S. Recent Progress in Advanced Organic Photovoltaics: Emerging Techniques and Materials. *ChemSusChem* **2022**, *15* (5). <https://doi.org/10.1002/cssc.202101067>.
- (4) Inganäs, O. Organic Photovoltaics over Three Decades. *Adv. Mater.* **2018**, *30* (35), 1800388. <https://doi.org/10.1002/adma.201800388>.
- (5) Chong, K.; Xu, X.; Meng, H.; Xue, J.; Yu, L.; Ma, W.; Peng, Q. Realizing 19.05% Efficiency Polymer Solar Cells by Progressively Improving Charge Extraction and Suppressing Charge Recombination. *Adv. Mater.* **2022**, *34* (13), 2109516. <https://doi.org/10.1002/adma.202109516>.
- (6) Karki, A.; Gillett, A. J.; Friend, R. H.; Nguyen, T. The Path to 20% Power Conversion Efficiencies in Nonfullerene Acceptor Organic Solar Cells. *Adv. Energy Mater.* **2021**, *11* (15), 2003441. <https://doi.org/10.1002/aenm.202003441>.
- (7) Wadsworth, A.; Moser, M.; Marks, A.; Little, M. S.; Gasparini, N.; Brabec, C. J.; Baran, D.; McCulloch, I. Critical Review of the Molecular Design Progress in Non-Fullerene Electron Acceptors towards Commercially Viable Organic Solar Cells. *Chem. Soc. Rev.* **2019**, *48* (6), 1596–1625. <https://doi.org/10.1039/C7CS00892A>.
- (8) Tamai, Y. What's Next for Organic Solar Cells? The Frontiers and Challenges. *Adv. Energy Sustain. Res.* **2023**, *4* (1), 2200149. <https://doi.org/10.1002/aesr.202200149>.
- (9) Wang, Y.; Lee, J.; Hou, X.; Labanti, C.; Yan, J.; Mazzolini, E.; Parhar, A.; Nelson, J.; Kim, J.; Li, Z. Recent Progress and Challenges toward Highly Stable Nonfullerene Acceptor-Based Organic Solar Cells. *Adv. Energy Mater.* **2021**, *11* (5), 2003002. <https://doi.org/10.1002/aenm.202003002>.
- (10) Lu, L.; Zheng, T.; Wu, Q.; Schneider, A. M.; Zhao, D.; Yu, L. Recent Advances in Bulk Heterojunction Polymer Solar Cells. *Chem. Rev.* **2015**, *115* (23), 12666–12731. <https://doi.org/10.1021/acs.chemrev.5b00098>.
- (11) Wang, J.; Zhan, X. Fused-Ring Electron Acceptors for Photovoltaics and Beyond. *Acc. Chem. Res.* **2021**, *54* (1), 132–143. <https://doi.org/10.1021/acs.accounts.0c00575>.
- (12) Liang, Y.; Xu, Z.; Xia, J.; Tsai, S.-T.; Wu, Y.; Li, G.; Ray, C.; Yu, L. For the Bright Future-Bulk Heterojunction Polymer Solar Cells with Power Conversion Efficiency of 7.4%. *Adv. Mater.* **2010**, *22* (20), E135–E138. <https://doi.org/10.1002/adma.200903528>.
- (13) Li, H.; Earmme, T.; Ren, G.; Saeki, A.; Yoshikawa, S.; Murari, N. M.; Subramaniyan, S.; Crane, M. J.; Seki, S.; Jenekhe, S. A. Beyond Fullerenes: Design of Nonfullerene Acceptors for Efficient Organic Photovoltaics. *J. Am. Chem. Soc.* **2014**, *136* (41), 14589–14597. <https://doi.org/10.1021/ja508472j>.
- (14) Hwang, Y.-J.; Li, H.; Courtright, B. A. E.; Subramaniyan, S.; Jenekhe, S. A. Nonfullerene Polymer Solar Cells with 8.5% Efficiency Enabled by a New Highly Twisted Electron

- Acceptor Dimer. *Adv. Mater.* **2016**, *28* (1), 124–131. <https://doi.org/10.1002/adma.201503801>.
- (15) Lin, Y.; Wang, J.; Zhang, Z.-G.; Bai, H.; Li, Y.; Zhu, D.; Zhan, X. An Electron Acceptor Challenging Fullerenes for Efficient Polymer Solar Cells. *Adv. Mater.* **2015**, *27* (7), 1170–1174. <https://doi.org/10.1002/adma.201404317>.
- (16) Heeger, A. J. 25th Anniversary Article: Bulk Heterojunction Solar Cells: Understanding the Mechanism of Operation. *Adv. Mater.* **2014**, *26* (1), 10–28. <https://doi.org/10.1002/adma.201304373>.
- (17) Meredith, P.; Li, W.; Armin, A. Nonfullerene Acceptors: A Renaissance in Organic Photovoltaics? *Adv. Energy Mater.* **2020**, *10* (33), 2001788. <https://doi.org/10.1002/aenm.202001788>.
- (18) Zhang, M.; Zhu, L.; Zhou, G.; Hao, T.; Qiu, C.; Zhao, Z.; Hu, Q.; Larson, B. W.; Zhu, H.; Ma, Z.; Tang, Z.; Feng, W.; Zhang, Y.; Russell, T. P.; Liu, F. Single-Layered Organic Photovoltaics with Double Cascading Charge Transport Pathways: 18% Efficiencies. *Nat. Commun.* **2021**, *12* (1), 309. <https://doi.org/10.1038/s41467-020-20580-8>.
- (19) Li, S.; Zhan, L.; Jin, Y.; Zhou, G.; Lau, T.; Qin, R.; Shi, M.; Li, C.; Zhu, H.; Lu, X.; Zhang, F.; Chen, H. Asymmetric Electron Acceptors for High-Efficiency and Low-Energy-Loss Organic Photovoltaics. *Adv. Mater.* **2020**, *32* (24), 2001160. <https://doi.org/10.1002/adma.202001160>.
- (20) Yan, C.; Barlow, S.; Wang, Z.; Yan, H.; Jen, A. K.-Y.; Marder, S. R.; Zhan, X. Non-Fullerene Acceptors for Organic Solar Cells. *Nat. Rev. Mater.* **2018**, *3* (3), 18003. <https://doi.org/10.1038/natrevmats.2018.3>.
- (21) Hou, J.; Inganäs, O.; Friend, R. H.; Gao, F. Organic Solar Cells Based on Non-Fullerene Acceptors. *Nat. Mater.* **2018**, *17* (2), 119–128. <https://doi.org/10.1038/nmat5063>.
- (22) He, Q.; Kafourou, P.; Hu, X.; Heaney, M. Development of Non-Fullerene Electron Acceptors for Efficient Organic Photovoltaics. *SN Appl. Sci.* **2022**, *4* (9), 247. <https://doi.org/10.1007/s42452-022-05128-3>.
- (23) Kolhe, N. B.; West, S. M.; Tran, D. K.; Ding, X.; Kuzuhara, D.; Yoshimoto, N.; Koganezawa, T.; Jenekhe, S. A. Designing High Performance Nonfullerene Electron Acceptors with Rylene Imides for Efficient Organic Photovoltaics. *Chem. Mater.* **2020**, *32* (1), 195–204. <https://doi.org/10.1021/acs.chemmater.9b03329>.
- (24) Fisher, L.; Vázquez, R. J.; Howell, M.; Muthike, A. K.; Orr, M. E.; Jiang, H.; Dodgen, B.; Lee, D. R.; Lee, J. Y.; Zimmerman, P.; Goodson, T. Investigation of Thermally Activated Delayed Fluorescence in Donor–Acceptor Organic Emitters with Time-Resolved Absorption Spectroscopy. *Chem. Mater.* **2022**, *34* (5), 2161–2175. <https://doi.org/10.1021/acs.chemmater.1c03668>.
- (25) Muthike, A. K.; Carlotti, B.; Madu, I. K.; Jiang, H.; Kim, H.; Wu, Q.; Yu, L.; Zimmerman, P. M.; Goodson, T. The Role of the Core Attachment Positioning in Triggering Intramolecular Singlet Exciton Fission in Perylene Diimide Tetramers. *J. Phys. Chem. B* **2021**, *125* (19), 5114–5131. <https://doi.org/10.1021/acs.jpcc.1c02534>.
- (26) Madu, I. K.; Jiang, H.; Laventure, A.; Zimmerman, P. M.; Welch, G. C.; Goodson, T. Impact of Ring-Fusion on the Excited State Decay Pathways of N-Annulated Perylene Diimides. *J. Phys. Chem. C* **2021**, *125* (19), 10500–10515. <https://doi.org/10.1021/acs.jpcc.1c01964>.
- (27) Carlotti, B.; Cai, Z.; Kim, H.; Sharapov, V.; Madu, I. K.; Zhao, D.; Chen, W.; Zimmerman, P. M.; Yu, L.; Goodson, T. Charge Transfer and Aggregation Effects on the Performance of

- Planar vs Twisted Nonfullerene Acceptor Isomers for Organic Solar Cells. *Chem. Mater.* **2018**, *30* (13), 4263–4276. <https://doi.org/10.1021/acs.chemmater.8b01047>.
- (28) Williams, A. T. R.; Winfield, S. A.; Miller, J. N. Relative Fluorescence Quantum Yields Using a Computer-Controlled Luminescence Spectrometer. *The Analyst* **1983**, *108* (1290), 1067. <https://doi.org/10.1039/an9830801067>.
- (29) Melnikov, A. S.; Serdobintsev, P. Y.; Vedyaykin, A. D.; Khodorkovskii, M. A. Two-Photon Absorption Cross Section for Coumarins 102, 153 and 307. *J. Phys. Conf. Ser.* **2017**, *917*, 062029. <https://doi.org/10.1088/1742-6596/917/6/062029>.
- (30) Rurack, K.; Spieles, M. Fluorescence Quantum Yields of a Series of Red and Near-Infrared Dyes Emitting at 600–1000 Nm. *Anal. Chem.* **2011**, *83* (4), 1232–1242. <https://doi.org/10.1021/ac101329h>.
- (31) Berezin, M. Y.; Zhan, C.; Lee, H.; Joo, C.; Akers, W. J.; Yazdanfar, S.; Achilefu, S. Two-Photon Optical Properties of Near-Infrared Dyes at 1.55 Mm Excitation. *J. Phys. Chem. B* **2011**, *115* (39), 11530–11535. <https://doi.org/10.1021/jp207618e>.
- (32) Vázquez, R. J.; Kim, H.; Kobilka, B. M.; Hale, B. J.; Jeffries-EL, M.; Zimmerman, P.; Goodson, T. Evaluating the Effect of Heteroatoms on the Photophysical Properties of Donor–Acceptor Conjugated Polymers Based on 2,6-Di(Thiophen-2-Yl)Benzo[1,2-b:4,5-B']Difuran: Two-Photon Cross-Section and Ultrafast Time-Resolved Spectroscopy. *J. Phys. Chem. C* **2017**, *121* (27), 14382–14392. <https://doi.org/10.1021/acs.jpcc.7b01767>.
- (33) Ricci, F.; Mandal, H.; Wajahath, M.; Burdick, R. K.; Villabona-Monsalve, J. P.; Hussain, S.; Goodson, T. Investigations of Coherence in Perovskite Quantum Dots with Classical and Quantum Light. *J. Phys. Chem. C* **2023**, *127* (7), 3579–3593. <https://doi.org/10.1021/acs.jpcc.2c08455>.
- (34) Carlotti, B.; Madu, I. K.; Kim, H.; Cai, Zhengxu.; Jiang, H.; Muthike, A. K.; Yu, L.; Zimmerman, P. M.; Goodson, T. Activating Intramolecular Singlet Exciton Fission by Altering  $\pi$ -Bridge Flexibility in Perylene Diimide Trimers for Organic Solar Cells. *Chem. Sci.* **2020**, *11* (33), 8757–8770. <https://doi.org/10.1039/D0SC03271A>.
- (35) Chunosova, S. S.; Svetlichnyi, V. A.; Meshalkin, Y. P. Measurement of the Two-Photon Absorption Cross Sections of Dicyanomethylene-Pyrans by the  $z$ -Scan Method. *Quantum Electron.* **2005**, *35* (5), 415–418. <https://doi.org/10.1070/QE2005v035n05ABEH003405>.
- (36) Xu, C.; Webb, W. W. Measurement of Two-Photon Excitation Cross Sections of Molecular Fluorophores with Data from 690 to 1050 Nm. *J. Opt. Soc. Am. B* **1996**, *13* (3), 481. <https://doi.org/10.1364/JOSAB.13.000481>.
- (37) Eshun, A.; Cai, Z.; Awies, M.; Yu, L.; Goodson, T. Investigations of Thienoacene Molecules for Classical and Entangled Two-Photon Absorption. *J. Phys. Chem. A* **2018**, *122* (41), 8167–8182. <https://doi.org/10.1021/acs.jpca.8b06312>.
- (38) Adegoke, O. O.; Jung, I. H.; Orr, M.; Yu, L.; Goodson, T. Effect of Acceptor Strength on Optical and Electronic Properties in Conjugated Polymers for Solar Applications. *J. Am. Chem. Soc.* **2015**, *137* (17), 5759–5769. <https://doi.org/10.1021/ja513002h>.
- (39) Clark, T. B.; Orr, M. E.; Flynn, D. C.; Goodson, T. Synthesis and Optical Properties of Two-Photon Absorbing GFP-Type Probes. *J. Phys. Chem. C* **2011**, *115* (15), 7331–7338. <https://doi.org/10.1021/jp2005925>.
- (40) Flynn, D. C.; Ramakrishna, G.; Yang, H.-B.; Northrop, B. H.; Stang, P. J.; Goodson, T. Ultrafast Optical Excitations In Supramolecular Metallacycles with Charge Transfer Properties. *J. Am. Chem. Soc.* **2010**, *132* (4), 1348–1358. <https://doi.org/10.1021/ja9082655>.
- (41) Frisch, M. J., et al. (2016). Gaussian 16 Rev. C.01. Wallingford, CT.

## Chapter V

### Linear and Nonlinear Optical Properties of All-*cis* and All-*trans* Poly(*p*-phenylene vinylene)

#### V.1 Collaboration Statement

This Chapter describes the results and conclusion of a collaborative research investigation between between Professor Theodore G. Goodson III's group, Department of Chemistry and Macromolecular Science & Engineering, University of Michigan and Professor Quentin Michaudel's group, Department of Chemistry and Materials Science and Engineering, Texas A&M University. The authors of this research investigation (in ordered of first to corresponding) are: Dr. Haraprasad Mandal; Olusayo J. Ogunyemi; Jake L. Nicholson; **Meghan E. Orr**; Remy F. Lalisse; Ángel Rentería-Gómez; Achyut R. Gogoi; Osvaldo Gutierrez; Professor Quentin Michaudel; and Professor Theodore G. Goodson III. The first, second and fourth (*Collaborator 1*) authors are from Professor's Goodson group. The other authors are from Professor's Michaudel group (*Collaborator 2*). The contribution of first and second authors on this research investigation is: sample preparation for steady-state and quantum yield measurements, and for two-photon absorption (TPA) and entangled two-photon absorption (ETPA) experiments; conducting listed measurements and experiments; performing data analysis on listed measurements and experiments; and writing and editing paper for this research investigation. The contribution of *Collaborator 1* (**Meghan E. Orr**, author this dissertation) to this research investigation is: sample preparation for fluorescence upconversion and fs-TA experiments; conducting the previously

mentioned experiments; and performing data analysis on the previously mentioned experiments. The contribution of *Collaborator 2* to this research investigation is: synthesis of the samples; providing samples; performing density functional theory (DFT) and time-dependent DFT (TD-DFT) theoretical calculations; performing data analysis on theoretical calculations; and writing and editing the paper of this research investigation. This collaborative research investigation is published in the *Journal of Physical Chemistry C* – full citation: Mandal, H.; Ogunyemi, O. J.; Nicholson, J. L.; Orr, M. E.; Lalis, R. F.; Rentería-Gómez, Á.; Gogoi, A. R.; Gutierrez, O.; Michaudel, Q.; Goodson, T. Linear and Nonlinear Optical Properties of All- *Cis* and All- *Trans* Poly( *p* -Phenylenevinylene). *J. Phys. Chem. C* **2024**, *128* (6), 2518–2528. <https://doi.org/10.1021/acs.jpcc.3c07082>.<sup>72</sup>

## V.2 Abstract

Poly(*p*-phenylene vinylene)s (PPVs) are a staple of the family of conjugated polymers with desirable optoelectronic properties for applications including light-emitting diodes (LEDs) and photovoltaic devices. While the significant impact of olefin geometry on the steady state optical properties of PPVs has been extensively studied, PPVs with precise stereochemistry have yet to be investigated using nonlinear optical spectroscopy for quantum sensing, as well as light harvesting for biological applications. Herein, we report our investigation of the influence of olefin stereochemistry on both linear and nonlinear optical properties through the synthesis of all-*cis* and all-*trans* PPV copolymers. We performed two-photon absorption (TPA) using a classical and entangled light source and compared both classical TPA and entangled two-photon absorption (ETPA) cross-sections of these stereodefined PPVs. While the TPA cross section of the all-*trans* PPV was expectedly higher than that of all-*cis* PPV, presumably because of the larger transition dipole moment, the opposite trend was measured via ETPA with the all-*cis* PPV exhibiting the

highest ETPA cross section. DFT calculations suggest that this difference might stem from the interaction of entangled photons with lower lying electronic states in the all-*cis* PPV variant. Additionally, we explored the photo-induced processes for both *cis* and *trans* PPVs through time-resolved fluorescence up-conversion and femtosecond transient absorption techniques. This study revealed that the sensitivity of PPVs in two-photon absorption varies with classical versus quantum light and can be modulated through control of the geometry of the repeating alkenes, which is a key steppingstone toward their use in quantum sensing, bioimaging and the design of polymer-based light-harvesting systems.

### V.3 Introduction

Over the years, there has been increased interest in utilizing conjugated polymers with unique electroluminescence properties for applications in organic light-emitting diodes (OLEDs) in display technologies, organic semiconductors in photovoltaic cells for energy conversion and in energy storage devices, and as solid-state laser materials.<sup>1,2</sup> Among these, the properties of poly(*p*-phenylene vinylene) (PPV) and its derivatives have been extensively studied, which has paved the way for their use in optical devices and bulk-heterojunction solar cells.<sup>3-8</sup> PPVs consist of alternating *p*-phenylene and vinylene subunits with higher stability compared to polyacetylene and more flexibility compared to polyphenylene.<sup>2,4</sup> The parent unsubstituted PPV has a band gap of 2.5 eV with a broad spectrum in the visible region, both features that can be modulated through structural derivatization, which is crucial for implementation into photoluminescence devices.<sup>9</sup> The structure and conformation of conjugated polymers is known to determine the fluorescence lifetime, photoluminescence efficiency, as well as electron and charge mobilities in resulting devices. For example, the alkenes in the PPV backbone can exhibit either *cis* or *trans* configurations, which dictates the overall chain conformation. High *trans* content typically results

in rod-like structures that favor  $\pi$ - $\pi$  stacking and therefore aggregation, whereas high *cis* content leads to more coiled and twisted structures with reduced conjugation length.<sup>10-12</sup> Both  $\pi$ - $\pi$  stacking and conjugation length drastically affect the charge transport mobility of the polymer along with the composition of its backbone. It has been observed that polymers with linear backbones have higher charge transfer properties than polymers with flexible or wave-like backbone.<sup>13,14</sup> The modularity of synthetic methods<sup>1,2</sup> to modify the PPV scaffold via copolymerization or post polymerization functionalization have permitted the synthesis of numerous derivatives with improved conjugation length, solubility, and packing along the polymer backbone through the addition of non-conjugated carbon bridges or conjugated  $\pi$ -linkers. Efficient packing leads to improved optical, charge transport and sensing properties.<sup>15-19</sup> In addition to being pursued for applications discussed above (OLED, photovoltaics, etc.), PPV also exhibits biocompatibility, low toxicity, and high fluorescence quantum yields making them promising fluorophores for bioimaging applications.<sup>20</sup> For example, in a recent study by Tanja Junkers and co-workers, amphiphilic PPV copolymers were synthesized to form fluorescent micelles for drug delivery that were imaged using classical light and laser scanning confocal microscopy.<sup>21</sup>

The use of PPV materials in nonlinear optical (NLO) applications is especially intriguing, since NLO effects can be exploited for optical communication, frequency doubling and tripling, and photorefractive effect.<sup>22,23</sup> While several studies have allowed the identification of the structural parameters of organic materials responsible for NLO,<sup>24-26</sup> it remains crucial to design new organic chromophores to further understand and optimize NLO phenomena prior to their technological implementation. Of particular interest, some organic materials have been shown recently to exhibit NLO phenomena sensitive to the use of entangled photons.<sup>27-30</sup> The two

entangled photons generated by the process of spontaneous parametric down-conversion (SPDC) share a coupled eigenstate where the properties of each of the photons cannot be isolated

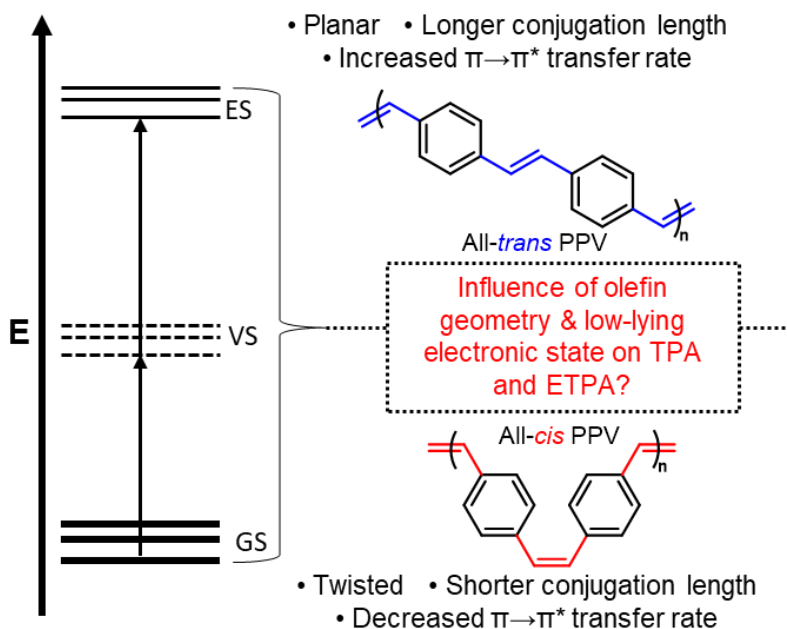


**Figure V.1:** Schematic energy diagram of a two-photon absorption process happens from ground state (GS) through virtual state (VS) to two-photon excited state (ES). The olefin geometry of all-trans PPV and all-cis PPV investigated here is also shown.

separately.<sup>31,32</sup> Unlike classical two-photon absorption (TPA), strong temporal and spatial correlations of the entangled photon pair lead to the simultaneous absorption of the two photons (**Figure V.1**), at the condition that the absorption occurs within a time window known as the entanglement time,  $T_e$ .<sup>29,33</sup> And, this phenomenon is known as entangled-two photon absorption (ETPA). Unlike classical TPA where the TPA has a quadratic on input photon flux, theoretical studies have shown that ETPA rate exhibits a linear dependence on the excitation flux<sup>28,30</sup>. This linear dependency is dominant only when the flux intensities are sufficiently low.<sup>34,35</sup> Entangled two-photon absorption therefore allows for improved resolution and sensitivity at lower excitation flux compared to classical TPA, which is promising for applications in quantum sensing, optical



communication, and bioimaging.<sup>32</sup> Because of their synthetic versatility, the PPV family offers a lot of opportunities to investigate the relationships between the precise molecular structure of organic materials and NLO behaviors with both classical and entangled light.

Accessing PPVs with >99% *cis* alkenes has been a longstanding synthetic challenge due to the thermodynamic bias for the *trans* vinylene phenylene motif,<sup>1,2</sup> which has limited nonlinear spectroscopy studies to PPVs with mostly *trans* alkenes or *cis/trans* mixtures. For example, Lavrentiev *et al.* theoretically investigated the low-lying electronic structure of PPV,<sup>36</sup> while Guo and Shih extensively studied the low-lying two-photon excited states in TPA spectroscopy with substituted and unsubstituted PPVs.<sup>37</sup> Ghosh *et al.* explored the exciton dynamics and formation mechanism of polymeric nanostructures based on poly(2-methoxy-5-(2'-ethylhexyloxy)-*p*-phenylene vinylene) (MEH-PPV) by using a femtosecond Ti:sapphire pulse laser as the light source.<sup>38</sup> In addition, De Boni *et al.* reported the degenerate non-linear absorption spectrum of MEH-PPV in chloroform using a femtosecond Z-scan technique.<sup>39</sup> The TPA cross-section spectrum of poly(2-methoxy-5-(2'2'-ethylhexyloxy)-1,4-phenylenevinylene) was also determined by Oliveria *et al.*<sup>40</sup> using a white-light continuum (WLC) Z-scan technique.

Herein, we discuss our investigation of the interaction of two diblock copolymers containing either an all-*cis* or an all-*trans* PPV segment (**Figure V.1**) with both classical and entangled light in two-photon absorption. The diblock copolymers were synthesized via a stereoselective ring-opening metathesis polymerization (ROMP) of paracyclophane diene monomers used in combination with a norbornene imide derivative. We then measured the TPA and ETPA of both diblock copolymers and explored their photo-induced relaxation processes by time-resolved fluorescence up-conversion and femtosecond transient absorption techniques to investigate their intrachain charge transfer nature.

## V.4 Experimental Section

### V.4.a Synthesis of Monomers and Polymers

Monomers **1** and **2** were synthesized according to literature procedures<sup>41, 42</sup> (see Supporting Information for more details). To synthesize all-*cis* block copolymer poly-*cis-1-b-cis-2*, monomer **1** (73.3 mg, 296.4  $\mu\text{mol}$ , 30 equiv) was first measured into a reaction vial charged with a stir bar inside a nitrogen filled glove box. Ruthenium catalyst Ru-St (8.6 mg, 9.9  $\mu\text{mol}$ , 1 equiv) dissolved in deoxygenated THF (0.10 mL) was then added to the vial and stirred for 1 h at room temperature. Into a second reaction vial containing monomer **2** and a stir bar, 0.08 mL of the mixture was then transferred. The reaction was run in the dark at 40 °C for 2 h before cooling to room temperature and quenching with excess ethyl vinyl ether (0.1 mL). After leaving for an additional 30 min at room temperature, two cycles of precipitation with addition of methanol, centrifugation, and decantation afforded the isolated polymer. After wrapping in aluminum foil and concentrating under reduced pressure, 23 mg of poly-*cis-1-b-cis-2* was then dissolved in 23 mL of DCM and irradiated for 1 h at room temperature using two 350 nm UV lamps placed 1 cm away from the sample to afford poly-*cis-1-b-trans-2*. The sample was wrapped in aluminum foil and concentrating under reduced pressure. All polymer samples were fully dried, kept wrapped in aluminum foil, and stored under an inert atmosphere at -20 °C.

### V.4.b Entangled Two-Photon Absorption

The entangled two photon absorption experimental setup which had been previously described was used for the purpose of this study.<sup>43</sup> Type I noncollinear spontaneous parametric down-conversion (SPDC) was generated using a Type I BBO crystal with a potable CW laser. The 405 nm light generated from the CW laser goes through a variable neutral density filter which is used to adjust the pump power into the BBO crystal, resulting in SPDC and entangled photon

production. After passing through the sample in the cuvette, the entangled photons are refocused via a band pass filter with a plano-convex lens before entering the avalanche photodiode (APD). A final band pass filter was introduced to remove any extra wavelength of light other than the entangled light that may have entered the system because of entangled photons (EP) interactions with the material that resulted in fluorescence or emission.

To measure the EP transmission rate using an APD, the ETPA experiment starts by introducing a pure chloroform into the cuvette. The variable neutral density filter (NDF) was used to optimize the power of the laser going into the BBO crystal and, as a result, the intensity of the entangled light that interacts with the sample can be controlled. To calibrate the stage, a maximum of  $5.5 \times 10^6$  uncorrected photon counts per second (cps) is targeted. Once this maximum input photon rate is set, the ETPA scan is taken for a total of ten input photon rate values. After a baseline absorbance for the pure solvent has been found, the solvent is replaced with a diluted PPV dissolved in chloroform so that EP transmission can be measured again. The loss in EP transmission seen between the sample solution and pure solvent is due to ETPA absorption. At least three measurements are taken of each PPV to ensure the best signal-to-noise ratio. Since ETPA is done at such a low photon input intensity, it usually takes more than one measurement to get a stable set of readings.

## **V.5 Result and Discussion**

### *V.5.a Design and synthesis of PPVs for this study*

To access stereodefined PPVs with either >99% *cis* or >99% *trans* alkenes, we relied on a two-step approach: First stereoretentive ring-opening metathesis polymerization (ROMP)<sup>44-46</sup> of

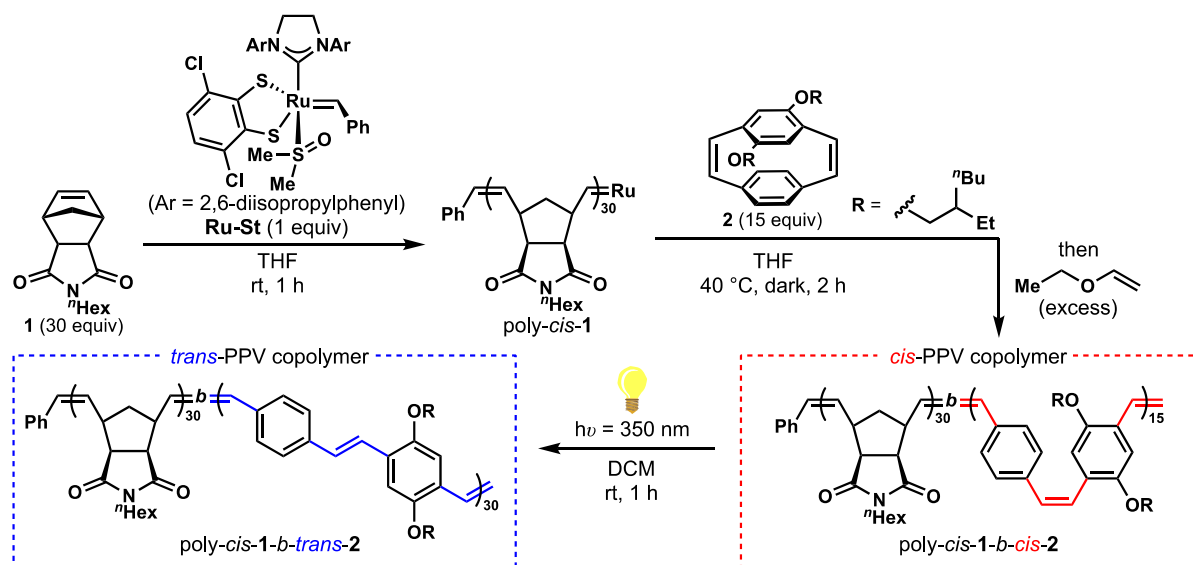


**Figure V.2:** Synthesis of diblock copolymers containing either an all-*cis* or an all-*trans* PPV segment: Sequential stereoretentive ROMP of monomers **1** and **2** using catalyst **Ru-St** delivered poly-*cis*-1-*b*-*cis*-2. Subsequent PPV-selective photoisomerization afforded poly-*cis*-1-*b*-*trans*-2.

paracyclophane diene monomers<sup>47-51</sup> would deliver an all-*cis* PPV segment, then selective photoisomerization of the PPV block would provide the all-*trans* congener.<sup>52</sup> To optimize the solubility in organic solvents of both *cis* and *trans* PPVs, we designed block copolymers containing a solubilizing poly(norbornene imide) segment stitched to the stereodefined PPV. Additionally, 2-ethylhexyloxy side chains that are known to impart high solubility to conjugated polymers were selected as substituents of the PPV.<sup>53</sup> Adapting a protocol recently developed by Michaudel and coworkers,<sup>10,54</sup> two stereodefined copolymers were synthesized and isolated for two-photon absorption spectroscopy (**Figure V.2**). The all-*cis* poly(norbornene imide) segment was first synthesized using a 30:1 ratio of monomer **1** to **Ru-St** initiator. Chain extension using 15 equivalents of monomer **2** followed by termination with excess ethyl vinyl ether afforded all-*cis* block copolymer poly-*cis*-1-*b*-*cis*-2. The *cis*-selectivity of the polymerization (>99%) was assessed using NMR spectroscopy. SEC analysis revealed a narrow dispersity ( $\mathcal{D} = 1.20$ ) and good agreement between the theoretical and experimental number average molecular weight.

Photoisomerization of the PPV block under UV light (350 nm) delivered the *trans* PPV variant poly-*cis-1-b-trans-2* with exquisite selectivity (>99% *trans* PPV) and no isomerization of the poly(norbornene imide) block as shown by NMR spectroscopy.

V.5.b Steady-state absorption and emission:

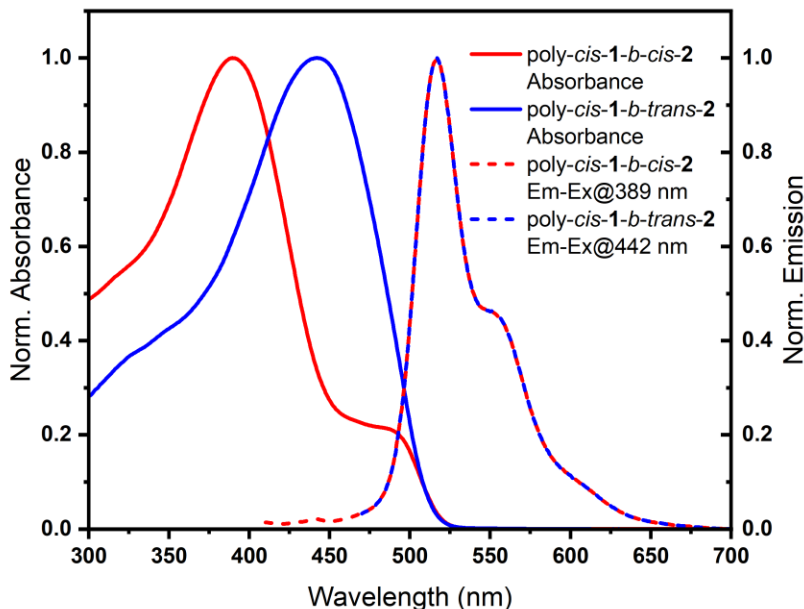


**Figure V.3:** Normalized steady state absorption ( $C = 25.0$  and  $12.5 \mu\text{g/mL}$ , respectively) and emission ( $C = 4.2$  and  $1.6 \text{ ng/mL}$ , respectively) spectra of poly-*cis-1-b-cis-2* and poly-*cis-1-b-trans-2* in chloroform. Excitations for poly-*cis-1-b-cis-2* and poly-*cis-1-b-trans-2* were 389 and 442 nm, respectively.

UV-vis absorption measurements for poly-*cis-1-b-cis-2* and poly-*cis-1-b-trans-2* were carried out in chloroform at room temperature with maximum  $\pi-\pi^*$  absorptions of 389 nm and 442 nm, respectively, indicating a red-shift after photoisomerization consistent with previous studies<sup>10,54-56</sup> (**Figure V.3**). Interestingly, emission spectra for poly-*cis-1-b-cis-2* and poly-*cis-1-b-trans-2* collected following excitation at 389 and 442 nm, respectively, were almost identical. An emission maximum was observed at 517 nm in both spectra (**Figure V.2**). In addition, another

weak band at the region of 555 nm for both PPV samples was observed and is consistent with a previous report.<sup>10</sup> Relative quantum yields were determined, and poly-*cis-1-b-trans-2* was found to have a quantum yield 20% higher than poly-*cis-1-b-cis-2*. All steady-state results are summarized in **Table V.1**. The narrower optical bandgap and higher quantum yield observed for poly-*cis-1-b-trans-2* suggest a more efficient intramolecular charge transfer (ICT) compared to poly-*cis-1-b-cis-2*.

**Table V.1:** Steady-state Absorption and Emission Properties of poly-*cis-1-b-cis-2* and poly-*cis-1-b-trans-2* in chloroform.

Samples	Absorption (nm)	Emission (nm)	$\Phi_n$ (%)
<b>poly-<i>cis-1-b-cis-2</i></b>	389	517, 555	36.3
<b>poly-<i>cis-1-b-trans-2</i></b>	442	517, 555	56.5

#### V.5.c Classical Two-Photon Absorption

The nonlinear optical properties of poly-*cis-1-b-cis-2* and poly-*cis-1-b-trans-2* were then analyzed using classical TPA ( $\lambda_{\text{exc}} = 800$  nm) with induced fluorescence detection to gain insight into the charge transfer characters. It has been observed that the transition probability of TPA increases with increasing ICT character.<sup>57</sup> The logarithmic plot of the intensity (counts per second) versus the laser power (mW) shows a linear fit with a slope value of about 2 for both PPV samples (**Figure V.4.a**). This indicates that a two-photon excitation process is allowed in both poly-*cis-1-b-cis-2* and poly-*cis-1-b-trans-2*. **Figure V.4a** shows the power dependent two-photon excited fluorescence spectra while **Figure V.4.b** is the two-photon emission which correlates well with the steady-state emission spectra. The slope values obtained from the power-dependence logarithm plot was used to calculate the two-photon absorption cross section.<sup>58</sup> The TPA cross sections were calculated using the following equation:

**Equation V.1**

$$\sigma_{sample} = \frac{10^{b_{sample}-b_{std}} \phi_{std} \sigma_{std} [c]_{std} n_{std}}{\phi_{sample} [c]_{sample} n_{sample}}$$

where  $\phi$  is the emission quantum yield,  $n$  is the solvent refractive index,  $b$  is the intercept in the linear fit of the quadratic power dependence, and  $[c]$  is the concentration. The two-photon photoluminescence spectra were measured by exciting the sample at 800 nm and collecting the photoluminescence at 520 nm, the two-photon excited fluorescence maxima (**Figure V.4.b**). In all cases, the two-photon excited emission spectra are very similar to the one-photon steady state emission spectra (**Figure V.3**). The TPA cross-section values for both poly-*cis-1-b-cis-2* and poly-*cis-1-b-trans-2* at the same concentration were found to be 11.4 GM and 1490 GM (1 Göppert-Mayer =  $10^{-50}$  cm<sup>4</sup> s photon<sup>-1</sup>) respectively, as listed in Table 2. The TPA cross-section for poly-*cis-1-b-trans-2* was found to be much higher than that of poly-*cis-1-b-cis-2* indicating efficient intramolecular charge transfer nature of poly-*cis-1-b-trans-2* which is useful for OLED, two-photon imaging, and photovoltaic applications. It has been observed that the transition probability of TPA increases with increasing ICT character.<sup>57</sup> This higher TPA cross-section was ascribed to the increased conjugation length and higher  $\pi$ - $\pi$  interaction present in poly-*cis-1-b-trans-2* as a result of the more rodlike structure of the *trans* PPV segment, which allows for more effective charge mobility along the polymer backbone. In order to better understand the TPA cross-section in terms of dipole moments and the different TPA mechanisms, the random (classical) TPA expression can also be written as:<sup>57</sup>

**Equation V.2**

$$\delta_R = \frac{B}{\hbar^2 \epsilon_0^2} \omega_1^0 \omega_2^0 \delta(\epsilon_f - \epsilon_g - 2\omega_0) \times \left| \frac{1}{(\omega_0 + \epsilon_g - \epsilon_e) - ik_e/2} \mu_{fe} \cdot e \mu_{eg} \cdot e + \frac{1}{\omega_0 - \frac{ik_g}{2}} \mu_{fg} \cdot e \mu_{gg} \cdot e + \frac{1}{\omega_0 - \frac{ik_f}{2}} \mu_{ff} \cdot e \mu_{fg} \cdot e \right|^2$$

The first term in **Equation V.2** describes TPA through an intermediate level. Alternatively, the second and third terms in **Equation V.2** describe TPA through the transition dipole pathway where the ground and final states are strongly coupled to each other. Therefore, in the transition dipole pathway intermediate states are not involved. Chouk *et al.* described that the transition dipole-moment of *trans*-PPV is three times greater due to higher electron mobility created by a lower overall torsional level and higher planarity than *cis*-PPV.<sup>59</sup> We also calculated the transition dipole moment for all PPVs, which was found to be 2.59 and 0.23 Debye for poly-*cis*-1-*b*-*trans*-2 and poly-*cis*-1-*b*-*cis*-2 respectively. The strong dependence of the random TPA cross section on the transition dipole moment (**Equation V.1**) therefore explains why poly-*cis*-1-*b*-*trans*-2 has a greater TPA cross-section value compared to poly-*cis*-1-*b*-*cis*-2.

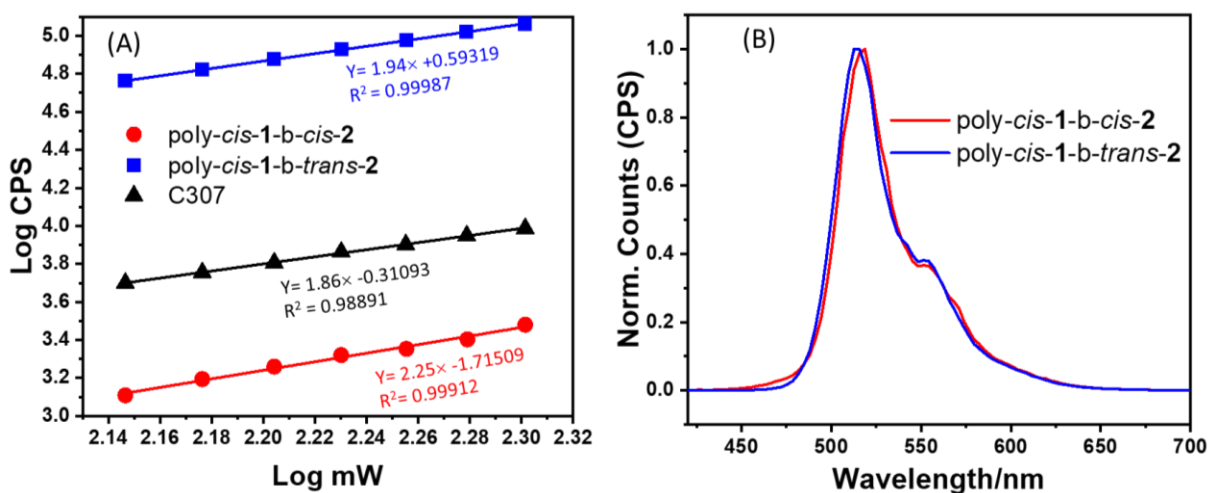


**Figure V.4:** (a) Excitation power dependent classical TPA fluorescence (at 520 nm) and (b) two-photon excited fluorescence spectra of the investigated compounds. The excitation wavelength was 800 nm.

**Table V.2:** Summary of Classical TPA Cross-sections of the Copolymers in Chloroform

Samples	Concentration (M)	TPA Cross-section (GM)
poly- <i>cis</i> -1- <i>b</i> - <i>cis</i> -2	$3.97 \times 10^{-6}$	11.4
poly- <i>cis</i> -1- <i>b</i> - <i>trans</i> -2	$3.97 \times 10^{-6}$	1490



#### V.5.d Time-resolved Fluorescence Upconversion

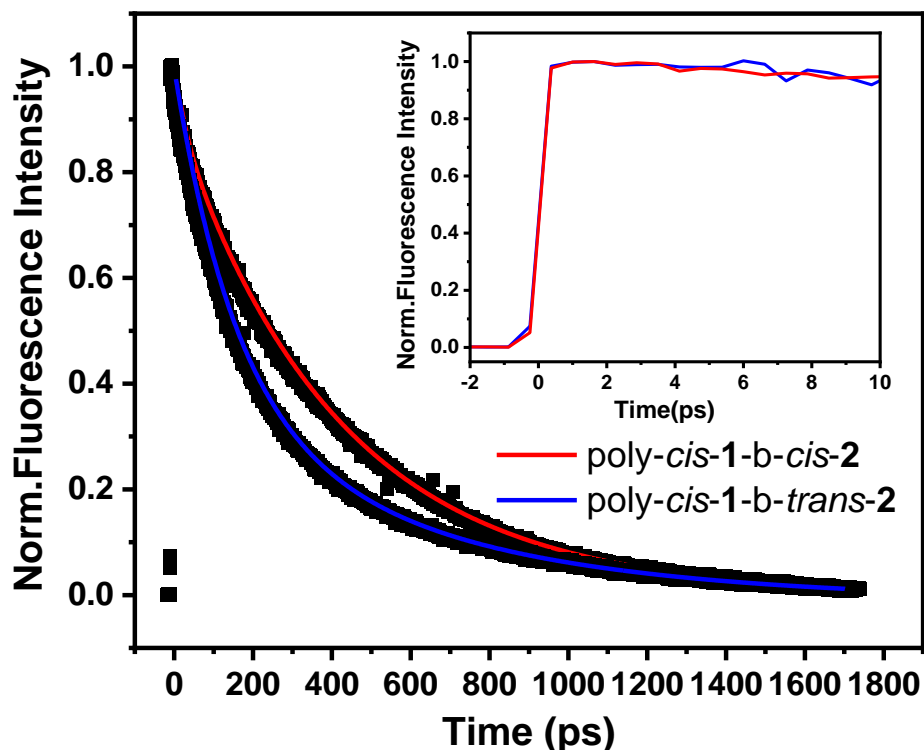


**Figure V.5:** Fluorescence decay traces of poly-cis-1-b-cis-2 and poly-cis-1-b-trans-2 at the emissive wavelength of 517 nm after excitation at 400 nm. Inset are the emissive decay traces in 10 ps time window.

In order to have insight into early time relaxation dynamics, time-resolved fluorescence studies of poly-cis-1-b-cis-2 and poly-cis-1-b-trans-2 were performed at the emission wavelength of 517 nm upon excitation at 400 nm, using fluorescence up-conversion technique (**Figure V.5**). As shown in **Figure V.5**, decay curves clearly show that there is a faster fluorescence decay for poly-cis-1-b-trans-2 compared to poly-cis-1-b-cis-2. All the time profiles are tri-exponentially fit with a relatively fast rise component of  $\sim 0.153$ – $0.166$  ps and predominant slow components in ps time domain. All the fitted decay parameters are given in Table 3. Both poly-cis-1-b-cis-2 and poly-cis-1-b-trans-2 show almost identical rise times. However, the fluorescence decay lifetimes for both PPVs are different. For poly-cis-1-b-trans-2, the shorter time constant becomes faster

from 155 ps to 28.1 ps along with a rise of very fast time constant (0.166 ps). Again, the longer component changes from 604 ps to 413 ps indicates a decrease in radiative processes in the case of poly-*cis-1-b-trans-2* relative to poly-*cis-1-b-cis-2*. The decrease in radiative processes of the decay dynamics suggest the more efficient charge transfer occurs in poly-*cis-1-b-trans-2*.

**Table V.3:** Summary of the Fluorescence Up-conversion with both Copolymers<sup>a</sup>

Samples	$\tau_1$ (ps) (a1%)	$\tau_2$ (ps) (a2%)	$\tau_3$ (ps) (a3%)
poly- <i>cis-1-b-cis-2</i>	$0.153 \pm 0.004$ (-100)	$155 \pm 1.22$ (63)	$604 \pm 10.4$ (37)
poly- <i>cis-1-b-trans-2</i>	$0.166 \pm 0.002$ (-100)	$28.1 \pm 1.00$ (10)	$413 \pm 0.66$ (90)

<sup>a</sup>A negative amplitude indicates that the corresponding components are rise components.

### V.5.e Femtosecond Transient Absorption

To gain more insight into the charge carrier distribution in the excited state and their relaxation and recombination dynamics of both PPVs in a sub-picosecond to picosecond time scale, we further performed time-resolved transient absorption (TA) experiments. **Figures V.6a** and **V.b** presents the time-resolved TA spectra of the excited state population following photoexcitation of the PPV samples in chloroform at room temperature. The pump source at 400 nm was used for both poly-*cis-1-b-cis-2* and poly-*cis-1-b-trans-2*, with probing of the entire visible region. The initial spectra consist of a stimulated emission (SE) around 500 nm (for poly-*cis-1-b-cis-2*) and 490 nm (poly-*cis-1-b-trans-2*) which overlaps with ground state bleach (GSB) for poly-*cis-1-b-cis-2* and poly-*cis-1-b-trans-2*, respectively, and the broad excited state absorption (ESA) band beyond 600 nm peaking at 724 and 750 nm for poly-*cis-1-b-cis-2* and poly-*cis-1-b-trans-2* respectively. A blue shift (like steady state emission spectra) and spectral narrowing of the SE peak is observed for poly-*cis-1-b-trans-2* relative to poly-*cis-1-b-cis-2*. **Figure V.6.c** shows the SE dynamics of poly-*cis-1-b-cis-2* and poly-*cis-1-b-trans-2* at 500 and 490 nm, respectively. **Figure 6.d** shows the ESA dynamics of poly-*cis-1-b-cis-2* and poly-*cis-1-b-trans-2* at 724 and 750

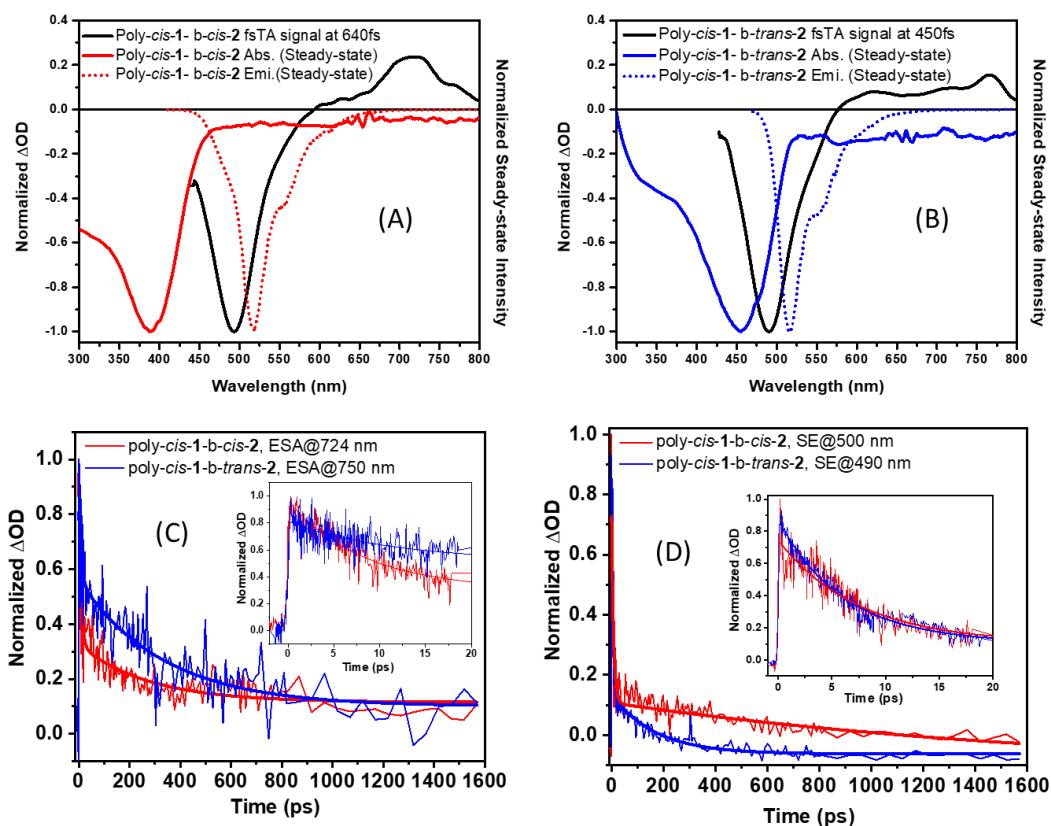


**Figure V.6:** Femtosecond transient absorption spectra (fsTAS) for poly-cis-1-b-cis-2 (a) and poly-cis-1-b-trans-2 (b) corroborated with steady state absorption and emission spectra. Lower panel shows time traces of poly-cis-1-b-cis-2 and poly-cis-1-b-trans-2 in 1.6 ns and 20 ps (inset) time windows. The excitation wavelength for both compounds was 400 nm.

nm, respectively. Inset of **Figures 6.c & 6.d** represents rise/decay dynamics in 20 ps time domain to get better understanding in ultrafast timescale. All SE decays were well fitted by bi-exponential functions with characteristic lifetime values of 7.5 ps (73%) & >1600 ps (27%) (greater than the experimental time window) for poly-cis-1-b-cis-2 and 5.8 ps (78.8%) & 167 ps (21.2%) for poly-cis-1-b-trans-2, respectively, which nicely corroborates with the fluorescence decay time measured by the fluorescence upconversion technique. The shortening of time signifies the faster excited state energy/electron transfer which eventually makes the bleach recovery faster in case of poly-cis-1-b-trans-2. In addition, all ESA decays were also fitted biexponentially with lifetimes

values of 7.1 ps (67%) & 275 ps (33%) for poly-*cis-1-b-cis-2* at 724 nm; and 8.3 ps (64%) & 332 ps (36%) at 750 nm for poly-*cis-1-b-trans-2*, respectively. Instead of ESA decay, we can also see a very fast rise component with lifetime values of 0.249 ps (for poly-*cis-1-b-cis-2*) and 0.273 ps (for poly-*cis-1-b-trans-2*), respectively. All TA data listed in Table 5 are consistent with literature reports:<sup>60-64</sup> The early relaxation originates from a strong coupling between electronic and vibrational states. Hence, the fast kinetic processes are attributed to delocalized exciton states (sub ps) and vibrational cooling (few ps).<sup>65</sup> Subsequently, the excited state dynamics is dominated by intrachain charge/energy transfer on a characteristic timescale of tens of ps.<sup>66,67</sup> This electronic charge/energy transfer occurs prior to emission which generally stems from localized low-energy sites.<sup>68-71</sup>

In case of SE dynamics, the  $t_1$  component [for poly-*cis-1-b-cis-2*,  $t_1 = 7.5$  ps and for poly-*cis-1-b-trans-2*,  $t_2 = 5.8$  ps] is assigned to the vibrational cooling of  $S_1$  state. Whereas the  $t_2$  component [for poly-*cis-1-b-cis-2*,  $t_2 = >1600$  ps and for poly-*cis-1-b-trans-2*,  $t_2 = 167$  ps] is assigned for the relaxation time from  $S_1$  to ground state ( $S_0$ ). The shortening of time constant signifies the more efficient excited state energy/electron transfer which eventually makes the recombination faster in case of poly-*cis-1-b-trans-2* because of its effective conjugation length, high dipole moment, and increased  $\pi$ - $\pi$  stacking compared to poly-*cis-1-b-cis-2*.

The three excited state components are characterized as hot  $S_1$  (hot singlet state),  $S_1$  (singlet state), and  $S_1$  to ground state ( $S_0$ ). The hot  $S_1$  is short lived (249 fs for poly-*cis-1-b-cis-2* and 273 fs for poly-*cis-1-b-trans-2*) that is attributed to the initial excitation to the hot  $S_1$  state of the PPVs. The hot  $S_1$  state decays very fast to the vibrationally relaxed  $S_1$  state whose lifetime is found to be 7.1 ps for 8.3 ps for poly-*cis-1-b-cis-2* and poly-*cis-1-b-trans-2*, respectively. Finally, it recombines to ground state ( $S_0$ ) with the time constant of 275 ps and 332 ps for poly-*cis-1-b-cis-2*

and poly-*cis-1-b-trans-2*, respectively. The time scale of the ES decay of  $S_1 - S_0$  is found to be very close to upconversion decay trace. It is important to note that the excited state decay for poly-*cis-1-b-trans-2* is relatively slower than poly-*cis-1-b-cis-2* which is due to the efficient charge transfer nature of poly-*cis-1-b-trans-2* and generation of a long-lived CT state which is beneficial for a light harvesting system.

**Table V.4:** Transient Absorption Data for poly-*cis-1-b-cis-2* and poly-*cis-1-b-trans-2*.<sup>a</sup>

<b>Stimulated Emission dynamics</b>			
<b>Samples</b>	<b>t<sub>1</sub> (ps), (a<sub>1</sub>%)</b>	<b>t<sub>2</sub> (ps), (a<sub>2</sub>%)</b>	
poly- <i>cis-1-b-cis-2</i>	7.5 ± 0.38 (73)	>1600 ± 344 (27)	
poly- <i>cis-1-b-trans-2</i>	5.8 ± 0.21 (78.8)	167 ± 22 (21.2)	
<b>Excited state absorption dynamics</b>			
<b>Samples</b>	<b>t<sub>1</sub> (ps), (a<sub>1</sub>%)</b>	<b>t<sub>2</sub> (ps), (a<sub>2</sub>%)</b>	<b>t<sub>3</sub> (ps), (a<sub>3</sub>%)</b>
poly- <i>cis-1-b-cis-2</i>	0.249±0.09 (-100)	7.1±0.56 (67)	275±77 (33)
poly- <i>cis-1-b-trans-2</i>	0.273±0.12 (-100)	8.3±0.52 (64)	332±64 (36)

<sup>a</sup>A negative amplitude indicates that the corresponding components are rise components.

#### V.5.f Entangled Two-photon Absorption

Entangled two-photon absorption (ETPA), a non-linear optical process, was utilized to acquire a better understanding of how quantum light (non-classical) interacts with poly-*cis-1-b-cis-2* and poly-*cis-1-b-trans-2*. The mechanism for this transition involves the absorption of two

entangled photons which are quantum correlated with each other and induce unique photophysics during the ETPA transition. In classical TPA, the two photons are not correlated with each other and so neither are the two absorption events since the two photons can be absorbed randomly. Hence, ETPA scales linearly with the input photon rate, rather than quadratically for classical TPA. The linear trend yields an enhancement in the absorption rate at low input intensities compared to classical TPA, allowing two-photon transitions to be probed at extremely small photon rates where the molecule cannot be damaged. Thus, this study enhances the molecular sensitivity in probing the photophysical characteristics of poly-*cis*-1-*b*-*cis*-2 and poly-*cis*-1-*b*-*trans*-2 with extremely low photon flux preventing photobleaching and light-mediated toxicity.

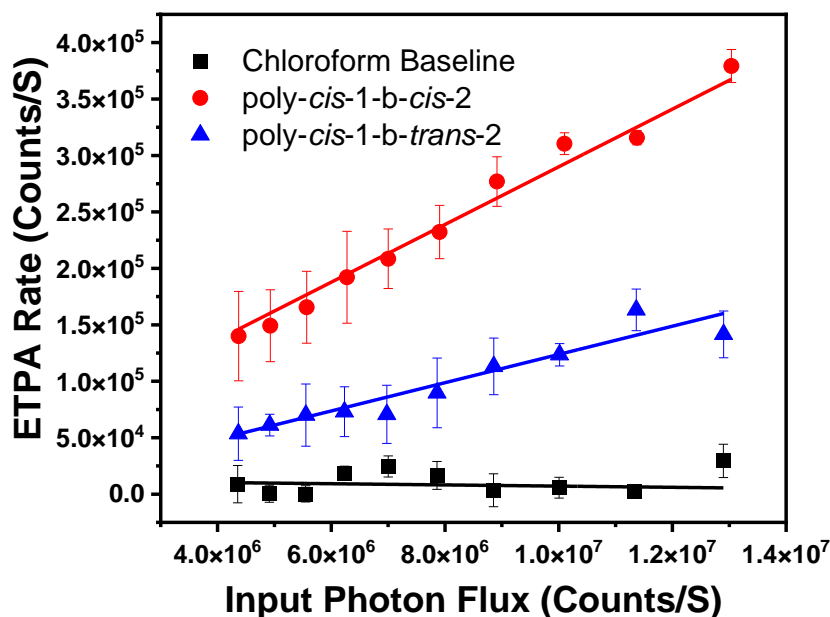


**Figure V.7:** Entangled two-photon absorption as a function of input photon flux (i.e., excitation power) for poly-*cis*-1-*b*-*cis*-2 and poly-*cis*-1-*b*-*trans*-2 in chloroform solution. ETPA scales linearly with the input photon flux, rather than quadratically for classical TPA. The linear trend yields an enhancement in the absorption rate at low input intensities compared to classical TPA. The ETPA rate is determined to be the difference between the photon counts per second transmitted through the solvent (chloroform) and the sample (PPVs) solution for a given input photon flux.

**Figure V.7** shows the ETPA rate as a function of input photon flux for poly-*cis-1-b-cis-2* and poly-*cis-1-b-trans-2* in chloroform. Both poly-*cis-1-b-cis-2* and poly-*cis-1-b-trans-2* absorbed entangled light in magnitude higher than the baseline as expected. Furthermore, at relatively similar concentrations, poly-*cis-1-b-cis-2* exhibited a higher ETPA absorption than poly-*cis-1-b-trans-2*. This finding implies that poly-*cis-1-b-cis-2* absorb entangled photons better than poly-*cis-1-b-trans-2* in chloroform solution. In general, ETPA cross-section,  $\sigma_e$  is given by:<sup>72</sup>

**Equation V.3**

$$\sigma_e = \frac{2\pi}{(\hbar\epsilon_0 c)^2 A_e T_e} \omega_i \omega_s \delta(\epsilon_f - \epsilon_i - \omega_i - \omega_s) \times \left\{ \left\{ \sum_j \left\{ D_{is}^{(j)} \frac{1 - \exp[-iT_e \Delta_j^{(i)}]}{\Delta_j^i} + D_{si}^{(j)} \frac{1 - \exp[-iT_e \Delta_j^{(s)}]}{\Delta_j^s} \right\} \right\} \right\}^2$$

where  $\hbar$  is Plank's constant,  $\epsilon_0$  is vacuum permittivity,  $c$  is the speed of light,  $A_e$  and  $T_e$  are entanglement area and entanglement time, respectively,  $\omega_i$  and  $\omega_s$  are the frequencies of the idler and signal photons,  $\delta(\epsilon_f - \epsilon_i - \omega_i - \omega_s)$  enforces energy conservation, and  $\epsilon_i$  are the energy eigenvalues of the ground and excited states, respectively,  $D_{is}^{(j)} = \langle \Psi_i | e_i \mu | \Psi_j \rangle \langle \Psi_j | e_s \mu | \Psi_f \rangle$  gives the transition dipole matrix elements, and  $\Delta_j^{(k)} = \epsilon_j - \epsilon_i - \omega_k$  is the detuning energy where  $k = i$  or  $s$  refers to the signal and idler photons. Like classical TPA, the ETPA cross-section is also directly proportional to the transition dipole moment, thus a similar trend in ETPA cross-section would be expected. Interestingly, the ETPA cross-section (Table 5) for poly-*cis-1-b-cis-2* ( $5 \times 10^{-18}$  cm<sup>2</sup>/molecule) was found to be twice as large as that of poly-*cis-1-b-trans-2* ( $2.2 \times 10^{-18}$  cm<sup>2</sup>/molecule) indicating that *cis*-PPV is more sensitive to entangled light which can be useful for quantum sensing and quantum imaging applications. The capability of these PPVs to absorb entangled light may be the cause of this opposite trend. However, the ETPA cross-section also depends on electronic energy levels of the molecule. Generally, in each molecule, there are certain electronic energy states which are not easily accessible by classical light but may be

accessible with entangled light. It has been described by Chouk et al that *cis*-PPV has higher energy band gap and lower HOMO level than *trans*-PPV.<sup>52</sup> In our TD-DFT studies performed on *trans*- and *cis*-PPV, we observed a similar decrease in the HOMO energy level by -0.40 eV from *trans*- to *cis*-PPV (Figures 8 and S9), respectively. The decrease in the HOMO orbital energy coupled with the increase in energy of the LUMO and LUMO+1 orbitals increased the band gap of the *cis*-PPV. Interestingly, the HOMO-1 orbital also decreased in energy level by -0.12 eV (**Figure V.8**). Presumably this lower-lying HOMO-1 electronic energy state could enable *cis*-PPV to absorb a substantial quantity of entangled two-photons, leading to a greater ETPA cross-section than *trans*-PPV. To gain a better understanding as to why the *cis*-PPV observed a lower HOMO-1 energy level, we sought to simulate the amount of orbital delocalization in the *trans*- vs. *cis*-PPV systems by measurement of the orbital delocalization index (ODI) for HOMO and HOMO-1 orbitals. Interestingly, while both HOMO and HOMO-1 orbitals were lower in energy for the *cis*-PPV, less orbital delocalization was observed contrary to what would be expected. As a result, single point calculations at the CAM-B3LYP-D3/6-311G(d,p)-SMD(CHCl<sub>3</sub>) level of theory were performed on the individual styrene (1)/(3) and 1,4-dimethoxy-2-vinylbenzene (2)/(4) fragments of *cis*- and *trans*-PPV. Plotting the HOMO-1, HOMO, LUMO, and LUMO+1 energies of each fragment, we determined that the HOMO and HOMO-1 orbitals significantly decreased in energy from *trans*- to *cis*-PPV for the majority of fragments (Figure S15). The styrene fragment 1 (*trans*-PPV(1) vs. *cis*-PPV(1)) saw the largest decrease in HOMO orbital energy from *trans*- to *cis*-PPV ( $\Delta E_{\text{HOMO}}(1) = -0.16$  eV). The 1,4-dimethoxy-2-vinylbenzene fragment 2 (*trans*-PPV(2) vs. *cis*-PPV(2)) saw the largest decrease in HOMO-1 orbital energy from *trans*- to *cis*-PPV ( $\Delta E_{\text{HOMO-1}}(2) = -0.32$  eV), leading to a decrease in the entire *cis*-PPV HOMO-1 orbital energy (Table S10). These results suggest that the quantum interference between entangled photons and the interacting



matter can provide changes to two-photon absorption signals that are not observed classically due to a lower lying HOMO-1 electronic state in *cis*-PPV.

**Table V.5:** ETPA Cross-sections for poly-*cis*-1-*b*-*cis*-2 and poly-*cis*-1-*b*-*trans*-2 in chloroform.

Samples	Conc. ( $\mu\text{M}$ )	ETPA Cross-section ( $\text{cm}^2/\text{molecule}$ )
poly- <i>cis</i> -1- <i>b</i> - <i>trans</i> -2	8.4	$2.2 \times 10^{-18}$
poly- <i>cis</i> -1- <i>b</i> - <i>cis</i> -2	8.9	$5.0 \times 10^{-18}$

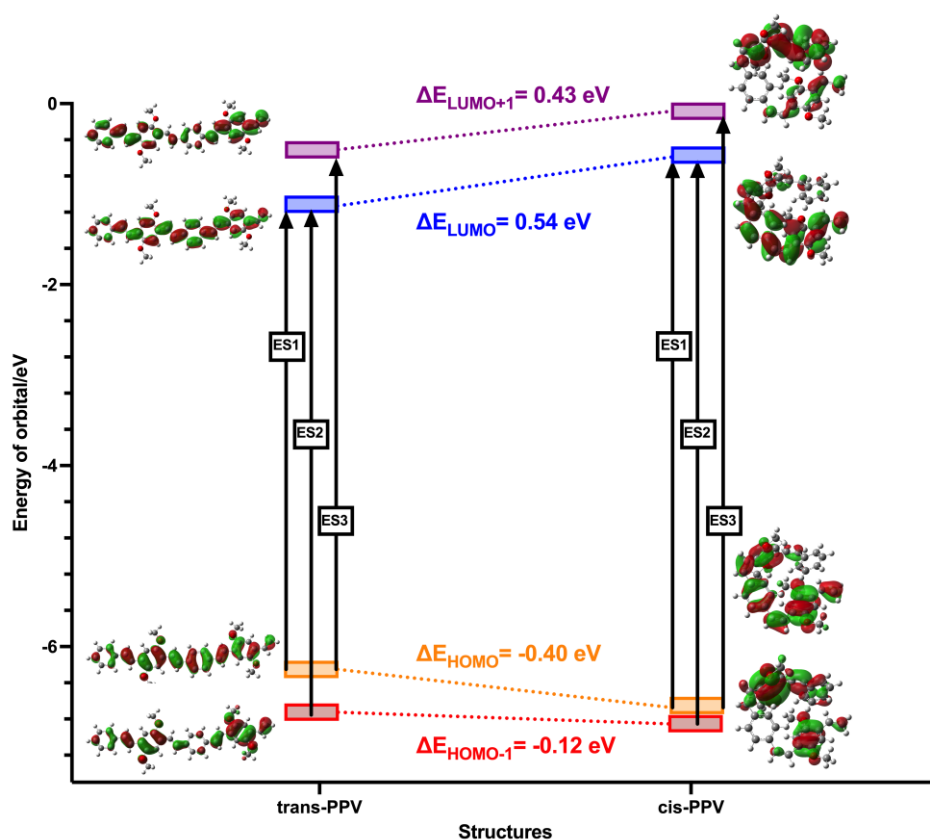


**Figure V.8:** Frontier molecular HOMO–1 through LUMO+1 orbitals of *trans*- (left panel) and *cis*-PPV (right panel) calculated at the CAM-B3LYP-D3/6-311+G(d,p)-SMD(CHCl<sub>3</sub>) level of theory.

## V.6 Conclusion

This comprehensive spectroscopic investigation of poly-*cis-1-b-cis-2* and poly-*cis-1-b-trans-2* demonstrates that the olefin geometry of the conjugated polymer significantly impacts the two-photon absorption properties. When TPA cross-sections are compared, poly-*cis-1-b-trans-2* has a greater classical TPA cross-section than poly-*cis-1-b-cis-2*, suggesting a more efficient intramolecular charge transfer, which is in line with our femtosecond transient absorption studies where we found a relatively long-lived CT state for poly-*cis-1-b-trans-2*. These findings might have strong implications for the potential uses of PPVs as fluorophores. Indeed, while all-*trans* PPV might be suitable applications including OLED, two-photon imaging, and photovoltaic applications because of a more efficient intramolecular charge transfer, all-*cis* PPV appears to be more sensitive to entangled light (larger ETPA cross section), which is desirable for quantum sensing and quantum imaging applications. DFT calculations supports our hypothesis that the all-*cis* PPV variant possesses a lower lying HOMO-1 state comparatively to the all-*trans* congener, which suggests a more energetically favorable interaction with entangled photons that could result in the larger ETPA cross section observed experimentally. We anticipate that the ability to tune both classical TPA and non-classical ETPA cross sections through synthetic structural modification of the olefin geometry in PPVs will help inform future design of chromophores for applications in this field.

## V.7 References

1. Zaquen, N., Lutsen, L., Vanderzande, D. & Junkers, T. Controlled/living polymerization towards functional poly(*p*-phenylene vinylene) materials. *Polym. Chem.* **2016**, *7*, 1355–1367.
2. Blayney, A. J., Perepichka, I. F., Wudl, F. & Perepichka, D. F. Advances and Challenges in the Synthesis of Poly(*p*-phenylene vinylene)-Based Polymers. *Isr. J. Chem.* **2014**, *54*, 674–688.
3. Burroughes, J. H.; Bradley, D. D. C.; Brown, A. R.; Marks, R. N.; Mackay, K.; Friend, R. H.; Burns, P. L.; Holmes, A. B. Light-Emitting Diodes Based on Conjugated Polymers. *Nature* **1990**, *347*, 539–541.
4. Halls, J. J. M.; Walsh, C. A.; Greenham, N. C.; Marseglia, E. A.; Friend, R. H.; Moratti, S. C.; Holmes, A. B. Efficient photodiodes from interpenetrating polymer networks. *Nature* **1995**, *376*, 498–500.
5. Kraft, A.; Grimsdale, C. A.; Holmes, B. A. Electroluminescent Conjugated Polymers-Seeing Polymers in a New Light. *Angew Chem Int Ed Engl.* **1998**, *37*, 402–428.
6. Freitag, M., Teuscher, J., Saygili, Y. *et al.* Dye-sensitized solar cells for efficient power generation under ambient lighting. *Nature Photon* **2017**, *11*, 372–378.
7. Grimsdale, A. C., Chan, K. L., Martin, R. E., Jokisz, P. G. & Holmes, A. B. Synthesis of light-emitting conjugated polymers for applications in electroluminescent devices. *Chem. Rev.* **2009**, *109*, 897–1091.
8. Brabec, C., Dyakonov, V. & Scherf WILEY-, U. *Organic photovoltaics: materials, device physics, and manufacturing technologies.* (2011).
9. Friend, R. H.; Gymer, R. W.; Holmes, A. B.; Burroughes, J. H.; Marks, R. N.; Taliani, C.; Bradley, D. D. C.; Dos Santos, D. A.; Brédas, J. L.; Lögdlund, M.; Salaneck, W. R. Electroluminescence in conjugated polymers. *Nature* **1999**, *397*, 121–128.
10. Hsu, T. W., Kim, C. & Michaudel, Q. Stereoretentive Ring-Opening Metathesis Polymerization to Access All- cis Poly(*p*-phenylenevinylene)s with Living Characteristics. *J. Am. Chem. Soc.* **2020**, *142*, 11983–11987.
11. Shin, S.; Menk, F.; Kim, Y.; Lim, J.; Char, K.; Zentel, R.; Choi, T.-L. Living Light-Induced Crystallization-Driven Self-Assembly for Rapid Preparation of Semiconducting Nanofibers. *J. Am. Chem. Soc.* **2018**, *140*, 6088.
12. Wang, F.; He, F.; Xie, Z.; Li, M.; Hanif, M.; Gu, X.; Yang, B.; Zhang, H.; Lu, P.; Ma, Y. A Solution-Processible Poly(*p*-phenylene vinylene) without Alkyl Substitution: Introducing the cis- Vinylene Segments in Polymer Chain for Improved Solubility, Blue Emission, and High Efficiency. *J. Polym. Sci., Part A: Polym. Chem.* **2008**, *46*, 5242.
13. Lei, T., Dou, J. H., Cao, X. Y., Wang, J. Y. & Pei, J. Electron-Deficient Poly(*p*-phenylene vinylene) Provides Electron Mobility over 1 cm<sup>2</sup> V<sup>-1</sup> s<sup>-1</sup> under Ambient Conditions. *J. Am. Chem. Soc.* **2013**, *135*, 12168–12171.
14. Osaka, I., Abe, T., Shinamura, S. & Takimiya, K. Impact of isomeric structures on transistor performances in naphthodithiophene semiconducting polymers. *J. Am. Chem. Soc.* **2011**, *133*, 6852–6860.
15. Chen, L. *et al.* From the Cover: Highly sensitive biological and chemical sensors based on reversible fluorescence quenching in a conjugated polymer. *Proc. Natl. Acad. Sci. U. S. A.* **1999**, *96*, 12287.
16. Vanden Bout, D. A. *et al.* Discrete intensity jumps and intramolecular electronic energy

- transfer in the spectroscopy of single conjugated polymer molecules. *Science* **1997**, *277*, 1074–1077.
17. Chaieb, A. *et al.* PL and EL properties of oligo (p-phenylene vinylene) (OPPV) derivatives and their applications in organic light-emitting diodes (OLED). *Opt. Mater. (Amst)*. **2008**, *31*, 68–74.
  18. Dilonardo, E. *et al.* Tailoring Optical Properties of Blue-Gap Poly(p-phenylene Vinylene)s for LEDs Applications. *Adv. Sci. Technol.* **2010**, *75*, 118–123.
  19. Hu, D. *et al.* Collapse of stiff conjugated polymers with chemical defects into ordered, cylindrical conformations. *Nat.* **2000**, *405*, 1030–1033.
  20. Peters, M. *et al.* PPV-Based Conjugated Polymer Nanoparticles as a Versatile Bioimaging Probe: A Closer Look at the Inherent Optical Properties and Nanoparticle-Cell Interactions. *Biomacromolecules* **2016**, *17*, 2562–2571.
  21. Zaquen, N. *et al.* Profluorescent PPV-Based Micellar System as a Versatile Probe for Bioimaging and Drug Delivery. *Biomacromolecules* **2016**, *17*, 4086–4094.
  22. Garmire, Elsa. Nonlinear Optics in Daily Life. *Optics Express*, **2013**, *21*, 30532.
  23. Verbiest, T.; Parsoons, A. Nonlinear Optical Properties of Polymeric Materials and Polymer Films: Recent Developments and Future Trends. *Macromol. Symp.* **1996**, *102*, 347–354.
  24. Castet, F.; Rodriguez, V.; Pozzo, J.L.; Ducasse, L.; Plaque, A.; Champagne, B. Design and Characterization of Molecular Nonlinear Optical Switches. *Acc. Chem. Res.* **2013**, *46*, 2656–2665.
  25. Li, D.Q; Ratner, M.A.; Marks, T.J. Molecular and Macromolecular Nonlinear Optical Materials. Probing Architecture/Electronic Structure/Frequency Doubling Relationships via an SCF-LCAO MECI .Pi. Electron Formalism. *J. Am. Chem. Soc.* **1988**, *110*, 1707– 1715.
  26. Marder, S.R.; Kippelen, B.; Jen, A.K.Y. Design and Synthesis of Chromophores and Polymers for Electro-optic and Photorefractive Applications. *Nature*, **1997**, *388*, 845–851.
  27. Saleh, B.; Jost, B.; Fei, H.B.; Teich, M. Entangled-Photon Virtual State Spectroscopy. *Phys. Rev. Lett.* **1998**, *80*, 33483.
  28. Fei, H.B., Jost, B., Popescu, S., Saleh, B., Teich, M. Entanglement-Induced Two Photon Transparency. *Phys. Rev. Lett* **1997**, *78*, 1679
  29. Eshun, A.; Gu, B.; Varnavski, O.; Asban, S.; Dorfman, KE.; Mukamel,S.; Goodson, T. Investigations of molecular optical properties using quantum light and Hong–Ou–Mandel interferometry. *J. Am. Chem. Soc.* **2021**, *143*, 9070–9081
  30. Donehue, JE.; Varnavski, OP.; Cemborski, R.; Iyoda, M.; Goodson, T.; Probing coherence in synthetic cyclic light-harvesting pigments. *Journal of the American Chemical Society* **2011** *133*, 4819-4828.
  31. Song, J.-A.; Peterson, G. I.; Bang, K.-T.; Ahmed, T. S.; Sung, J.-C.; Grubbs, R. H.; Choi, T. L. Ru-catalyzed, *cis*-selective ring opening metathesis polymerization of various monomers, including a dendronized macromonomer, and implications to enhanced shear stability. *J. Am. Chem. Soc.* **2020**, *142*, 10438-10445.
  32. Eshun, A.; Varnavski, O.; Villabona-Monsalve, J. P.; Burdick, R. K.; Goodson, III. T. "Entangled Photon Spectroscopy" *Acc. Chem. Res.* **2022**, *55*, 7, 991-1003.
  33. Burdick, R. K.; Schatz, G. C.; Goodson, III. T. "Enhancing Entangled Two-Photon Absorption for Picosecond Quantum Spectroscopy ", *J. Am. Chem. Soc.* **2021**, *143*, 41, 16930-16934.
  34. Varnavski,O.; Goodson, T. Two-photon fluorescence microscopy at extremely low excitation intensity: The power of quantum correlations. *Am. Chem. Soc.* **2020**, *142*, 12966–

- 12975.
35. Varnavski, O.; Gunthardt, C.; Rehman, A.; Luker, G. D.; Goodson, III. T. "Quantum Light-Enhanced Two-Photon Imaging of Breast Cancer Cells" *J. Phys. Chem. Lett.* **2022**, *13*, 12, 2772-2781
  36. M. Y. Lavrentiev, W. Barford, S. J. Martin and H. Daly. Theoretical investigation of the low-lying electronic structure of poly(*p*-phenylene vinylene). *Phys. Rev. B: Condens. Matter Mater. Phys.* **1999**, *59*, 9987–9994.
  37. Guo, F.; Shih, Y. Z. Low-lying two-photon excitations in poly(*p*-phenylene vinylene) and its derivatives. *Chemical Physics Letters* **2003**, *370*, 572–577.
  38. Ghosh, A.; Jana, B.; Chakraborty, S.; Maiti, S.; Jana, B.; Ghosh, H. N.; Patra, A. Exciton Dynamics and Formation Mechanism of MEH-PPV Polymer-Based Nanostructures. *J. Phys. Chem. C* **2017**, *121*, 21062–21072.
  39. De Boni, L.; Andrade, A. A.; Correa, D. S.; Balogh, D. T.; Zilio, S. C.; Misoguti, L.; Mendonca, C. R. Nonlinear absorption spectrum in MEH-PPV/Chloroform solution: A competition between two-photon and saturated absorption processes. *J. Phys. Chem. B* **2004**, *108*, 5221–5224.
  40. Oliveira, S. L.; Correa, D. S.; De Boni, L.; Misoguti, L.; Zilio, S. C.; Mendonca, C. R. Two-photon absorption cross spectrum of a pi-conjugated polymer obtained using the white-light continuum Z-scan technique. *Appl. Phys. Lett.* **2006**, *88*, 021911.
  41. Hancock, S. N.; Yuntawattana, N.; Valdez, S. M.; Michaudel, Q. Expedient synthesis and ring-opening metathesis polymerization of pyridinonorbornenes. *Polym. Chem.* **2022**, *12*, 5530-5535.
  42. Lidster, B. J.; Behrendt, J. M.; Turner, M. L.; Monotelechelic poly(*p*-phenylenevinylene)s by ring opening metathesis polymerization. *Chem. Commun.* **2014**, *50*, 11867–11870.
  43. Villabona-Monsalve, J. P.; Burdick, R. K.; Goodson, III. T. "Measurements of Entangled Two-Photon Absorption in Organic Molecules with CW-Pumped Type-I Spontaneous Parametric Down-Conversion", *J. Phys. Chem. C* **2020**, *124*, 24526-24532.
  44. Khan, R. K. M.; Torker, S.; Hoveyda, A. H. Readily accessible and easily modifiable Ru-based catalysts for efficient and Z-selective ring-opening metathesis polymerization and ring-opening/cross-metathesis. *J. Am. Chem. Soc.* **2013**, *135*, 10258–10261.
  45. Song, J.-A.; Peterson, G. I.; Bang, K.-T.; Ahmed, T. S.; Sung, J.-C.; Grubbs, R. H.; Choi, T. L. Ru-catalyzed, *cis*-selective ring opening metathesis polymerization of various monomers, including a dendronized macromonomer, and implications to enhanced shear stability. *J. Am. Chem. Soc.* **2020**, *142*, 10438–10445.
  46. Kempel, S. J.; Hsu, T.-W.; Michaudel, Q. Stereoretentive olefin metathesis: A new avenue for the synthesis of all-*cis* poly(*p*-phenylene vinylene)s and stereodefined polyalkenamers. *Synlett*, **2021**, *32*, 851–857.
  47. Yu, C.-Y.; Turner, M. L. Soluble Poly(*p*-phenylenevinylene)s through ring-opening metathesis polymerization. *Angew. Chem. Int. Ed.* **2006**, *45*, 7797–7800.
  48. Yu, C.-Y.; Horie, M.; Spring, A. M.; Tremel, K.; Turner, M. L. Homopolymers and block copolymers of *p*-phenylenevinylene-2,5-diethylhexyloxy-*p*-phenylenevinylene and *m*-phenylenevinylene-2,5-diethylhexyloxy-*p*-phenylenevinylene by ring-opening metathesis polymerization. *Macromolecules* **2010**, *43*, 222–232.
  49. Menk, F.; Mondeshki, M.; Dudenko, D.; Shin, S.; Schollmeyer, D.; Ceyhun, O.; Choi, T.-L.; Zentel, R. Reactivity studies of alkoxy-substituted [2.2]Paracyclophane-1,9-dienes and specific coordination of the monomer repeating unit during ROMP. *Macromolecules* **2015**,

- 48, 7435–7445.
50. Lidster, B. J.; Kumar, D. R.; Spring, A. M.; Yu, C.-Y.; Helliwell, M.; Raftery, J.; Turner, M. L. Alkyl substituted [2.2]paracyclophane-1,9-dienes. *Org. Biomol. Chem.* **2016**, *14*, 6079–6087.
  51. Kumar, D. R.; Lidster, B. J.; Adams, R. W.; Turner, M. L. Mechanistic investigation of the ring opening metathesis polymerisation of alkoxy and alkyl substituted paracyclophanedienes. *Polym. Chem.* **2017**, *8*, 3186–3194.
  52. Shin, S.; Menk, F.; Kim, Y.; Lim, J.; Char, K.; Zentel, R.; Choi, T.-L. Living light-induced crystallization-driven self-assembly for rapid preparation of semiconducting nanofibers. *J. Am. Chem. Soc.* **2018**, *140*, 6088–6094.
  53. Gorman, C. B.; Ginsburg, E. J.; Grubbs, R. H. Soluble, highly conjugated derivatives of polyacetylene from the ring-opening metathesis polymerization of monosubstituted cocloctatetraenes: synthesis and the relationship between polymer structure and physical properties. *J. Am. Chem. Soc.* **1993**, *115*, 1397–1409.
  54. Hsu, T.-W, Kempel, S. J., Michaudel, Q. All-cis poly(p-phenylene vinylene)s with high molar masses and fast photoisomerization rates obtained through stereoretentive ring-opening metathesis polymerization of [2,2]paracyclophane dienes with various aryl substituents. *J. Polym. Sci.* **2022**, *60*, 569–578.
  55. Katayama, H.; Nagao, M.; Nishimura, T.; Matsui, Y.; Umeda, K.; Akamatsu, K.; Tsuruoka, T.; Nawafune, H.; Ozawa, F. Stereocontrolled synthesis and optical properties of all-cis poly(phenylene vinylenes) (PPVs): A method for direct patterning of PPVs. *J. Am. Chem. Soc.* **2005**, *127*, 4350–4353.
  56. Moslin, R. M.; Espino, C. G.; Swager, T. M. Synthesis of conjugated polymers containing cis-phenylenevinylenes by titanium-mediated reductions. *Macromolecules* **2009**, *42*, 452–454.
  57. Upton, L.; Harpham, M.; Suzer, O.; Richter, M.; Mukamel, S.; Goodson, T. Optically Excited Entangled States in Organic Molecules Illuminate the Dark. *J. Phys. Chem. Lett.* **2013**, *4*, 2046–2052.
  58. Villabona-Monsalve, J. P., Varnavski, O., Palfey, B. A. & Goodson, T. Two-Photon Excitation of Flavins and Flavoproteins with Classical and Quantum Light. *J. Am. Chem. Soc.* **2018**, *140*, 14562–14566.
  59. Chouk, R.; Bergaoui, M., Jaballah, N.; Majdoub, M.; Khalfaoui, M. Shedding light on structural, optoelectronic and charge transport properties of PPV stereoisomers for multilayer OLED application: A first principle computational studies. *J. Mol. Liq.* **2019**, *284*, 193–202.
  60. Peng, Z. & Yu, L. Synthesis of conjugated polymers containing ionic transition metal complexes. *J. Am. Chem. Soc.* **1996**, *118*, 3777–3778.
  61. Wang, Q., Wang, L., Yu, L. Synthesis and unusual physical behavior of a photorefractive polymer containing tris (bipyridyl) ruthenium (II) complexes as a photosensitizer and exhibiting a low. *J. Am. Chem. Soc.* **1998**, *120*, 12860–12868.
  62. Wang, Q. & Yu, L. Conjugated polymers containing mixed-ligand ruthenium(II) complexes. Synthesis, characterization, and investigation of photoconductive properties. *J. Am. Chem. Soc.* **2000**, *122*, 11806–11811.
  63. Sumpter, B. G. *et al.* Computational study of the structure, dynamics, and photophysical properties of conjugated polymers and oligomers under nanoscale confinement. *ACS Publ.* **2005**, *109*, 7671–7685.

64. Correia, H., Ramos, M. Modelling the effect of nonplanarity on charge transport along conjugated polymer chains. *Materials Science and Engineering C* **2007**, *27*, 1133–1137.
65. Ghosh, A. *et al.* Exciton Dynamics and Formation Mechanism of MEH-PPV Polymer-Based Nanostructures. *J. Phys. Chem. C* **2017**, *121*, 21062–21072.
66. Meskers, S. C. J., Janssen, R. A. J., Haverkort, J. E. M., & Wolter, J. H. Relaxation of photoexcitations in films of oligo- and poly- (para-phenylene vinylene) derivatives. *Chemical Physics* **2000**, *260*, 415–439.
67. Herz, L. M., Silva, C., Grimsdale, A. C., Müllen, K. & Phillips, R. T. Time-dependent energy transfer rates in a conjugated polymer guest-host system. *Phys. Rev. B – Condens. Matter Mater. Phys.* **2004**, *70*, 1–9.
68. Nguyen, T. Q., Wu, J., Doan, V., Schwartz, B. J. & Tolbert, S. H. Control of energy transfer in oriented conjugated polymer-mesoporous silica composites. *Science* **2000**, *288*, 652–656.
69. Carlotti, B.; Cai, Z.; Kim, H.; Sharapov, V.; Madu, I. K.; Zhao, D.; Chen, W.; Zimmerman, P. M.; Yu, L.; Goodson, T., III Charge Transfer and Aggregation Effects on the Performance of Planar vs Twisted Nonfullerene Acceptor Isomers for Organic Solar Cells. *Chem. Mater.* **2018**, *30*, 4263–4276.
70. Madu, I. K.; Muller, E. W.; Kim, H.; Shaw, J.; Burney-Allen, A. A.; Zimmerman, P.; Jeffries-el, M.; Goodson, T., III Heteroatom and Side Chain Effects on the Optical and Photophysical Properties: Ultrafast and Nonlinear Spectroscopy of New Naphtho[1,2-b:5,6-b']difuran Donor Polymers. *J. Phys. Chem. C* **2018**, *122*, 17049–17066.
71. Keller, B.; McLean, A.; Kim, B. G.; Chung, K.; Kim, J.; Goodson, T., III Ultrafast Spectroscopic Study of Donor-Acceptor Benzodithiophene Light Harvesting Organic Conjugated Polymers. *J. Phys. Chem. C* **2016**, *120*, 9088–9096.
72. Eshun, A.; Cai, Z.; Awies, M.; Yu, L.; Goodson III, T. Investigations of thienoacene molecules for classical and entangled two-photon absorption. *The Journal of Physical Chemistry A* **2018**, *122*, 8167–8182.
73. Mandal, H.; Ogunyemi, O. J.; Nicholson, J. L.; Orr, M. E.; Lalis, R. F.; Rentería-Gómez, Á.; Gogoi, A. R.; Gutierrez, O.; Michaudel, Q.; Goodson, T. Linear and Nonlinear Optical Properties of All- *Cis* and All- *Trans* Poly( *p* -Phenylenevinylene). *J. Phys. Chem. C* **2024**, *128* (6), 2518–2528. <https://doi.org/10.1021/acs.jpcc.3c07082>.

## Chapter VI

### Effect of Long-Lived Ground State Diradicaloids on the Photophysics of Semi-Ladder Thiophene-Based Polymer Aggregates for Organic Light Emitting Transistor (OLET) Applications

#### VI.1 Collaboration Statement

This Chapter describes the results of a collaborative research investigation between Professor Theodore G. Goodson III's group (first author and *Collaborator 1*), Department of Chemistry and Macromolecular Science & Engineering, University of Michigan, Professor Angela K. Wilson's group (*Collaborator 2*), Department of Chemistry, Michigan State University and Professor Luping Yu's group (*Collaborator 3*), Department of Chemistry and The James Franck Institute, The University of Chicago. The authors of this collaborative research investigation are (in order of first to corresponding): Angalar K. Muthike; Mohammad Ahmad Awais; Cong Wang; **Meghan E. Orr**; Nuno M.S. Almeida; Sasha C. North; Professor Luping Yu; Professor Angela K. Wilson; and Professor Theodore G. Goodson III. The contribution of the first author to this research investigation is: sample preparation for steady-state and quantum yield measurements and time resolved fluorescence (time-correlated single photon counting (TCSPC) and fluorescence upconversion (UpC)), nanosecond transient absorption (ns-TA) and electron paramagnetic resonance experiments; conducting the listed measurements and experiments; performing data analysis on the listed measurements and experiments; writing and editing the paper for this research investigation. The contribution of *Collaborator 1* (**Meghan E. Orr**, author of this dissertation) is sample preparation for femtosecond transient absorption experiments and conducting and



performing data analysis of fs-TA experiments. The contribution of *Collaborator 2* is performing density functional theory (DFT) and time-dependent (DFT) (TD-DFT) theoretical calculations; conducting data analysis of theoretical calculations; and writing and editing the paper for this research investigation. The contribution of *Collaborator 3* is providing samples for this research investigation.

## VI.2 Abstract

To fully utilize the immense potential that lies within organic light emitting transistors (OLETs), a class of optoelectronic applications, more studies are needed to completely dissect the mechanism of charge transfer in these devices. However, most of these studies lean towards understanding either organic light-emitting diodes (OLEDs) or organic field-effect transistors (OFETs). So far, there is promise in open-shell structures which have been reported to enhance the spin density that is delocalized along the planar  $\pi$  –conjugated backbone, ultimately affecting their charge transfer and overall device performance efficiency. These structures tend to have low-lying triplets and small singlet-triplet bandgaps which are favorable for charge and energy transfer. Open-shells in form of diradicals have been reported to enhance the efficiency of OLEDs by offering intermolecular spin-spin interactions which lead to  $\sigma$  –aggregation. This  $\sigma$  –aggregation eventually leads to the formation of  $\sigma$  –polymerization affecting intermolecular stacking and charge transport, which has proved to be good for OLEDs. It has been reported that these low bandgaps, intimate intermolecular interactions, and redox amphoterism increase the overall efficiency of OFETs. However, there is no report on how these diradical states affect the efficiency of OLETs. To the best of our knowledge, this is the first report highlighting the formation of ground state diradicals in OLET systems. We use time-resolved and nonlinear optical spectroscopy as well as computational methods, to show the existence of long-lived diradical states in the

thiophene-based polymer chains. On the other hand, the furan-based polymer chains show the formation of long-lived zwitterions. We propose that the formed diradical character with a lifetime of 25  $\mu$ s lowers the charge transport in the resonant structures, reducing charge transfer and negatively affecting the external quantum efficiency of the thiophene-based OLETs.

### **VI.3 Introduction**

Organic light emitting transistors (OLETs), first reported in 2003, is a rising class of organic optoelectronic devices that have a unique advantage of combining the electrical switching functionality of organic field-effect transistors (OFETs), and the light generation capability of organic light emitting diodes (OLEDs) in a single device.<sup>1-3</sup> While the technology of OFETs and OLEDs are individually and significantly developed, the working mechanisms and principles of OLETs and their potential have not been exploited enough.<sup>2-4</sup> The existing research has shown that OLETs have an immense potential to reduce the complexity and enhance the performance of next-generation pixel circuitry.<sup>2</sup> Thus far, OLETs have shown magnificent potential in a diverse range of applications like optical communications systems, electroluminescent displays, electrically pumped organic lasers and solid-state lighting sources.<sup>2,5</sup> However, the applicability of these OLETs is far from implementation due to their poor performance in terms of low brightness, low carrier mobility and high driving voltage.<sup>6</sup> These properties have been reported in organic semiconducting (OSC) materials and have been used as the active materials of the OLETs.

A good material for this application is supposed to show high and balanced ambipolar field effect transport charge mobilities as well as increased fluorescence quantum yield in the same material.<sup>7</sup> Recent reports have shown that OSC materials for these OLET devices are made of small molecules and polymers which hold the right luminescent properties: a small bandgap in the visible region of the electromagnetic spectra to minimize charge injection barriers; possess high;

balanced and ideally ambipolar charge carrier mobility for light emission; and have high shelf-life.<sup>8</sup> The increased interest in small molecules as potential OLET active materials is due to their molecular structure and high-mobility characteristics.<sup>9</sup> The delocalization of  $\pi$ -bonds in these small molecules and polymers lead to good photoabsorption, charge carrier photogeneration and transport making these materials great for OLET applications. So far, the organic materials that have been considered and used to engineer highly performing OLETs can be grouped into: fluorenes; oligothiophenes; phenylene-vinylene-based polymers; biphenyls; acenes; oligothiophenes; thiophene/phenylene co-oligomers; furan-incorporated oligomers; spirobifluorenes; phosphorescent materials; and so on. Although conjugated polymers have shown a lot of promise as OLET materials, a major drawback in using these light emitting polymers is their low charge carrier mobility, which limits the device performance. A lower bandgap of the conjugated polymers is preferable to enhance the intramolecular charge transfer across the main donor-acceptor chain, with a lower-lying lowest unoccupied molecular orbital (LUMO) which is better for n-type OLETs.<sup>10</sup> In addition, these donor-acceptor polymers induce intermolecular interactions through increased molecular ordering resulting from the self-assembly of polymer chains, and this effect has led to high field-effect mobility in OFETs.<sup>11</sup>

While single-component OLETs have been successfully developed, only an external quantum efficiency (EQE) of 1.61% has been obtained.<sup>12</sup> Due to the difficulties in attaining large mobilities in single OLET materials, multilayer devices where different functions are delegated to different materials have been developed leading to improved EQEs of up to 9.01%.<sup>6</sup> For the multilayered devices, however, the device fabrication process becomes extremely complicated as more layers are added since it becomes very difficult to control the mutually exclusive device properties of the OSC active materials while keeping their optoelectronic performance optimal.<sup>9</sup> For instance,

high mobility materials show efficient intermolecular charge transport owing to their optimal  $\pi - \pi$  stacking and electronic coupling; the efficient  $\pi - \pi$  stacking may lead to the formation of excited state dimers or other charge transfer states which quench fluorescence and reduces the performance of OLETs.<sup>3</sup> Therefore, it is important to find a balance between the multiple parameters that should be considered when fabricating high-performance OLET systems: suitable energy levels, optimal fluorescent quantum yields, optimal charge mobility and correct aggregation state.<sup>7,9,10,13</sup>

Recently, Yuan and et al. synthesized semi-ladder polymer systems that not only address the above issues, but also the first-of-a-kind OLET systems that exhibit a folding structure only previously observed and well-studied in biological systems.<sup>5</sup> These biological macromolecules have shown the existence of foldamers that adopt highly ordered and helical self-assembled structures through noncovalent interactions.<sup>5,14-16</sup> The idea was that this structural twist would improve the materials' electrical and light-emitting properties.<sup>5</sup> Shown in **Figure VI.1** are the structures of the two investigated polymers, as well as the thiophene-based acceptor (TPTQ Acceptor). Here, two different acceptor (A) monomers: thienopyridothienoquinoline which has a thiophene incorporated (TPTQ) and thienopyridothienoquinoline with a furan molecule incorporated (TPTQF), each acceptor coupled to a carbazole donor (D) monomer moiety, were synthesized.<sup>5</sup> These  $D - A - D$  polymers were synthesized based on the idea that ring fusion in ladder building blocks can enhance rigidity in the molecular system, which minimizes the non-radiative decay and thus improve fluorescence quantum yield. Interestingly, they reported that these structures can exist in their electron resonant forms as a result of their quadrupole interactions forming a  $D - A^- - D^+$  structures, which tend to display non-Kasha spectroscopic behavior.<sup>5,13,17</sup> Furan derivatives have been reported to be better than thiophene derivatives in terms of solubility,

increased power conversion efficiencies, and formation of quinoidal structures owing to the lack of aromaticity in sulfur in comparison to thiophene.<sup>1</sup> While thiophene based molecules have been highly investigated due to their abilities to increase molecular conjugation, furan-based counterparts are seemingly promising due to their reported tendency to increase conjugation and improve the charge transport properties.<sup>18</sup> The furan-based molecules have shown enhanced performance which has been linked to their increased dipole moments, due to the large electronegativity of oxygen, and weak solid-state interaction between furan moieties making them highly soluble.

Additionally, Yuan and et al. report that these polymers have the special ability to form foldable structures and exist in their resonant forms.<sup>5</sup> Before this report, literature research showed that folding structures form ordered and helical self-assembled structures through non-covalent interactions.<sup>5,14,15</sup> The molecular conformation is rigidified by intramolecular hydrogen bonding, leading to strong interactions between the discs.<sup>19</sup> These  $\pi$ -conjugated compounds are believed to form a helical conformation through solvophobic interactions in polar solvents and unravel into a random coil in chloroform.<sup>20</sup> Moreover, quinoline structures have shown the capability of existing in their electron resonant forms while carbazole-based molecules have shown their capabilities to form zwitterions and diradicals which then affect the energy and charge transfer mechanisms of their derivatives.<sup>21–24</sup> Interestingly, some of these zwitterions have displayed diradical character and in other cases, photocatalyzation of different materials through proton transfer followed by electron re-organization may convert the zwitterions into diradical intermediates.<sup>23,25</sup>

Unfortunately, most literature reports use diradicals and biradicals interchangeably which leads to confusing and conflicting information regarding their respective photophysical properties and their effect on device performance. While both are defined by the presence of two unpaired

non-bonding and degenerate electrons (radicals) in an open-shell structure, the distance between the two unpaired electrons ( $r$ ) as well as the electron exchange integral ( $J$ ) can be used to differentiate between these two states. In the case of the biradicals, the distance between the two non-bonding electrons is so long that the electron exchange interaction is negligible, or almost zero. On the other hand, when the coupling between the two non-bonding electrons is strong, due to a large magnitude of dipole-dipole interaction in a molecule, the distance between the electrons is ideally zero and these two electrons are referred to as diradicals.<sup>26</sup> For nearly degenerate molecular orbitals, the terms used are diradicaloids or biradicaloids for diradicals and biradicals, respectively.

Recently, organic semiconductors that show open-shell diradical character that could be used in organic electronics like organic light emitting diodes (OLEDs), organic photovoltaics (OPVs) and organic field effect transistors (OFETs) have been reported.<sup>24,27-31</sup> Increased diradical character has been reported to activate exothermic singlet exciton fission which increases the performance and stability of OPVs.<sup>32</sup> Diradical character has also been reported to affect the optical, electronic, magnetic properties, as well as the chemical reactivity of organic optoelectronic materials.<sup>33</sup> This is due to the presence of unpaired electrons which take part in the low- to high-spin state transitions. In addition, various reports have shown the diradical effect on OFETs where they increase the stability and half-life of these optoelectronics.<sup>34-36</sup> In a recent review, Dong and Li mention that the ground state of these materials are highly controversial due their high reactivity towards oxygen. To mitigate stability issues, they suggested using various substituents like mesityl on S-atom acene analogues and using bulky compounds led to half-lives of more than a month.<sup>36</sup> Delocalization of these radicals on the organic  $\pi$ -system dilates the spin density of the molecules and therefore reduces their reactivity. In another report, neutral radicals from various open-shell

molecules have been used to fabricate OLEDs with up to 10% external quantum efficiency.<sup>30,37</sup> Because luminescent radicals emit from the radiative decay of doublet excitons, the theoretical internal quantum efficiency (IQE) can be up to 100%. However, while a lot of research has been done in synthesizing these materials, very little is known about the photophysics and charge transfer mechanisms that affect their EQEs. To the best of our knowledge, no one has reported the existence of diradical character in OLET foldamers which would highly affect their energy transfer process and efficiency.

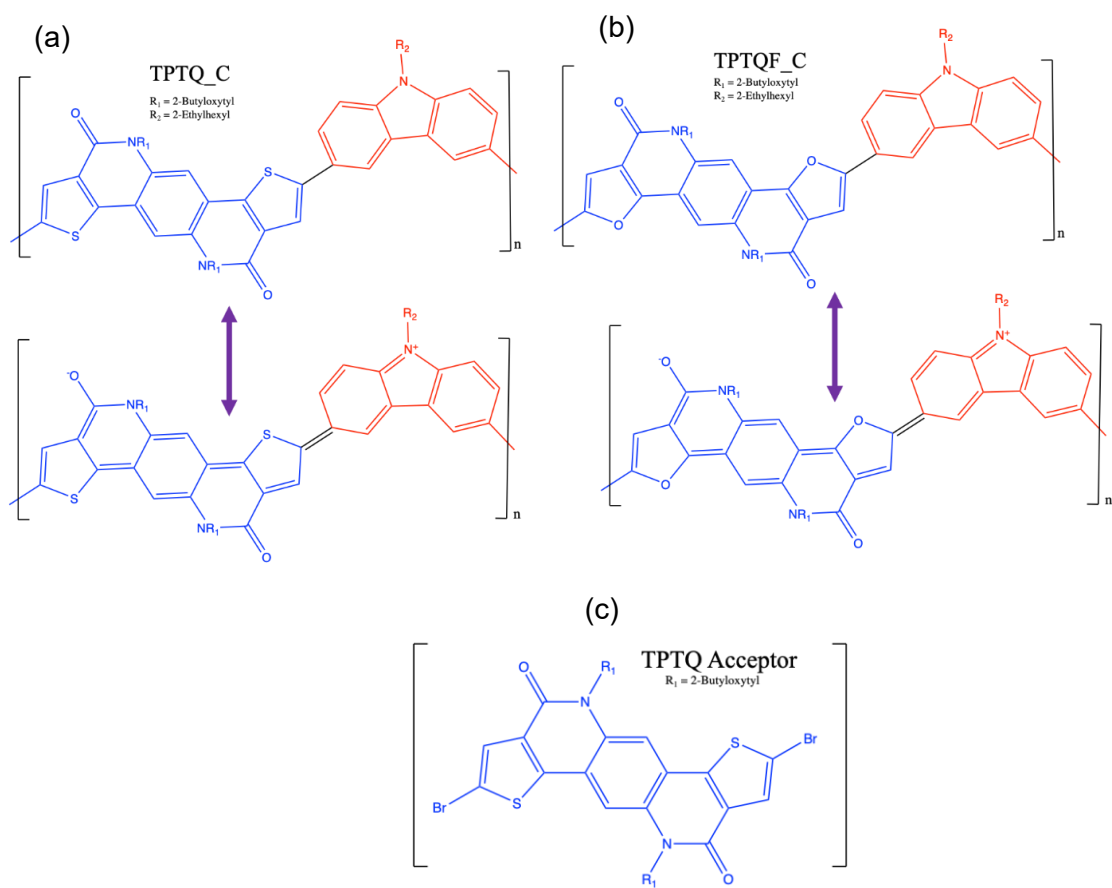


**Figure VI.1:** Structures of the investigated polymers (TPTQ\_C and TPTQF\_C and their respective resonant forms) as well as the TPTQ Acceptor.

In this study, time-resolved and nonlinear spectroscopic techniques, as well as computational methods, are used in a groundbreaking report, that shows the formation and effect of triplet ground state diradicaloids on the photophysical properties of the previously synthesized carbazole-donor based foldable polymers for OLET applications. We find that thiophene-acceptor-based foldamers show a diradical character with reduced dipole moments which lowers the charge separation in the resonance structures, reducing the charge transfer and the external quantum efficiency of the TPTQ\_C molecule (0.005%). However, there is no observed diradical character in the furan-based foldamers, exhibiting superior device performance with 3.5% EQE. Our results will be a step towards producing materials that can be used for high-performance devices.

## VI.4 Results

### VI.4.a Steady State Measurements

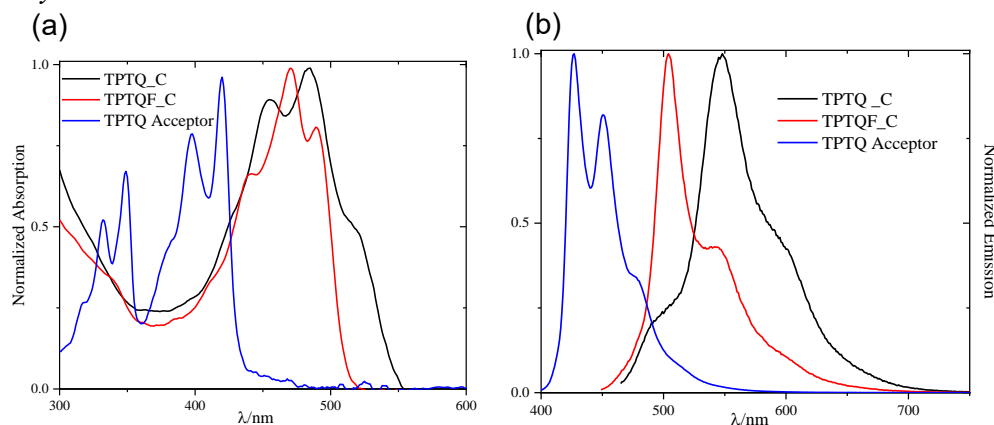


**Figure VI.2:** Absorption (a.) and emission (b) spectra of the two investigated polymers as well as the parent thiophene-based acceptor.

Shown in **Figure VI.2** are the steady-state absorption and emission spectra for the investigated polymers, TPTQ\_C and TPTQF\_C and the TPTQ acceptor. These measurements were done in chloroform and their data is summarized in **Table VI.1**. In **Figure VI.2.a**, both of the polymers show two distinct absorption bands which has been reported for donor-acceptor polymers. The two absorption bands for the TPTQ acceptor also show some level of charge transfer



happening within the acceptor itself. In addition, the full-width half max (FWHM) of the polymers' absorption spectrum (right absorption band) is significantly bigger than that of the TPTQ acceptor. This larger FWHM shows that the polymers have a better capability to harvest sunlight.<sup>38</sup>

The steady-state absorption shows two absorption bands in both investigated polymers and the TPTQ acceptor. These bands have been associated with charge transfer from the donor to the acceptor. For the polymers, the broader absorption maxima peaks which are red-shifted can be attributed to the highest occupied molecular orbital (HOMO) → lowest unoccupied molecular orbital (LUMO) transition which signifies intramolecular charge transfer between the donor and the acceptor. The slightly red-shifted absorption spectra of the TPTQ\_C indicates that this polymer has a lower HOMO-LUMO bandgap and is expected to show enhanced charge transfer capabilities compared to its furan-based TPTQF\_C analogue. Interestingly, a weak low energy shoulder is very visible in the broadened absorption of the TPTQ\_C molecule at 520 nm. However, the absorption bands in the blue have been attributed to localized  $\pi$ - $\pi^*$  transitions.<sup>39</sup> The steady-state absorption for TPTQF\_C is narrower, and its maximum peak is blue-shifted in comparison to that of TPTQ\_C which is an indicator of a good emissive material.

The decrease in the 0–0/0–1 absorption intensity ratio as one compares the absorption spectra of the TPTQ acceptor to those of the polymer molecules shows that the polymers form H-aggregates. These H-aggregates exist even at the level of a single polymer chain as shown by the consistent spectral appearance at very low concentrations (**Figure VI.2**). This result means that the polymer is folded to enhance H-aggregation, leading to intrachain H-aggregation. Previous studies have shown that in semiconducting polymers, H-aggregates are due to strong intrachain interactions.<sup>40</sup> Therefore, it is proposed that these polymers form folded chains and movement of charge is through intrachain charge transfer. The extinction coefficient of both polymers at their

highest absorption wavelengths and the TPTQ acceptor are shown in **Table VI.1**. Although the absorptivity is similar for the investigated polymers, TPTQF\_C has a slightly higher molar extinction coefficient in the solution. Its molar extinction coefficient at the maximum absorption wavelength (470 nm) is  $42505 \text{ M}^{-1}\text{cm}^{-1}$ . This slight increase is quite interesting given that the TPTQ\_C polymer counterpart has a broadened and red-shifted absorption and is expected to show a higher extinction coefficient.

In addition, the absorption spectra of both polymers show well-resolved vibronic transitions. Compared to the TPTQ acceptor absorption, the 0–0 transitions of the polymers are significantly different where their 0–0 transition intensity is significantly reduced, and 0–1 transition becomes the strongest; this change in the feature intensity indicates the formation of H-aggregates. In addition, there is a significant enhancement of the 0–0 transition peak at 470 nm of TPTQF\_C compared to the 0–0 transition peak of TPTQ\_C at 483 nm indicating stronger aggregation of the TPTQF\_C polymer chain.

**Table VI.1:** Linear optical properties for the investigated polymers, TPTQ\_C and TPTQF\_C, and the TPTQ Acceptor in chloroform.

Compound	$\lambda_{\text{abs}}$ nm	$\lambda_{\text{em}}$ nm	$\lambda_{\text{Phosph.}}$ nm	Stokes Shift $\text{cm}^{-1}$	$\epsilon$ $\text{M}^{-1}\text{cm}^{-1}$	$\phi_{\text{F}}$ % (UP)	$\phi_{\text{F}}$ % (P)	$\delta\text{TPA/GM}$ $\lambda_{\text{exc}} = 790$ nm
TPTQ Acceptor	332, 348, 397, <b>419</b>	<b>426</b> , 450, 477	844	392	4261	14	11	67.4
TPTQ_C	455, <b>483</b> , 520	492, <b>548</b> , 600	970	2456	42437	38	36	223
TPTQF_C	440, <b>470</b> , 489	<b>504</b> , 544	944	1435	42505	44	42	289

The emission spectra of both polymers and the acceptor, which were obtained in chloroform, are shown in **Figure VI.2** and the relevant data recorded in **Table VI.1**. Structurally, it is clear that the thiophene based polymer, TPTQ\_C has an additional emissive peak around 490 nm. The emission spectra of the rigid TPTQF\_C is blue shifted compared to that of TPTQ\_C. A smaller Stokes Shift and higher fluorescence quantum yields (**Table VI.1**) are observed for TPTQF\_C compared to TPTQ\_C which may be attributed to the heavy atom effect in TPTQ\_C. The decreased Stokes Shift of TPTQF\_C confirms its increased backbone rigidity compared to that of TPTQ\_C.<sup>5</sup> Compared to both polymers, the fluorescence quantum yield of the TPTQ Acceptor is more than two times lower. However, an intense fluorescence in the furan-based polymer (TPTQF\_C) was observed which has been associated with decreased intersystem crossing due to lack of the heavier atom, sulfur.<sup>5</sup> Here, the increased fluorescence quantum yield shows enhanced radiative decay pathways. For the case of the TPTQ\_C polymer, the decreased fluorescence quantum yield has been associated with enhanced non-radiative processes. In all the investigated materials, an approximately ~2% decrease in fluorescence quantum yield is observed upon oxygen purging.

Concentration dependence of absorption measurements were used to check evidence of polymer aggregate chain formation or polymer folding. In both polymer cases, decrease in concentration does not change the shape of the spectra indicating that the H-aggregates exist even at the level of a single polymer chain (in very low concentrations). This means that the polymer is folded to enhance H-aggregation, leading to intrachain H-aggregation.

In addition, temperature-dependence of emission measurements were carried out to check the possibility of triplet formation in these molecules through phosphorescence. It has been reported that an increase in temperature induces intersystem crossing (ISC) of singlet ( $S_1$ ) to triplet

(T<sub>1</sub>) leading to a decrease in fluorescence intensity. Since triplets are usually at lower energies compared to singlet states, the temperature-dependent emission is usually observed in the near infra-red region. Therefore, these measurements show the presence of phosphorescence and can be used to determine the energy of triplets. As shown in, temperature-dependent emission is observed in all the investigated molecules. For the TPTQ Acceptor, two bands are observed, one peaked at 844 nm and the other one peaked at 906 nm (see **Table VI.1**). The 844 nm peak decreases in intensity as the temperature of the solution increases from 77 K to 273 K. On the contrary, the intensity of the 906 nm peak increases as the temperature increases. Given that high temperatures quench triplet emission, it is safe to assign 844 nm to triplet state. Therefore, the energy of the TPTQ Acceptor triplet is 1.469 eV. For the thiophene-based compound TPTQ\_C and the furan-based compound TPTQF\_C, the emission band whose intensity decreases as the temperature of their respective solutions increase from 77 K to 273 K are peaked at 970 nm and 944 nm, respectively. As such, their triplet energies are 1.28 eV and 1.31 eV for TPTQ\_C and TPTQF\_C, respectively.

#### VI.4.b Two-photon Absorption or Two-photon Excited Fluorescence

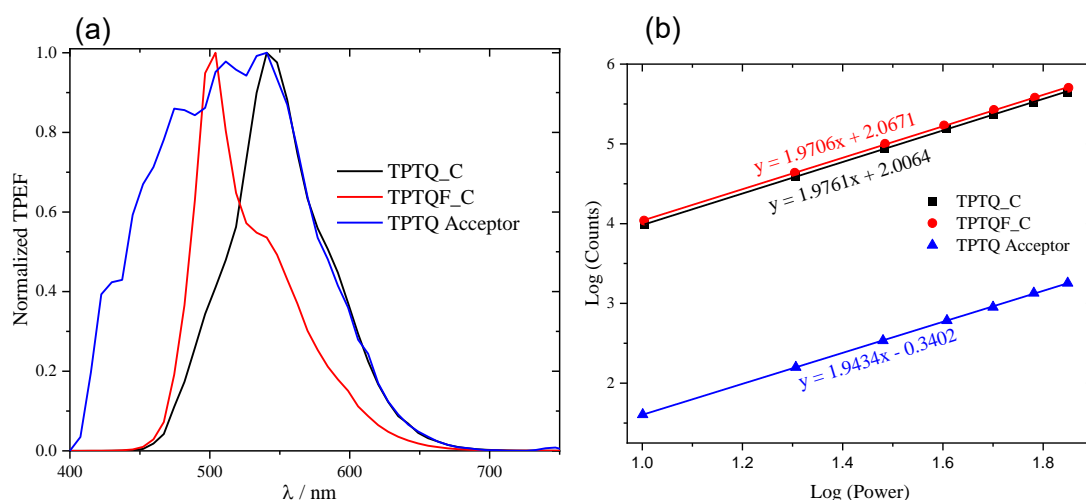


**Figure VI.3:** Two photon emission spectra (a.) and power dependence of the two photon excited emission (b.) of the investigated polymers in chloroform upon 800 nm excitation.

The two-photon absorption (TPA) cross sections show remarkable values of hundreds of GM (see **Table VI.1** and **Figure VI.3**). The TPA cross section for the TPTQF\_C polymer is 1.3 times more than that of TPTQ\_C. TPA cross section has been directly related to the change in static and transition dipole moments, which are directly proportional to the charge transfer character of a molecule.<sup>41</sup> Therefore, from the obtained TPA results, TPTQF\_C has enhanced intrachain charge transfer compared to its thiophene-based analogue (TPTQ\_C). The increased transition dipole moments in TPTQF\_C is due to the increased electronegativity of the oxygen atom. These increased transition dipole moments could suggest a better interaction between the donor-acceptor junctions, which leads to a more efficient charge transfer. The increased TPA cross-section in TPTQF\_C may be attributed to its expanded  $\pi$ -conjugation which increases the number of  $\pi$ -delocalized electrons as well as the delocalized degree of  $\pi$ -electrons.

#### VI.4.c Time-resolved Measurements

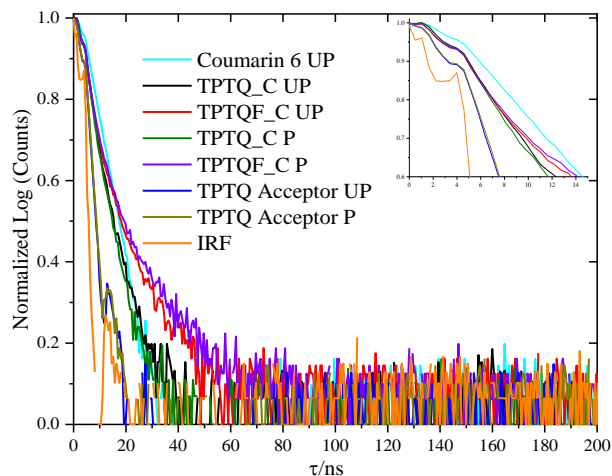


**Figure VI.4:** Fluorescence decay lifetimes of the investigated polymers obtained using time correlated single photon counting experiments. The inset shows the decay dynamics at earlier times.

To understand the fluorescence dynamics of these polymers, time-correlated single photon counting (TCSPC) and fluorescence upconversion (FUC) measurements were carried out. The

decay kinetics are in **Figure VI.4** and the fitted data are in **Table VI.2**. At the emission maximum, a mono-exponential decay function was used to fit the used reference, Coumarin 6, the unpurged and purged spectra of the TPTQ acceptor as well as the thiophene-based TPTQ\_C polymer. However, a bi-exponential decay function was used to fit both the unpurged and purged data of the TPTQF\_C polymer. The fluorescence lifetime of the Coumarin 6 reference was found to be 2.8 ns (**Table VI.2**) which matches very well with the reported 2.4 ns.<sup>42</sup> While both polymers' decay at earlier times starts off at the same rate, the decay of the furan-based polymer slows down midway showing a bi-exponential decay. At ambient conditions,  $\tau_1$  contribution in the furan-based polymer is 28% leaving only 72% for  $\tau_2$ . However, when oxygen is purged out, the  $\tau_1$  contribution drops to 24% while  $\tau_2$  contribution increases to 76%. Since oxygen has been reported to quench triplet excitons and with the rule 25% singlet and 76% triplet excitons rule, we can assign the slowly decaying component of the TPTQF\_C to triplet species. This contribution is shown by the lifetimes reported on **Table VI.2**. For TPTQ\_C polymer, only one species is observed which decays within 3.2 ns and its lifetime is not affected by oxygen purging, meaning that this contribution is from singlet species. However, the TPTQ acceptor, which also decays mono-exponentially, decays more than two times faster compared to TPTQ\_C polymer and the first component of the TPTQF\_C polymer as shown in **Figure VI.4** and **Table VI.2**.

**Table VI.2:** Time resolved excited state lifetime dynamics of the investigated foldable polymers as well as the TPTQ acceptor in chloroform at the underlined wavelengths.

Compound	$\lambda_{em}$ / nm	$\tau_1$ (UP)	$\tau_2$ (UP)	$\tau_1$ (P)	$\tau_2$ (P)
TPTQ Acceptor	<u>426</u> , 450, 477	1.3	N/A	1.3	N/A
TPTQ_C	492, <u>548</u> , 600	3.2	N/A	3.2	N/A
TPTQF_C	<u>504</u> , 544	2.9	7.4	2.9	9.0
Coumarin 6		2.8	-	-	-

Interestingly, fluorescence dynamics were also checked at other emitting wavelengths for both polymers. For the furan-based polymer (TPTQF\_C), the species at longer wavelengths (542 nm) emits faster compared to those found at the maximum emission peak (504 nm). In the thiophene-based polymer, however, the low wavelength species emits the fastest. The similarity in decay kinetics between the 498 nm and the 598 nm could mean that these are similarly emissive species. However, it is clear that 548 nm species emits differently and can be assigned to different species.

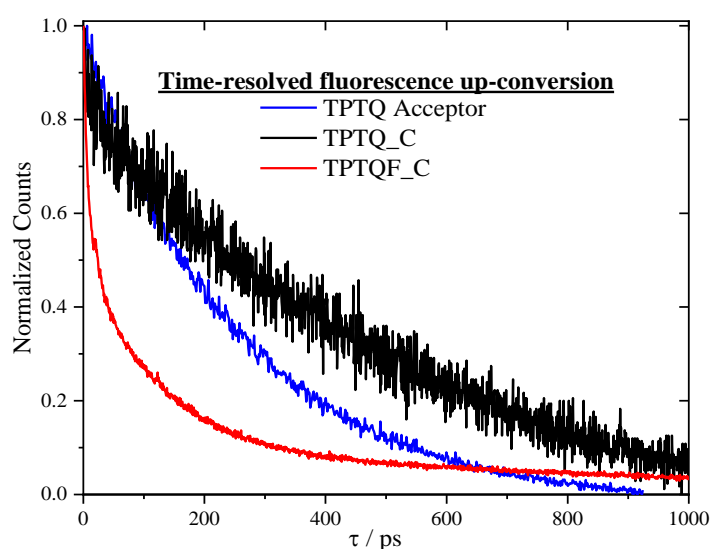


**Figure VI.5:** Ultrafast fluorescence kinetics of the investigated polymers and TPTQ Acceptor using fluorescence upconversions

Time-resolved fluorescence up-conversion measurements are used to resolve the fast fluorescence of these investigated compounds. As shown in **Figure VI.5**, the three compounds have different decay dynamics which were fitted and reported in **Table VI.3**. While the TPTQ acceptor fitted into a bi-exponential function, both polymers fitted in a tri-exponential function. The earlier two decay components for both polymers are very fast, however, that of TPTQ\_C portrays faster dynamics (1 ps and 23 ps) compared to the 5 ps and 51 ps decay time of TPTQF\_C. Interestingly, the final polymer decay-component which does not necessarily decay completely

shows that TPTQF\_C decays 2.3 times faster compared to the TPTQ\_C. The result showing the third ultrafast decay component of the polymers being faster in TPTQF\_C matches well with the results obtained using the time-correlated single photon counting, where the decay time of the earlier components of the furan-based polymer is faster compared to the thiophene-based counterpart. Therefore, comparing just the polymers, the fluorescence decay results trend obtained using ultrafast up-conversion results (later component) matches those obtained using the time correlated single photon counting (earlier component). At earlier times, however, the TPTQ acceptor decay time is significantly slower (more than an order of magnitude) than that of both polymer systems. This could indicate that at these earlier times, the polymers are forming a fast species which is not observed in the TPTQ acceptor.

**Table VI.3:** Ultrafast time resolved excited state lifetime dynamics of the investigated foldable polymers as well as the TPTQ acceptor in chloroform at the underlined wavelengths.

<b>Compound</b>	$\lambda_{em} / \text{nm}$	$\tau_1$	$\tau_2$	$\tau_3$
<b>TPTQ Acceptor</b>	480	61	264	N/A
<b>TPTQ_C</b>	500	4	50	651
<b>TPTQF_C</b>	500	16	205	N/A

#### *VI.4.d Transient Absorption Spectroscopy*

Both nanosecond and femtosecond transient absorption measurements were used to probe the excited state dynamics of the investigated molecules. The nanosecond transient absorption spectroscopy (nsTAS) measurements were used to probe the long-lived excited state dynamics



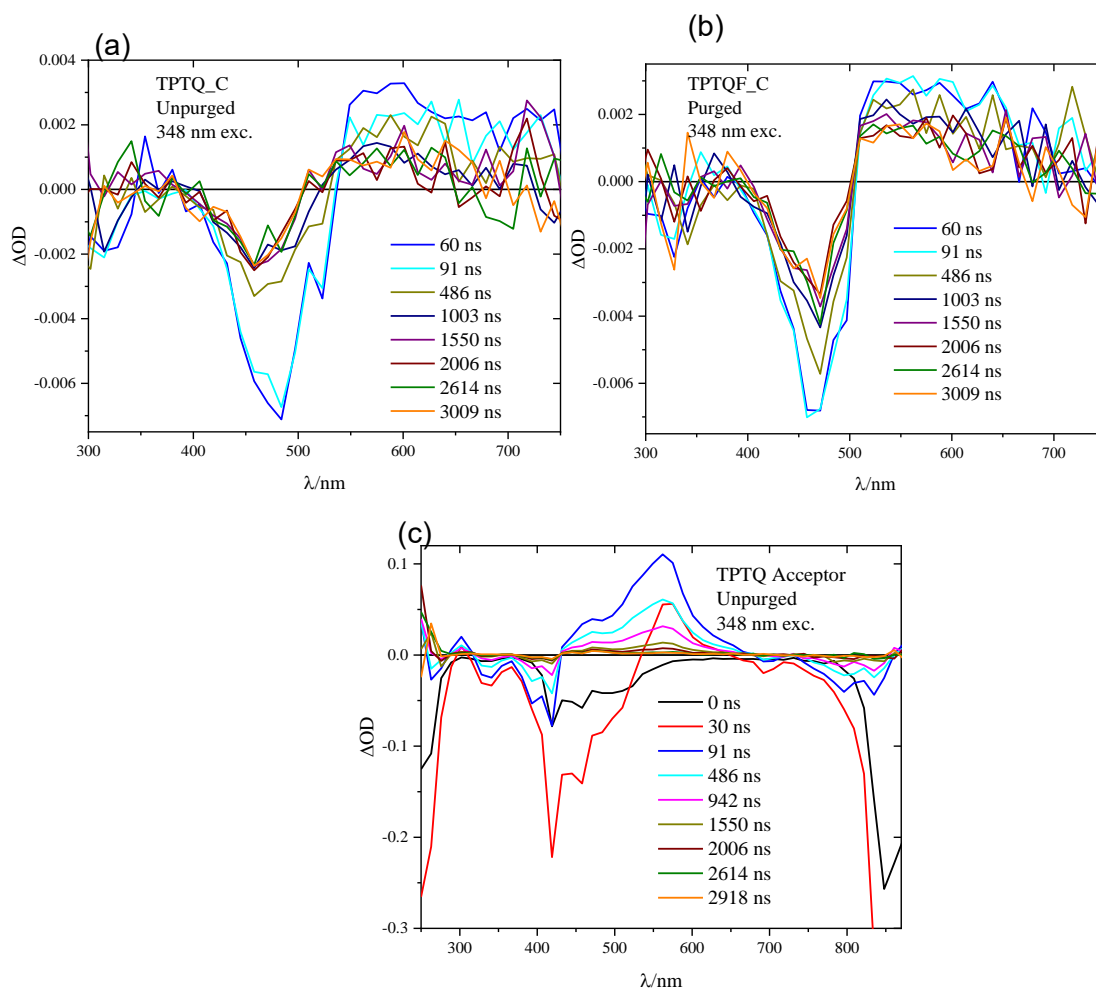


**Figure VI.6:** Time resolved nanosecond transient absorption (nsTA) spectra of the investigated polymers with UV excitation of  $\sim 2.3$  mJ.

while the femtosecond transient absorption spectroscopy (fsTAS) was used to probe the contribution of short-lived states in the photophysics of these materials. Time-resolved spectra, of both ns- and fs-TAS, shows depletion of the ground state, also known as the ground state bleach (GSB). For the nsTAS, the compounds were excited using both low (absorption maxima of the measurements were done at low fluence ( $\sim 1.2$  mJ) excitation. With a visible wavelength excitation (483 nm for TPTQ\_C and 470 nm for TPTQF\_C), a broad and intense stimulated emission that decays within 100 ns is observed for both polymers. Without the fluorescence background subtraction and exciting at the compounds at their respective maximum absorptions, both polymers

show a very small ESA. The peak of these ESAs can be estimated to be around 560 nm and 536 nm for both TPTQ\_C and TPTQF\_C, respectively. The respective materials) and high (348 nm) energies. All GSBs, whose peak maxima match well with the compounds' absorption spectra, are observed for both molecules. This similarity is evidence that the GSB peaks are as a result of ground state depletion. The observed ESAs are more clear and less noisy when the compounds were excited using higher energy (348 nm) as shown in **Figure VI.6**. The spectra and ESA kinetics of these polymers did not change when the two molecules were excited in the UV with the fluence kept low.

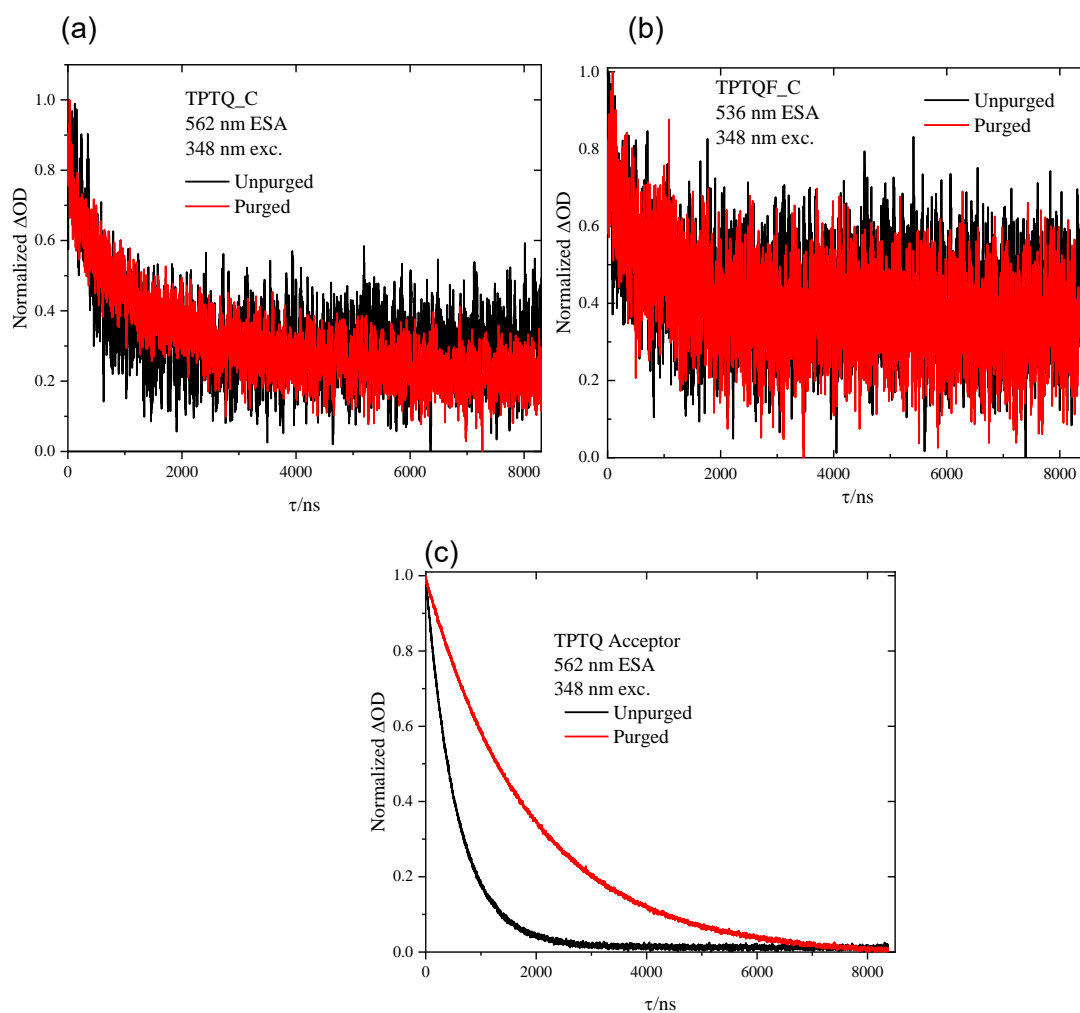


**Figure VI.7:** Nanosecond transient absorption ESA kinetics of the investigated polymers with UV excitation of  $\sim 2.3$  mJ.

As shown in **Figure VI.7**, a GSB which resembles the one previously obtained in is observed. The small ESA that is seen at around 560 nm for TPTQ\_C and 536 nm for TPTQF\_C becomes more prominent as shown in **Figure VI.7**. For the TPTQ\_C compound, the lifetime of the GSB observed at 484 nm increases slightly upon oxygen purging, which may be an indicator of non-singlet species in the molecule. However, the ESA decay time from this molecule does not change upon oxygen-purging which showing that this ESA is as a result of non-triplet species (**Figure VI.6**). For the case of the TPTQF\_C compound, both the ESA as well as its GSB are not affected by oxygen purging at all, showing that this ESA is as a result of purely singlet states (see **Figure VI.6**).

**Table VI.4:** Purged (p) and unpurged (up) nsTAS ESA and GSB lifetime dynamics of the investigated molecules as well as the TPTQ acceptor in chloroform at their indicated wavelengths.

Compound	ESA			GSB				
	$\lambda_{em}$ / nm	$\tau_1$ (UP) (ns)	$\tau_1$ (P) (ns)	$\lambda_{em}$ / nm	$\tau_1$ (UP) (ns)	$\tau_2$ (UP) (ns)	$\tau_1$ (P) (ns)	$\tau_2$ (P) (ns)
TPTQ Acceptor	302	591	2098	420	584	N/A	4415	N/A
	562	568	1922	844	563	N/A	3793	N/A
TPTQ_C	562		1164/24,954	484	233	472	214	1294
TPTQF_C	536		1129/61,214	470	447	801	180	1242

The TPTQ Acceptor molecule shows very straightforward dynamics where a GSB with a maximum peak at 420 nm which matches well with the ground state absorption was observed as shown in **Figure VI.6**. Two ESA bands are also observed where the ESA at 302 nm decays slower compared to that observed at 562 nm as shown in **Table VI.4**. The lifetimes of both of these ESAs are enhanced upon oxygen purging showing that these are as a result of triplets (**Figure VI.8c**). In

addition, the GSB decay time is also enhanced by oxygen purging which further proves the existence of triplet species. Interestingly, there is another GSB peak observed at 844 nm, whose decay time is also enhanced by oxygen purging. This 844 nm peak matches well with the phosphorescence peak observed in the steady state studies in **Table VI.1**.

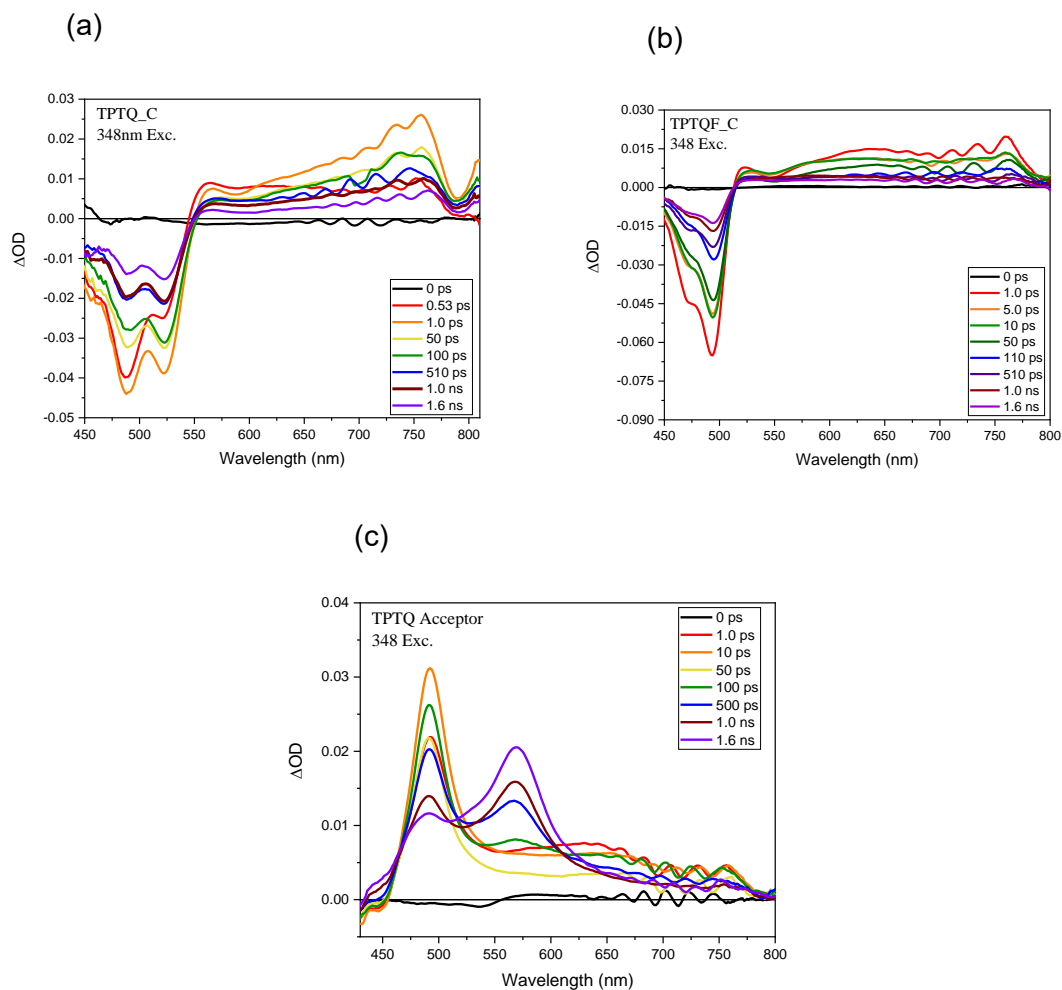


**Figure VI.8:** Time resolved femtosecond transient absorption (fsTA) spectra of both the TPTQ\_C and TPTQF\_C polymers, as well as the TPTQ Acceptor at 348 nm excitation.

Femtosecond transient absorption spectroscopy (fsTAS) measurements are done to look into the faster dynamics of all the investigated molecules. For both polymer molecules, a GSB that matches well with the respective absorption spectra was observed. At both excitations (respective

absorption maxima and 348 nm excitation), the GSB of both polymers forms within 1.00 ps before decaying back slowly (see **Figure VI.8**). In both cases, the GSB does not decay completely to zero which agrees well with the nsTAS results that show long-lived GSB. Additionally, a similar ESA observed around the same range of wavelength as that in nsTAS was observed for both molecules. For both polymers, the GSB formation and decay happens at the same time as the ESA formation and decay (see **Figure VI.8**) indicating that the ESA observed is of a singlet character, which agrees with the nsTAS results.

For the TPTQ Acceptor, a very intense ESA with two bands was observed. Interestingly, as the ESA at 489 nm decayed, the ESA at 566 nm formed (see **Figure VI.8**). This decay and formation which happens at approximately the same rate is evidence that singlets were transferred through ISC to the triplets. The ESA at 566 nm is consistent with the ESA observed in the nsTAS measurements, and whose decay time is 568 ns. The reason why the singlet species are not observed using the nsTAS is clearly because their decay time is ~600 ps which is too fast to be resolved by our nsTAS whose instrument response function (IRF) is only 7 ns.

#### VI.4.e Electron Paramagnetic Resonance (EPR) Spectroscopy

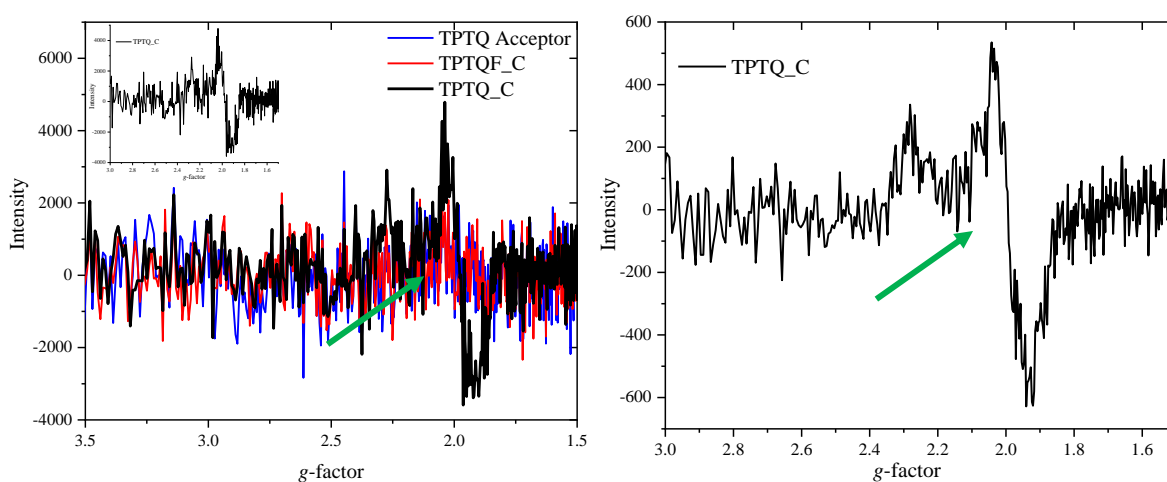


**Figure VI.9:** Electron paramagnetic resonance (EPR) measurements of the investigated molecules. On the right, the TPTQ\_C measurements were repeated at a lower concentration.

Since it was predicted that the TPTQ\_C and TPTQF\_C molecules can exist in their resonance states, EPR spectroscopic measurements were done at ~100K to check the presence of unpaired electrons in these polymer samples, as well as the TPTQ Acceptor. Interestingly, only one of the investigated samples, TPTQ\_C, showed a derivative peak where the *g-factor* of the formally forbidden double quantum transition is ~1.9726 as shown by the green arrows in the spectra in **Figure VI.9**. This *g-factor* shows the presence of organic radicals and has been reported in multiple studies.<sup>42,43</sup> It is worth noting that there is an additional peak at higher *g-factor* values and peaked at 2.2811. The difference between this peak and the peak derivative is 0.3085.

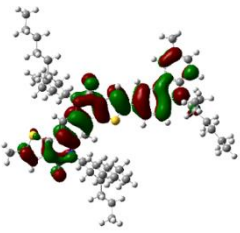
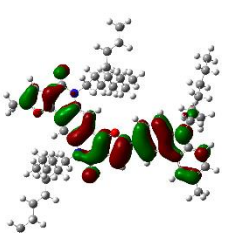
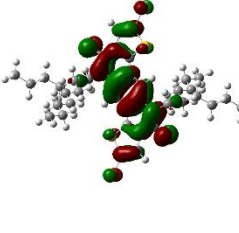
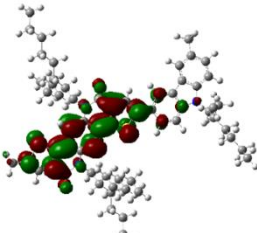
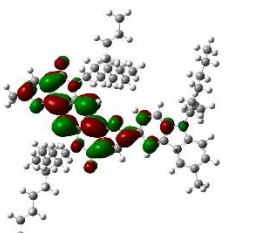
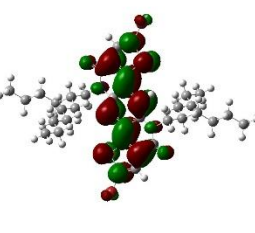
#### VI.4.f Quantum Chemical Calculations

**Table VI.5:** Absorption spectra (nm) for TPTQ\_C, TPTQF\_C, and TPTQ acceptors from experiment and computational approaches. S<sub>0</sub>, S<sub>1</sub>, and T<sub>1</sub> stand for the singlet ground, first singlet excited, and first triplet excited states, respectively. Values in parentheses indicate oscillator strengths.

Wavelength/nm	TPTQ_C	TPTQF_C	TPTQ acceptor
S <sub>0</sub> ->S <sub>1</sub>	446(0.97)	428(0.93)	419(0.69)
S <sub>0</sub> ->T <sub>1</sub> <sup>a</sup>	607(0.00)	580 (0.00)	578 (0.00)
Experiment	455, <b>483</b> , 520	440, <b>470</b> , 489	332, 348, 397, <b>419</b>

<sup>a</sup>Zero oscillator strength due to no spin-orbit coupling in the calculations.

Due to the scope of the present study, no emission spectra nor higher excited states have been calculated. However, the focus of these quantum chemical calculations is the vertical excitations. The details of computational methodologies are presented in the SI. The predicted absorption wavelengths are presented in **Table VI.5**, and are consistent with the trend of experimental results (strongest absorption wavelength TPTQ\_C > TPTQF\_C > TPTQ acceptor). The natural transition orbitals (NTOs) in **Figure VI.10** indicate charge transfer from the nitrogen

	TPTQ_C	TPTQF_C	TPTQ acceptor
	$\lambda = 0.99$		$\lambda = 0.98$
Electron			
Hole			

**Figure VI.10:** NTOs for TPTQ\_C, TPTQF\_C, and TPTQ acceptors.  $\lambda$  indicates the eigenvalue of the transition.

to the oxygen sides, via  $\pi \rightarrow \pi^*$  excitations in the aromatic rings. The quantum chemical calculations show that TPTQ\_C has a smaller HOMO-LUMO bandgap (2.25 eV) compared to the TPTQF\_C (2.38 eV). Incorporating the furan in the electron-deficient material interestingly leads to higher energies of both HOMO (-5.42 eV) and LUMO (-3.04 eV). However, TPTQ\_C has a slightly lower HOMO (-5.44 eV) and lower LUMO (-3.19 eV). These results indicate there should be a better intrachain charge transfer from the donor to the acceptor of the TPTQ\_C polymer, compared to the charge transfer in TPTQF\_C.<sup>44</sup>

The structures as well as ground and excited information for both polymers are illustrated in **Figure VI.11** and **Table VI.6**. The carbon-carbon bond distance C-C 3 shrinks from the ground to the excited state (1.462 Å to 1.437 Å for TPTQ\_C and 1.452 Å to 1.425 Å for TPTQF\_C), which indicates the excited state has a larger weight of the diradical response form than the ground state. Notice the partial atomic charges in sulfur and carbon change from the ground to excited

states in a similar amount in nitrogen, suggesting that the charge transfer covers a range of atoms.

The general picture from partial charge is consistent with the NTOs.

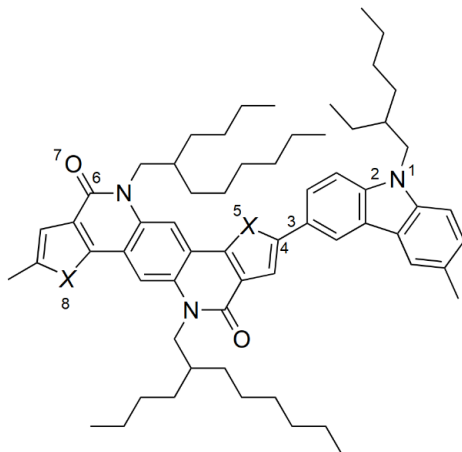


**Figure VI.11:** Structure for TPTQ\_C (X=S) and TPTQF\_C (X=O)

**Table VI.6:** Partial NPA charges (atomic unit) and bond distances (Å) in the ground and excited states of TPTQ\_C and TPTQF\_C.

		N1	C4	X5	O7	X8	N-C 2	C-C 3	C-O 6
TPTQ_C	S0	-0.386	-0.177	0.443	-0.628	0.439	1.386	1.462	1.231
	S1	-0.345	-0.211	0.392	-0.632	0.404	1.379	1.437	1.234
TPTQF_C	S0	-0.483	0.374	-0.550	-0.735	-0.553	1.385	1.452	1.229
	S1	-0.384	0.322	-0.457	-0.626	-0.460	1.378	1.425	1.234

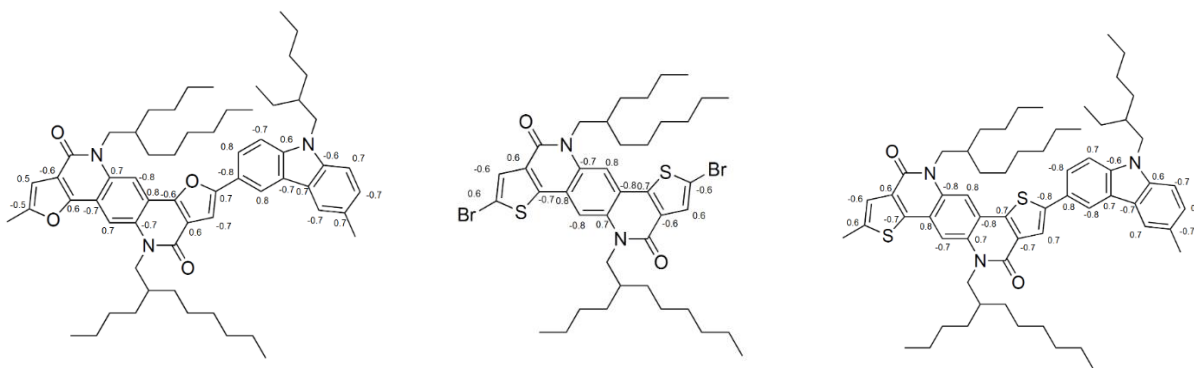


**Figure VI.12:** Mulliken spin densities for TPTQ\_C, TPTQF\_C, and TPTQ acceptor. Absolute values greater than 0.3 are labelled near the associated atoms.



**Table VI.7:** Diradical characters of TPTQ\_C, TPTQF\_C, and TPTQ acceptor, characterized by the unrestricted Hartree Fock (UHF) spin value  $\langle S^2 \rangle$  and NOON.

	TPTQ_C	TPTQF_C	TPTQ acceptor
Ground state (S0) $\langle S^2 \rangle$	2.68	2.54	1.46
Ground state (S0) NOON	1.64, 0.36	1.66, 0.34	1.68, 0.32
Excited state (S1) NOON	1.22, 0.75	1.25, 0.73 *	1.04, 0.98
Computed Diradical Character, $y$ (ground state (S0) NOON)	0.09	0.08	0.07
Computed Diradical Character $y'$ , (excited state (S1) NOON)	0.5	*	0.09

To characterize the diradical characters of the molecules, the natural orbital occupation number (NOON) of the ground and excited states of TPTQ\_C, TPTQF\_C, and TPTQ acceptor were evaluated and presented in **Table VI.7**. The Mulliken spin densities were presented in **Figure VI.12**, that indicate the spatial locations of spin polarized electrons.

## VI.5 Discussion

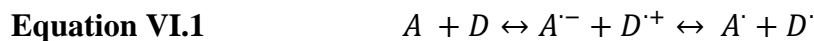
In this study, we report the photophysical properties of previously synthesized semi-ladder polymers consisting of two different acceptor monomers: thienopyridothienoquinoline which has a thiophene incorporated (TPTQ) and thienopyridothienoquinoline with a furan molecule incorporated (TPTQF), both acceptors coupled to a carbazole donor monomer moiety.<sup>5</sup> Previous reports have shown the photo-induced radical polymerization of quinolines through intramolecular charge transfer which cleaves certain C-O bonds to form the radicals.<sup>45</sup> Elsewhere, carbazole-donor-based fullerene polymers have been reported to form long-lived singlet diradicals upon light absorption.<sup>46</sup> To the best of our knowledge, no one has reported the time-resolved and nonlinear optical properties and the charge transfer mechanism that involves the formation of diradicaloids foldable ladder-type polymer aggregates for organic light-emitting transistors (OLET) applications. As a result, this report investigates the self-doping intramolecular electron transfer in aromatically stable zwitterions to form diradicaloids which lower the charge separation process

and reduce the charge and energy transfer rate of the thiophene-carbazole-based OLET polymers. The reduced energy transfer process leads to decreased overall external quantum efficiency (EQE) of the resultant OLETs with diradicaloid character.

From the steady-state absorption, and just considering the maximum absorption (**Figure VI.2 and Table VI.1**), it is clear that TPTQ\_C has a slightly lower HOMO-LUMO bandgap (2.567 eV) compared to the TPTQF\_C (2.638 eV). Here, the HOMO-LUMO bandgap of the furan-based polymer is 0.071 eV higher than the generally suggested difference of 0.3-0.4 eV.<sup>47</sup> The weak low-energy shoulder observed at 520 nm has been reported to originate from low-lying singlet states which are mostly because of doubly excited electronic configuration (HH/LL) and indicate the presence of open-shell singlet ground states in the form of diradicaloids.<sup>29,48-51</sup> This weak, and low-energy shoulder is the first evidence that shows the presence of diradical character in only the TPTQ\_C molecule and backed-up by its lowest HOMO-LUMO bandgap. The red-shifted emission of the TPTQ\_C compound can also be attributed to its larger diradical character and has been reported to improve the electron delocalization and the compounds, effectively reducing their optical energy gaps.<sup>24</sup>

Additionally, the faster fluorescence decay kinetics, as well as lower fluorescence quantum yield, indicate fluorescence quenching in the thiophene-based polymer (TPTQ\_C) compared to its counterpart TPTQF\_C. This quenching can be associated with increased molecular aromatization and conjugation which increases the fluorophores density.<sup>52</sup> Due to its high aromatic stability, TPTQ\_C can form neutral zwitterions through cleaving of the  $C = O$  in the thiophene acceptor and then going through an electronic reorganization to form a cation on the amine side of the carbazole donor. This cation formation can be followed by self-doping leading to the formation of diradicals as shown in **Equation VI.1** and reported elsewhere.<sup>31</sup> However, the presence of furan

in TPTQF\_C reduces its aromaticity and increases the quinoidal interactions which inhibit the diradical formation. Similar results were observed by Xue et al. and Sander.<sup>50,53</sup> Similarly, low fluorescence quantum yields have been reported for materials with increased diradical character.<sup>51</sup>



Given the reported steady-state results, a few parameters were obtained to calculate the singlet diradical character,  $y$ , of the investigated materials using the expression (**Equation VI.2**) derived and reported by Kamada et al.<sup>54</sup>

**Equation VI.2** 
$$y = 1 - \sqrt{1 - \left( \frac{E_{S_{1u}S_{1g}} - E_{T_{1u}S_{1g}}}{E_{S_{2g},S_{1g}}} \right)^2}$$

where:

$E_{S_{1u}S_{1g}}$  is given by the lowest energy peak of the one-photon absorption spectra,

$E_{T_{1u}S_{1g}}$  is obtained from phosphorescence peak measurements and

$E_{S_{2g},S_{1g}}$  corresponds to the lowest energy peak of the two-photon absorption spectra.

Based on these steady-state parameters, the diradical character calculated shows an element of diradical character in these molecules with the TPTQ\_C molecule showing the largest  $y$  (**Table VI.8**).

**Table VI.8:** Calculated diradical character,  $y$ ,  $\Delta E_{ST}$  and  $J$  from the steady state measurements and two-photon absorption or two-photon excited fluorescence

Compound	$l_{S_{1u}S_{1g}}$ nm	$E_{S_{1u}S_{1g}}$ eV	$l_{T_{1u}S_{1g}}$ nm	$E_{T_{1u}S_{1g}}$ eV	$l_{S_{2g},S_{1g}}$ nm	$E_{S_{2g},S_{1g}}$ eV	$y$	$\Delta E_{ST}$	$J$
TPTQ Acceptor	419	2.9541	844	1.469	540	4.592	0.053	1.485	0.74
TPTQ_C	522	2.375	970	1.278	600	2.296	0.122	1.097	0.55
TPTQF_C	496	2.500	944	1.313	540	4.592	0.034	1.186	0.59

Additionally, the singlet-triplet energy gap ( $\Delta E_{ST}$ ) was calculated by subtracting the triplet state energy ( $E_T$ ) from the singlet state energy ( $E_S$ ). Here, TPTQ\_C shows a lower  $\Delta E_{ST}$  bandgap compared to TPTQF\_C. Previous studies have used the singlet-triplet energy gap of diradicaloids to not only rule out the possibility of biradical formation, but also determine the spin multiplicity of the diradicals. Su *et al.* report that diradicaloids can be characterized by a positive electron exchange interaction,  $J$ , which means that there is some level of coupling between the non-bonding electrons.<sup>55</sup>

**Equation VI.3** 
$$\Delta E_{ST} = E_S - E_T = 2J$$

The presence of electron exchange interaction indicates that there is some coupling between the nonbonding electrons which eliminates the possibility that the nonbonding electrons could be forming diradicals instead of biradicals. The diradical character in TPTQ\_C is also ascertained by the signal observed in the EPR measurements. The appearance of the EPR Spectra observed in our results can be explained by the forbidden  $\Delta ms = \pm 2$  EPR transitions which become weakly allowed by the second order perturbation in the zero-field splitting Hamiltonian to produce distinct states.<sup>56</sup> The intensity of the half-field transitions is therefore much weaker as shown at 3167G and 3514G. The EPR allowed transitions of the TPTQ\_C molecule leads to degenerate  $E_x$  and  $E_y$ . As a result,  $E_x$  and  $E_y = 3241$ G while  $E_z = 3167$ G. This information can be used to calculate the zero field splitting parameters, E and D.<sup>26</sup>  $D/2 = 74$ G,  $D = 148$ G. Since  $D = 3E$ ,  $E = 49.3$ G. The experimentally computed D parameter can therefore be used to determine the spin-spin distance ( $r$ ) using **Equation VI.4** below.

**Equation VI.4** 
$$D = 1.39 \times 10^4 (g/r^2)$$

where,  $g$ = the  $g$ -factor and  $r$  is the spin-spin distance. From the above equation, the spin-spin distance,  $r$ , is **5.8Å**. This calculated spin-spin distance is smaller than the previously reported spin-spin distance between two non-bonding electrons (6.4Å) of a stable diradical emitter.<sup>57</sup>

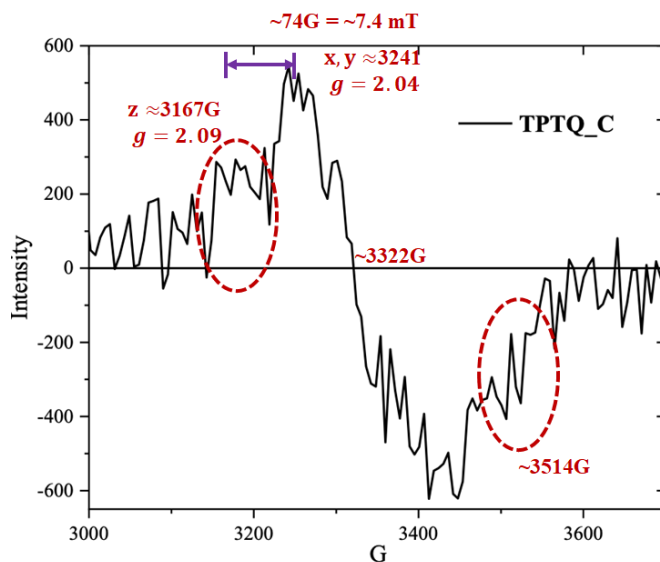


**Figure VI.13:** EPR data of the TPTQ\_C compound analyzed.

From the transient absorption, the positive excited state absorption which, according to our fsTAS, has a growth and decay time equivalent to that of their respective ground state depletion, is assigned to singlet states. This assignment to singlet states is further reinforced by the nsTAS measurements where the ESA lifetimes are not enhanced in nitrogen-rich environments. Surprisingly, lifetimes of these ESAs are beyond usual singlet states lifetimes of a couple 10s-100 nanoseconds. Here, we obtain 25  $\mu$ s and 60  $\mu$ s for TPTQ-C and TPTQF\_C, respectively. The TPTQ\_C ESA is assigned to diradicaloids. These long lifetime diradicaloid species whose lifetime is not affected by purging out oxygen, have been reported in previous studies.<sup>58</sup> The kinetics are summarized in the proposed energy level diagram shown in **Figure VI.14** below and it is possible that the long lifetime observed for the TPTQF\_C is as a result of zwitterions.<sup>59-61</sup> The Mulliken

spin density in **Figure VI.14** suggests all three systems are more of diradicals rather than biradicals, namely, the polarized electrons are not located in two spatial centers.

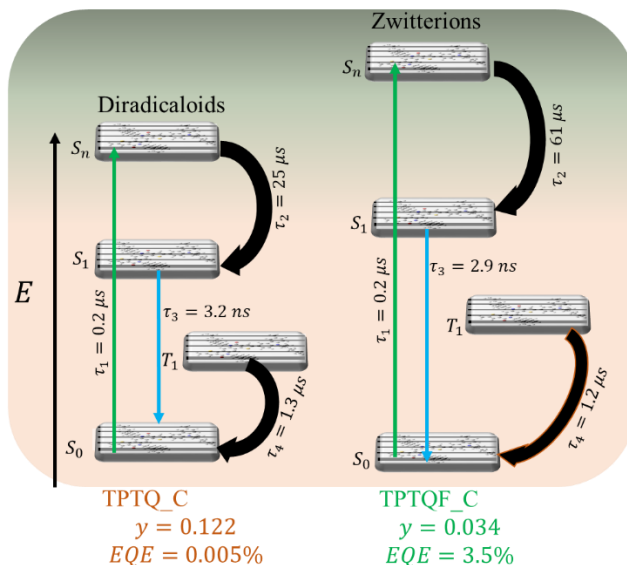


**Figure VI.14:** Proposed energy level diagram for the diradicaloids observed for the TPTQ\_C and the zwitterions formed in the case of the TPTQF\_C.

To compare the diradical characters among TPTQ\_C, TPTQF\_C, and TPTQ acceptor, the values of  $\langle S^2 \rangle$  and NOON in **Table VI.7** were adopted. Larger  $\langle S^2 \rangle$  and deviations from the values 2.0 and 0.0 suggest stronger diradical character<sup>59-61</sup>. The  $\langle S^2 \rangle$  and NOON in Table 7 indicate that TPTQ\_C and TPTQF\_C have significant diradical characters, both of which are stronger than that of TPTQ acceptor. This may be explained by TPTQ\_C and TPTQF\_C having more extended conjugated ranges than the acceptor, similar to the increasingly large diradical characters observed in higher order acenes<sup>60</sup> TPTQ\_C exhibits a slightly larger diradical character than TPTQF\_C ( $\langle S^2 \rangle$  are 2.68 and 2.54 for TPTQ\_C and TPTQF\_C, respectively). This may be explained by the fact that the atomic orbital energy of sulfur 3p (-0.263 Hartree) is closer to carbon 2p (-0.199 Hartree), than oxygen 2p (-0.338 Hartree) is to carbon 2p (-0.199 Hartree)<sup>62</sup>.

From previous studies<sup>5,13,17</sup> it is possible for quinoline derivatives like TPTQ\_C and TPTQF\_C to exist in their resonant forms as shown in **Figure VI.1**. Due to the presence of sulfur, the thiophene-based polymer resonant structure becomes more unreactive due to its high aromatic stability compared to the furan-based counterparts. The TPTQF\_C, which is more reactive, is extremely unstable and its resonant structure is very short lived. Similar results were reported by Jursic where sulfur heterocyclic compounds showed the highest resonance stability while their furan derivatives were the most reactive.<sup>63</sup> Previous polymer studies show that furan has reduced aromaticity which increases the contribution from quinoidal resonance structure in polyfurans making furan-containing polymers more rigid with a planar conformation as well as an overly increased conjugation.<sup>64</sup> This decrease in aromaticity around the furan moiety tends to enhance the probability of additional reactions like that of singlet oxygen and light, compared to their counterpart thiophene based polymers.<sup>64</sup> This is an interesting observation since previous decrease in aromaticity has been related to increase in diradical character of molecules.<sup>65</sup> The saturation of this  $\pi$  conjugation leads to the unexpected shift of the absorption maximum to high energies. However, the lone pair of electrons on the sulfur atom in the TPTQ\_C polymer leads to p- $\pi$  conjugation extending the overall conjugation of the thiophene-based TPTQ\_C polymer. This extended conjugation leads to intensified absorption which is shifted to longer wavelengths as confirmed by the TPTQ\_C absorption in **Figure VI.2a**.

## **VI.6 Conclusion**

The presence of unpaired electrons in open-shells has been reported to form resonant structures with enhanced spin density that is delocalized along the planar  $\pi$ -conjugation backbone influencing the charge transfer. The existence of degenerate or nearly degenerate nonbonding orbitals containing radicals can offer intermolecular spin-spin interactions which lead

to  $\sigma$  –aggregation and formation of  $\sigma$  –polymerization which affects intermolecular stacking and charge transport which has proved to be good for OLEDs. Per our experimental work, we believe that the thiophene- based compound (TPTQ\_C) displays a diradical character. This is evidenced by a number of properties: 1) The weak low-energy shoulder observed at 520 nm has been reported to originate from low-lying singlet states which are mostly as a result of doubly excited electronic configuration (HH/LL) and indicate the presence of open-shell singlet ground states in the form of diradicaloids; 2) fluorescence quenching observed in the thiophene-based polymer can be associated with increased molecular aromatization and conjugation which increases the fluorophores density, low fluorescence quantum yields and lower two-photon absorption cross sections have been reported for materials with increased diradical character; 3) Based on these steady-state studies, the diradical character ( $\gamma$ ) calculated shows that the TPTQ\_C molecule has the largest  $\gamma$ . In addition, the calculation of the electron exchange interaction shows that there is some interaction between the two unpaired electrons, which means that the open-shell formed is a diradical and not a biradical; 4) TPTQ\_C has the lowest singlet-triplet energy gap ( $\Delta E_{ST}$ ); 5) a signal is observed from EPR measurements with a  $g$ -factor of  $\sim 2.000$  which is typical of organic radicals and; 6) the unusually long-lived excited state absorption ( $25 \mu s$ ) with a singlet character that was observed for the TPTQ\_C compound has also been reported in other rylene diradical states and is assigned to the singlet diradicaloid states for this compound. These results will be useful in designing highly efficient OLET devices.



## VI.7 References

- (1) Hepp, A.; Heil, H.; Weise, W.; Ahles, M.; Schmechel, R.; von Seggern, H. Light-Emitting Field-Effect Transistor Based on a Tetracene Thin Film. *Phys Rev Lett* **2003**, *91* (15). <https://doi.org/10.1103/PhysRevLett.91.157406>.
- (2) Liu, C. F.; Liu, X.; Lai, W. Y.; Huang, W. Organic Light-Emitting Field-Effect Transistors: Device Geometries and Fabrication Techniques. *Advanced Materials*. Wiley-VCH Verlag December 27, 2018. <https://doi.org/10.1002/adma.201802466>.
- (3) Yuan, D.; Sharapov, V.; Liu, X.; Yu, L. Design of High-Performance Organic Light-Emitting Transistors. *ACS Omega*. American Chemical Society January 14, 2020, pp 68–74. <https://doi.org/10.1021/acsomega.9b03630>.
- (4) Ojha, S. K.; Kumar, B. Parameter Extraction of High-Performance Material Based Organic Light-Emitting Transistors (OLETs). *Silicon* **2021**. <https://doi.org/10.1007/s12633-021-01149-6>.
- (5) Yuan, D.; Awais, M. A.; Sharapov, V.; Liu, X.; Neshchadin, A.; Chen, W.; Bera, M.; Yu, L. Foldable Semi-Ladder Polymers: Novel Aggregation Behavior and High-Performance Solution-Processed Organic Light-Emitting Transistors. *Chem Sci* **2020**, *11* (41), 11315–11321. <https://doi.org/10.1039/d0sc04068a>.
- (6) Chen, H.; Xing, X.; Miao, J.; Zhao, C.; Zhu, M.; Bai, J. W.; He, Y.; Meng, H. Highly Efficient Flexible Organic Light Emitting Transistor Based on High-k Polymer Gate Dielectric. *Adv Opt Mater* **2020**, *8* (6). <https://doi.org/10.1002/adom.201901651>.
- (7) Yuan, D.; Awais, M. A.; Sharapov, V.; Liu, X.; Neshchadin, A.; Chen, W.; Yu, L. Synergy between Photoluminescence and Charge Transport Achieved by Finely Tuning Polymeric Backbones for Efficient Light-Emitting Transistor. *J Am Chem Soc* **2021**, *143* (13), 5239–5246. <https://doi.org/10.1021/jacs.1c01659>.
- (8) Feldmeier, E. J.; Schidleja, M.; Melzer, C.; von Seggern, H. A Color-Tuneable Organic Light-Emitting Transistor. *Advanced Materials* **2010**, *22* (32), 3568–3572. <https://doi.org/10.1002/adma.201000980>.
- (9) Soldano, C. Engineering Dielectric Materials for High-Performance Organic Light Emitting Transistors (Olets). *Materials* **2021**, *14* (13). <https://doi.org/10.3390/ma14133756>.
- (10) Feng, G.; Xu, Y.; Xiao, C.; Zhang, J.; Zhang, X.; Li, C.; Wei, Z.; Hu, W.; Wang, Z.; Li, W. Poly(Pentacyclic Lactam-Alt-Diketopyrrolopyrrole) for Field-Effect Transistors and Polymer Solar Cells Processed from Non-Chlorinated Solvents. *Polym Chem* **2016**, *7* (1), 164–170. <https://doi.org/10.1039/c5py01406a>.
- (11) Tanaka, H.; Kajii, H.; Ohmori, Y. Effects of Molecular Packing on the Field-Effect Mobility and External Quantum Efficiency of Ambipolar Polymer Light-Emitting Transistors Incorporating a Donor-Acceptor Polymer. *Synth Met* **2015**, *203*, 10–15. <https://doi.org/10.1016/j.synthmet.2015.02.008>.
- (12) Qin, Z.; Gao, H.; Liu, J.; Zhou, K.; Li, J.; Dang, Y.; Huang, L.; Deng, H.; Zhang, X.; Dong, H.; Hu, W. High-Efficiency Single-Component Organic Light-Emitting Transistors. *Advanced Materials* **2019**, *31* (37). <https://doi.org/10.1002/adma.201903175>.
- (13) Zheng, C.; Zhong, C.; Collison, C. J.; Spano, F. C. Non-Kasha Behavior in Quadrupolar Dye Aggregates: The Red-Shifted H-Aggregate. *Journal of Physical Chemistry C* **2019**, *123* (5), 3203–3215. <https://doi.org/10.1021/acs.jpcc.8b11416>.
- (14) Kelley, R. F.; Rybtchinski, B.; Stone, M. T.; Moore, J. S.; Wasielewski, M. R. Solution-Phase Structure of an Artificial Foldamer: X-Ray Scattering Study. *J Am Chem Soc* **2007**, *129* (14), 4114–4115. <https://doi.org/10.1021/ja068213x>.

- (15) Hu, X.; Lindner, J. O.; Würthner, F. Stepwise Folding and Self-Assembly of a Merocyanine Folda-Pentamer. *J Am Chem Soc* **2020**, *142* (7), 3321–3325. <https://doi.org/10.1021/jacs.9b12599>.
- (16) Fauvell, T. J.; Zheng, T.; Jackson, N. E.; Ratner, M. A.; Yu, L.; Chen, L. X. Photophysical and Morphological Implications of Single-Strand Conjugated Polymer Folding in Solution. *Chemistry of Materials* **2016**, *28* (8), 2814–2822. <https://doi.org/10.1021/acs.chemmater.6b00734>.
- (17) Terenziani, F.; Painelli, A.; Katan, C.; Charlot, M.; Blanchard-Desce, M. Charge Instability in Quadrupolar Chromophores: Symmetry Breaking and Solvatochromism. *J Am Chem Soc* **2006**, *128* (49), 15742–15755. <https://doi.org/10.1021/ja064521j>.
- (18) Cao, H.; Rugar, P. A. Recent Advances in Conjugated Furans. *Chemistry - A European Journal* **2017**, *23* (59), 14670–14675. <https://doi.org/10.1002/chem.201703355>.
- (19) Sergeants-and-Soldiers Principle in Chiral Columnar Stacks of Disc-Shaped Molecules with C<sub>3</sub> Symmetry.
- (20) Nelson, J. C.; Saven, J. G.; Moore, J. S.; Wolynes, P. G. *Solvophobicity Driven Folding of Nonbiological Oligomers*; Plenum, 1995; Vol. 267.
- (21) Håheim, K. S.; Urdal Helgeland, I. T.; Lindbäck, E.; Sydnes, M. O. Mapping the Reactivity of the Quinoline Ring-System – Synthesis of the Tetracyclic Ring-System of Isocryptolepine and Regioisomers. *Tetrahedron* **2019**, *75* (21), 2949–2957. <https://doi.org/10.1016/j.tet.2019.04.026>.
- (22) Hosmane, R. S.; Liebman, J. F. Paradoxes and Paradigms: Why Is Quinoline Less Basic than Pyridine or Isoquinoline? A Classical Organic Chemical Perspective. *Struct Chem* **2009**, *20* (4), 693–697. <https://doi.org/10.1007/s11224-009-9464-6>.
- (23) Xue, G.; Hu, X.; Chen, H.; Ge, L.; Wang, W.; Xiong, J.; Miao, F.; Zheng, Y. Understanding the Nature of Quinoidal and Zwitterionic States in Carbazole-Based Diradicals. *Chemical Communications* **2020**, *56* (38), 5143–5146. <https://doi.org/10.1039/d0cc01948h>.
- (24) Chen, L. M.; Lin, I. H.; You, Y. C.; Wei, W. C.; Tsai, M. J.; Hung, W. Y.; Wong, K. T. Substitution Effect on Carbazole-Centered Donors for Tuning Exciplex Systems as Cohost for Highly Efficient Yellow and Red OLEDs. *Mater Chem Front* **2021**, *5* (13), 5044–5054. <https://doi.org/10.1039/d1qm00425e>.
- (25) Chestat, C. A.; Whitten, D. G. *Photocyclization Of-Keto Amides in Homogeneous Solution and Aqueous Cyclodextrin Media. The Role of Zwitterions and Diradicals in Photoinduced Electron Transfer Reactions*; 1992; Vol. 114.
- (26) Abe, M. Diradicals. *Chemical Reviews*. September 11, 2013, pp 7011–7088. <https://doi.org/10.1021/cr400056a>.
- (27) Li, Y.; Li, Y.; Li, L.; Wu, Y. A Review on the Origin of Synthetic Metal Radical: Singlet Open-Shell Radical Ground State? *Journal of Physical Chemistry C* **2017**, *121* (15), 8579–8588. <https://doi.org/10.1021/acs.jpcc.6b12936>.
- (28) Yuen, J. D.; Wang, M.; Fan, J.; Sheberla, D.; Kemei, M.; Banerji, N.; Scarongella, M.; Valouch, S.; Pho, T.; Kumar, R.; Chesnut, E. C.; Bendikov, M.; Wudl, F. Importance of Unpaired Electrons in Organic Electronics. *J Polym Sci A Polym Chem* **2015**, *53* (2), 287–293. <https://doi.org/10.1002/pola.27321>.
- (29) Kamada, K.; Fuku-En, S. I.; Minamide, S.; Ohta, K.; Kishi, R.; Nakano, M.; Matsuzaki, H.; Okamoto, H.; Higashikawa, H.; Inoue, K.; Kojima, S.; Yamamoto, Y. Impact of Diradical Character on Two-Photon Absorption: Bis(Acridine) Dimers Synthesized from an Allenic Precursor. *J Am Chem Soc* **2013**, *135* (1), 232–241. <https://doi.org/10.1021/ja308396a>.
- (30) Cui, Z.; Ye, S.; Wang, L.; Guo, H.; Obolda, A.; Dong, S.; Chen, Y.; Ai, X.; Abdurahman, A.; Zhang, M.; Wang, L.; Li, F. Radical-Based Organic Light-Emitting Diodes with Maximum

External Quantum Efficiency of 10.6%. *Journal of Physical Chemistry Letters* **2018**, 9 (22), 6644–6648. <https://doi.org/10.1021/acs.jpcclett.8b03019>.

(31) Tang, H.; Liu, Z.; Tang, Y.; Du, Z.; Liang, Y.; Hu, Z.; Zhang, K.; Huang, F.; Cao, Y. Organic Diradicals Enabled N-Type Self-Doped Conjugated Polyelectrolyte with High Transparency and Enhanced Conductivity. *Giant* **2021**, 6. <https://doi.org/10.1016/j.giant.2021.100053>.

(32) Nagami, T.; Okada, K.; Miyamoto, H.; Yoshida, W.; Tonami, T.; Nakano, M. Molecular Design Principle for Efficient Singlet Fission Based on Diradical Characters and Exchange Integrals: Multiple Heteroatom Substitution Effect on Anthracenes. *Journal of Physical Chemistry C* **2020**, 124 (22), 11800–11809. <https://doi.org/10.1021/acs.jpcc.0c02369>.

(33) Zeng, Z.; Shi, X.; Chi, C.; López Navarrete, J. T.; Casado, J.; Wu, J. Pro-Aromatic and Anti-Aromatic  $\pi$ -Conjugated Molecules: An Irresistible Wish to Be Diradicals. *Chemical Society Reviews*. Royal Society of Chemistry September 21, 2015, pp 6578–6596. <https://doi.org/10.1039/c5cs00051c>.

(34) Zong, C.; Zhu, X.; Xu, Z.; Zhang, L.; Xu, J.; Guo, J.; Xiang, Q.; Zeng, Z.; Hu, W.; Wu, J.; Li, R.; Sun, Z. Isomeric Dibenzothiazethrenes for Air-Stable Organic Field-Effect Transistors. *Angewandte Chemie - International Edition* **2021**, 60 (29), 16230–16236. <https://doi.org/10.1002/anie.202105872>.

(35) Yuan, D. Stable N-Doped Conductors Enabled by Organic Diradicals. *Chem* **2019**, 5 (4), 744–745. <https://doi.org/10.1016/j.chempr.2019.03.018>.

(36) Dong, S.; Li, Z. Recent Progress in Open-Shell Organic Conjugated Materials and Their Aggregated States. *J Mater Chem C Mater* **2022**. <https://doi.org/10.1039/d1tc04598a>.

(37) Ai, X.; Evans, E. W.; Dong, S.; Gillett, A. J.; Guo, H.; Chen, Y.; Hele, T. J. H.; Friend, R. H.; Li, F. Efficient Radical-Based Light-Emitting Diodes with Doublet Emission. *Nature* **2018**, 563 (7732), 536–540. <https://doi.org/10.1038/s41586-018-0695-9>.

(38) Miao, J.; Meng, B.; Liu, J.; Wang, L. An A-D-A'-D-A Type Small Molecule Acceptor with a Broad Absorption Spectrum for Organic Solar Cells. *Chemical Communications* **2018**, 54 (3), 303–306. <https://doi.org/10.1039/c7cc08497h>.

(39) Wang, M.; Wang, H.; Yokoyama, T.; Liu, X.; Huang, Y.; Zhang, Y.; Nguyen, T. Q.; Aramaki, S.; Bazan, G. C. High Open Circuit Voltage in Regioregular Narrow Band Gap Polymer Solar Cells. *J Am Chem Soc* **2014**, 136 (36), 12576–12579. <https://doi.org/10.1021/ja506785w>.

(40) Spano, F. C. The Spectral Signatures of Frenkel Polarons in H- And J-Aggregates. *Acc Chem Res* **2010**, 43 (3), 429–439. <https://doi.org/10.1021/ar900233v>.

(41) Eggeling, C.; Brand, L.; Seidel, C. Laser-Induced Fluorescence of Coumarin Derivatives in Aqueous Solution: Photochemical Aspects for Single Molecule Detection. *Bioimaging* **1997**, 5 (3), 105–115. [https://doi.org/10.1002/1361-6374\(199709\)5:3<105::AID-BIO4>3.3.CO;2-H](https://doi.org/10.1002/1361-6374(199709)5:3<105::AID-BIO4>3.3.CO;2-H).

(42) Jezierski, A.; Czechowski, F.; Jerzykiewicz, M.; Golonka, I.; Drozd, J.; Bylinska, E.; Chen, Y.; Seaward, M. R. D. Quantitative EPR Study on Free Radicals in the Natural Polyphenols Interacting with Metal Ions and Other Environmental Pollutants; 2002; Vol. 58.

(43) Paul, A.; Stösser, T. R.; Zehl, A.; Zwirnmann, E.; Vogt, R. D.; Steinberg, C. E. W. Nature and Abundance of Organic Radicals in Natural Organic Matter: Effect of PH and Irradiation. *Environ Sci Technol* **2006**, 40 (19), 5897–5903. <https://doi.org/10.1021/es060742d>.

(44) Li, Y.; Zou, Y. Conjugated Polymer Photovoltaic Materials with Broad Absorption Band and High Charge Carrier Mobility. *Advanced Materials* **2008**, 20 (15), 2952–2958. <https://doi.org/10.1002/adma.200800606>.

- (45) Goto, A.; Scaiano, J. C.; Maretta, L. Photolysis of an Alkoxyamine Using Intramolecular Energy Transfer from a Quinoline Antenna - Towards Photo-Induced Living Radical Polymerization. *Photochemical and Photobiological Sciences* **2007**, *6* (8), 833–835. <https://doi.org/10.1039/b705671k>.
- (46) Thomas, R. N. *Acid Catalyzed Fullerenation of Carbazole Polymer*.
- (47) Gidron, O.; Varsano, N.; Shimon, L. J. W.; Leitun, G.; Bendikov, M. Study of a Bifuran vs. Bithiophene Unit for the Rational Design of  $\pi$ -Conjugated Systems. What Have We Learned? *Chemical Communications* **2013**, *49* (56), 6256–6258. <https://doi.org/10.1039/c3cc41795f>.
- (48) di Motta, S.; Negri, F.; Fazzi, D.; Castiglioni, C.; Canesi, E. V. Biradicaloid and Polyenic Character of Quinoidal Oligothiophenes Revealed by the Presence of a Low-Lying Double-Exciton State. *Journal of Physical Chemistry Letters* **2010**, *1* (23), 3334–3339. <https://doi.org/10.1021/jz101400d>.
- (49) Shi, X.; Quintero, E.; Lee, S.; Jing, L.; Heng, T. S.; Zheng, B.; Huang, K. W.; López Navarrete, J. T.; Ding, J.; Kim, D.; Casado, J.; Chi, C. Benzo-Thia-Fused [N] Thienoacenequinodimethanes with Small to Moderate Diradical Characters: The Role of pro-Aromaticity versus Anti-Aromaticity. *Chem Sci* **2016**, *7* (5), 3036–3046. <https://doi.org/10.1039/c5sc04706d>.
- (50) Xue, G.; Hu, X.; Chen, H.; Ge, L.; Wang, W.; Xiong, J.; Miao, F.; Zheng, Y. Understanding the Nature of Quinoidal and Zwitterionic States in Carbazole-Based Diradicals. *Chemical Communications* **2020**, *56* (38), 5143–5146. <https://doi.org/10.1039/d0cc01948h>.
- (51) Ni, Y.; Lee, S.; Son, M.; Aratani, N.; Ishida, M.; Samanta, A.; Yamada, H.; Chang, Y.-T.; Furuta, H.; Kim, D.; Wu, J. A Diradical Approach towards BODIPY-Based Dyes with Intense Near-Infrared Absorption around  $\lambda = 1100$  nm. *Angewandte Chemie* **2016**, *128* (8), 2865–2869. <https://doi.org/10.1002/ange.201511151>.
- (52) Hackley, P. C.; Jubb, A. M.; Burruss, R. C.; Beaven, A. E. Fluorescence Spectroscopy of Ancient Sedimentary Organic Matter via Confocal Laser Scanning Microscopy (CLSM). *Int J Coal Geol* **2020**, *223*. <https://doi.org/10.1016/j.coal.2020.103445>.
- (53) Sander, W. *Carbonyl Oxides : Zwitterions or Diradicals?*
- (54) Kamada, K.; Ohta, K.; Shimizu, A.; Kubo, T.; Kishi, R.; Takahashi, H.; Botek, E.; Champagne, B.; Nakano, M. Singlet Diradical Character from Experiment. *Journal of Physical Chemistry Letters* **2010**, *1* (6), 937–940. <https://doi.org/10.1021/jz100155s>.
- (55) Su, Y.; Wang, X.; Wang, L.; Zhang, Z.; Wang, X.; Song, Y.; Power, P. P. Thermally Controlling the Singlet-Triplet Energy Gap of a Diradical in the Solid State. *Chem Sci* **2016**, *7* (10), 6514–6518. <https://doi.org/10.1039/c6sc01825d>.
- (56) Chen, H.; Maryasov, A. G.; Rogozhnikova, O. Y.; Trukhin, D. v.; Tormyshev, V. M.; Bowman, M. K. *Electron Spin Dynamics and Spin-Lattice Relaxation of Trityl Radicals in Frozen Solutions*; 2016.
- (57) Feng, Z.; Chong, Y.; Tang, S.; Fang, Y.; Zhao, Y.; Jiang, J.; Wang, X. A Stable Triplet Diradical Emitter. *Chem Sci* **2021**, *12* (45), 15151–15156. <https://doi.org/10.1039/D1SC04486A>.
- (58) Wang, Z.; Yadav, P.; Abe, M. Long-Lived Localised Singlet Diradicaloids with Carbon-Carbon  $\pi$ -Single Bonding (C- $\pi$ -C). *Chemical Communications* **2021**, *57* (86), 11301–11309. <https://doi.org/10.1039/d1cc04581d>.
- (59) Lee, J.; Head-Gordon, M. Distinguishing Artificial and Essential Symmetry Breaking in a Single Determinant: Approach and Application to the C<sub>60</sub>, C<sub>36</sub>, and C<sub>20</sub> Fullerenes. *Physical Chemistry Chemical Physics* **2019**, *21* (9), 4763–4778. <https://doi.org/10.1039/c8cp07613h>.

- (60) Bendikov, M.; Duong, H. M.; Starkey, K.; Houk, K. N.; Carter, E. A.; Wudl, F. Oligocenes: Theoretical Prediction of Open-Shell Singlet Diradical Ground States. *J Am Chem Soc* **2004**, *126* (24), 7416–7417. <https://doi.org/10.1021/ja048919w>.
- (61) Sun, Z.; Zeng, Z.; Wu, J. Zethrenes, Extended p-Quinodimethanes, and Periacenes with a Singlet Biradical Ground State. *Acc Chem Res* **2014**, *47* (8), 2582–2591. <https://doi.org/10.1021/ar5001692>.
- (62) NIST (Updated 2017, April 24<sup>th</sup>) “Atomic Reference Data for Electronic Structure Calculations, Atomic Total Energies and Eigenvalues (HTML)” <https://www.nist.gov/pml/atomic-reference-data-electronic-structure-calculations/atomic-reference-data-electronic-7>
- (63) Theoretical Study of Thieno[3,4-d]Thiepin and Furo[3,4-d]Thiepin as Dienes in the Diels-alder Reaction.
- (64) Cao, H.; Rugar, P. A. Recent Advances in Conjugated Furans. *Chemistry - A European Journal* **2017**, *23* (59), 14670–14675. <https://doi.org/10.1002/chem.201703355>.
- (65) Stuyver, T.; Danovich, D.; Shaik, S. Captodative Substitution Enhances the Diradical Character of Compounds, Reduces Aromaticity, and Controls Single-Molecule Conductivity Patterns: A Valence Bond Study. *Journal of Physical Chemistry A* **2019**, *123* (32), 7133–7141. <https://doi.org/10.1021/acs.jpca.9b06096>.

## **Chapter VII**

### **Summary of Dissertation and Future Outlook**

#### **VII.1 Summary of dissertation**

The main objective of correlations and conclusions determined from the research investigations discussed in this dissertation is to increase the knowledge of ultrafast charge dynamics occurring within organic semiconducting materials for optoelectronic applications. These discovered correlations and conclusions have the potential to make an impact in the scientific community by assisting with finding the optimal molecular structures of organic semiconducting materials that will lead to high efficiencies, effectiveness and low cost devices used in optoelectronic applications. As shown in this dissertation, I have had the opportunity to investigate and study a wide range of organic semiconducting materials. Through these investigations of various organic semiconducting materials, this lead to the discovery of correlations between molecular structures of these materials and ultrafast charge dynamics. The significance of ultrafast charge dynamics is these dynamics are considered as the driving motion of charges moving or transporting within materials or a system of materials and how charges are transported within devices for optoelectronic applications. The section below describes the main conclusions and correlations discovered in the research investigations discussed in this dissertation (Chapters III – VI). The correlations discovered from these research investigations can be used to finding an optimal structural design on organic semiconducting materials that will lead to increase the efficiency or effectiveness of devices used in optoelectronic applications.

### *VII.1.a Summary of main results and conclusions of Chapters III – VI*

The title of Chapter III is *The Investigation of Ultrafast Dynamics within Organic Conjugated Ladder Oligomers Used in Optoelectronic Applications*. Chapter III describes the results and conclusions of the research investigation that focused on studying the ultrafast charge dynamics of BTps. From the fs-TA results, the charge transport rates,  $k_{comb}$ , of the BTps are determined. For the high energy excitation wavelength, the  $k_{comb}$  of BTp-5 is 1.6x faster than the  $k_{comb}$  of BTp-7. For the middle energy excitation wavelength, the  $k_{comb}$  of BTp-5 is 8.5x faster compared to BTp-7. The correlation discovered between the structure and  $k_{comb}$  is as the conjugation increases, the  $k_{comb}$  decreases. The  $k_{comb}$  calculated for the BTps provided a quantitative value describing the electron-phonon and reorganization rates of these OLOs. Due to a slower  $k_{comb}$ , BTp7 will have a higher charge carrier mobility compared to BTp-5. The slower  $k_{comb}$  of BTp-7 is due to weaker electron-phonon interaction and slower reorganization decay as a result of the longer conjugation length of these OLO. The results discussed in this research investigation showed that longer conjugation OLOs will lead to a more efficient charge transport for transistor and solar cell optoelectronic applications.

The title of Chapter IV is *Probing the Exciton Dynamics of Naphthalene-imide Based Nonfullerene Acceptors for Organic Photovoltaics*. Chapter IV contains results and conclusion of the research investigation studying the exciton dynamics and intramolecular charge generation of acceptor-donor-acceptor small molecule NFAs, called BNiAs. The fs-TA results show geminate decay (charge recombination decay and exciton decay) of NIBT is roughly **5x – 6x** slower than the decay of NITV and NIDT. From the theoretical calculations and femtosecond transient absorption results an energy diagram of the intramolecular charge generation occurring in the BNiAs is created. The energy diagram shows the reorganization energy between exciton and

charge transfer states of NIBT is **31%** smaller compared to the other BNIAAs. As a result of the  $\pi$  bridges, NIBT has an efficient intramolecular charge generation and exciton dynamics compared to NITV and NIDT. The structure of a FREA small molecule needs to have an additional  $\pi$  bridge – such as benzothiadiazole  $\pi$ -bridge – between donor unit and acceptor unit in order to have efficient intramolecular charge generation and exciton dynamics within the small molecule NFA. This correlation could provide insight to understanding the structure-function relationship of small molecule NFAs and PCE of OPVs.

The title of Chapter V is *Linear and Nonlinear Optical Properties of All-cis and All-trans Poly(p-phenylene vinylene)*. This collaborative research investigation studied the excited state dynamics of all *trans* and all *cis* PPV. From ultrafast time-resolved and non-linear laser spectroscopy and theoretical calculations, the photophysics of all *trans* and all *cis* PPV is investigated. Due to the faster excited state and fluorescence dynamics of *trans* (is better for the optoelectronic application of organic light emitting diodes OLEDs) since this isomer had faster excited state and fluorescence dynamics compared to all *cis* PPV. Then all *cis* PPV, it is better for quantum light application due to its relatively slow excited state and fluorescence dynamics. The main conclusion of this investigation is provide insight into which isomer of PPV will be better suited for optoelectronic application of organic light emitting diodes or quantum light; specifically, all *cis* PPV is better for OLEDs and all *trans* PPV is better suited for quantum light applications.

The titled of Chapter VI is titled *Effect of Long-Lived Ground State Diradicaloids on the Photophysics of Semi-Ladder Thiophene-Based Polymer Aggregates for Organic Light Emitting Transistor (OLET) Applications*. This collaborative research investigation studied the excited state and radical character foldable donor-acceptor polymer for optoelectronic application of organic light emitting transistor (OLET). By utilizing fs-TA spectroscopy, the dynamics of excited singlet



states and formation of excited triplet states within these polymers are investigated. From other ultrafast laser spectroscopy and electron paramagnetic resonance experiments, the results from the experiments determined that the semi-ladder donor-acceptor polymer that consisted of thiophene within its acceptor unit had more diradical character compared to semi-ladder donor-acceptor polymer that consisted of furan within its acceptor. The main conclusion of this Chapter is provide insight into the structural guideline of semi-ladder foldable donor-acceptor polymer for OLETs.

The correlations and conclusions discovered from the research investigations discussed in this dissertation provides information that can be used as guidelines for which structural design of an organic semiconducting materials will increase the efficiency and effectiveness of devices used in optoelectronic applications. Specifically, the correlations and conclusions can be used as guidelines for organic semiconducting materials that are designed for optoelectronic applications of solar energy, transistor, light emitting diodes and quantum information. A possible new molecular structure design for organic semiconducting materials is to increase the conjugation or adding  $\pi$ -bridge to the structural framework of small molecule Y6 or a derivative of Y6.<sup>1,2</sup> Research has shown the Y6 has one the highest PCE for OPV devices due to its branched acceptor-donor-acceptor structural framework.<sup>3-6</sup> Two main correlations discussed in this dissertation are: 1) increasing conjugation to create an effective charge transport (Chapter III) and 2) the additional of  $\pi$ -bridge creates strong exciton dynamics and efficient intramolecular charge generation (Chapter IV). By combining these two correlations to one of optimal molecular structure for organic semiconducting materials, Y6, this could create a better performance material for devices used in optoelectronic applications. Another possible outcome is this new molecular structure will provide insight to the right combination between conjugation length,  $\pi$ -bridge and acceptor-donor-acceptor structural framework and show the Y6 has the optimal molecular structure for organic

semiconducting materials. Regardless, of the end result of this potential molecular structure design, the discovered correlation from this research investigation will increase the knowledge of structure-function relationships between organic semiconducting materials and optoelectronic applications.

## **VII.2 Future Outlook of Research Investigating Organic Semiconducting Materials for Optoelectronic Applications**

Despite the decades and current research being conducted on organic semiconducting materials for optoelectronic applications, there is still a need to continue this type of research because the molecular structures of organic semiconducting materials that will lead to high performance devices that will make a positive impact in society has not been discovered yet. As mentioned in Chapter I, Introduction, devices of optoelectronic applications are a main technology that is used daily in society. The SETO has developed objectives for the next few decades and Energy Act of 2020, the Clean Energy Innovation, bill shows the significant investment in this type of research and technology.<sup>7-10</sup> Since these devices have a huge impact in society, it is important to continue this type of research and achieve objectives that will improve and make a positive impact in society. The challenging part of this research is determining which molecular structure of organic semiconducting materials can be utilized for optoelectronic applications.

In my perspective, one approach for overcoming this challenge is finding an universal numerical parameter that is associated with various optoelectronic applications and using that parameter to determine which organic semiconducting material can be utilized in more than one optoelectronic application. Research has shown that the numerical parameter called charge carrier mobility ( $\mu$ ) can become an universal or a good parameter to determine where an organic semiconducting material can be used for an optoelectronic application. Recall,  $\mu$  determines the

speed of charges going through a material as a results of an applied voltage.<sup>11-13</sup> Charge carrier mobility of a material has been used in research to determine if a material can be utilized in various optoelectronic applications.<sup>14-17</sup> Recall, research has been conducted on the acceptor-donor-acceptor small molecule, Y6, to show this small molecule is not only useful for OPVs; however, it can be used in organic field effect transistor application as well.<sup>4,18</sup> For both solar energy and transistor optoelectronic application, the  $\mu$  of Y6 has been determined.<sup>4,18</sup> By investigating the  $\mu$  of an organic semiconducting material, this will create opportunities to determine which molecular structure of an organic semiconducting material can be used for more than one optoelectronic application. In short, finding a universal parameter to evaluate an organic semiconducting material for more than one optoelectronic application has the potential to increase knowledge and the pace of finding the optimal material for applications.

### **VII.3 Future Outlook of Ultrafast Laser Spectroscopy Research**

The future outlook of ultrafast laser spectroscopy research is to develop new experiments that could increase the knowledge of excited state dynamics within materials. By utilizing ultrafast laser spectroscopy, the excited state and charge dynamics of materials are investigated to determine which material has effective or efficient dynamics that will lead to high performance devices for optoelectronic applications. The challenge of this type of research is the current experiments do not measure all the excited state or charge dynamics that could be occurring within materials and effect the performance of devices for optoelectronic applications. Another perspective is there are not enough experiments to support that all the excited state and charge dynamics of materials are known and have already been discovered. From my perspective, the goal of ultrafast laser spectroscopy research is to collect as much information as possible about the excited state of materials in order to determine the effectiveness or efficiency of the dynamics to a device for

optoelectronic application or other technology application. Currently, there are new experiments being conducted utilizing entangled light to investigate the excited state dynamics of materials and increase the knowledge of structure-function relationships.<sup>19-21</sup> Another advantage of entangled laser spectroscopy is this increases that types of materials that can be investigated.<sup>20,21</sup> Research has shown entangled laser spectroscopy can be utilized to investigate the dynamics of biological materials and decrease the likelihood of causing photo damaged to the material.<sup>20,21</sup> Another recent advantage of ultrafast laser spectroscopy is the development of x-ray ultrafast laser spectroscopy to increases the knowledge of excited state dynamics of materials and how those dynamics affect the functionality of materials.<sup>22,23</sup> In short, the future outlook of ultrafast laser spectroscopy depends on developing new experiments that will increase knowledge or support the current understanding of excited state and charge dynamics of materials in order to find materials that will improve devices and technology for society.

In conclusion, from my perspective, the future outlook of research is forming and maintaining collaborations between researchers from different science, technology, engineering and mathematics (STEM) fields. It is important to develop and maintaining collaborations, if possible, with a wide range of researchers that are experts in different STEM fields because this will help increase knowledge and increase the possibility of discovering new and innovate ideas. To be clear, this approach is already happening in research and the STEM community in general, which is supported by the collaborative research investigation discussed in this dissertation. Even though this approach is known and already being used, it is important to remind the community that this approach is beneficial and impactful since it allows the opportunity for researchers to discover new innovative ideas that could make an impact in society. As discussed throughout this dissertation, one of the main objective of the collaborative research investigations is to find a

correlation between molecular structure of organic semiconducting materials and a functionality of that material in order to discover a correlation that will lead to improving the performance of devices designed for optoelectronic applications. All of the research investigations described in this dissertation had a collaboration with a materials or organic synthesis researcher who created the investigated materials of the described investigations. By having these collaborations, creates the opportunity to share knowledge that will help inspire the next molecular structure of organic semiconducting materials that have the potential to create high performance devices for optoelectronic applications. Another opportunity that could happening is creating the opportunity for physical experimental chemists to develop an innovative experiment that will increase the knowledge of the excited states of materials. By creating new experiments that could increase the knowledge of excited states of materials, this new knowledge has the potential to lead to new devices that can utilize all excited state dynamics to improve device performance. In conclusion, collaborations are a beneficial increasing knowledge and making an impact in the STEM community and society.

## VII.4 References

- (1) Feng, L.; Yuan, J.; Zhang, Z.; Peng, H.; Zhang, Z.-G.; Xu, S.; Liu, Y.; Li, Y.; Zou, Y. Thieno[3,2-*b*]Pyrrolo-Fused Pentacyclic Benzotriazole-Based Acceptor for Efficient Organic Photovoltaics. *ACS Appl. Mater. Interfaces* **2017**, *9* (37), 31985–31992. <https://doi.org/10.1021/acsami.7b10995>.
- (2) Wei, Q.; Yuan, J.; Yi, Y.; Zhang, C.; Zou, Y. Y6 and Its Derivatives: Molecular Design and Physical Mechanism. *Natl. Sci. Rev.* **2021**, *8* (8), nwab121. <https://doi.org/10.1093/nsr/nwab121>.
- (3) Yuan, J.; Zhang, Y.; Zhou, L.; Zhang, G.; Yip, H.-L.; Lau, T.-K.; Lu, X.; Zhu, C.; Peng, H.; Johnson, P. A.; Leclerc, M.; Cao, Y.; Ulanski, J.; Li, Y.; Zou, Y. Single-Junction Organic Solar Cell with over 15% Efficiency Using Fused-Ring Acceptor with Electron-Deficient Core. *Joule* **2019**, *3* (4), 1140–1151. <https://doi.org/10.1016/j.joule.2019.01.004>.
- (4) Liu, F.; Zhou, L.; Liu, W.; Zhou, Z.; Yue, Q.; Zheng, W.; Sun, R.; Liu, W.; Xu, S.; Fan, H.; Feng, L.; Yi, Y.; Zhang, W.; Zhu, X. Organic Solar Cells with 18% Efficiency Enabled by an Alloy Acceptor: A Two-in-One Strategy. *Adv. Mater.* **2021**, *33* (27), 2100830. <https://doi.org/10.1002/adma.202100830>.
- (5) Natsuda, S.; Sakamoto, Y.; Takeyama, T.; Shirouchi, R.; Saito, T.; Tamai, Y.; Ohkita, H. Singlet and Triplet Excited-State Dynamics of a Nonfullerene Electron Acceptor Y6. *J. Phys. Chem. C* **2021**, *125* (38), 20806–20813. <https://doi.org/10.1021/acs.jpcc.1c06448>.
- (6) Yuk, D.; Jee, M. H.; Koh, C. W.; Park, W.; Ryu, H. S.; Lee, D.; Cho, S.; Rasool, S.; Park, S.; Kwon, O.; Kim, J. Y.; Woo, H. Y. Simplified Y6-Based Nonfullerene Acceptors: In-Depth Study on Molecular Structure–Property Relation, Molecular Dynamics Simulation, and Charge Dynamics. *Small* **2023**, *19* (10), 2206547. <https://doi.org/10.1002/smll.202206547>.
- (7) U.S. Department of Energy Office Solar Energy Technologies Office. <https://www.energy.gov/eere/solar/organic-photovoltaics-research> (accessed 2024-01-19).
- (8) U.S. Department of Energy Office Solar Energy Technologies Office. <https://www.energy.gov/eere/solar/goals-solar-energy-technologies-office> (accessed 2024-01-03).
- (9) Feblowitz, J. Renewable Energy World, 2021. <https://www.renewableenergyworld.com/solar/government-and-private-funding-we-need-both-for-the-energy-transition/#gref> (accessed 2024-02-02).
- (10) Committee on Science Space and Technology, 2020. <https://science.house.gov/2020/12/energy-act-of-2020> (accessed 2024-02-03).
- (11) Paterson, A. F.; Singh, S.; Fallon, K. J.; Hodsdon, T.; Han, Y.; Schroeder, B. C.; Bronstein, H.; Heeney, M.; McCulloch, I.; Anthopoulos, T. D. Recent Progress in High-Mobility Organic Transistors: A Reality Check. *Adv. Mater.* **2018**, *30* (36), 1801079. <https://doi.org/10.1002/adma.201801079>.

- (12) Coropceanu, V.; Cornil, J.; Da Silva Filho, D. A.; Olivier, Y.; Silbey, R.; Brédas, J.-L. Charge Transport in Organic Semiconductors. *Chem. Rev.* **2007**, *107* (4), 926–952. <https://doi.org/10.1021/cr050140x>.
- (13) Reese, C.; Bao, Z. Organic Single-Crystal Field-Effect Transistors. *Mater. Today* **2007**, *10* (3), 20–27. [https://doi.org/10.1016/S1369-7021\(07\)70016-0](https://doi.org/10.1016/S1369-7021(07)70016-0).
- (14) Ostroverkhova, O.; Cooke, D. G.; Shcherbina, S.; Egerton, R. F.; Hegmann, F. A.; Tykwinski, R. R.; Anthony, J. E. Bandlike Transport in Pentacene and Functionalized Pentacene Thin Films Revealed by Subpicosecond Transient Photoconductivity Measurements. *Phys. Rev. B* **2005**, *71* (3), 035204. <https://doi.org/10.1103/PhysRevB.71.035204>.
- (15) Brédas, J.-L.; Beljonne, D.; Coropceanu, V.; Cornil, J. Charge-Transfer and Energy-Transfer Processes in  $\pi$ -Conjugated Oligomers and Polymers: A Molecular Picture. *Chem. Rev.* **2004**, *104* (11), 4971–5004. <https://doi.org/10.1021/cr040084k>.
- (16) Sirringhaus, H. 25th Anniversary Article: Organic Field-Effect Transistors: The Path Beyond Amorphous Silicon. *Adv. Mater.* **2014**, *26* (9), 1319–1335. <https://doi.org/10.1002/adma.201304346>.
- (17) Dong, H.; Fu, X.; Liu, J.; Wang, Z.; Hu, W. 25th Anniversary Article: Key Points for High-Mobility Organic Field-Effect Transistors. *Adv. Mater.* **2013**, *25* (43), 6158–6183. <https://doi.org/10.1002/adma.201302514>.
- (18) Xiao, C.; Li, C.; Liu, F.; Zhang, L.; Li, W. Single-Crystal Field-Effect Transistors Based on a Fused-Ring Electron Acceptor with High Ambipolar Mobilities. *J. Mater. Chem. C* **2020**, *8* (16), 5370–5374. <https://doi.org/10.1039/D0TC00587H>.
- (19) Varnavski, O.; Goodson, T. Two-Photon Fluorescence Microscopy at Extremely Low Excitation Intensity: The Power of Quantum Correlations. *J. Am. Chem. Soc.* **2020**, *142* (30), 12966–12975. <https://doi.org/10.1021/jacs.0c01153>.
- (20) Varnavski, O.; Gunthardt, C.; Rehman, A.; Luker, G. D.; Goodson, T. Quantum Light-Enhanced Two-Photon Imaging of Breast Cancer Cells. *J. Phys. Chem. Lett.* **2022**, *13* (12), 2772–2781. <https://doi.org/10.1021/acs.jpcllett.2c00695>.
- (21) Eshun, A.; Varnavski, O.; Villabona-Monsalve, J. P.; Burdick, R. K.; Goodson, T. Entangled Photon Spectroscopy. *Acc. Chem. Res.* **2022**, *55* (7), 991–1003. <https://doi.org/10.1021/acs.accounts.1c00687>.
- (22) Geneaux, R.; Marroux, H. J. B.; Guggenmos, A.; Neumark, D. M.; Leone, S. R. Transient Absorption Spectroscopy Using High Harmonic Generation: A Review of Ultrafast X-Ray Dynamics in Molecules and Solids. *Philos. Trans. R. Soc. Math. Phys. Eng. Sci.* **2019**, *377* (2145), 20170463. <https://doi.org/10.1098/rsta.2017.0463>.
- (23) Yano, J.; Yachandra, V. K. X-Ray Absorption Spectroscopy. *Photosynth. Res.* **2009**, *102* (2–3), 241–254. <https://doi.org/10.1007/s11120-009-9473-8>.

## **Appendices**



## **Appendix A: Supporting Information for Chapter I**

### **Table of Contents**

<b>A.1 Prelude .....</b>	<b>200</b>
<b>A.2 Additional Background Information on Solar Energy .....</b>	<b>200</b>
<b>A.3 References .....</b>	<b>203</b>

## **A.1 Prelude**

Appendix A provides additional background information for Chapter I. This background information does not need to be included in the main portion of Chapter I.

## **A.2 Additional Background Information on Solar Energy**

Over the years, the U.S. DOE and another world organization have collected information and data on solar energy and other energy sources which have been helpful to show how these energy sources impact the world. From that collected information and data, U.S. DOE and U.S. Congress increased their financial investment into research that focuses on solar energy. Since the 1970s, there has been a need to develop alternative sources of energy to fossil fuels; since fossil fuels have the potential to have higher costs.<sup>6,9,10</sup> During 1973 to 1974 timeframe, the oil prices in the U.S. increased from \$2.90 a barrel to \$11.65 a barrel (note the dollar amount listed is based on 1973 and 1974 dollars) due to an embargo on the U.S. that was enforced by the Organization of Arab Petroleum Exporting Countries in October 1973.<sup>9</sup> Due to this embargo, this altered the perspective of energy sources by ensuring there is more than one energy source and not only relying on fossil fuels.<sup>6</sup> Examples of fossil fuels used as energy sources are: coal; oil; natural gas; and petroleum. The prices of fossil fuels have fluctuated since the 1970s, as shown in a report created by the U.S. Energy Information Administration (EIA).<sup>11</sup> The U.S. EIA is an agency under the DOE that collects, shares, and analyzes information on energy to advance policymaking, markets, and the public view on energy and how it connects to the economy and environment.<sup>12,13</sup> The *Annual Energy Review* report, published in September 2012 by the U.S. EIA, shows the costs associated with fossil fuels has steadily increase from 1949 – 2021.<sup>11</sup> Recently, in a report created by the Organisation for Economic Co-operation and Development (OCED) shows the amount of money used to support fossil fuels has almost doubled from 2021 to 2022.<sup>14</sup> The OCED is an

international organization that focuses on building better policies that will improve lives and encourage prosperity, equality and opportunities for everyone.<sup>15</sup> The OECD report, published in December 2023, contains data and information on 82 countries that used fossil fuel as an energy source from 2013 – 2022.<sup>14</sup> In 2022, the OECD report states that approximately \$36.1 billion was used to invest in support measures of coal and other fossil fuels, while approximately \$10 billion was used to invest in support measure for other energy sources. According to the U.S. DOE, over the years, the cost of solar energy has significantly decreased, which has made it the fastest growing and most affordable source of new electricity. As a result, this has led to ensuring the U.S. Congress and U.S. DOE investing hundreds of millions of dollars into research that focuses on the solar energy applications, as shown in the Energy Act of 2020 and U.S. DOE website. In 2020, U.S. Congress passed the Energy Act of 2020, the Clean Energy Innovation, a bill that shows the government will invest approximately \$2.6 billion in solar energy research and technology, such as solar tech and energy storage, between 2021 to 2025.<sup>3,4</sup> The significance of this investment is it will help change the type energy sources used society and will assist with making solar energy more commercially available to everyone in society. The positive impact of solar energy is it help lower energy costs in society and provide a cleaner environment. To ensure that solar energy can will make a positive impact, the U.S. DOE has created Offices that developed goals and objectives for solar energy.

Under the U.S. DOE, there are two Offices that focuses on creating a clean energy economy and provides funding for research areas regarding solar energy. The two Offices are called the Office of Energy Efficiency and Renewable Energy (EERE) and the Solar Energy Technologies Office (SETO). The objective of the EERE is to develop an economy based on clean energy for everyone in the U.S.. The mission of the EERE is to assist increasing research, deployment,

development and demonstration of technologies and solutions that will lead to a low-cost net-zero gas emissions economy for everyone in the U.S. country by 2050. Under the Office of EERE, there is another Office called SETO that supports the mission of EERE by: supporting innovation of technology; ensuring accessible solar; developing manufacturing and job growth in various applications. The SETO provides financial support to many research areas, such as: photovoltaics (PV); concentrating solar-thermal power; systems integration; manufacturing and competitiveness; soft costs; and solar workforce development. For each research areas, SETO creates objectives and targets for all of the areas. For the research area PV, the SETO has been creating objectives and targets for this area since 2011. In 2011, the SETO released the *SunShot Initiative* that focuses on making solar-generated electricity competitive to other sources by 2020. For utility-scale photovoltaic installations, SETO met that goal three year before 2020. In 2020, the SETO assisted with the production of large utility-scale systems and costs of 5¢/kWh or lower. An outcome of this accomplishment is this type utility-scale systems became the least expensive form of new electricity generation. To continue this success, the SETO has continued to develop other goals and targets through series called *SunShot Vision Study* in 2012 and *On the Path to SunShot* in 2016. The current and third series is called *Solar Futures Study*.

### A.3 References

- (1) U.S. Department of Energy. <https://www.energy.gov/solar> (accessed 2024-01-15).
- (2) U.S. Department of Energy Office Solar Energy Technologies Office. <https://www.energy.gov/eere/solar/photovoltaics> (accessed 2024-01-20).
- (3) Feblowitz, J. Renewable Energy World, 2021. <https://www.renewableenergyworld.com/solar/government-and-private-funding-we-need-both-for-the-energy-transition/#gref> (accessed 2024-02-02).
- (4) Committee on Science Space and Technology, 2020. <https://science.house.gov/2020/12/energy-act-of-2020> (accessed 2024-02-03).
- (5) U.S. Department of Energy Office Solar Energy Technologies Office. <https://www.energy.gov/eere/solar/organic-photovoltaics-research> (accessed 2024-01-19).
- (6) Inganäs, O. Organic Photovoltaics over Three Decades. *Adv. Mater.* **2018**, *30* (35), 1800388. <https://doi.org/10.1002/adma.201800388>.
- (7) Sharma, T.; Mahajan, P.; Adil Afroz, M.; Singh, A.; Yukta; Kumar Tailor, N.; Purohit, S.; Verma, S.; Padha, B.; Gupta, V.; Arya, S.; Satapathi, S. Recent Progress in Advanced Organic Photovoltaics: Emerging Techniques and Materials. *ChemSusChem* **2022**, *15* (5). <https://doi.org/10.1002/cssc.202101067>.
- (8) Tamai, Y. What's Next for Organic Solar Cells? The Frontiers and Challenges. *Adv. Energy Sustain. Res.* **2023**, *4* (1), 2200149. <https://doi.org/10.1002/aesr.202200149>.
- (9) Corbett, M. Federal Reserve History. <https://www.federalreservehistory.org/essays/oil-shock-of-1973-74> (accessed 2024-01-16).
- (10) Beasley, B. A. Energy History Online - Yale University, 2023. <https://energyhistory.yale.edu/the-oil-shocks-of-the-1970s/> (accessed 2024-01-16).
- (11) U.S. Energy Information. Annual Energy Review 2011. **2012**.
- (12) U.S. Energy Information Administration. <https://www.eia.gov/about/> (accessed 2024-01-14).
- (13) U.S. Energy Information Administration. [https://www.eia.gov/about/mission\\_overview.php](https://www.eia.gov/about/mission_overview.php) (accessed 2024-01-14).
- (14) OECD. *OECD Inventory of Support Measures for Fossil Fuels 2023*; 2023. <https://doi.org/10.1787/87dc4a55-en>.

## **Appendix B: Collaborator Experimental Information**

### **Table of Content**

<b>B.1 Prelude.....</b>	<b>205</b>
<b>B.2 Fluorescence Quantum Yield Calculation.....</b>	<b>205</b>
<b>B.3 Two-photon Absorption .....</b>	<b>206</b>
<b>B.4 References .....</b>	<b>208</b>

## B.1 Prelude

This Appendix provides fundamental information on the experimental that is conducted by *Collabroators* on research investigations discussed in this dissertation. The experimental details of discussed in this Appendix are discussed in the main Chapters of the dissertation. In addition, the main Chapters describe which measurements and/or experiments are conducted by *Collaborators* in the main Chapters of the dissertation.

## B.2 Fluorescence Quantum Yield Calculation

Fluorescence quantum yield ( $\Phi_F$ ) is a numeral value that describes the efficiency of photons emitted versus absorbed.<sup>1,2</sup> In other words,  $\Phi_F$  is the ratio between emitted photons versus absorbed photons. A common measurement done to determine  $\Phi_F$  is the Williams comparative method () of the BNIA small molecules in liquid solutions.<sup>1,2</sup> The Williams method using **Equation B.1** to determine the  $\Phi_F$  of a molecule:

**Equation B.1**

$$\Phi_F = \Phi_{STD} \frac{Grad_x \eta_x^2}{Grad_{STD} \eta_{STD}^2}$$

where  $\Phi_F$  was calculated quantum yield;  $\eta$  was refractive index of the solvent; *Grad* was the slope obtained from the fluorescence area versus the optical density plot; *STD* was the reference standard; and *x* referred to information for the investigated BNIA small molecules. In order to determine the reference standard that should be used for this measurement, the steady-state absorption spectrum of the reference standard need to be in the same range of the steady-state absorption spectrum of the molecule. The main criteria to consider for the reference standard is the amount of absorption at the excitation wavelength used to collect the steady-state emission spectrum of the molecule.  $\Phi_F$  provides information on how fluorescent or the probability of fluorescence occurring within a molecule. This information can be useful to provide supporting

evidence that a molecule will be better suited for one optoelectronic application to another application.

### B.3 Two-photon Absorption

Two-photon absorption (TPA) is an experiment that uses two photons to excite a molecule and provides insight into the transition dipole moment or charge transfer dynamics of a molecule.<sup>4,5</sup> In order to quantify the transition dipole moment or charge transfers of a molecule, the TPA cross-section of a molecule is determined.<sup>4,5</sup> **Equation B.2** shows the formula for calculating the TPA cross-section<sup>4,5</sup>

$$\text{Equation B.2} \quad \frac{10^{sample-std-yint} \times \phi_{fluor} \times \delta_{std} \times [ ]_{std} \times n_{std}}{\phi_{fluosample} \times [ ]_{sample} \times n_{sample}} = \delta_{TPA}$$

where,  $\delta_{TPA}$  is the TPA cross-section;  $10^{sample-std-yint}$  is the sample intercept and standard intercept obtained for the TPA experiment;  $\phi_{fluor}$  is fluorescence quantum yield of the sample;  $\delta_{std}$  is the TPA cross section of the standard;  $[ ]_{std}$  is the concentration of the standard;  $n_{std}$  is the index of refraction of the solvent used to create the reference standard solution;  $\phi_{fluosample}$  is fluorescence quantum yield of the sample;  $[ ]_{sample}$  is the concentration of the sample;  $n_{sample}$  is index of refraction of the solvent used to create the sample solution.

During TPA experiment the two-photon induced fluorescence is collected for a molecule. The molecule is excited by two-photon using a Spectra-Physics Millennia Pro laser and Tsunami Ti:Sapphire, mode-locked laser that has a repetition rate of 80MHz and pulse width of approximately 100fs. The range of Tsunami is 750nm – 810nm. Typically, the output power of the Tsunami is between 200mW – 100mW; however, the power depends on the molecule and which power will increase the likely hood of TPA occurring within a molecule. The two-photon



fluorescence of a molecule is collected by a photomultiplier tube, photocounting unit and monochromator. In order to collect the fluorescence, the sample is placed perpendicular from the photomultiplier tube and monochromator. To verify that two-photon absorption is occurring within a molecule, power dependence of power versus count intensity is done. A log-log plot of the two-photon induced fluorescence count intensity versus power is plotted to determine the slope of the linear dependence. If the slope of this dependence is roughly  $\sim 2.0$ , then this supports TPA is occurring within a molecule. Research has shown that TPA depends on the molecular structure of a molecule. If the molecular structure of a molecule shows there is change of dipole moment, then this will increase the probability of TPA occurring within a molecule.

## B.4 References

- (1) Ricci, F.; Mandal, H.; Wajahath, M.; Burdick, R. K.; Villabona-Monsalve, J. P.; Hussain, S.; Goodson, T. Investigations of Coherence in Perovskite Quantum Dots with Classical and Quantum Light. *J. Phys. Chem. C* **2023**, *127* (7), 3579–3593.
- (2) Williams, A. T. R.; Winfield, S. A.; Miller, J. N. Relative Fluorescence Quantum Yields Using a Computer-Controlled Luminescence Spectrometer. *The Analyst* **1983**, *108* (1290), 1067. <https://doi.org/10.1039/an9830801067>.
- (3) Makarov, N. S.; Drobizhev, M.; Rebane, A. Two-Photon Absorption Standards in the 550–1600 Nm Excitation Wavelength Range. *Opt. Express* **2008**, *16* (6), 4029. <https://doi.org/10.1364/OE.16.004029>.
- (4) Xu, C.; Webb, W. W. Measurement of Two-Photon Excitation Cross Sections of Molecular Fluorophores with Data from 690 to 1050 Nm. *J. Opt. Soc. Am. B* **1996**, *13* (3), 481. <https://doi.org/10.1364/JOSAB.13.000481>.
- (5) Vázquez, R. J.; Kim, H.; Kobilka, B. M.; Hale, B. J.; Jeffries-EL, M.; Zimmerman, P.; Goodson, T. Evaluating the Effect of Heteroatoms on the Photophysical Properties of Donor–Acceptor Conjugated Polymers Based on 2,6-Di(Thiophen-2-Yl)Benzo[1,2-b:4,5-B']Difuran: Two-Photon Cross-Section and Ultrafast Time-Resolved Spectroscopy. *J. Phys. Chem. C* **2017**, *121* (27), 14382–14392. <https://doi.org/10.1021/acs.jpcc.7b01767>.

## **Appendix C: Supporting Information for Chapter III**

### **The Investigation of the Ultrafast Dynamics within Organic Ladder Oligomers used in Optoelectronics Applications**

#### **Table of Contents**

<b>C.1 Steady-state Absorption and Emission Results .....</b>	<b>210</b>
<b>C.2 femtosecond Transient Absorption (fs-TA) Results .....</b>	<b>214</b>

### C.1 Steady-state Absorption and Emission Results

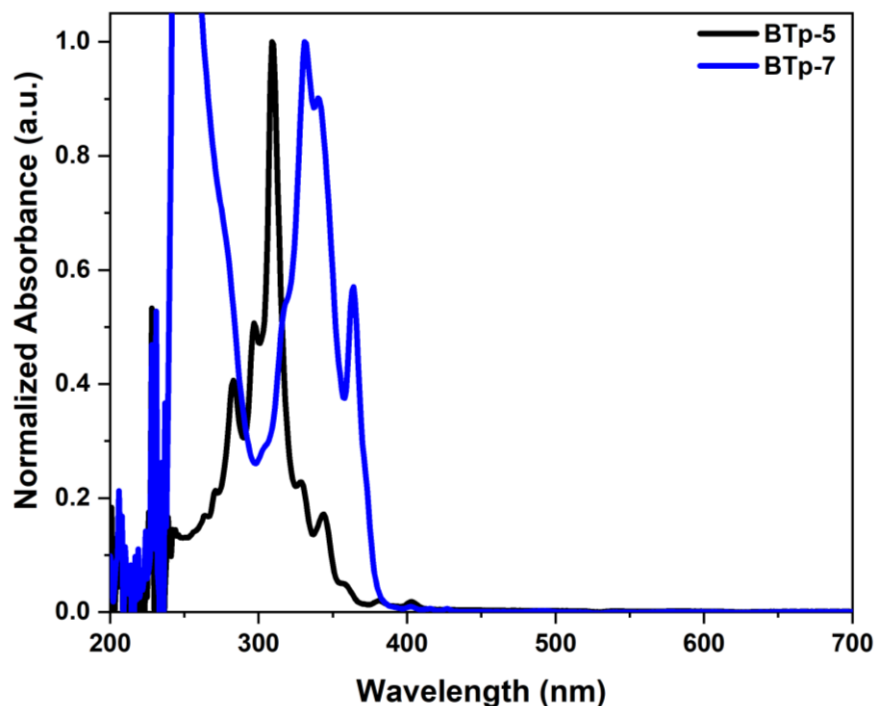


**Figure C.1:** Normalized steady-state absorption spectra of the BTp solutions in chloroform from 200nm – 700nm. The purpose of this Figure is to show the capabilities of new UV-Vis spectrophotometer, Agilent Cary 60 UV-Vis Spectrophotometer. The new UV-Vis spectrophotometer has the capability of measuring a steady-state absorption spectrum from 190nm – 1100nm. For the steady-state absorption measurements of the BTp solutions, the range of 200nm – 700nm was used.

**Table C.1:** Summary of emission peaks observed in the steady-state emission spectra of the BTp solutions in chloroform

Steady-state emission peaks (nm)				
Oligomer	Peak 1	Peak 2	Peak 3	Peak 4
<b>BTp-5</b>	407	430	458	488
<b>BTp-7</b>	429	440	455	484

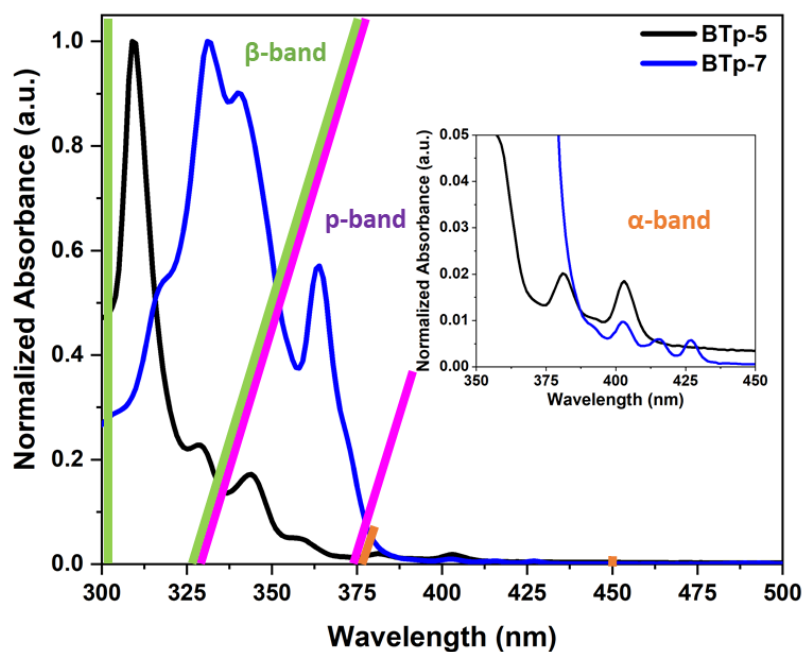


**Figure C.2:** Showing the location of the  $\beta$ -, p- and  $\alpha$ - bands on the normalized steady-state absorption spectra of BTp solutions in chloroform

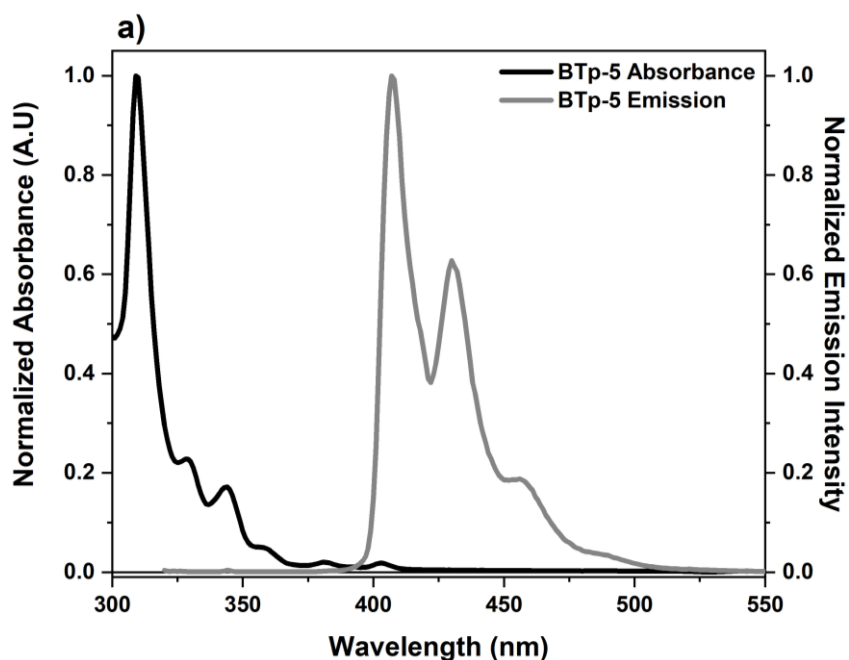


**Figure C.3:** Normalized steady-state absorption and emission spectra of the BTp solutions in chloroform on one graph: (a) BTp-5, for emission spectrum, 310nm excitation is utilized and (b) BTp-7, for emission spectrum, 332nm excitation is utilized

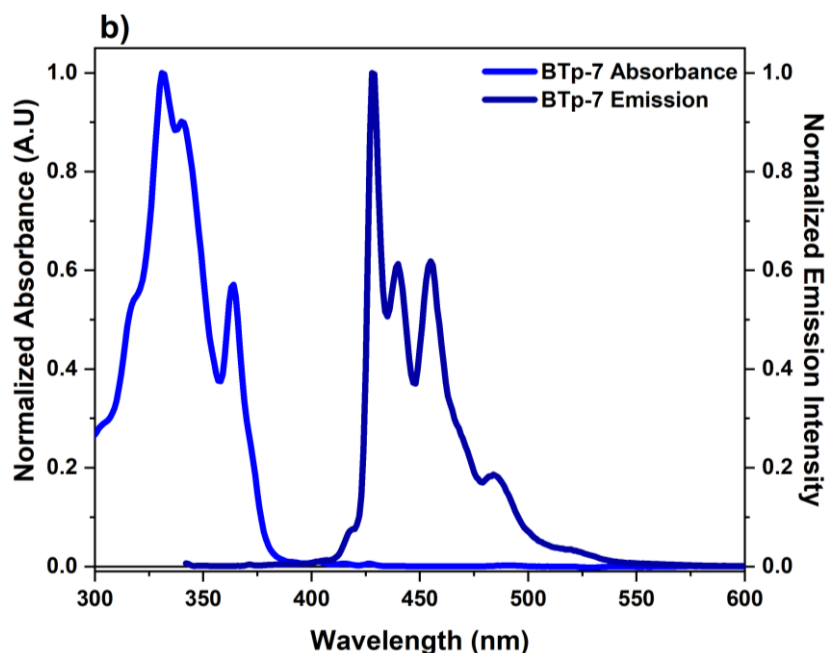


**Figure C.3 (continued):** Normalized steady-state absorption and emission spectra of the BTp solutions in chloroform on one graph: **(a)** BTp-5, for emission spectrum, 310nm excitation is utilized and **(b)** BTp-7, for emission spectrum, 332nm excitation is utilized

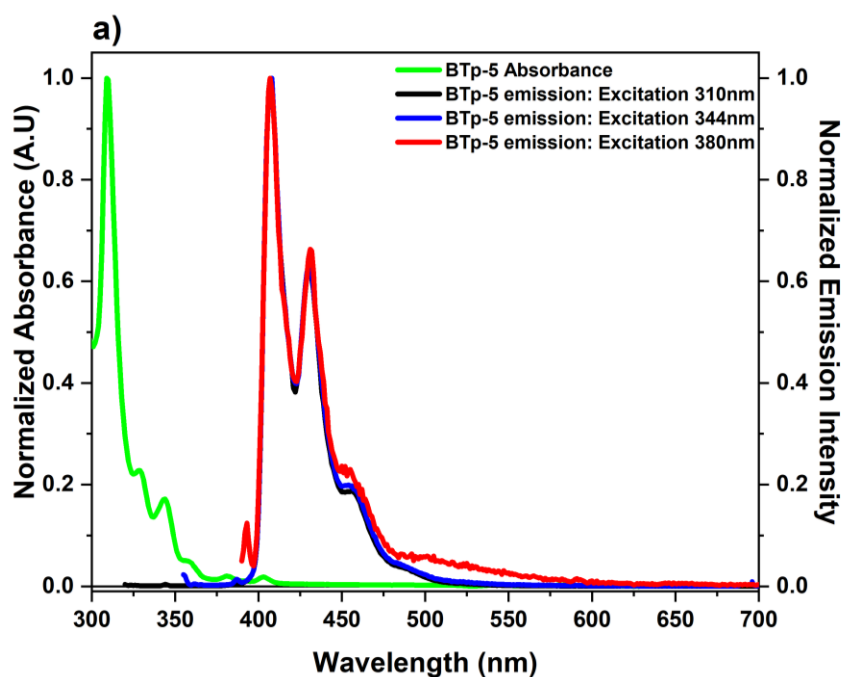


**Figure C.4:** Normalized steady-state emission spectra of BTp solutions in chloroform obtained from different excitation wavelengths: **(a)** BTp-5 and **(b)** BTp-7. The emission spectra is not dependent on excitation wavelength for both BTps.

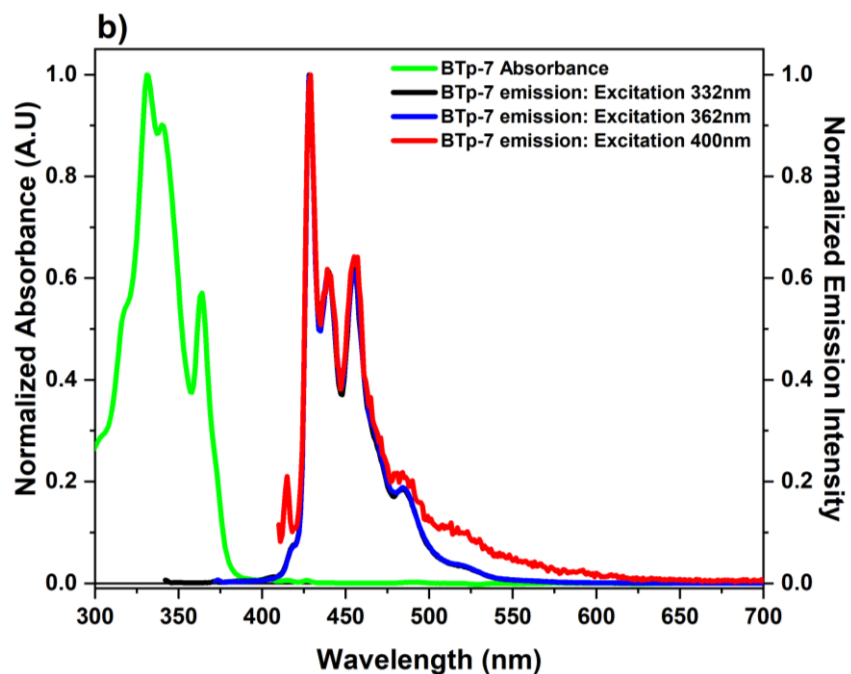


**Figure C.4 (continued):** Normalized steady-state emission spectra of BTp solutions in chloroform obtained from different excitation wavelengths: **(a)** BTp-5 and **(b)** BTp-7. The emission spectra is not dependent on excitation wavelength for both BTPs solutions.

## D.2 femtosecond Transient Absorption (fs-TA) Results

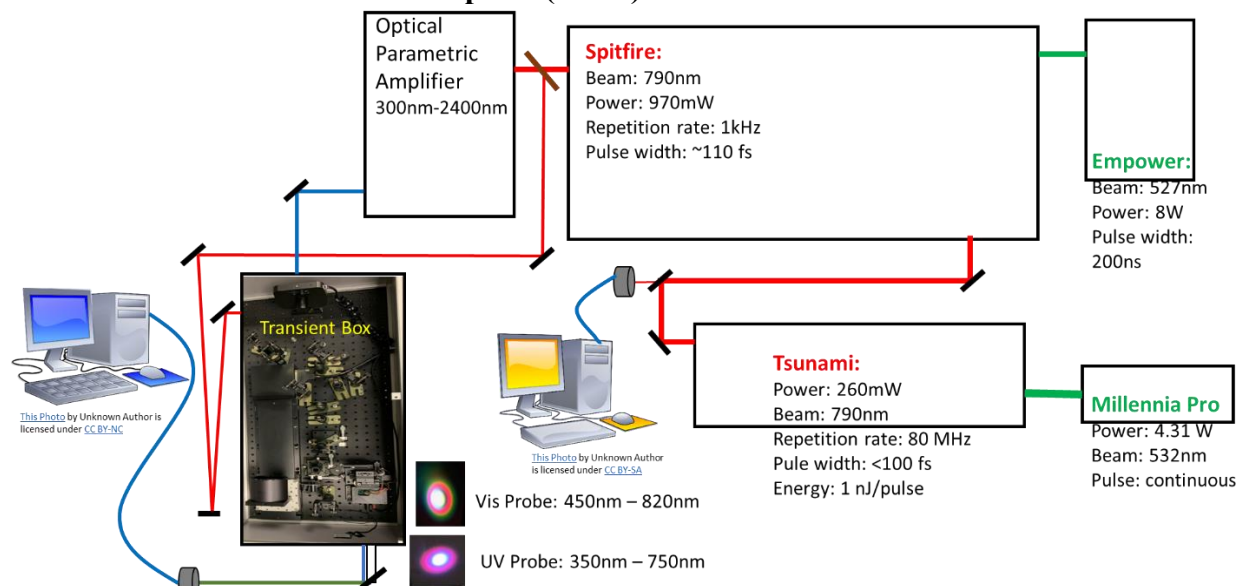


**Figure C.5:** General schematic of ultraviolet (UV) and visible (Vis) femtosecond transient absorption (fs-TA) utilized to conducted experiments on BTP solutions. The UV probe is an extension to Vis probe fs-TA experiment used in previous studies. The UV probe is generated from a calcium fluoride ( $\text{CaF}_2$ ) crystal. The range of the UV probe is 350nm – 750nm.

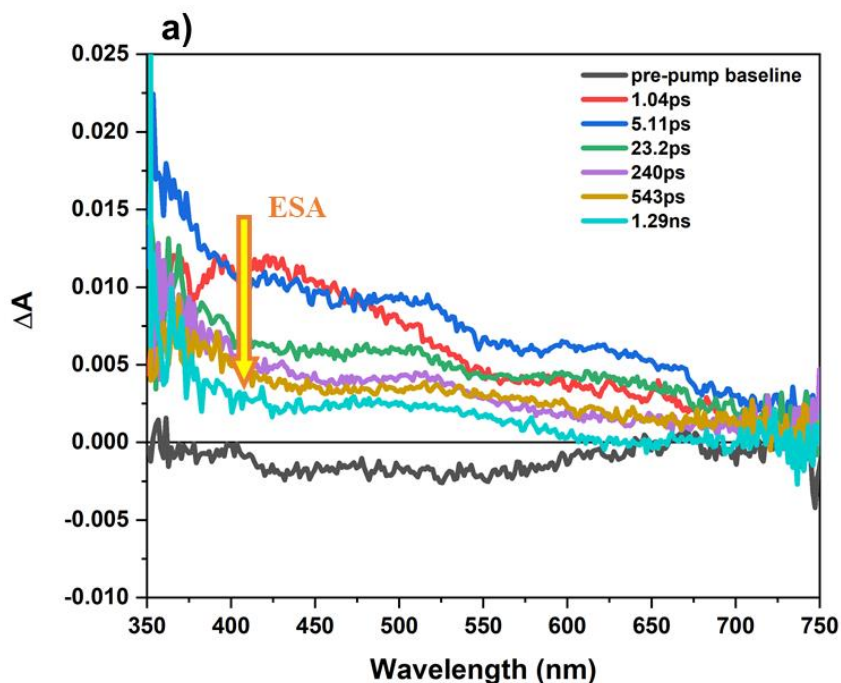


**Figure C.6:** Time-resolved femtosecond transient absorption (fs-TA) spectra, from 0ps (pre-pump baseline) – 1.3ns, of BTP solutions obtained from  $\beta$ -band pump excitation wavelength: (a) BTP-5 and (b) BTP-7



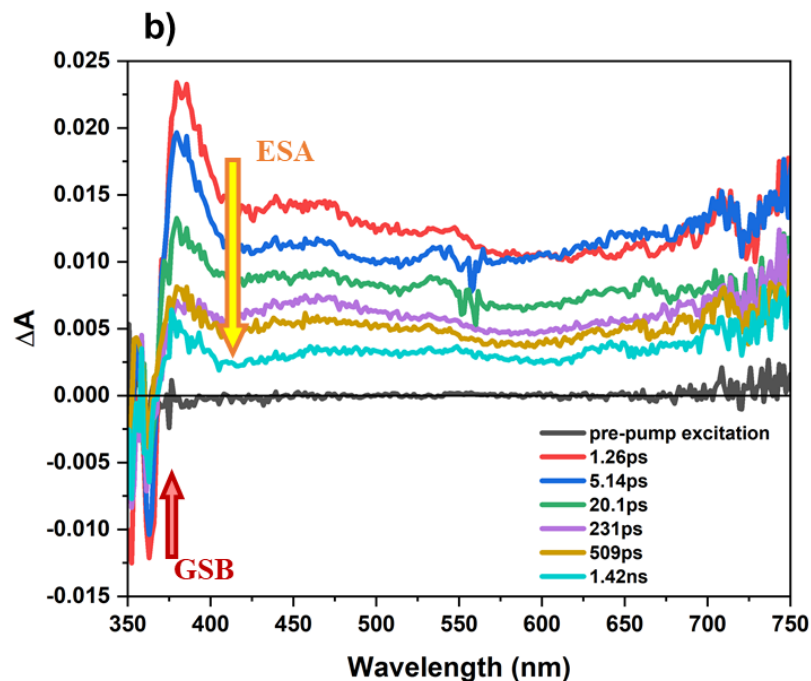


**Figure C.6 (continued):** Time-resolved femtosecond transient absorption (fs-TA) spectra, from 0ps (pre-pump baseline) – 1.4ns of BTP solutions obtained from  $\beta$ -band pump excitation wavelength: (a) BTP-5 and (b) BTP-7

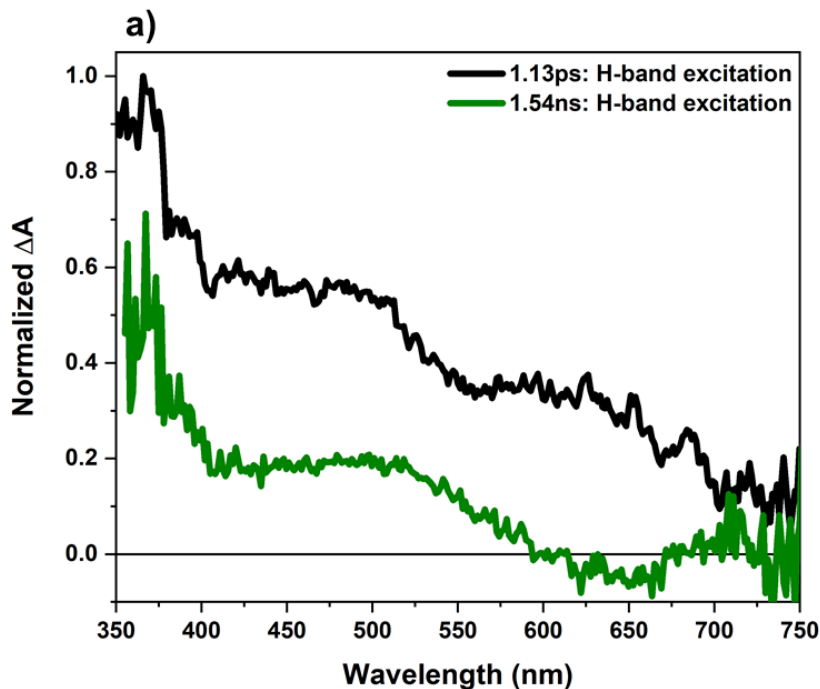


**Figure C.7:** Comparing differences in ESA signals from roughly 1.2ps to 1.4ns obtained from  $\beta$ -band pump excitation wavelength of BTP solutions: (a) BTP-5 and (b) BTP-7

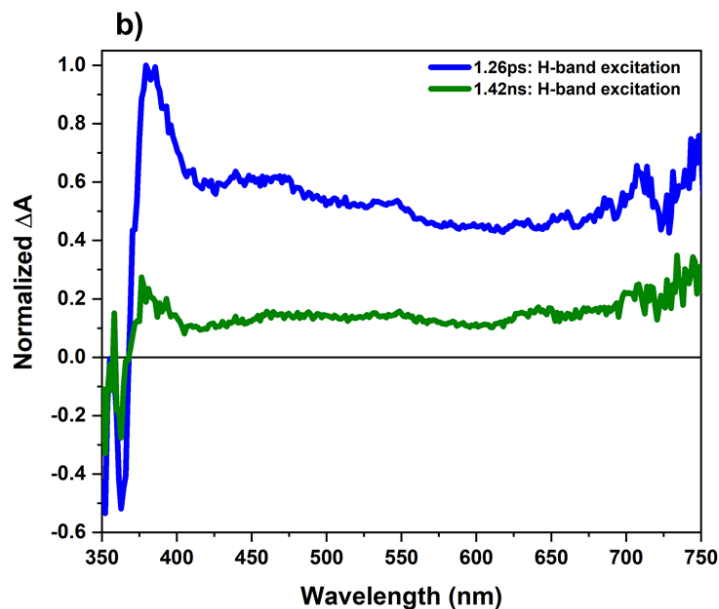


**Figure C.7 (continued):** Comparing differences in ESA signals from roughly 1.2ps to 1.4ns obtained from  $\beta$ -band pump excitation wavelength of BTp solutions: **(a)** BTp-5 and **(b)** BTp-7

**Table C.2:** Summary of time components and rates obtained from kinetic traces due to  $\beta$ -band pump excitation wavelength: **(a)** BTp-5 and **(b)** BTp-7

**a)**

$\beta$ -band time components, $\tau$ , (ps) and rates, $k_n$ , ( $s^{-1}$ ) of BTp-5					
ESA 360nm		ESA 392nm		ESA 502nm	
$\tau_1$ :15	$k_1$ : $7 \times 10^{10}$	$\tau_1$ :11	$k_1$ : $9 \times 10^{10}$	$\tau_1$ :6.2	$k_1$ : $2 \times 10^{11}$
$\tau_2$ :588	$k_2$ : $1.7 \times 10^9$	$\tau_2$ : 570	$k_2$ : $1.8 \times 10^9$	$\tau_2$ : 442	$k_2$ : $2.2 \times 10^9$

**b)**

$\beta$ -band time components, $\tau$ , (ps) and rates, $k_n$ , ( $s^{-1}$ ) of BTp-7					
GSB 364nm		ESA 488nm		ESA 392nm	
$\tau_1$ : 4.6	$k_1$ : $2 \times 10^{11}$	$\tau_1$ : 10	$k_1$ : $1 \times 10^{11}$	$\tau_1$ : 5.3	$k_1$ : $2 \times 10^{11}$
NA	NA	$\tau_2$ : 958	$k_2$ : $1.0 \times 10^9$	$\tau_2$ : 718	$k_2$ : $1.4 \times 10^9$

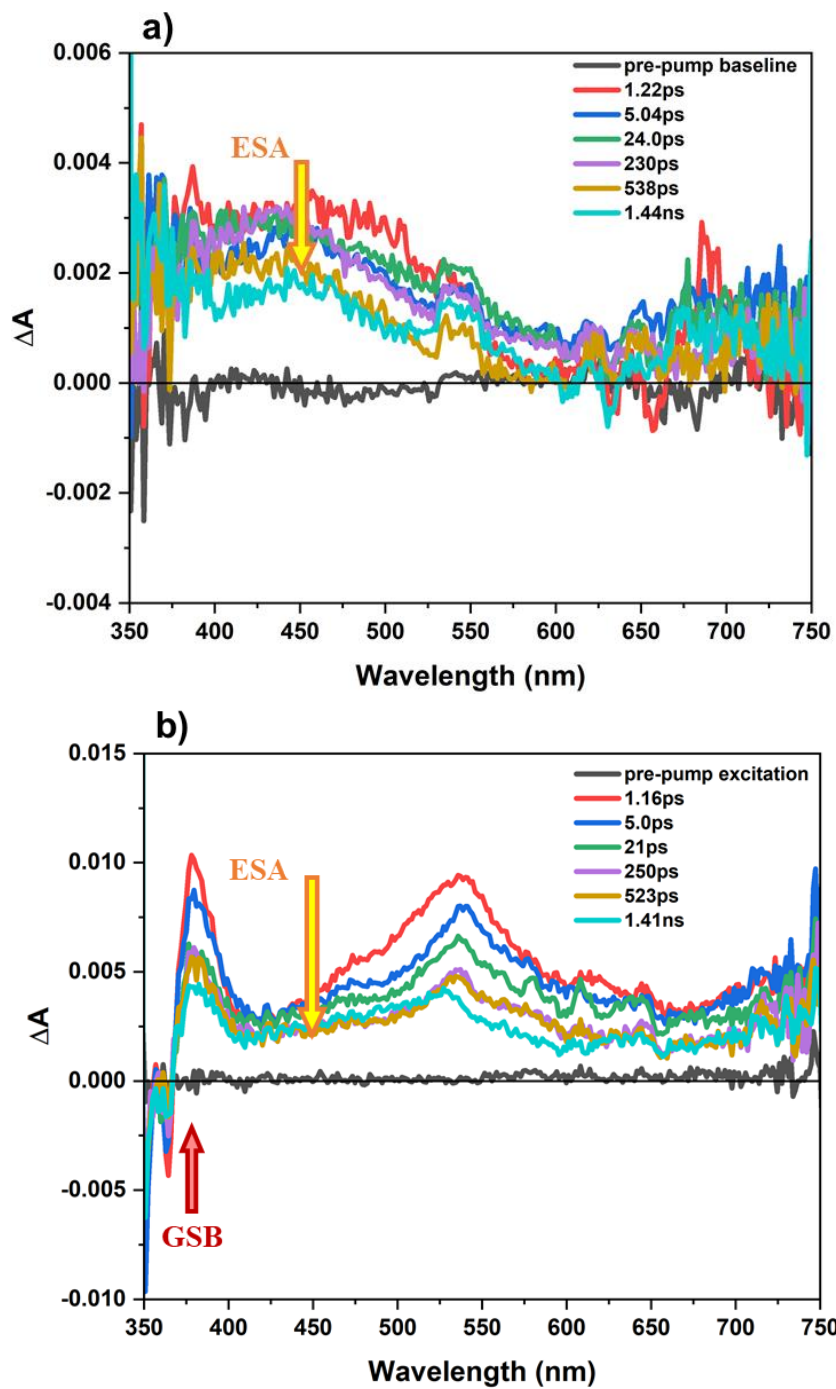


**Figure C.8:** Time-resolved femtosecond transient absorption (fs-TA) spectra, from 0ps (pre-pump baseline) – 1.4ns, of BTp solutions obtained from p-band pump excitation wavelength: (a) BTp-5 and (b) BTp-7

**Table C.3:** Summary of time components and rates obtained from kinetic traces due to p-band pump excitation wavelength: (a) BTP-5 and (b) BTP-7

a) BTP-5

p-band time components, $\tau$ , (ps) and rates, $k_n$ , ( $s^{-1}$ ) of BTP-5					
GSB 364nm		ESA 536nm		ESA 745nm	
$\tau_1$ : 3.1	$k_1$ : $3 \times 10^{11}$	$\tau_1$ : 48	$k_1$ : $2 \times 10^{10}$	$\tau_1$ : 6.5	$k_1$ : $2 \times 10^{11}$
$\tau_2$ : 98	$k_2$ : $1.0 \times 10^{10}$	$\tau_2$ : 649	$k_2$ : $1.5 \times 10^9$	$\tau_2$ : 1298	$k_2$ : $7.7 \times 10^8$

b) BTP-7

p-band time components, $\tau$ , (ps) and rates, $k_n$ , ( $s^{-1}$ ) of BTP-7					
GSB 364nm		ESA 536nm		ESA 745nm	
$\tau_1$ : 3.1	$k_1$ : $3 \times 10^{11}$	$\tau_1$ : 48	$k_1$ : $2 \times 10^{10}$	$\tau_1$ : 6.5	$k_1$ : $2 \times 10^{11}$
$\tau_2$ : 98	$k_2$ : $1.0 \times 10^{10}$	$\tau_2$ : 649	$k_2$ : $1.5 \times 10^9$	$\tau_2$ : 1298	$k_2$ : $7.7 \times 10^8$

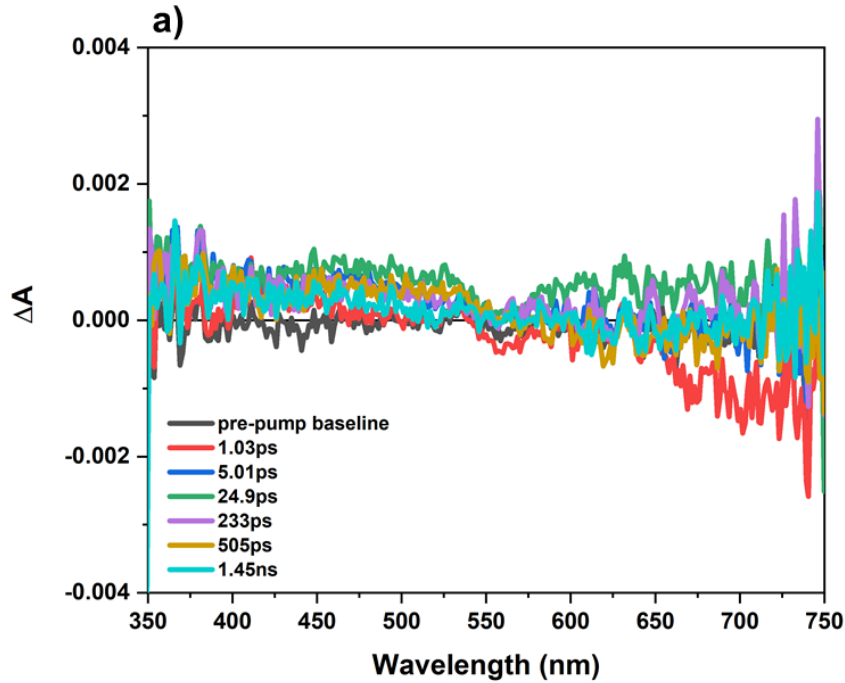


**Figure C.9:** Time-resolved femtosecond transient absorption (fs-TA) spectra, from 0ps (pre-pump baseline) – 1.4ns of BTP solutions obtained from  $\alpha$ -band pump excitation wavelength: (a) BTP-5 and (b) BTP-7

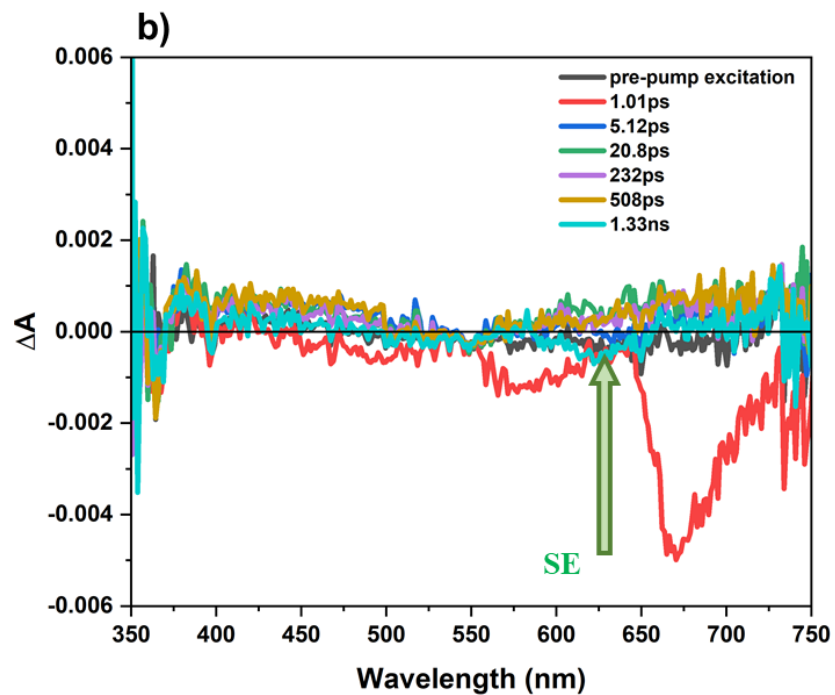


**Figure C.9 (continued):** Time-resolved femtosecond transient absorption (fs-TA) spectra, from 0ps (pre-pump baseline) – 1.4ns of BTp solutions obtained from  $\alpha$ -band pump excitation wavelength: **(a)** BTp-5 and **(b)** BTp-7

## Appendix D: Supporting Information for Chapter IV

### Probing the Exciton Dynamics of Naphthalene-imide Based Nonfullerene Acceptors for Organic Photovoltaics

#### Table of Contents

<b>D.1 Steady-state Absorption and Emission Results .....</b>	<b>221</b>
<b>D.2 Two-photon Absorption (TPA) and Fluorescence Quantum Yield Results .....</b>	<b>224</b>
<b>D.3 Time-resolved Fluorescence Upconversion (UpC) results .....</b>	<b>226</b>
<b>D.4 femtosecond Transient Absorption (fs-TA) Results .....</b>	<b>227</b>
<b>D.5 Theoretical Calculation Results .....</b>	<b>239</b>

## D.1 Steady-state Absorption and Emission Results

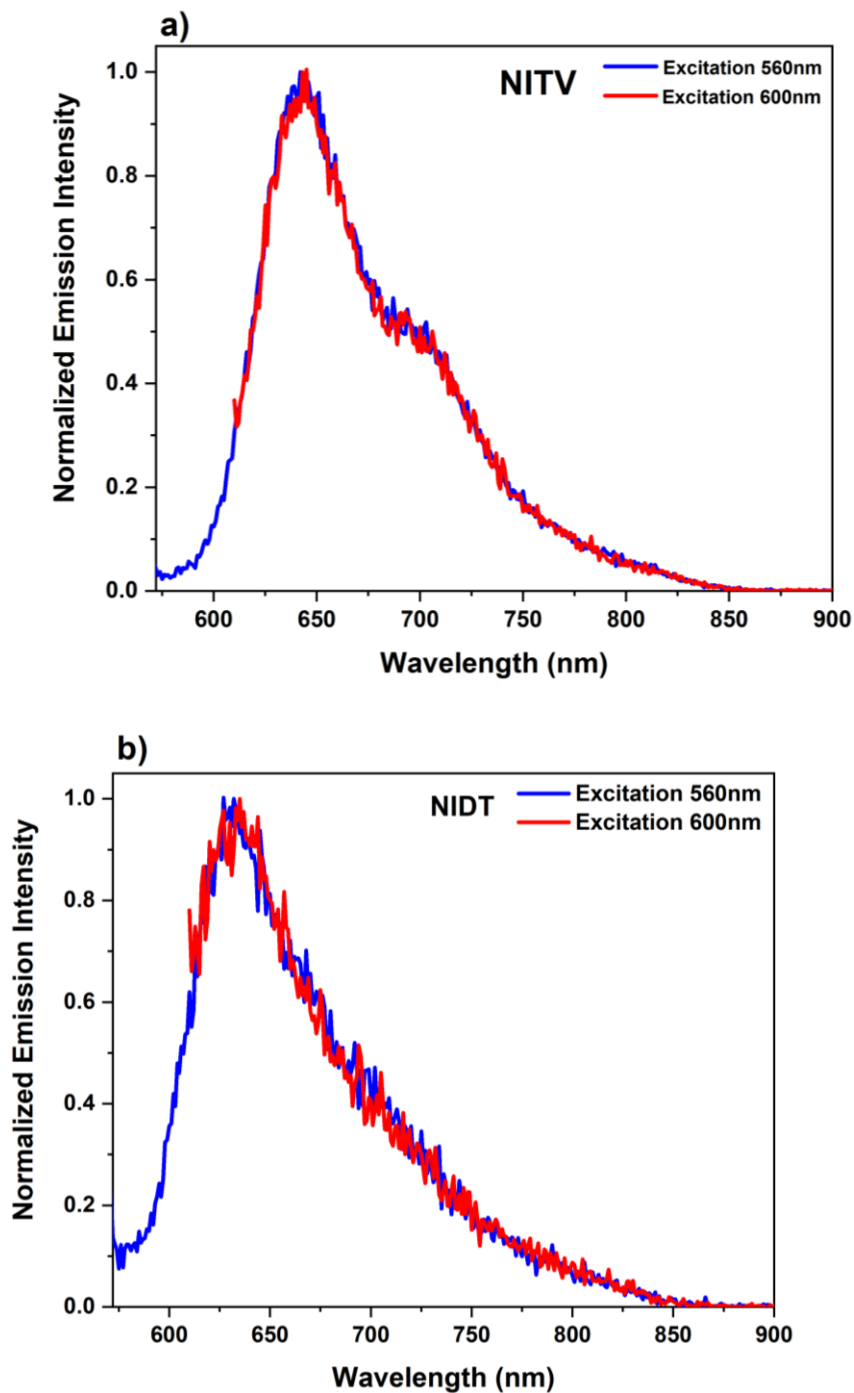


**Figure D.1:** Normalized emission spectra of BNIA in chloroform due to different excitation wavelengths – a) NITV; b) NIDT; and c) NIBT. For all BNIA, the emission maximum peak is not dependent on excitation wavelength.

For all BNIA, the emission spectra measured by 600nm excitation is reported in the paper.

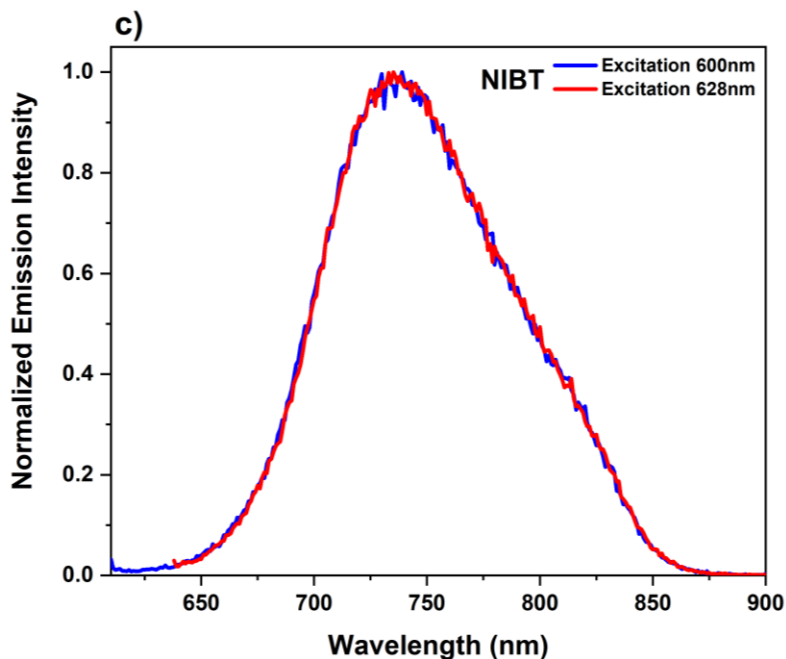


**Figure D.1 (continued):** Normalized emission spectra of BNIAs in chloroform due to different excitation wavelengths – a) NITV; b) NIDT; and c) NIBT. For all BNIA, the emission maximum peak is not dependent on excitation wavelength.

For all BNIA, the emission spectra measured by 600nm excitation is reported in the paper.

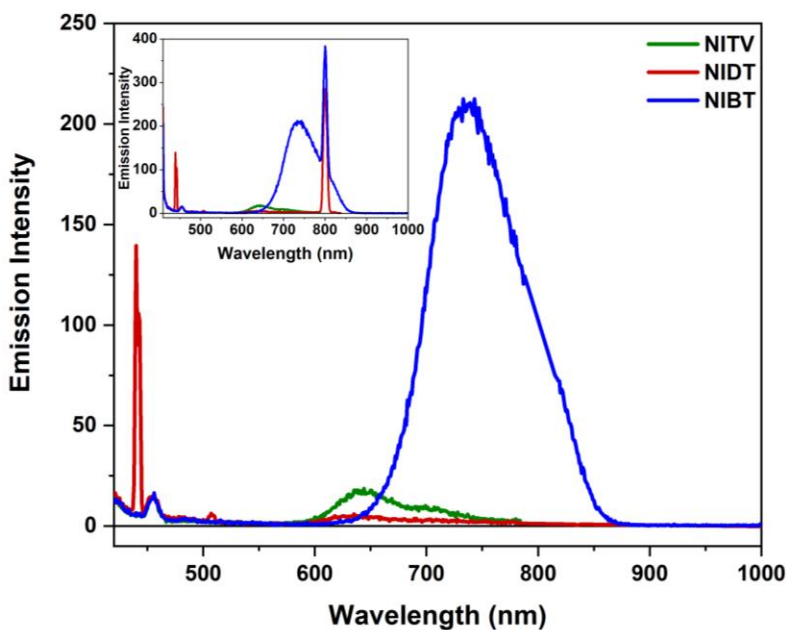


**Figure D.2:** Corrected emission spectra of BNIA in chloroform due to 400nm excitation.

**Insert graph:** Shows uncorrected emission spectra of BNIA. The additional peak at 800nm is a result of second harmonic generation due to 400nm excitation.



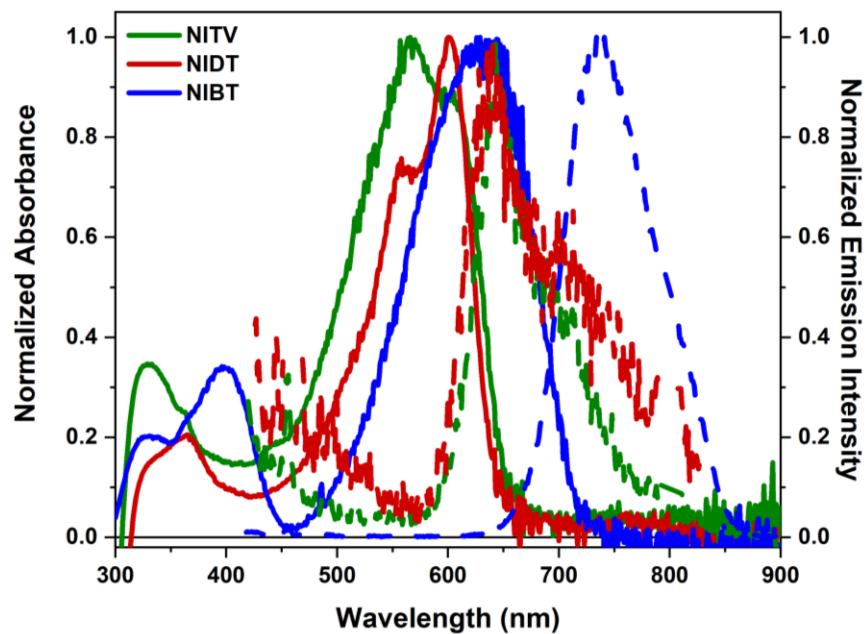


**Figure D.3:** Normalized absorbance and emission spectra of BNIA in chloroform. The emission spectra is corrected emission spectra due to 400nm excitation.

## D.2 Two-photon Absorption (TPA) and Fluorescence Quantum Yield Results

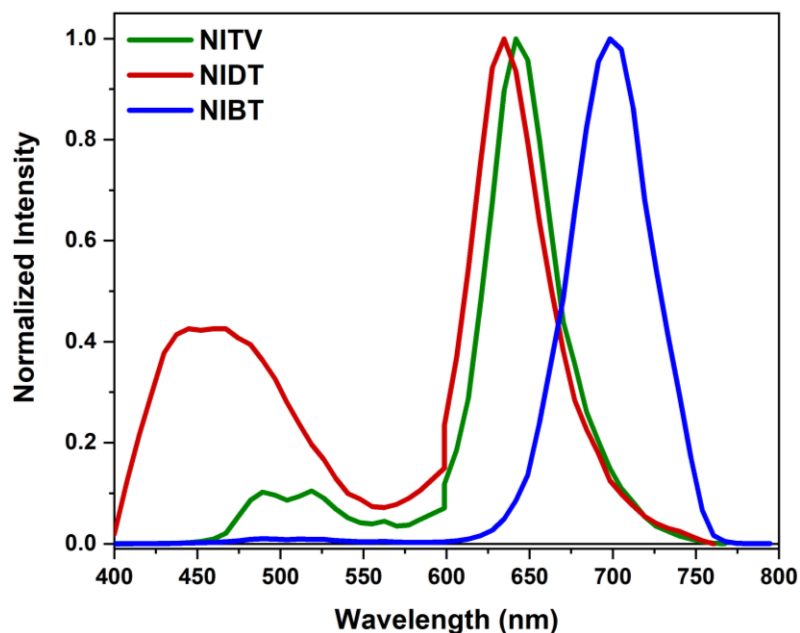


**Figure D.4:** Two-absorption emission spectra of BNIAs using 800nm excitation from two-photon absorption (TPA) experiment.

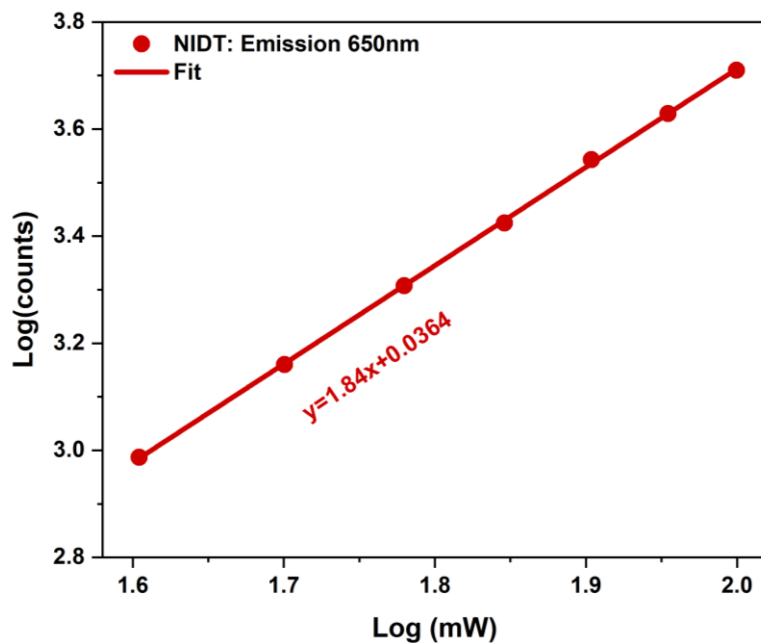


**Figure D.5:** Log-log plot of NIDT in chloroform obtained from two-photon absorption (TPA) experiments using 650nm emission

**Table D.1:** Summary two-photon absorption (TPA) cross sections ( $\delta_{\text{TPA}}$ ) and fluorescence quantum yield ( $\Phi_{\text{Fl}}$ ) of BNIA in chloroform using 800nm excitation for 640nm and 650nm emission

Molecule	TPA Emission Wavelength (nm)	$\delta_{\text{TPA}}$ (GM)	$\Phi_{\text{Fl}}$ (% , $\pm 0.02$ )
NITV	650	96.8	0.4
NIDT	650	73.8	0.3

### D.3 Time-resolved Fluorescence Upconversion (UpC) Results

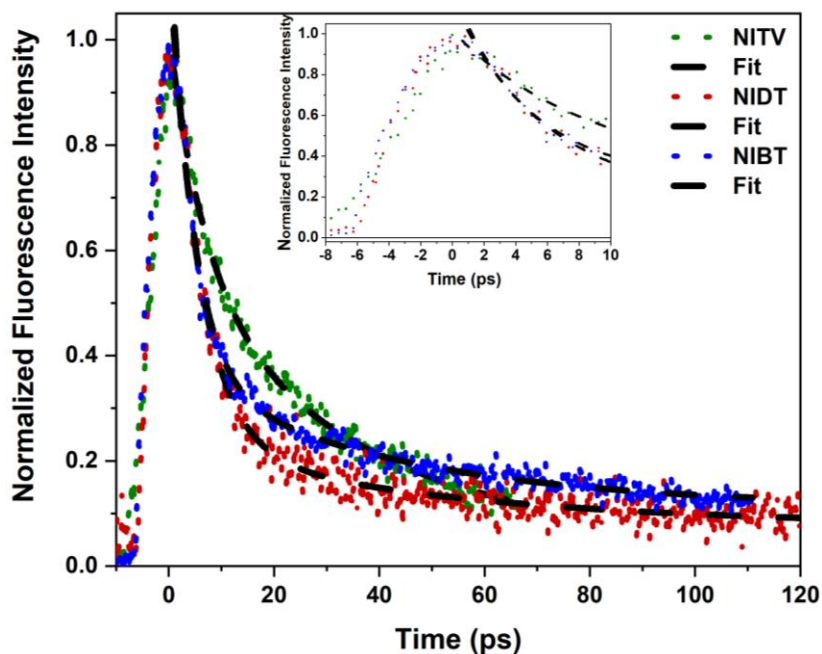


**Figure D.6:** Normalized time-resolved fluorescence upconversion (UpC) kinetics of BNIA in chloroform using 400nm excitation. For all BNIA, 650nm emission is used to measure fluorescence kinetics

**Insert Graph:** Shows rise time of fluorescence decay for all BNIA.

**Table D.2:** Time-resolved fluorescence upconversion (UpC) time components in picosecond (ps) of BNIA in chloroform

\*\*The long  $\tau_{rise}$  is due to the samples being run to reflective mode of UpC

BNIA	** $\tau_{rise}$ (ps)	$\tau_1$ (ps)	A1 (%)	$\tau_2$ ( $\tau_{fluor}$ ) (ps)	A2 (%)
NITV	$18 \pm 3.5$	$6.9 \pm 0.71$	73	$36 \pm 6.8$	27
NIDT	$3.4 \pm 0.28$	$5.8 \pm 0.19$	95	$50 \pm 9.9$	5
NIBT	$4.3 \pm 0.32$	$4.4 \pm 0.12$	93	$41 \pm 2.8$	7

#### D.4 femtosecond Transient Absorption (fs-TA) Results

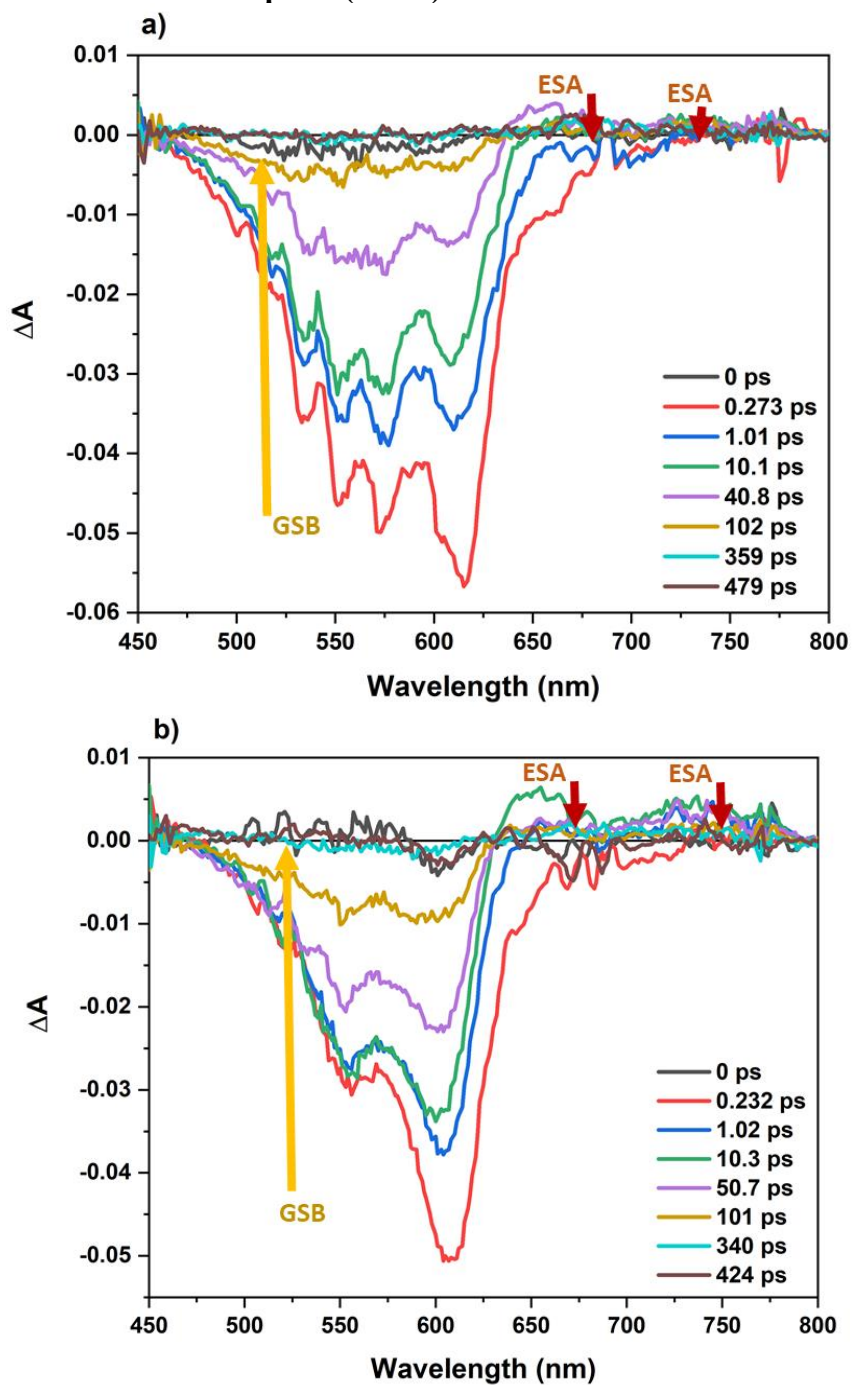


**Figure D.7:** Time-resolved femtosecond transient absorption (fs-TA) spectra of BNIAs in chloroform using 600nm pump – **a)** NITV and **b)** NIDT. The recovery of ground state bleach (GSB) signal is shown using golden/yellow arrows in all three BNIAs. The decay of excited state absorption (ESA) signal(s) is shown using red arrows.

The time-resolved fs-TA of NIBT is reported in the paper (see **Figure 5**)

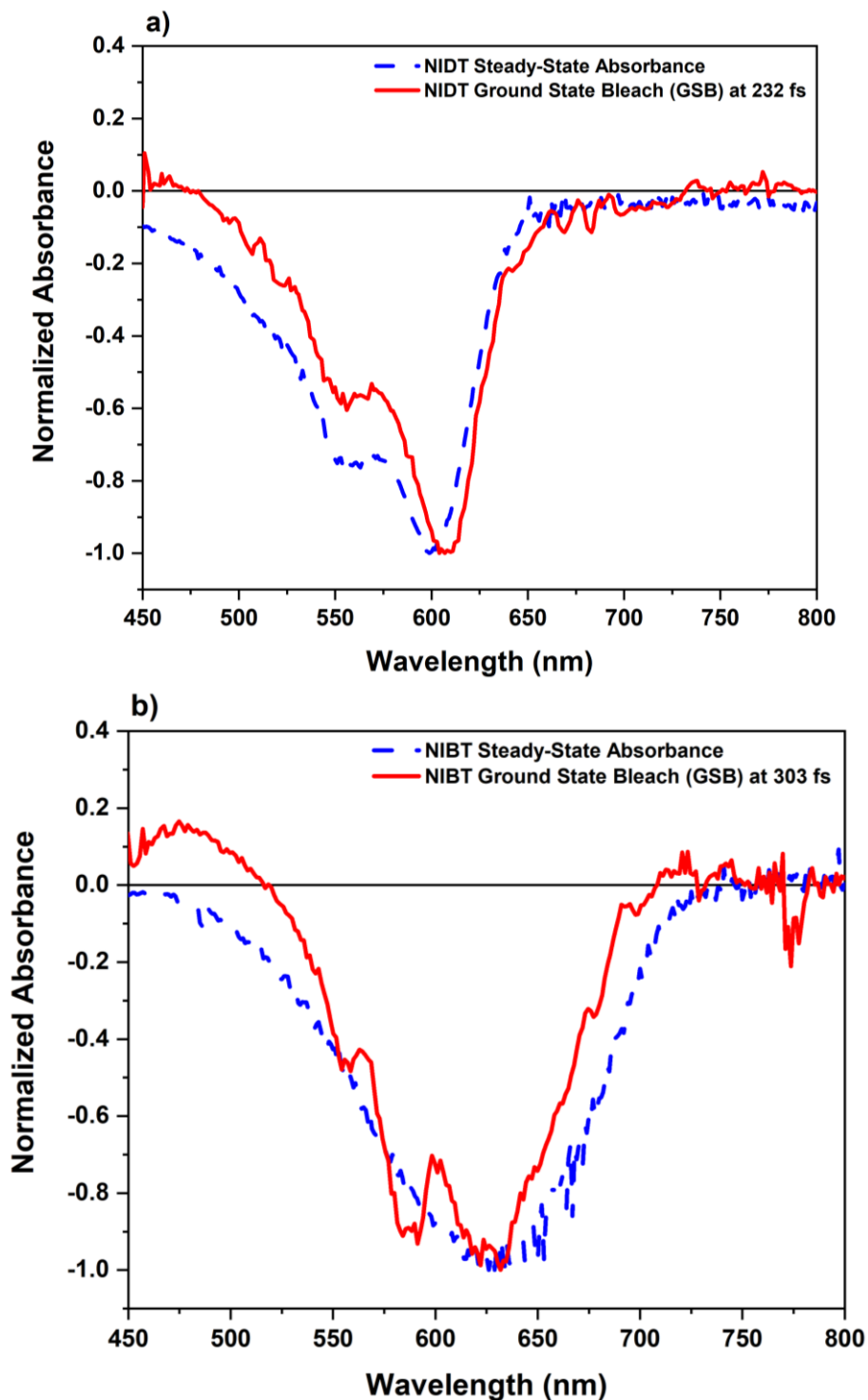


**Figure D.8:** Comparison of steady-state absorption spectrum to the early time of ground state bleach (GSB) signal from femtosecond transient absorption (fs-TA) results of BNIA in chloroform using 600nm excitation – **a)** NIDT and **b)** NIBT

The comparison of steady-state absorption spectrum to early time of GSB signal of NITV is reported in the paper.

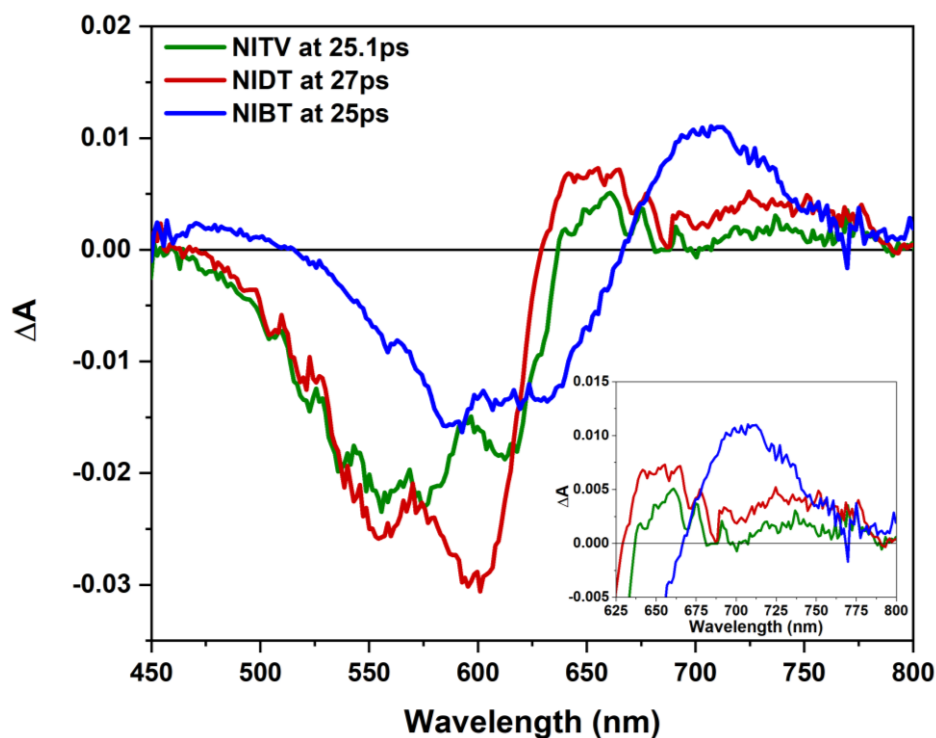


**Figure D.9:** Comparison of femtosecond transient absorption (fs-TA) excited state absorption (ESA) signals of BNIA in chloroform at a specific time using 600nm pump. This figure shows the un-normalized femtosecond transient absorption (fs-TA) spectra.

**Table D.3:** Time components, in picosecond (ps), of ground state bleach (GSB) signals at 600nm from femtosecond transient absorption (fs-TA) results of BNIA in chloroform using 600nm pump

\*time component cannot be resolved since the component is within IRF (160fs)

\*\*Rate: shows that rate of  $\tau_3$  time component

Time components and Amplitude percentages of GSB peak 600nm for all BNIA								
BNIA	$\tau_{rise}$ (ps)	$\tau_1$ (ps)	A1 (%)	$\tau_2$ (ps)	A2 (%)	$\tau_3$ (ps)	**Rate (s <sup>-1</sup> )	A3 (%)
NITV	0.391 ± 1.1	*0.102 ± 0.036	27	1.24 ± 0.44	16	43.5 ± 1.5	2.3e10	57
NIDT	0.333 ± 1.9	0.195 ± 0.10	17	6.36 ± 4.9	11	67.0 ± 2.7	1.4e10	72
NIBT	*0.0790 ± 0.079	*0.142 ± 0.022	28	4.80 ± 1.2	12	245 ± 19	4.1e9	61

**Table D.4:** Time components in picosecond (ps) of ground state bleach (GSB) signals at various wavelengths from femtosecond transient absorption (fs-TA) results of BNIA in chloroform using 600nm pump

\*time component cannot be resolved since the components are within IRF (160fs)

\*\*time component cannot be resolved due to the large standard deviation

BNIA	GSB peak (nm)	* $\tau_{rise}$ (ps)	$\tau_1$ (ps)	A1 (%)	$\tau_2$ (ps)	Rates	A2 (%)
NITV	560	$0.0819 \pm 0.014$	$0.186 \pm 0.13$	36	$52.1 \pm 1.0$		64
NIDT	554	$0.0828 \pm 0.023$	** $-5.99 \pm 13$	0.34	$73.2 \pm 2.5$		99.7
NIBT	629	$0.106 \pm 0.064$	$0.227 \pm 0.040$	46	$273 \pm 23$		54

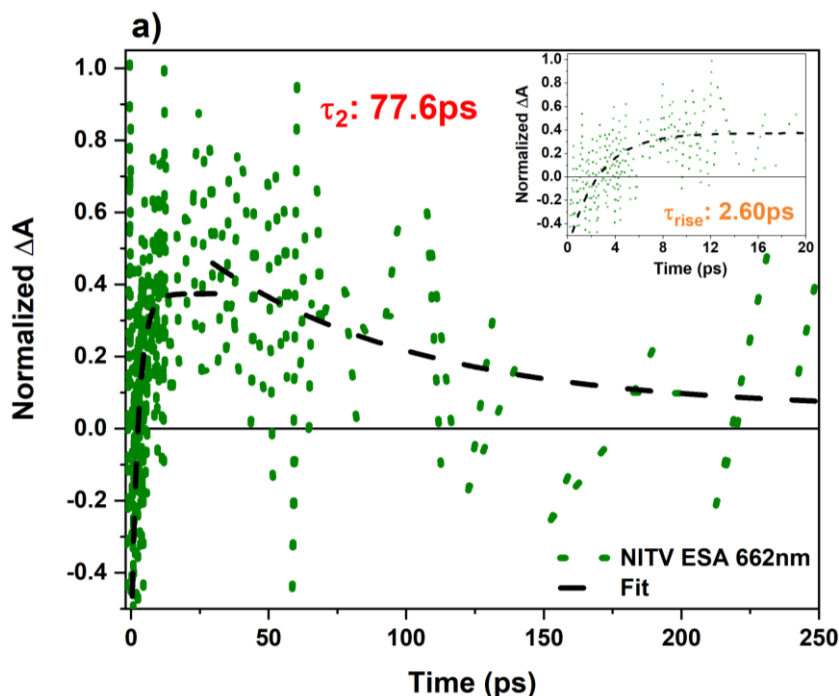


**Figure D.10:** Kinetics of excited state absorption (ESA) signals from femtosecond transient absorption (fs-TA) of BNIA in chloroform using 600nm – a) NITV; b) NIDT and c) NIBT

**Insert Graph:** zoomed in scale of kinetics of ESA signals, showing the rise time,  $\tau_{rise}$ , of ESA signals



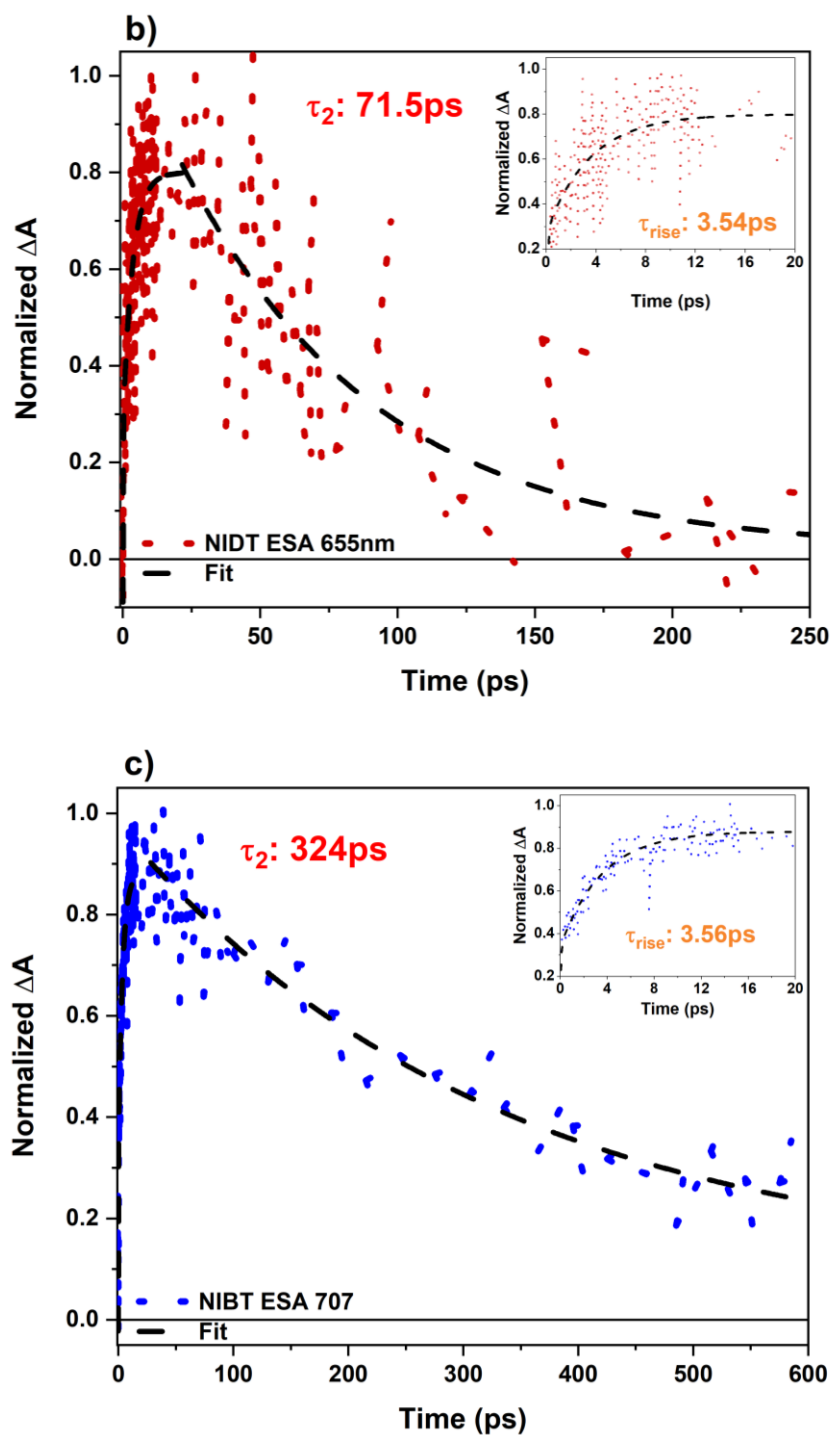


**Figure D.10 (continued):** Kinetics of excited state absorption (ESA) signals from femtosecond transient absorption (fs-TA) of BNIA in chloroform using 600nm – **a)** NITV; **b)** NIDT and **c)** NIBT

**Insert Graph:** zoomed in scale of kinetics of ESA signals, showing the rise time,  $\tau_{\text{rise}}$ , of ESA signals

**Table D.5:** Time components in picosecond (ps) of ground state bleach (GSB) and excited state absorption (ESA) signals from femtosecond transient absorption (fs-TA) results of BNIA in chloroform

\* $\tau_{rise*}$ : this time component cannot be resolved, since it is within the IRF (160fs). Since this time component cannot be resolved, it is not the main rise time of the ESA. This time component helped fit the data.

\*\*Rate: shows that rate of  $\tau_1$  time component

BNIA	ESA peak (nm)	* $\tau_{rise*}$ (ps)	$\tau_{rise}$ (ps)	A <sub>rise</sub> (%)	$\tau_1$ (ps)	**Rate (s <sup>-1</sup> )	A1 (%)
NITV	743	0.0170 ± 0.024	1.10 ± 0.24	48	63.9 ± 14	1.6e10	52
NIDT	730	0.147 ± 0.049	3.06 ± 0.86	24	58.0 ± 5.1	1.7e10	76
NIBT	715	0.0626 ± 0.018	4.92 ± 0.38	35	354 ± 42	2.8e9	65

**Table D.6:** Time components in picosecond (ps) of ground state bleach (GSB) and excited state absorption (ESA) signals from femtosecond transient absorption (fs-TA) results of BNIA in chloroform

\* $\tau_{rise*}$ : this time component cannot be resolved, since it is within the IRF (160fs). Since this time component cannot be resolved, it is not the main rise time of the ESA. This time component is helpful to fit the data.

BNIA	ESA peak (nm)	* $\tau_{rise*}$ (ps)	$\tau_{rise}$ (ps)	A <sub>rise</sub> (%)	$\tau_1$ (ps)	A1 (%)
NITV	662	NA	2.60 ± 0.47	62	77.6 ± 45	38
NIDT	655	0.0872 ± 0.025	3.54 ± 0.80	33	71.5 ± 11	67
NIBT	707	0.0493 ± 0.019	3.56 ± 0.25	38	324 ± 38	62

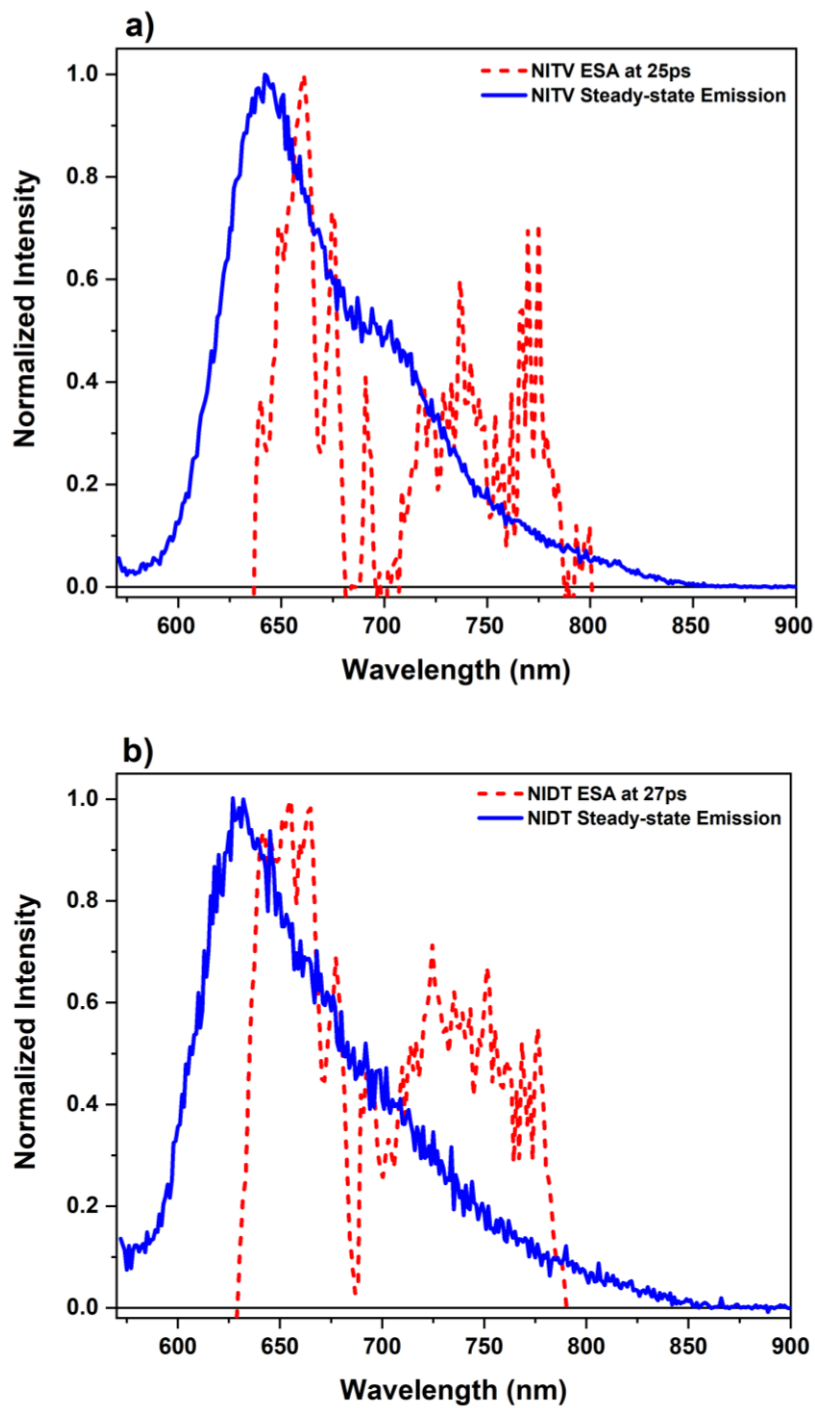


**Figure D.11:** Comparison of steady-state emission spectra to femtosecond transient absorption (fs-TA) excited state absorption (ESA) spectra of BNIA in chloroform using 600nm pump – a) NITV; b) NIDT and c) NIBT.

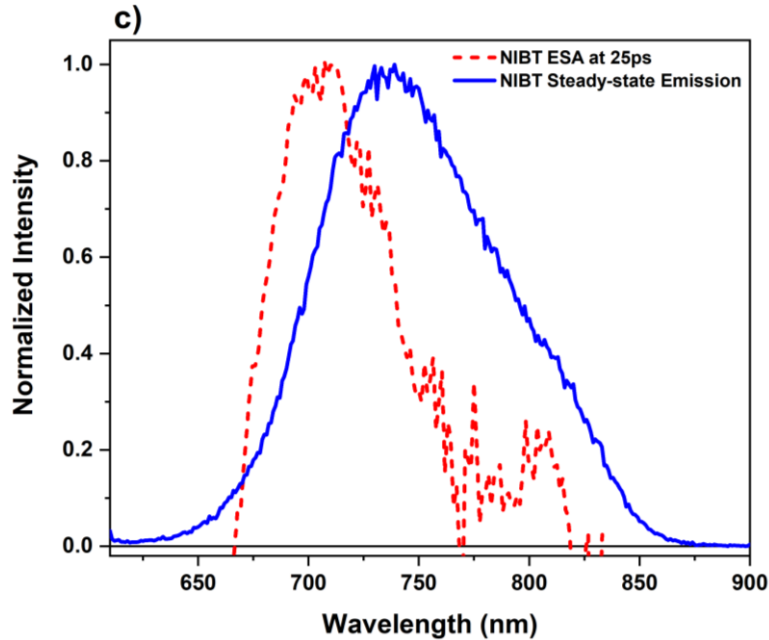


**Figure D.11 (continued):** Comparison of steady-state emission spectra to femtosecond transient absorption (fs-TA) excited state absorption (ESA) spectra of BNIAs in chloroform using 600nm pump – a) NITV; b) NIDT and c) NIBT.

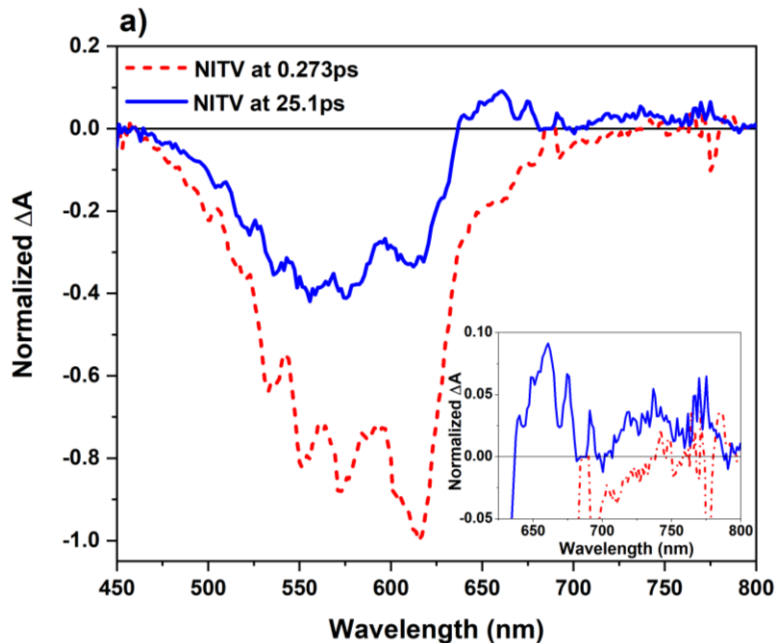


**Figure D.12:** Comparing early time femtosecond transient absorption (fs-TA) spectra to a later time fs-TA– a) NITV; b) NIDT and c) NIBT. By comparing two times, this shows approximation of percentage of exciton generated to transfer to charge transfer (CT) state (ESA signal) and have the potential to become free charges.

a) NITV: approximately 10%; b) NIDT: approximately 15%; and c) NIBT: approximately 40%

The approximation is determined by normalizing the early time of fs-TA spectra to the highest value. Then, dividing later time fs-TA spectrum by the highest value for the early time fs-TA spectrum

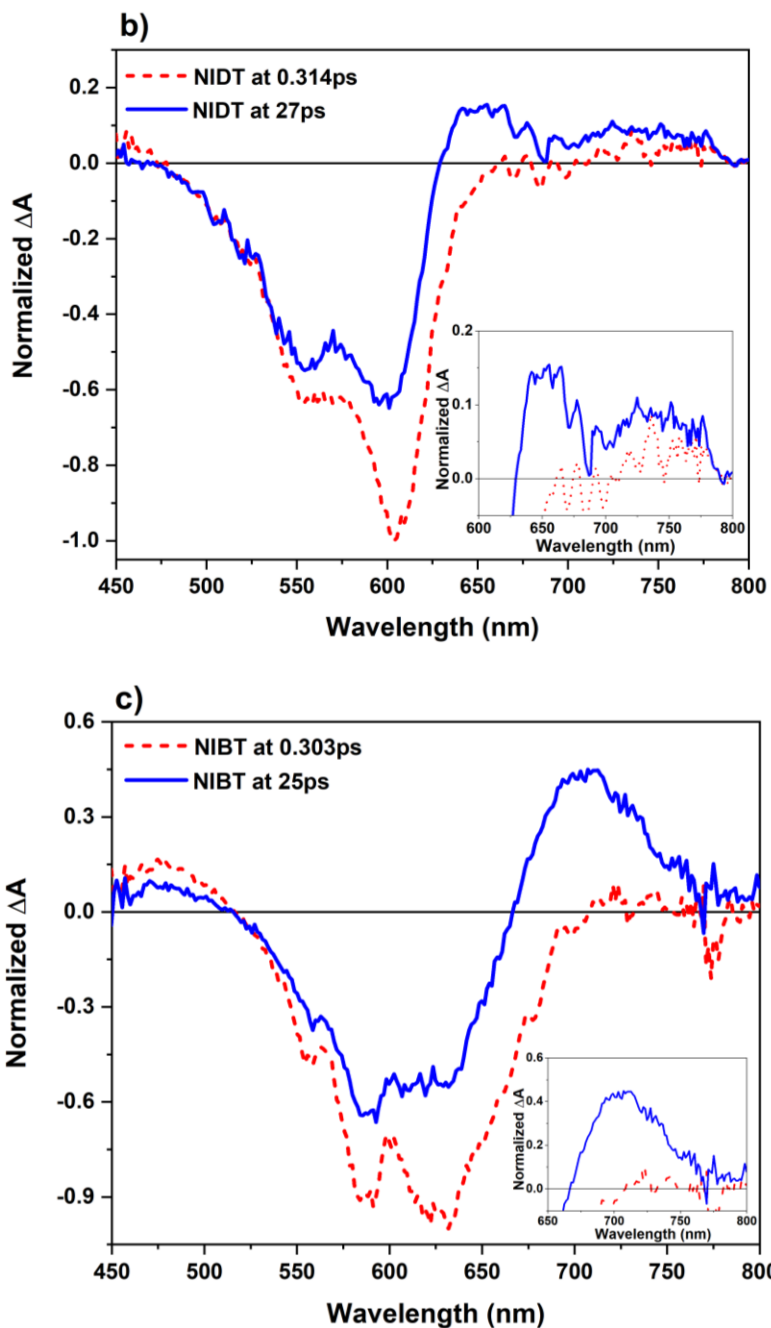


**Figure D.12 (continued):** Comparing early time femtosecond transient absorption (fs-TA) spectra to a later time fs-TA– a) NITV; b) NIDT and c) NIBT. By comparing two times, this shows approximation of percentage of exciton generated to transfer to charge transfer (CT) state (ESA signal) and have the potential to become free charges.

a) NITV: approximately 10%; b) NIDT: approximately 15%; and c) NIBT: approximately 40%

The approximation is determined by normalizing the early time of fs-TA spectra to the highest value. Then, dividing later time fs-TA spectrum by the highest value for the early time fs-TA spectrum

The normalized spectra is reported in paper. For all BNIA, the fs-TA spectra are normalized to the highest value of ground state bleach (GSB) signal in the spectra.

**Table D.7:** Stokes Shift (difference in nm) and difference between steady-state absorption, emission and ESA peaks

The information provides information for the proposed mechanism diagram of the BNIA, **Figure IV.11** in paper

a) NITV – Table units nm and eV

NITV					
Absorption (nm)	Absorption (eV)	Emission (nm)	Emission (eV)	Difference (nm)	Difference (meV)
566	2.19	643	1.93	77.00	262
600	2.07	643	1.93	43.00	138
Emission (nm)	Emission (eV)	ESA (nm)	ESA (eV)	Difference (nm)	Difference (meV)
643	1.93	662	1.87	19.00	55
643	1.93	743	1.67	100.00	260
Absorption (nm)	Absorption (eV)	ESA (nm)	ESA (eV)	Difference (nm)	Difference (meV)
566	2.19	662	1.87	96.00	318
600	2.07	743	1.67	143.00	398
566	2.19	743	1.67	177.00	522
600	2.07	662	1.87	62.00	194

a.i) NITV – Table unit  $\text{cm}^{-1}$

NITV		
Absorption ( $\text{cm}^{-1}$ )	Emission ( $\text{cm}^{-1}$ )	Difference ( $\text{cm}^{-1}$ )
1.77E+04	1.56E+04	2.12E+03
1.67E+04	1.56E+04	1.11E+03
Emission ( $\text{cm}^{-1}$ )	ESA ( $\text{cm}^{-1}$ )	Difference ( $\text{cm}^{-1}$ )
1.56E+04	1.51E+04	4.46E+02
1.56E+04	1.35E+04	2.09E+03
Absorption ( $\text{cm}^{-1}$ )	ESA ( $\text{cm}^{-1}$ )	Difference ( $\text{cm}^{-1}$ )
1.77E+04	1.51E+04	2.56E+03
1.67E+04	1.35E+04	3.21E+03
1.77E+04	1.35E+04	4.21E+03
1.67E+04	1.51E+04	1.56E+03

b) NIDT – Table units nm and eV

NIDT					
Absorption (nm)	Absorption (eV)	Emission (nm)	Emission (eV)	Difference (nm)	Difference (meV)
560	2.21	630	1.97	70	246
604	2.05	630	1.97	26	85
Emission (nm)	Emission (eV)	ESA (nm)	ESA (eV)	Difference (nm)	Difference (meV)
630	1.97	655	1.89	25	75
630	1.97	730	1.70	100	270
Absorption (nm)	Absorption (eV)	ESA (nm)	ESA (eV)	Difference (nm)	Difference (meV)
560	2.21	655	1.89	95.00	321
604	2.05	730	1.70	126.00	354
560	2.21	730	1.70	170.00	516
604	2.05	655	1.89	51.00	160

b.i) NIDT – Table unit  $\text{cm}^{-1}$

NIDT		
Absorption ( $\text{cm}^{-1}$ )	Emission ( $\text{cm}^{-1}$ )	Difference ( $\text{cm}^{-1}$ )
1.79E+04	1.59E+04	1.98E+03
1.66E+04	1.59E+04	6.83E+02
Emission ( $\text{cm}^{-1}$ )	ESA ( $\text{cm}^{-1}$ )	Difference ( $\text{cm}^{-1}$ )
1.59E+04	1.53E+04	6.06E+02
1.59E+04	1.37E+04	2.17E+03
Absorption ( $\text{cm}^{-1}$ )	ESA ( $\text{cm}^{-1}$ )	Difference ( $\text{cm}^{-1}$ )
1.79E+04	1.53E+04	2.59E+03
1.66E+04	1.37E+04	2.86E+03
1.79E+04	1.37E+04	4.16E+03
1.66E+04	1.53E+04	1.29E+03

c) NIBT – Table units nm and eV

NIBT					
Absorption (nm)	Absorption (eV)	Emission (nm)	Emission (eV)	Difference (nm)	Difference (meV)
628	1.97	737	1.68	109	292
628	1.97	810	1.53	182	444
Emission (nm)	Emission (eV)	ESA (nm)	ESA (eV)	Difference (nm)	Difference (meV)
737	1.68	707	1.75	-30	-71
737	1.68	715	1.73	-22	-52
Absorption (nm)	Absorption (eV)	ESA (nm)	ESA (eV)	Difference (nm)	Difference (meV)
628	1.97	707	1.75	79	220
628	1.97	715	1.73	87	240

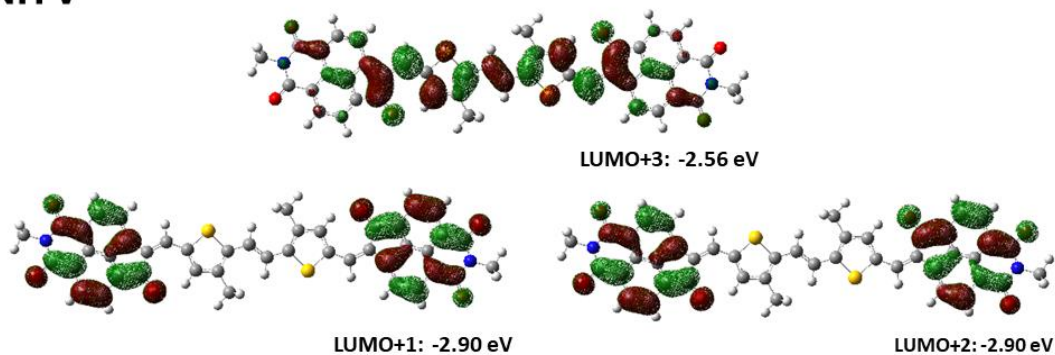
c.i) NIBT – Table unit  $\text{cm}^{-1}$

NIBT		
Absorption ( $\text{cm}^{-1}$ )	Emission ( $\text{cm}^{-1}$ )	Difference ( $\text{cm}^{-1}$ )
1.59E+04	1.36E+04	2.36E+03
1.59E+04	1.23E+04	3.58E+03
Emission ( $\text{cm}^{-1}$ )	ESA ( $\text{cm}^{-1}$ )	Difference ( $\text{cm}^{-1}$ )
1.36E+04	1.41E+04	-5.76E+02
1.36E+04	1.40E+04	-4.17E+02
Absorption ( $\text{cm}^{-1}$ )	ESA ( $\text{cm}^{-1}$ )	Difference ( $\text{cm}^{-1}$ )
1.59E+04	1.41E+04	1.78E+03
1.59E+04	1.40E+04	1.94E+03

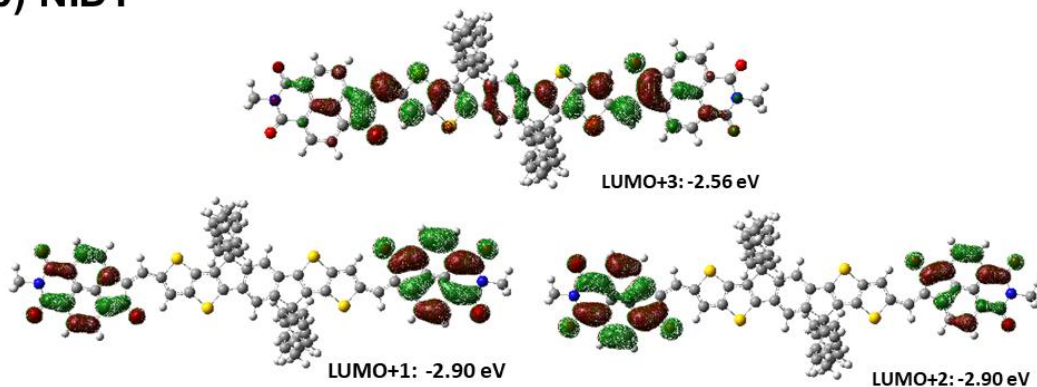


## D.5 Theoretical Calculation Results

### a) NITV



### b) NIDT



### c) NIBT

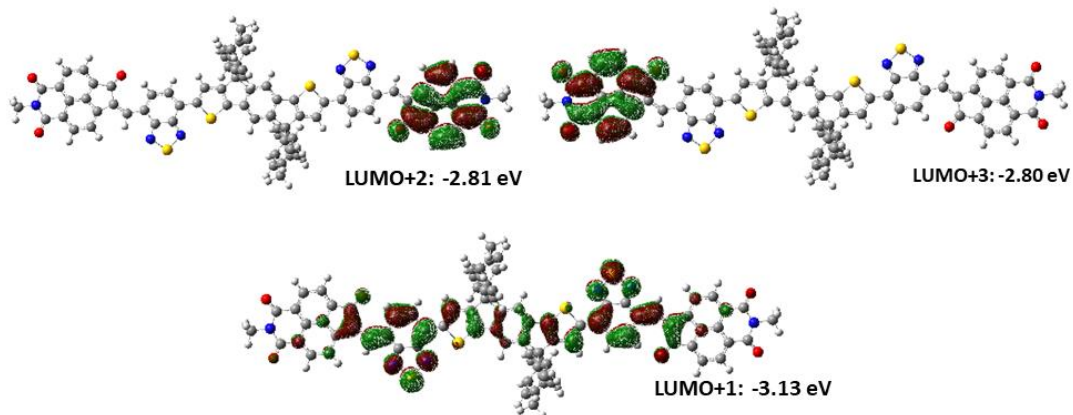


**Figure D.13:** Calculated higher excited states of lowest occupied molecular orbitals – LUMO+1, LUMO+2 and LUMO+3 – of BNIA from time-dependent density functional theory (TD-DFT) using B3LYP/6-31G(d,p) – a) NITV; b) NIDT; and c) NIBT

**Table D.8:** Summary of calculated oscillator strength values from time-dependent density functional theory (TD-DFT) using B3LYP/6-31G(d,p)

\*\*Vertical transition: positive direction of movement from the ground state to an excited state:  
 $S_0 \rightarrow S_n$

NITV		NIDT		NIBT	
**Vertical transition (nm)	Oscillator Strength	**Vertical transition (nm)	Oscillator Strength	**Vertical transition (nm)	Oscillator Strength
647	3.17	661	3.36	817	2.90
583	0.020	610	0.0011	614	0.0030
433	0.12	608	0.031	523	0.13
412	0.042	459	0.041	493	0.0018
		459	0.0099	471	0.53
		429	0.0067	470	0.13
		423	0.32	468	0.42
		415	0.016	465	0.016
		414	0.0002	465	0.0002